~~THE~~ BEHAVIOUR OF SWIRLING TURBULENT BOUNDARY LAYERS NEAR WALLS

by

BHARAT I. SHARMA, B.S., M.S., M.S.

Thesis submitted for the degree of
Doctor of Philosophy
in the Faculty of Engineering
University of London

and

for the Diploma of Membership
of
Imperial College of Science and Technology

September 1975

ABSTRACT

The thesis reports the outcome of an experimental and numerical study of turbulent shear flows generated or affected by swirling motion. The theoretical exploration has covered a wide range of axisymmetric flows for which experimental data are available including flow near spinning cones, discs, cylinders and an annulus with rotating core tube. The turbulence models employed are a version of the mixing length hypothesis and the two-equation energy-dissipation model.

The development of turbulent shear layers on rotating surfaces is usually characterised by a strong effect of streamline curvature on the turbulence structure. To account for this curvature the mixing length which would prevail in the absence of swirl is made a linear function of the local 'swirling flow' Richardson number. The direct effect of streamline curvature in the energy-dissipation model of turbulence is limited to a single empirical coefficient whose magnitude is directly proportional to the ratio of the time scale for significant rotational distortion to that of the energy containing turbulent motions. Agreement with available experimental data for these geometries is generally good. At high swirl rates, however, a few systematic differences between experiment and calculation become evident which are probably attributable to the non-isotropic nature of the effective viscosity in such complex strain fields.

To supplement the scarce experimental data of flow near spinning surfaces turbulence and mean velocity measurements are reported of flow near an 80 degree spinning cone in still air. Agreement between calculated and measured velocity and turbulence energy profiles at various spin Reynolds numbers is satisfactorily close.

ACKNOWLEDGEMENTS

I wish to express my sincere gratitude to my supervisor, Dr. B.E. Launder, for his advice, guidance and assistance throughout all stages of the project. His constructive suggestions and criticism on my writing have been so helpful in presenting this thesis. I am also indebted to Dr. F.C. Lockwood for his interest and valuable suggestions.

Thanks are also due to our librarian, Miss Archer, and the technical staff, in particular Mr. Bob King and Mr. Oscar Vis, who have contributed at various stages to the successful completion of this work. The excellent work of Miss Margaret Hudgell for the final typing of the thesis is deeply appreciated.

I am so indebted and grateful to my family for their constant encouragement, [illegible] understanding, and patience during the conduct of this work.

Finally, the financial support by the Science Research Council through contract B/RG/1863 is gratefully acknowledged.

CONTENTS

Page

APPENDICES

CHAPTER 1

INTRODUCTION

1.1 The problem considered and the present contribution

There are numerous practically important flows in the fields of turbomachinery and space projectiles where a fluid stream flows over a body rotating about its axis of symmetry. The rotating motion of the body generates shear stresses within the fluid imparting a swirl component of velocity in the flow. Rotation of the flow may occur as an initial swirl or else through the action of a body force field. An important feature of most swirling flows is the existence of streamline curvature that introduces a pressure variation in a direction perpendicular to the main flow. An engineer's principal hope of understanding and solving such complex flow problems is either through numerical computations or through laboratory simulations. The former approach has only been successful in laminar swirling flows where the transport properties are known. When, as is usually the case, the flow near the body is turbulent the analytic treatment of the rotating flows through numerical techniques is hampered because of the lack of information on the turbulent transport coefficients. For the relatively simple case of a turbulent core vortex, the values of turbulent viscosity suggested in the literature vary ten fold. Until the arrival of large, high speed computers and the development of a generalized turbulence theory the models of turbulence based on the eddy viscosity hypothesis will continue to be useful tools in the analytic prediction of complex turbulent processes.

Two such turbulence models extensively tested in the present study are a version of the mixing length hypothesis (MLH) and the two-equation energy-dissipation model. The numerical predictions of surface friction and heat and mass transfer for axisymmetric two dimensional boundary layers over spinning cones, discs, cylinders and an annulus with rotating core tube are obtained employing these models of turbulence. Agreement with available experimental data for these geometries is generally good. The main objective here has been to determine what level of predictive accuracy may be expected with these models and to discover in what respects the models require improvement (or replacement) to bring entirely satisfactory agreement.

The development of universal turbulence models and their subsequent testing must rely heavily on the available experimental data. To this end, and to supplement the scarce experimental data near spinning surfaces, turbulence and mean velocity measurements near an 80 degree cone rotating in still air are obtained by hot wire anemometry. Agreement between calculated and measured velocity and turbulence energy profiles at various spin Reynolds numbers is satisfactorily close.

1.2 Brief literature survey

A comprehensive survey of rotating flows, and of the various procedures to predict them in existence up to 1958 has been provided by Dorfman (1). Another extensive review of subsequent advances in the field has been made by Kreith (2). Both the works contribute substantially to the understanding of swirling flows and are standard references. The field of rotating flows is so extensive that the present review limits attention to turbulent wall flows where there is a single predominant direction and diffusive fluxes are significant only normal to this direction; these flows are commonly termed boundary layer. Analytical treatment of the flow field is discussed first, followed by a discussion on heat and mass transfer results, and then the available experimental data near spinning surfaces are reviewed.

Th. von Kármán (3) investigated the turbulent boundary layer on a disc spinning in stagnant surroundings by solving the integral forms of the momentum equations. The variation of the tangential velocity component through the boundary layer was assumed to obey the 1/7-th-power law and Blassius' friction formula for smooth pipes was used to calculate wall shear stress. The moment coefficient C_M was shown to be equal to $0.146\ Re^{-1/5}$. An approximate calculation based on the logarithmic velocity-distribution law was performed by Goldstein (4) who found the following formula for the moment coefficient:

$$\frac{1}{\sqrt{C_M}} = 1.97 \log (Re \sqrt{C_M}) + 0.03 \ .$$

Dorfman (5), like Goldstein, using a logarithmic velocity distribution obtained the overall drag on the disc. His calculation procedure was based on the use of self similar solutions and the moment coefficient C_M was shown to be equal to $0.157\ Re^{-1/5}$. Of the above three, Dorfman's results attained the best agreement with the experimental data. Kreith (6) generalized the turbulent boundary layer analysis of von Kármán for a rotating disc to cones of arbitrary vertex angles. He assumed the following velocity profiles to be in accord with the 1/7-th-power law for turbulent flow field in the vicinity of the cone:

$$U = U_o (z/\delta)^{1/7} (1 - z/\delta)$$

and

$$V_\theta = \omega x \sin\alpha \ [1 - (z/\delta)^{1/7}]$$

where U_o is a reference velocity obtained from shear stress relation. Performing a similarity analysis Kreith obtained a relation identical to von Kármán's for the moment coefficient i.e. $C_M = 0.146\ Re^{-1/5}$. Re here is the spin Reynolds number for the cone defined in the Nomenclature. The constant in this relation is about 7% below Dorfman's value of 0.157. Kreith's analysis and satisfactory agreement of his results with available experimental data thus showed that the usual boundary layer assumptions can be used with satisfactory accuracy to analyze the flow and drag characteristics of cones with vertex angles between 60 and 180 degrees in turbulent flow.

Cham and Head (7) calculated the development of the turbulent boundary layer on a disc rotating in free air, using tangential and radial momentum integral equations and an auxiliary equation of entrainment. In the calculations, circumferential velocity profiles were represented by a two parameter family, namely $V_\theta/r\omega = V_\theta/r\omega\,(H, R_\theta, z/\theta_{11})$, while radial profiles were given by a quadratic expression of the type: $U/r\omega = V_\theta/r\omega(1-z/\delta)^2 \tan\gamma$. All the symbols are defined in the Nomenclature. The entrainment, in dimensionless form, was assumed to be determined uniquely by the circumferential velocity profile. Cham and Head's calculations of entrainment and velocity-distributions were in good agreement with their detailed measurements on the rotating disc. From their experimental and theoretical results it was evident that the turbulent boundary layer on a rotating disc can be treated as a function of a single variable Re, the Reynolds number based on the radius. Parr (8) predicted the development of axial and circumferential momentum thicknesses on a rotating cylinder in an axial stream by solving the momentum integral equations. He obtained satisfactory agreement with his experimental data. Cham and Head extended their earlier method (7) to predict this flow situation. The mean velocity profiles were again represented by a two parameter family essentially similar to that used in their earlier study of flow near a rotating disc i.e. the profiles were specified by H and R_θ. The rate of entrainment of free stream fluid by the turbulent boundary layer was made a function of the velocity defect in the outer part of the layer and the ratio of circumferential to free stream velocity. Their method of calculation was a stepwise forward calculation starting from given initial conditions which were obtained from Parr's experiment; the starting position for each calculation was downstream of the transition point in all cases. Cham and Head's calculated velocity profiles agreed closely with those measured by Parr. Their overall satisfactory agreement of calculated torque coefficient with experiment also showed that all their assumptions were justifiable and their integral method of solution should be sufficiently accurate for engineering purposes. Furuya *et al.* (10) solved the momentum integral equations with fourth order polynomial representation of velocity components to obtain fair agreement with their data of velocity field over a rotating cylinder in an axial stream.

Recently, several workers have made use of finite difference procedures to predict swirling flows. Bayley and Owen (11,12) and Owen (13) obtained numerical solutions of the swirling, turbulent boundary layer equations using GENMIX, the finite difference procedure of Patankar and Spalding (14). The radial and circumferential shear stress components in the momentum equations were respectively expressed as:

$$\tau_{x,z} = \mu_{x,z} \frac{\partial U}{\partial z} \quad \text{and} \quad \tau_{z,\theta} = \mu_{z,\theta} \frac{\partial V_\theta}{\partial z} .$$

The effective viscosities $\mu_{x,z}$ and $\mu_{z,\theta}$ were calculated from the following extension of Prandtl's (15) mixing length hypothesis (MLH):

$$\mu_{x,z} = \mu + \rho \ell^2 \left|\frac{\partial U}{\partial z}\right| \quad \text{and} \quad \mu_{z,\theta} = \mu + \rho \ell^2 \left|\frac{\partial V_\theta}{\partial z}\right| .$$

In the region close to the wall the Van Driest (16) damping function with $\kappa = 0.4$ was employed i.e.

$$\mu_{x,z} = \mu + \rho\kappa^2 z^2 [1 - \exp(-z\sqrt{\rho\tau_{x,z}} / 26\mu)]^2 \left|\frac{\partial U}{\partial z}\right|$$

$$\mu_{z,\theta} = \mu + \rho\kappa^2 z^2 [1 - \exp(-z\sqrt{\rho\tau_{z,\theta}} /26\mu)]^2 \left|\frac{\partial V_\theta}{\partial z}\right| .$$

Far from the solid boundaries the mixing length ℓ was assumed equal to half the spacing between two walls of the stator and rotor of a parallel disc system with radial outflow. The above authors obtained qualitative agreement of circumferential drag and radial pressure distributions between their predictions and their experimental measurements over the whole range of data. Quantitative discrepancies, however, brought to light the non-universality of their simple mixing length approach.

Cooper (17) solved the continuity and momentum equations for the case of a free rotating disc by a two dimensional finite difference method. He modelled the Reynolds stress terms by a two layer scalar effective viscosity. In the layer close to the wall the effective viscosity was computed from the resultant of the radial and circumferential velocity gradients. The complete effective viscosity was calculated as:

$$\mu_{eff} = \mu_{x,z} = \mu_{z,\theta} = \mu + \rho\kappa^2 z^2 [1 - \exp(-z\sqrt{\rho\tau}/26\mu)]^2$$

$$\left[\left(\frac{\partial U}{\partial z}\right)^2 + \left(\frac{\partial V_\theta}{\partial z}\right)^2 \right]^{\frac{1}{2}}$$

where $\kappa = 0.4$, and τ is the local effective shear stress. For the outer part of the layer the viscosity was assumed proportional to the circumferential velocity displacement thickness and an intermittency factor. Cooper started his computations at the centre of the disc and assumed a step transition from laminar to turbulent flow at spin Reynolds number of 3.04×10^5. His predictions compared satisfactorily with the circumferential drag and velocity field data.

Koosinlin (18) has very recently obtained numerical solutions to the problem of the flow past a rotating cylinder using an energy-length model of turbulence. The turbulence energy k and the product of turbulence energy and length scale $k\ell$ are calculated by way of transport equations which are solved simultaneously with the conservation equations for the mean flow. The effective viscosity is then calculated from the relation originally suggested by Kolmogorov (19)

$$\mu_{eff} = \mu + \rho . k^{\frac{1}{2}} \ell \quad .$$

The 'k∿kℓ' model has been extensively used for fully turbulent non-swirling flows. But due to the uncertainty of the behaviour of k∿kℓ in the sub-layer Koosinlin used the turbulent solution of the Couette flow equations for the inner boundary specification. A 'log-law' type relation was assumed for the circumferential and axial velocities for the case of a rotating cylinder in an axial stream. The same relation is also applicable to circumferential velocity on a disc (20) but not for the radial velocity. This is because the centrifugal forces acting in the radial direction are analogous to a strongly varying cross-stream pressure gradient. The radial velocity profile has a maximum close to the wall in the region where the flow is not fully turbulent. The profile cannot therefore be described by a generally applicable relation like the log-law. For this reason, Koosinlin was unable to obtain reliable predictions for the disc flow using the 'k∿kℓ' model. Fairly good predictions of the boundary layer thicknesses and circumferential drag were obtained for the case of flow past the rotating cylinder by manipulation of the adjustable constants in the turbulence model.

Koosinlin also proposed and used a turbulence model derived from an analysis of the differential equations for the Reynolds stresses to obtain numerical solutions for the case of flow past a rotating cylinder. Transport equations were solved for the energy and length scale but six Reynolds stress components were expressed in terms of implicit algebraic relations containing time averaged velocity components, the turbulence energy and its rate of dissipation, and the stresses themselves. The turbulence model was restricted to regions where the local turbulence Reynolds number was high. To overcome this restriction the near-wall values of the two main Reynolds stresses $-\rho\overline{uv_\theta}$ and $-\rho\overline{v_\theta w}$ were determined from the modified van Driest mixing length expressions. Satisfactory agreement with velocity field data of Furuya *et al.* and with Parr's measurements of axial and circumferential momentum thicknesses was achieved. The turbulence model, however, lacks universality as some of the coefficients in the model require different values for different flow situations to obtain satisfactory agreement between predictions and experiment.

Turbulent heat transfer predictions for a disc rotating in stagnant surroundings were presented by Dorfman (5). He employed von Kármán's (3) results for the frictional drag, assumed a quadratic variation of surface temperature, and applied Reynolds analogy. He solved the energy equation assuming a one parameter family of temperature profiles. The constants in this equation were determined by the application of Reynolds analogy. Dorfman concluded that the Nusselt number varies with Reynolds number to the 0.8 power, and with Prandtl number to the 0.6 power. Davies (21) solved the case of an isothermal disc in air. He assumed 1/7-th-power velocity law and solved the integral radial momentum equation using von Kármán's results to obtain the radial component of shear stress. The diffusivity of the radial momentum was then equated to the diffusivity of heat and the temperature equation solved to determine the heat transfer. Davies found similar dependence to Dorfman's of Nusselt number on Reynolds number. Hartnett *et al.* (22) extended Davies solution procedure to non-isothermal discs, but equated the circumferential instead of the radial diffusivity of momentum to the diffusivity of heat. Their own predictions, along with those of Dorfman and Davies, were compared with the experimental heat and mass transfer data for isothermal discs rotating in stagnant surroundings. The predictions of Dorfman were the most reliable.

Tien (23) showed that the analytical treatment of Davies (21) to predict heat-transfer for isothermal discs could be extended to obtain solutions for non-isothermal cones, and also for discs and cones having a step distribution of surface temperature. Kreith (24) using law of the wall type velocity profiles (25) and Reynolds analogy solved the energy equation. He showed that the Nusselt number for isothermal cones varies with Reynolds number to the 0.8 power and with Prandtl number to the 0.75 power.

The reliable experimental data for flows on spinning surfaces are limited; but they are none-the-less the only ones available for comparison with numerical predictions. The following review therefore covers the most reliable experimental measurements for the few geometries when several set of data are available. A table at the end of this section establishes the different measurements available according to their relative value in developing and refining turbulence models.

One of the earliest reported experiments is that of Theodorsen and Regier (26) who measured the drag on a disc rotating in still air. Their turbulent flow measurements and the more recent measurements of Owen (13) confirm Dorfman's numerical predictions. Measurements of the velocity field near a rotating disc in the laminar, transitional and turbulent flow regimes were made by Gregory *et al.* (27). They found the transition Reynolds number to lie between 2.7×10^5 and $3. \times 10^5$. Their tangential velocity profiles were in good agreement with Cochran's (28) predictions for laminar flow, but the agreement for the radial velocity profiles was not good. For turbulent flow, both the 1/7-th-power profile assumed by von Kármán (3) and the logarithmic profile assumed by Goldstein (4) represented well the circumferential velocity measurements. The radial velocity profile was in good agreement with von Kármán's power law assumption close to the surface, but Goldstein's logarithmic profile was superior away from the surface.

Cham and Head (7) recently have reported comprehensive measurements of the velocity field and entrainment into the boundary layer on a free rotating disc. These authors obtained good agreement with their calculations using the tangential and radial momentum equation with an auxiliary equation for entrainment. Erian and Tong (29) while reporting the only experimental measurements of turbulence quantities for a disc rotating in still air also measured the velocity field. Because of experimental difficulties their measurements were incomplete.

Kreith *et al.* (30) investigated the transition characteristics of cones rotating in still medium. They found a rapid increase in the transition Reynolds number with increasing cone vertex angle. Kreith (24) also obtained a few measurements of the drag on a 60 degree cone rotating in still air. His experimental data substantiate well his theoretical predictions.

Koosinlin (18) has recently obtained turbulent velocity field measurements on an 80 degree rotating cone. Due to the inability of his pressure sensing instrumentation to measure low dynamic pressures accurately there is uncertainty about his measurements in the outer part of the boundary layer.

Parr (8) and Furuya *et al.* (10) have measured the velocity distribution on a cylinder rotating in an axial stream. The measurements have been well predicted by Cham and Head's (9) integral profile method. Extensive experimental data of annular, turbulent flow with rotating core tube have recently been obtained by Kuzay (52). The experimental studies of Kuzay were made in a vertical large gap annulus. The hydraulic diameter was 76 mm and the radius ratio, r_i/r_o was 0.56. For the first 14 hydraulic diameters the axial flow developed over a stationary section of core tube. There followed a section of rotating core tube 36 hydraulic diameters in length. In this configuration a series of experiments was made for Reynolds numbers from 17,000 to 65,000 and for rotational velocities of the core tube from zero to almost three times the bulk axial velocity. Outer wall static pressure and profiles of total pressure and flow angle were measured by means of total head probes. From these data profiles of static pressure and of axial and circumferential velocity were evaluated. One of the most striking features of the Kuzay data was that, provided the rotational velocity of the core tube was greater than the bulk axial velocity, the change in angular momentum from $r_i^2\omega$ at the core tube surface to zero at the outer wall was confined, almost entirely, to the two sub-layer/buffer zones adjacent to each cylinder. The whole of the fully turbulent region was rotating at essentially constant angular momentum.

The average turbulent heat transfer from an isothermal disc rotating in still air has been measured by Cobb and Saunders (31), McComas and Hartnett (32), and Dennis *et al.* (33). Mass transfer measurements at Schmidt number of 2.4 have been reported by Kreith *et al.* (34). Average mass transfer data at Schmidt number of 2.4 have also been reported by Tien and Campbell (35) for rotating cones of 60 to 180 degree vertex angles. Recently mass transfer data at high Schmidt numbers for a free rotating disc have been reported by Ellison (36) and Daguenet (37). The range of Schmidt numbers in Ellison's experiments extends from 34 to 1300 while that in Daguenet's extends from 345 to 6450. Local heat transfer coefficients on the rotating disc in still air have only recently been reported by Popiel and Boguslawski (38). Their measurements include laminar, transitional, and turbulent regions up to Reynolds number of 6.5×10^5.

The availability of reliable experimental data is of major importance in the effort to develop and test universal turbulence models. The following table lists the different available measurements according to their relative value in developing and refining turbulence models.

Table 1. Reliable measurements near spinning surfaces

Reynolds stresses (1)	Mean velocity (2)	Local heat/ mass transfer (3)	Average heat/ mass transfer (4)
	Cham-Head (7)	Popiel-Boguslawski (38)	Cobb-Saunders (31)
	Erian-Tong (29)		McComas-Hartnett (32)
	Koosinlin (18)		Kreith (24)
	Parr (8)		Kreith *et al.* (34)
	Furuya *et al.* (10)		Tien-Campbell (35)
	Kuzay (52)		Ellison (36)
			Daguenet (37)

A glance at the table shows that most of the data are category 4, followed by mean velocity measurements. There are no reliable data at all of the Reynolds stresses near spinning surfaces, a deficiency that ought to be removed.

1.3 Organisation of thesis

This thesis is divided into five chapters, of which this introduction presents the first.

The second chapter presents the relevant governing equations of fluid motion, the geometry and the nomenclature for swirling flows studied here. The derivation of the complete conservation equations is presented in Appendix 1. Included in this chapter is also a brief description of GENMIX, the computer program based on the finite difference procedure of Patankar and Spalding.

Chapter three containing the theoretical contribution forms the major portion of the thesis. The chapter is divided into six main sections. A brief description of the mixing length hypothesis for swirling flows is presented in the first section. This section is also concerned with the effect of stream line curvature on the mixing length. The reader is introduced to a 'swirling flow' Richardson number in this section. The energy-dissipation model of turbulence is presented in section two. The inclusion of the term containing the effect of stream line curvature and the complete governing turbulent transport equation set for swirling flow are respectively presented also in this section. The details of derivation are reserved for Appendices 2 and 3. Section three outlines the initial and boundary conditions; while section four lists some important computing details. Finally numerical predictions using the two turbulence models are systematically presented and discussed in detail in section five. Section six presents some concluding remarks on the performance of the two turbulence models.

Chapter four contains a description of the experimental contribution. It begins with a description of the experimental rig, the hot wire instrumentation, and the measurement details. The results obtained are then presented and discussed. The details of the hot wire signal analysis are presented in Appendix 4.

Finally chapter five summarizes the main conclusions from the present study. Recommendations are also made here for any possible further theoretical and experimental work.

CHAPTER 2

THE GOVERNING EQUATIONS OF MOTION

2.1 Geometry and the nomenclature for swirling flows

Figure 1 illustrates the geometry and the nomenclature for swirling flows considered in the present study. An axisymmetrical co-ordinate system for swirling flows is considered in Appendix 1, where the derivation of equations of motion is presented. The present work is confined to rotating cones, discs, and cylinders; for these geometries and flow situations the angle α has a constant value. The co-ordinates x, z, and θ are respectively the streamwise, cross-stream and circumferential directions. U, W, and V_θ are the respective velocity components in these directions. ω represents the angular velocity of the spinning surface.

2.2 The conservation equations

The elliptic forms of the conservation equations for mass, momentum, stagnation enthalpy and chemical species which describe the present class of axisymmetric flows are presented in Appendix 1. The boundary layer forms of the mass, streamwise and swirl momentum equations for a uniform-property, axisymmetric turbulent flow may be written:

$$\frac{\partial(rU)}{\partial x} + \frac{\partial(rW)}{\partial z} = 0 \qquad (2.1)$$

$$\rho U \frac{\partial U}{\partial x} + \rho W \frac{\partial U}{\partial z} = -\frac{\partial p}{\partial x} + \frac{1}{r}\frac{\partial}{\partial z}[r\mu_{eff}\frac{\partial U}{\partial z}] + \frac{\rho V_\theta^2}{r}\sin\alpha \qquad (2.2)$$

$$\rho U \frac{\partial(rV_\theta)}{\partial x} + \rho W \frac{\partial(rV_\theta)}{\partial z} = \frac{1}{r}\frac{\partial}{\partial z}[r^3\mu_{eff}\frac{\partial(V_\theta/r)}{\partial z}] \qquad (2.3)$$

where the notation is illustrated in Figure 1. The presence of swirl causes the static pressure to vary across the boundary layer. Provided the variation with x of the radius of curvature of the body is small, radial equilibrium may be assumed and hence:

$$\frac{\partial p}{\partial z} = \frac{\rho V_\theta^2}{r} \cos \alpha \tag{2.4}$$

The effective viscosity of the fluid, μ_{eff}, is taken as the sum of the molecular and turbulent contributions, i.e.

$$\mu_{eff} = \mu + \mu_t \tag{2.5}$$

Equations (2.1) to (2.4) constitute a closed set provided the fluid properties are known and a means is provided for determining μ_t. The determination of turbulent viscosity is the subject matter of the next chapter.

Heat and mass transfer rates from the surfaces are computed by solving the following equation for stagnation enthalpy $\hat{h}$ or the mass fraction of chemical species m:

$$\rho U \frac{\partial \hat{h}}{\partial x} + \rho W \frac{\partial \hat{h}}{\partial z} = \frac{1}{r} \frac{\partial}{\partial z} \left[r \frac{\mu_{eff}}{\sigma_{eff}} \frac{\partial h}{\partial z} + U\tau_{x,z} + V_\theta \tau_{\theta,z}\right] \tag{2.6}$$

$$\rho U \frac{\partial m}{\partial x} + \rho W \frac{\partial m}{\partial z} = \frac{1}{r} \frac{\partial}{\partial z} \left[r \frac{\mu_{eff}}{\sigma_{eff}} \frac{\partial m}{\partial z}\right] \tag{2.7}$$

Again, the derivation details are given in Appendix 1. In the above, the effective Prandtl/Schmidt number σ_{eff}, is related to the molecular and turbulent values by

$$\frac{\mu_{eff}}{\sigma_{eff}} = \frac{\mu}{\sigma} + \frac{\mu_t}{\sigma_t} \tag{2.8}$$

Equation (2.8) rests on the supposition that the effective transport coefficients for enthalpy and species are the sum of their molecular and turbulent values.

2.3 Numerical solution of the governing equations

Equations (2.1-2.4) and (2.6-2.7), together with the indicated auxiliary equations have been solved by means of GENMIX, the computer program based on the finite difference procedure of Patankar and Spalding (14). The success of the Patankar and Spalding finite difference procedure to solve two dimensional non-swirling flows has been established beyond doubt. The method is rapid and easy to use. The program deck used for the predictions presented here was developed from the simple disc version used by Koosinlin (18). The changes made to the original program of Patankar and Spalding are outlined in Appendix 5. The calculation procedure is well documented in reference (14) and it may therefore be sufficient only to outline the main features here.

The central feature of the method is the novel specification of the cross-stream co-ordinate. This co-ordinate is a dimensionless stream function ω defined as

$$\omega = \frac{\psi - \psi_I}{\psi_E - \psi_I} \qquad (2.9)$$

where ψ the stream function is defined by

$$\rho U = \frac{1}{r}\frac{\partial\psi}{\partial z} \qquad (2.10)$$

$$\rho W = -\frac{1}{r}\frac{\partial\psi}{\partial x} \qquad (2.11)$$

The quantities ψ_I and ψ_E are the values of ψ at the interior and exterior edges of the boundary layer. Thus, regardless of the width of the boundary layer, the co-ordinate ω always lies between zero and unity. Changes in the width of the finite difference grid or hence changes in the thickness of the boundary layer are determined from the rate of entrainment of fluid from the surroundings into the boundary layer. This practice confines the finite difference grid to the region of flow where the changes in the values of the dependent variables are relatively large. This feature results in great economy of computer time.

The governing partial differential equations (2.2-2.3) and (2.6-2.7) all possess the common form:

$$\frac{\partial\Phi}{\partial x} + (a + b\omega)\frac{\partial\Phi}{\partial\omega} = \frac{\partial}{\partial\omega}\left(c\frac{\partial\Phi}{\partial\omega}\right) + d \qquad (2.12)$$

where: $a = r_i\dot{m}_I/(\psi_E - \psi_I)$

$b = (r_E\dot{m}_E - r_I\dot{m}_I)/(\psi_E - \psi_I)$

$c = r^2\rho U\mu_{eff}/[(\psi_E - \psi_I)^2\,\sigma_{eff}]$

Here Φ stands for the dependent variable and d is the source term on the right-hand side which does not contain $\partial\Phi/\partial\omega$. $\dot{m}_I$ and $\dot{m}_E$ are the rates of mass transfer across the I and E surfaces. The common form allows a common numerical treatment for all the dependent variables except V_θ; only the exchange coefficients and the source term d are different for each dependent variable.

It should be noted that in the momentum equation for the swirl direction (2.3) the source term on the right-hand side has been entirely suppressed by making rV_θ the operand of the differentiations on the left and V_θ/r on the right. This necessitates some changes in the finite difference equations as outlined in (14). More details of these modifications and the computer program listing appear in Appendix 5.

The finite difference equivalent of equation (2.12) is obtained by means of a micro integral method. Each term of the equation is integrated over a small control volume around each node bounded by adjacent constant x and constant ω lines. On the assumption that Φ varies linearly with ω between grid nodes and stepwise in the x-direction, each term appears as an integrated average over the control volume. The use of the micro integral method ensures that the integral forms of the conservation equations are satisfied over any part of the boundary layer. The result of the integration yields the following finite difference equation:

$$\Phi_i = A\Phi_{i+1} + B\Phi_{i-1} + C \qquad (2.13)$$

where the subscript i designates a particular grid node. A, B and C are functions of the cross-stream grid spacing, the upstream values of Φ, and the coefficients of the differential equation (2.12). The set of equations (2.13) are solved to yield the values of the dependent variables in turn at each successive downstream grid location using a simple recurrence formula. In this way the solution progresses downstream in a marching fashion. Complete details of the above appear in reference (14).

Before application of the above solution procedure to turbulent swirling flows the accuracy of the finite difference procedure applied to swirling flows is tested. Figure 2 compares the finite difference predictions of the laminar flow induced by a spinning infinite disc with the similar solutions of Cochran (28) for the velocity field and Sparrow and Gregg (40) for the thermal field. The thermal solution is for a uniform disc temperature with a fluid Prandtl number of 0.7. The finite difference predictions of the radial and circumferential velocity profiles and of the temperature profile, are scarcely distinguishable from the "exact" similar solutions, the maximum discrepancy being less than 0.2%.

CHAPTER 3

TURBULENCE TRANSPORT MODELS

For turbulent flow calculations the effective viscosity μ_{eff} in equations (2.2-2.3) and (2.6-2.7) is taken as the sum of laminar and turbulent contributions i.e.

$$\mu_{eff} = \mu + \mu_t \qquad (3.1)$$

The present task is to propose and test a formula for the turbulent viscosity μ_t. In simple language, the term 'turbulence model' is used to describe the means whereby the turbulent viscosity μ_t is determined. Two such turbulence models considered and extensively tested in the present study are the Prandtl's (15) mixing length hypothesis (MLH) and Jones and Launder's (45) energy-dissipation model. Both the models rest on a well argued assumption that the turbulence is characterized by two quantities, a typical length scale ℓ and a fluctuating velocity v. From dimensional reasoning the turbulent viscosity is thus given by

$$\mu_t = \text{const.}\rho v \ell \qquad (3.2)$$

It is the different method of prescribing ℓ and v which differentiates the mixing length model from the energy-dissipation model of turbulence. The two turbulence models are separately discussed in detail next.

3.1 Mixing length hypothesis for swirling flows

Prandtl's (15) mixing length hypothesis (MLH) is one of the earliest and simplest proposed prescriptions for the calculation of turbulent viscosity, and has been widely used for non-swirling flow calculations. The physical basis on which the mixing length concept rests is not correct in all details, yet the model, because of its inherent simplicity and remarkable success, is still an attractive and useful proposition for the design engineer. The utility of the mixing length hypothesis has not been extensively explored for swirling flows. The present study therefore aims to investigate systematically the validity of the mixing length model for boundary layer flows near spinning surfaces.

For non-swirling flows, the fluctuating velocity component v appearing in equation (3.2) is presumed proportional to the absolute value of the gradient normal to the wall of the streamwise velocity U, i.e. $v = \ell \left|\frac{\partial U}{\partial z}\right|$. With the constant set to 1, the expression for the turbulent viscosity then becomes

$$\mu_t = \rho \ell^2 \left|\frac{\partial U}{\partial z}\right| . \tag{3.3}$$

Now, to account for the additional effect of swirl on the level of μ_t the following obvious simple extension of Prandtl's hypothesis is employed in the calculation of turbulent viscosity:

$$\mu_t = \rho \ell^2 \left[\left(\frac{\partial U}{\partial z}\right)^2 + \left(r \frac{\partial (V_\theta / r)}{\partial z}\right)^2 \right]^{\frac{1}{2}} \tag{3.4}$$

An alternative way (shown in Appendix 2) of arriving at equation (3.4) is to assume a local balance between the production and dissipation rates of turbulent kinetic energy ('local-equilibrium') and to represent the dissipation rate ε by $k^{3/2}/\ell$.

The above formulation used in (41) appeared superior to earlier proposals of Owen (13) and Lilly (42) in which the turbulent transport coefficient for angular momentum was held to depend only on gradients in swirling velocities, not axial ones. It should be noted that the gradient of V_θ/r and not of V_θ is employed in the last term of the equation (3.4) in order that μ_t becomes zero for the special case of solid body rotation. The chosen formulation implies that the turbulence is isotropic and this is its least attractive aspect. But it does, however, retain the basic simplicity of the mixing length formulation. No new physical constants are introduced.

3.1-1 The mixing-length distribution

Now all that remains in the determination of turbulent viscosity μ_t from equation (3.4) is the means to specify the mixing-length across the layer. A two part algebraic specification is adopted for the distribution of mixing length ℓ based on practices used by numerical workers for predicting flows without swirl. In the region where the presence of the wall affects the turbulence structure it is assumed that

$$\ell = \kappa z[1 - \exp(-D)] \tag{3.5}$$

where, following the recommendation of Launder and Priddin (43), the damping function D is taken as:

$$D = z_+ \tau_+^{3/2}/26 \tag{3.6}$$

when the variation of τ_+ across the viscous sublayer and 'buffer' regions is negligible, equation (3.6) is identical to Van Driest's (16) proposal for the damping of the mixing length at low Reynolds numbers. Launder and Priddin (43) have shown that the inclusion of $\tau_+^{3/2}$ gives better predictions where there is a rapid change in τ with z, as occurs in transpired boundary layers and flows with severe streamwise pressure gradient. It should be remarked that the local value of the resultant shear stress vector appears in equation (3.6).

In the outer region ℓ is given by:

$$\ell = \lambda\delta \tag{3.7}$$

δ being the effective thickness of the boundary layer. The constants κ and λ appearing in equations (3.5) and (3.7) are given the values 0.42 and 0.085 respectively, a consensus of values currently in use for plane external boundary layer flows. For internal flows, as discussed later, λ is given the value 0.14. Equation (3.7) is used in place of (3.5) at all positions further from the spinning surface greater than that at which ℓ given by (3.5) first exceeds the value given by (3.7).

3.1-2 Effect of swirl on mixing length

When the above turbulence model was applied to the calculation of turbulent flows on spinning surfaces it was learnt that the strong influence of streamline curvature was not well reproduced because the model did not take into account any direct influence of the swirl on the mixing length ℓ. Such shear flows with significant streamline curvature arise in many practically interesting flows. The importance of this subject has stimulated much experimental work that has recently been comprehensively reviewed by Bradshaw (44). The experimental studies have provided a qualitative understanding of the flow structure, the effect of curvature being to diminish turbulent transport in flows where the rate of change of angular momentum with radius is positive and *vice versa*. By analogy with the effects of density stratification in atmospheric turbulence Bradshaw (45) has proposed that the length scale in swirling flows be modified as follows

$$\ell = \ell_0(1 - \beta Ri) \tag{3.8}$$

where ℓ_0 is the level of mixing length prescribed by equations (3.5-3.7) above and Ri is the 'swirl flow' Richardson number:

$$Ri = \frac{\dfrac{2V_\theta \cos\alpha}{r^2} \dfrac{\partial (rV_\theta)}{\partial z}}{\left(\dfrac{\partial U}{\partial z}\right)^2 + \left(r \dfrac{\partial V_\theta / r}{\partial z}\right)^2} \tag{3.9}$$

which can be regarded as the ratio of the square of a typical frequency scale of the circumferential velocity fluctuations to the square of a frequency scale of the turbulence in the boundary layer. Because the circumferential velocity component is subject to centrifugal forces and is balanced by normal pressure gradient this highly unstable situation should give rise to large fluctuations. And if the frequency of turbulence is represented by some eddy frequency scale then the gradient of the resultant velocity can represent an appropriate scale. Next section and Appendix 3 in conjunction with the energy-dissipation model of turbulence discuss further the stability of a turbulent eddy in curved streamline flows. It should be noticed that $\cos\alpha$ is zero for flow near a spinning disc. In all the flows considered here (except the annulus with rotating core tube) rV_θ is maximum at the spinning surface and decreases uniformly to the edge of the boundary layer. For these cases the Richardson number is always negative and hence for positive β, ℓ is increased.

Predictions of the test flows were obtained for several values of β in the range from 1 to 15. The results presented here are for two values of β, 5 and zero. The latter corresponds with the 'standard' model for flows without swirl, the former is approximately that which gives the best overall level of agreement of predictions with measurement.

3.2 Energy-dissipation model of turbulence

In the last few years a number of models of turbulent momentum transport have been developed which take into account the effects of transport on turbulence. Models of this kind achieve significantly greater breadth of applicability than do the simple approaches based on mean flow quantities alone like the mixing length hypothesis. Such models can be constructed by taking the turbulent velocity scale as $k^{\frac{1}{2}}$ in equation (3.2). The turbulent viscosity formula then becomes

$$\mu_t = \text{const } \rho k^{\frac{1}{2}} \ell \qquad (3.10)$$

Thus, to determine μ_t two differential equations for the turbulence are formulated from which both velocity and length scale can be obtained. The turbulence kinetic energy equation is, without exception, one of those employed in these two-equation turbulence models. For the second variable it is often easier to derive an equation for some other quantity which can be related to a length scale of turbulence. Several workers have selected variables of the form $k^a \ell^b$ where $\underline{a}$ and $\underline{b}$ are constants. Examples of these can be found in reference (46). One of the more successful of these approaches is proposed by Jones and Launder (47) who solved an equation for the dissipation rate of turbulence energy ε, which can be related to length scale by the formula

$$\varepsilon = k^{3/2}/\ell \qquad (3.11)$$

This latter form has a number of advantages. This quantity appears directly in the equation for k, and so calculating it removes the need for any assumptions about this term. It is also a simple algebraic function of the fluctuating velocity gradients, and an exact equation can therefore be readily derived from the Navier-Stokes equations. The use of the ε-equation as the means of determining the turbulent length scale was shown by Launder *et al.* (48) to give the best predictions of the two-equation turbulence models tested for the case of free shear flows. Jones and Launder (47) also applied this model to strongly accelerated flow and subsequently to other low-Reynolds number flows (51, 50). Applications of the model for flows involving regions of recirculation appear in reference (49). For these reasons it is the Jones and Launder's low-Reynolds number k-ε model of turbulence that has been used in the present study. It should also be pointed out that no applications of the model have been reported, however, of its use to predict swirling flows, an omission that the present study remedies. The flows considered here produce very high gradients of swirl velocity in the vicinity of the spinning surface which in turn bring to prominence terms in the kinetic energy and dissipation equations that have formerly been absent or of only small importance. This extensive application thus provides a test of the generality of the model for an important class of fluid flows.

Combining equations (3.10) and (3.11) finally gives for the k-ε model the turbulent viscosity formula as

$$\mu_t = C_\mu \rho k^2/\varepsilon \tag{3.12}$$

where, at low Reynolds numbers, the quantity C_μ is a function of turbulent Reynolds number as prescribed below; at high Reynolds numbers it approaches a constant value. The two turbulence quantities appearing in (3.12), k and ε are obtained from the following pair of transport equations that are solved simultaneously with those governing the mean flow behaviour:

$$\rho \frac{Dk}{Dt} = \frac{\partial}{\partial x_j}\left[\left(\frac{\mu_t}{\sigma_k} + \mu\right)\frac{\partial k}{\partial x_j}\right] + \mu_t \frac{\partial U_i}{\partial x_j}\left(\frac{\partial U_i}{\partial x_j} + \frac{\partial U_j}{\partial x_i}\right) - \rho\varepsilon - 2\mu\left(\frac{\partial k^{\frac{1}{2}}}{\partial x_j}\right)^2 \tag{3.13}$$

$$\rho \frac{D\varepsilon}{Dt} = \frac{\partial}{\partial x_j}\left[\left(\frac{\mu_t}{\sigma_\varepsilon} + \mu\right)\frac{\partial \varepsilon}{\partial x_j}\right] + C_1 \mu_t \frac{\varepsilon}{k}\frac{\partial U_i}{\partial x_j}\left(\frac{\partial U_i}{\partial x_j} + \frac{\partial U_j}{\partial x_i}\right) - C_2 \frac{\rho\varepsilon^2}{k} + C_3 \nu\mu_t \left(\frac{\partial^2 U_i}{\partial x_k \partial x_j}\right)^2 \tag{3.14}$$

The derivation details of the above equations are given in Appendix 2. The empirical coefficients, after extensive testing, have been assigned the forms and values given in the table below; the quantity R_t stands for $\rho k^2/\mu\varepsilon$, the local Reynolds number of turbulence. A number of the coefficients have undergone small changes from those proposed in (47) due to an overall reoptimisation for free shear flows (48). However, for the flows considered here there would be only slight differences between the behaviour reported here and that which would have been obtained with the original set of coefficients.

Table 2. The empirically chosen coefficients

C_1	C_2	C_3	C_μ	σ_k	σ_ε
1.44	$1.92(1.-0.3\exp(-R_t^2))$	2.0	$0.09\exp(-3.4/(1+R_t/50)^2)$	1.0	1.3

3.2-1 Modification for streamline curvature

The k-ε model of turbulence presented so far assumes that there is no direct influence of rotation on turbulence. The aim here has been to build the idea of curvature dependence into the transport equation for the length scale of turbulence. Therefore the effects of streamline curvature in the present study are accounted for by making one of the coefficients in the transport equation for energy dissipation rate a function of a dimensionless group similar in character to the rotational Richardson number defined in section 3.1-2. Physical arguments in support of this modification are developed in terms of distorting effect of rotation on the length scale of energy containing motions. Complete details of this development and the reasons for the inclusion of a new source term in the transport equation for ε are presented in Appendix 3. Here the complete modified dissipation rate equation is written below:

$$\rho \frac{D\varepsilon}{Dt} = \frac{\partial}{\partial x_j}\left[\left(\frac{\mu_t}{\sigma_\varepsilon} + \mu\right)\frac{\partial \varepsilon}{\partial x_j}\right] + C_1 \frac{\varepsilon\mu_t}{k}\frac{\partial U_i}{\partial x_j}\left(\frac{\partial U_i}{\partial x_j} + \frac{\partial U_j}{\partial x_i}\right)$$

$$- C_2 \frac{\rho\varepsilon^2}{k}(1 - C_c Ri) + C_3 \nu\mu_t \left(\frac{\partial^2 U_i}{\partial x_k \partial x_j}\right) \qquad (3.15)$$

where Ri is the dimensionless parameter;

$$\frac{k^2}{\varepsilon^2}\frac{V_\theta}{r^2}\frac{\partial(rV_\theta)}{\partial r} \qquad (3.16)$$

which again may be regarded as a Richardson number wherein the time scale of the turbulence k/ε now replaces the mean flow time scale appearing in equation (3.9).

All coefficients in equation (3.15) retain the values assigned to them in Table 2 and the additional coefficient of the Richardson number term C_c is taken as 0.2 on the basis of extensive computer optimisations. It should be noted that when the angular momentum of the mean flow increases with radius Ri is positive and hence the new term will act to enlarge the level of ε and hence to reduce the turbulence kinetic energy. Consequently the inclusion of the Richardson number dependent term acts to diminish the turbulent viscosity (c.f. equation (3.12)). The reverse effects are produced in a flow where $\partial(rV_\theta)/\partial r$ is negative.

3.2-2 The governing turbulence transport equation set for axisymmetric swirling flow

The above sections have presented the turbulence transport equations in Cartesian tensor notation. When it comes to obtaining numerical solutions, however, it is strongly advantageous to convert to a co-ordinate system in which the solid surface coincides with a surface on which one of the independent variables is constant. For the flows on axisymmetric surfaces considered here the system of polar co-ordinates indicated in Figure 1 is the obvious choice. When account is taken of axial symmetry and the fact that significant gradients of the dependent variables occur only in the direction normal to the surface the k and ε equations (3.13) and (3.15) may respectively be written:

$$\rho U \frac{\partial k}{\partial x} + \rho W \frac{\partial k}{\partial z} = \frac{1}{r}\frac{\partial}{\partial z}\left[r\left(\frac{\mu_t}{\sigma_k} + \mu\right)\frac{\partial k}{\partial z}\right]$$

$$+ \mu_t \left[\left(\frac{\partial U}{\partial z}\right)^2 + \left(r\,\frac{\partial V_\theta/r}{\partial z}\right)^2 \right] - \rho\varepsilon - 2\mu \left(\frac{\partial k^{\frac{1}{2}}}{\partial z}\right)^2 \tag{3.17}$$

$$\rho U \frac{\partial \varepsilon}{\partial x} + \rho W \frac{\partial \varepsilon}{\partial z} = \frac{1}{r}\frac{\partial}{\partial z}\left[r\left(\frac{\mu_t}{\sigma_\varepsilon} + \mu\right)\frac{\partial \varepsilon}{\partial z}\right]$$

$$+ C_1 \frac{\varepsilon\mu_t}{k}\left[\left(\frac{\partial U}{\partial z}\right)^2 + \left(r\,\frac{\partial V_\theta/r}{\partial z}\right)^2 \right] - C_2 \frac{\rho\varepsilon^2}{k}\left(1 - C_c Ri\right)$$

$$+ C_3 \nu\mu_t \left\{ \frac{\partial}{\partial z}\left[\left(\frac{\partial U}{\partial z}\right)^2 + \left(r\,\frac{\partial V_\theta/r}{\partial z}\right)^2 \right]^{\frac{1}{2}} \right\}^2 \tag{3.18}$$

The algebraic details of the derivation of these equations are again reserved for Appendix 2. It should, however, be noted that the above system of equations differs from that of Jones and Launder (47) in that extra source terms involving gradients of (V_θ/r) appear in the equations for k and ε. Their appearance is due to the conversion of the Cartesian tensor form of the equations to the present co-ordinate frame. For example, the rate of production of turbulence energy by mean strain for plane shear flows is simply $\mu_t\left(\frac{\partial U}{\partial z}\right)^2$ in the Jones and Launder's version. But here this term is represented as

$$\mu_t\left[\left(\frac{\partial U}{\partial z}\right)^2 + \left(r\,\frac{\partial V_\theta/r}{\partial z}\right)^2 \right]$$

in both the k and ε equations. Similarly the term $C_3\nu\mu_t\left(\frac{\partial^2 U}{\partial z^2}\right)^2$ in the original ε-equation is now written as

$$C_3\nu\mu_t\left\{ \frac{\partial}{\partial z}\left[\left(\frac{\partial U}{\partial z}\right)^2 + \left(r\,\frac{\partial V_\theta/r}{\partial z}\right)^2 \right]^{\frac{1}{2}} \right\}^2 .$$

It should also be remarked that the Reynolds number functions C_μ and C_2 and the coefficient C_1 are slightly different from those proposed by Jones and Launder (47). This, as pointed out earlier, is the result of an overall computer re-optimisation of coefficients reported in (48).

The values of k and ε obtained from the solution of these equations (3.17 and 3.18) enable the turbulent viscosity to be obtained from equation (3.12), viz.

$$\mu_t = C_\mu \rho k^2/\varepsilon \quad .$$

3.3 Boundary and initial conditions

The boundary conditions for all flows computed and with both the turbulence models considered here were as follows. For the mean velocity field, both the axial and swirl velocities are set to zero at the edge of the boundary layer except for the case of flow past a rotating cylinder, where for axial velocity free stream velocity U_∞ is the appropriate quantity. At the spinning surface U is set to zero and V_θ to $r\omega$ where r and ω are the local radius and the angular velocity of the surface. These, and the boundary conditions for the other dependent variables $\hat{h}$ and m may be summarized as follows:

$$z = 0 : \quad \begin{aligned} U &= 0 \; ; & V_\theta &= r\omega \\ \hat{h} &= \hat{h}_w \; ; & m &= m_w \end{aligned} \tag{3.19}$$

$$z = z_{edge} : \quad \begin{aligned} U &= 0 \text{ or } U_\infty \; ; & V_\theta &= 0 \\ \hat{h} &= h_\infty \; ; & m &= m_\infty \end{aligned} \tag{3.20}$$

While making predictions with the energy-dissipation model of turbulence, the values of k and ε are set to very small values at the outer edge of the boundary layer as is appropriate to free stream conditions. Their value is set to zero at the wall: for k this corresponds with the fact that velocity fluctuations must vanish at a rigid surface. To explain the reason for making ε zero at the wall it should first be noted that within the viscous sublayer

$$\mu\overline{\left(\frac{\partial u_i}{\partial x_k}\right)^2} = 2\mu\left(\frac{\partial k^{\frac{1}{2}}}{\partial z}\right)^2 \tag{3.21}$$

A proof is provided by Launder and Jones in (47). Thus if ε stands for

$$\mu\overline{\left(\frac{\partial u_i}{\partial x_k}\right)^2} - 2\mu\left(\frac{\partial k^{\frac{1}{2}}}{\partial z}\right)^2$$

its value obviously goes to zero as the wall is approached. Beyond the viscous sublayer the term involving the gradient of $k^{\frac{1}{2}}$ is negligible and then ε represents the dissipation correlation $\mu\overline{(\partial u_i/\partial x_k)^2}$. The term $2\mu(\partial k^{\frac{1}{2}}/\partial z)^2$ is then subtracted from the right-hand side of the kinetic energy equation to compensate (cf. equation (3.17)). The reason for this apparently circuitous route is that by using the homogeneous boundary conditions on ε it was found to be easier to devise a suitable form for the ε-transport equation. Further discussion on this matter is provided in Appendix 2.

Starting profiles of all dependent variables had, of course, to be prescribed. In all cases estimates were based on experimental knowledge of the dependent variable distribution in the same or similar flows. Some further remarks on initial profiles for individual geometries appear in the next section. The actual profiles of the dependent variables (including k-ε) used in the present study are listed in Appendix 5. It should be emphasized however that in all the cases examined here the predicted flow behaviour, in the regions where comparison is drawn with experiment, is negligibly dependent upon uncertainties in the prescribed initial profiles.

3.4 Some computing details

The system of differential equations (2.2-2.3), (2.6-2.7) and (3.17-3.18), together with the indicated auxiliary equations have been solved by means of the modified version of GENMIX, the computer program outlined in Chapter 2. The actual detailed modifications for swirling flows to the computer program GENMIX are listed in Appendix 5. Here, some details about computing times and grid node specification for the two turbulence models are presented. For the case of flow over spinning discs and cones computations were started near the centre or apex where the flow was laminar, then the turbulent viscosity as calculated by mixing length hypothesis or by the solution of the k and ε equations was introduced later at the point where experiments suggested that transition occurs.

For predictions with the mixing length model forty cross-stream grid nodes were used nearly half of which were concentrated in the sublayer and buffer regions where gradients of dependent variables are steepest. The step size normally used varied between 2 to 5% of the boundary layer thickness. Computing time per run on a CDC 6600 computer was typically 10 s. More details for some individual cases studied appear under comparison of predictions and measurements in the next section.

With the energy-dissipation model of turbulence seventy grid nodes were used to span the boundary layer with a substantial concentration very near the wall. This is about 60% more than is needed to obtain grid independent results when the mixing length model is used. The forward step used here was typically 2.5% of the boundary layer thickness leading to computer times per run of about 50 s on the CDC 6600 computer. Again, more specific details about some individual cases are given in the next section.

3.5 Presentation and discussion of predictions

The numerical predictions obtained using the above turbulence models are compared with the available experimental data in this section. Since several flow configurations are examined each flow geometry is separately discussed in detail. Some remarks on the performance of the two turbulence models appear at the end of this section.

3.5-1 Flow near swirling disc

Comparison of predictions with measurements is drawn first for the important limiting case of a spinning disc in still air. The Richardson number Ri in this case is zero at all rotational speeds because the radii of curvature of the streamlines are virtually parallel with the disc surface. Calculations relating to turbulent flow near a spinning disc using both models of turbulence are presented in Figures 3-8. Mean velocity profiles are shown in Figures 3 and 4, the experimental data being those of Erian and Tong (29) and Cham and Head (7). Both components of velocity are normalized with respect to the surface velocity. The ordinate for Erian and Tong's experiment is $z\sqrt{\omega/\nu}$ whereas in Cham and Head's test case it is z/δ_2. All symbols are defined in the Nomenclature. The shape of the profiles is distinctly different from those for laminar flow in Figure 2. As in non-swirling flows, very steep velocity gradients occur in the immediate neighbourhood of a wall because stresses there are high but effective viscosities low. For both test conditions and with both turbulence models extremely close agreement is observed between measured and calculated components of swirl velocity. The axial velocity using the mixing length model is well predicted for Cham and Head's experiment and for values of $z\sqrt{\omega/\nu}$ up to 20 in Erian and Tong's work. Thereafter, however, the predicted velocity falls to zero much more quickly than the measured. With the $k-\varepsilon$ model the axial velocity is in close agreement with both the experimental data. To show the differences in predicted behaviour clearly velocity profiles with both the models are also shown on the same Figures 3b and 4b. It is uncertain which of the experimental axial velocity profiles is more correct. It should be noted, however, that in the region where there is disagreement between the mixing length predictions and Erian and Tong's data, the average velocity is only about 3% of the disc velocity. It would thus seem unlikely that failure to predict the mean velocity correctly would have noticeable effect on surface heat and mass transfer coefficients.

To make accurate predictions of torque coefficient and Nusselt/ Schmidt number, the Reynolds number Re_t at which the flow becomes turbulent must be prescribed (when the distance x is so small that the spin Reynolds number is less than Re_t the flow is taken as laminar and only the mean flow equations are solved). It may be expected that Re_t will vary a little from one apparatus to another because of detailed differences in apparatus design. The practice here has therefore been to choose the value of Re_t which seemed most consistent with any particular apparatus. For this reason different values of Re_t have sometimes been adopted for nominally the same geometry.

The corresponding variation of torque coefficient with spin Reynolds number for the rotating disc is shown in Figure 5; Re_t was taken as 2.8×10^5. Predictions with both turbulence models are almost identical and for this reason they are shown separately on two diagrams for completeness. The agreement with the measurements of Theodorsen and Regier (26) is within 5% over the whole range spanned by these data. The more recent measurements of Kreith (24) and Owen (13) give values of C_M which are 5-10% higher than those of (26). Thus it is probably the case that the predictions fall within the bounds of experimental uncertainty for this flow.

Predictions of average heat and mass transfer rates for the rotating-disc geometry are shown in Figures 6 and 7; the transition Reynolds number Re_t was taken as 2.4×10^5 and 2.0×10^5 respectively, i.e. a little lower than for the comparisons shown in Figure 5. For both the heat and mass transfer predictions σ_t in equation (2.8) is given the value of 0.9. The works of Kestin and Richardson (39) and Patankar and Spalding (14) support this hypothesis for wall boundary layers. The agreement of predictions with both the mixing length and k-ε models with the Nusselt number data of McComas and Hartnett (32) is complete over the Reynolds number range explored; the data of Cobb and Saunders (31) lie about 6% above this. The mass transfer predictions at Schmidt number of 2.4 are satisfactory for spin Reynolds number below 5×10^5. Above this value however, both the Tien and Campbell (35) data and those of Kreith *et al.* (34) display a faster rate of increase with spin Reynolds number than do the predictions. The average mass transfer predictions at high Schmidt numbers are compared with the data of Ellison (36) and Daguenet (37) in Figure 7. Ellison's data covered the Schmidt number range from 30 to 1000 at spin Reynolds number of 4.7×10^5, whereas in the experiments of Daguenet Schmidt number varied from 345 to 6150 at spin Reynolds number of 5.5×10^5. Agreement of predictions with both sets of data is close up to a Schmidt number of about 800, thereafter the predictions fall progressively below the data of Daguenet. Predictions with the k-ε model are marginally closer to the data of Daguenet than those with the mixing length model.

The relatively different behaviour for the heat and mass transfer at high spin Reynolds number (Fig.6), it is believed, is probably associated with the different molecular Prandtl/Schmidt number (0.7 and 2.4 respectively) and the effective viscosity becoming highly non-isotropic as the level of swirl increases (some evidence of this is provided later). If this is the case Figure 6 (and Figures 9-10 later) suggest that it is in the immediate near wall region where viscous damping is important that the turbulent transport coefficient is especially anistropic. For the heat transfer data are well predicted while the mass transfer data are not. Now for the present purposes the only significant difference between the heat and mass transport process is that the near-wall region offers proportionately a much greater resistance to mass transfer than heat transfer. The different behaviour could be explained if it is in the near-wall region that these turbulence models, so firmly based on the notion of an isotropic effective viscosity, break down. It would be valuable to extend the high Schmidt number data for higher spin Reynolds numbers. Agreement with the data of Ellison and Daguenet as noted above is satisfactorily close for the relatively low levels of spin Reynolds number in their experiments.

Predictions of *local* heat transfer rate from a spinning disc are compared with the very recent data of Popiel and Boguslawski (38) in Figure 8. The transition Reynolds number was again taken as 2.4×10^5. Agreement of predictions using both the turbulence models with the local Nusselt number data is satisfactorily close over the entire Reynolds number range explored. In the experiment, with laminar boundary layer the disc surface was maintained almost isothermal; with transition boundary layer it was isothermal within ±1.5%; and with the turbulent boundary layer it was isothermal within ±3%. The predictions for the turbulent boundary layer are within this ±3% deviation with both turbulence models. The small deviation of the measurements at low Reynolds numbers from the predicted values is probably due to the free convection effects having been neglected in the predictions.

3.5-2 Flow near spinning cones in still air

Predictions of convective transport from spinning cones of different vertex angles are shown in Figures 9-12. It should be noticed that as the cone angle diminishes the influence of streamline curvature becomes more important. Predictions using both the turbulence models with and without respective curvature correction are separately compared with the available experimental data. First, the predictions for the 120 degree cone are compared with the naphthalene (Sc = 2.4) diffusion measurements of Kreith *et al.* (24) and Tien and Campbell (35). No heat transfer or torque data appear to be available for the 120 degree cone. The two sets of data display a similar behaviour to the disc data. With a transition Reynolds number of 2×10^5, agreement of predictions with measurements is very close for Reynolds number up to 4×10^5; thereafter the data display progressively higher levels of Sherwood number than the calculated values. For both the turbulence models the inclusion of the curvature correction term raises the Sherwood number by about 5% for spin Reynolds number greater than about 3.5×10^5. Predictions with the k-ε model are marginally closer to the data than those with the mixing length model.

In the foregoing example the effect of streamline curvature on the flow structure was relatively small and consequently only modest advantage seems to be gained from using the swirl correction term with the mixing length and the curved surface version of the energy-dissipation model. The significance of flow curvature increases as the vertex angle decreases. It is seen from Figures 10-11 that substantially better agreement results from use of the models with curvature correction terms included for the 60 degree cone. All the 60 degree cone predictions were made with transition set at $Re_t = 10^5$, a value which seemed most consistent with both the heat and mass transfer data. Heat and mass transfer rates on a 60 degree cone are shown in Figure 10. With both turbulence models in the turbulent flow regime the heat transfer data fall approximately midway between the predicted curves with and without the curvature correction term, the former giving values approximately 5% greater than measured. The inclusion of the curvature term improves agreement with the mass transfer data of Kreith *et al.* (34). Even so, there seems to be a trend, for spin Reynolds numbers greater than about 3×10^5, for the measured

Sherwood number to rise more rapidly than the predictions indicate. This behaviour is of course consistent with the 120 degree cone and the disc data shown earlier. Again predictions with the k-ε model are marginally superior to those with the mixing length model.

Figure 11 shows the predicted torque coefficient for the 60 degree cone compared with Kreith's (24) high Reynolds number data. Here for spin Reynolds number greater than about 3×10^5 the level of C_M for $\beta = 5$ is some 10-12% higher than in the absence of a swirl correction ($\beta = 0$). With $C_C = 0.2$ almost similar results are obtained for spin Reynolds number greater than about 1.5×10^5. Kreith's data certainly support the higher values. At no point do the predicted values of C_M for $\beta = 5$ and $C_C = 0.2$ differ from the measured by more than 8%, a figure which lies well within the uncertainty limits of ±12% estimated by Kreith. Predictions with both the models without curvature correction give values approximately 20% less than the measured values.

The only velocity profile data of flow on cones seem to be those measured, on the same 80 degree cone, by Koosinlin (18) and by the writer. The former were obtained with a pitot tube, the latter with a hot wire anemometer. The hot wire data are limited to the range: $5 < z/r/Re^{\frac{1}{2}} < 30$ the lower limit being set by the physical size of the hot wire instrumentation and the upper limit being that beyond which the measured values lose significance due to large turbulence levels in the outer part of the flow. The pitot tube data are also subject to increasing uncertainty in the outer region associated with the small dynamic pressures and the associated difficulty of identifying the direction of the resultant velocity. The velocity profile data are compared with predictions in Figure 12. The inclusion of the swirl correction term in the respective turbulence models raises the viscosity in the outer region; consequently the tangential and axial velocities are higher. For the tangential velocity profile inclusion certainly improves the agreement with measurement, both sets of data essentially giving the same variation. For the component of flow parallel to the cone surface, the two sets of data show differences comparable with the difference between predictions with and without curvature term included. Somewhat better agreement is displayed closer to the wall, however, by the predictions including curvature effects. Overall it can be seen that the predictions with the $k-\varepsilon$ model here are superior to those with the mixing length model. The predicted axial velocity with the mixing length model approaches zero in the outer region of the boundary layer much more quickly than with the $k-\varepsilon$ model. Both the data support $k-\varepsilon$ predictions. Complete details for the present sets of data are provided in the next chapter where predicted and measured turbulence energy profiles are also shown.

3.5-3 Axial flow past spinning cylinders

The case of the external flow along a cylinder in which the cylinder is rotating about its axis is discussed here. Measured mean velocity profiles by Furuya *et al.* (10) are shown in Figure 13 for the case where the spin velocity at the surface of the cylinder is twice that of the axial free stream. The axial velocity here is normalized with respect to the free stream velocity whereas surface velocity is used for the swirl component. The ordinate is z/δ_{2x}. The predicted solutions for $\beta = 5$ and $C_C = 0.2$ are in close agreement with the measured profiles over the whole of the fully turbulent region. Both turbulence models yield about the same variations of velocity profiles. It should be noted, however, that the calculated profiles seem to exhibit a steeper slope in the immediate vicinity of the wall, especially the profile of circumferential velocity. The last feature is not entirely consistent with the variation of momentum thicknesses δ_{2x} and $\delta_{2\theta}$ along the cylinder shown in Figure 14.

Results using both turbulence models at three levels of Reynolds number are shown, the lower two being those of Furuya *et al.* (10) and at the highest Reynolds number, those of Parr (8). Results are almost identical with both models, those for k-ε being marginally superior. The rate of growth of swirl momentum thickness is evidently predicted satisfactorily for the cases where $\beta = 5$ and $C_C = 0.2$ (implying that the predicted velocity profile in fact has the correct slope in the neighbourhood of the wall). Too large a rate of growth of axial momentum thickness is predicted, however, the discrepancy being especially large for Parr's high spin rate data. An implication of the above result is that, to predict the correct rate of growth for the axial and swirl boundary layers, a non-isotropic effective viscosity would have to be used.

3.5-4 Flow through concentric annulus with rotating core tube

Finally, numerical predictions of fully developed turbulent flow through concentric annulus in which the core tube rotates about its axis are compared with the extensive experimental data of Kuzay (52) which span Reynolds number from 1.7×10^4 to 6.5×10^4 and with rotational speeds of the core tube varying from zero to nearly 2.8 times the mean axial velocity. In the experiments the hydraulic diameter D_H was 7.6 cm and the radius ratio, r_i/r_o was 0.56. The axial flow had 50 hydraulic diameters whereas the tangential velocity had only 36 hydraulic diameters for development lengths. For the first 14 hydraulic diameters the axial flow developed over a stationary section of the core tube. Outer wall static pressure and profiles of total pressure and flow angle were measured by means of total head probes. From these data profiles of static pressure and of axial and circumferential velocity were evaluated. Before comparisons between measured and calculated distributions of these quantities are made attention is first drawn to some interesting features of the experimental data and some novel practices which had to be incorporated to predict flow of such complexity.

One very striking feature of the Kuzay data was that, provided the rotational velocity of the core tube was greater than the mean axial velocity, the change in the angular momentum from $r_i^2\omega$ at the core tube surface to zero at the outer wall was confined, almost entirely, to the two sublayer/buffer zones adjacent to each cylinder. The whole of the fully turbulent region was rotating at essentially constant angular momentum. This feature posed interesting questions regarding the physical models presented here, because in the applications presented so far the modifying effect of streamline curvature caused by equations (3.8) and (3.18) was most marked beyond the buffer region. In the annular flow studied here, since the fully turbulent region was rotating at essentially constant angular momentum and assuming that the predicted behaviour displays similar behaviour, the Richardson number would be virtually zero. There would thus be a relatively small effect of swirl on the effective viscosity according to (3.8) and (3.18), and whatever effects were present would occur in the regions of low turbulent Reynolds numbers adjacent to the walls. It thus appeared doubtful whether the models presented here would be adequate for the annular flow geometry. Some detailed changes which became necessary to incorporate with the models and otherwise are discussed next.

For the application of the mixing length model a uniform level of mixing length in the core region of the annulus is assumed i.e.

$$\ell_o = \lambda(r_o - r_i)/2 \qquad (3.22)$$

Equation (3.22) is used in place of (3.5) at all positions from the spinning core tube greater than that at which ℓ given by equation (3.5) first exceeds the value given by (3.22). To retain strict analogy with equation (3.7) the coefficient λ should be taken as 0.085. However while equation (3.7) was concerned with external boundary layers, the present case is of an internal flow; in the latter flow turbulent mixing in the core region is substantially greater than in the outer region of a wall boundary layer. For this reason the apparent mixing length is larger. λ, therefore, is taken equal to 0.14 here; the value being selected as that giving the best agreement with axial flow velocity profiles here. This is somewhat greater than 0.12; the value giving the best agreement with friction factor for annular flow without swirl.

With the energy-dissipation model of turbulence no modifications were required. The model was applied in its entirety as defined by equations (3.12), (3.17) and (3.18).

On the actual computational aspects it should be said that it proved to be much more difficult to obtain numerical solutions for the present class of flows than for the external boundary layer flows reported above. The reason seemed to be due to the guess-and-correct method adopted in (14) for internal flows for obtaining the change of static pressure over one forward step. Except when the fully-developed state has been reached, in flows with swirl, the streamwise pressure gradient is not uniform across the flows and the practice of using "upstream" velocity profiles to estimate cross-stream pressure variations tended to produce somewhat irregular streamwise pressure changes, particularly near the walls. This in turn would produce kinks in the axial velocity profile which would then be amplified as the solution proceeded downstream.

In order to eliminate such unstable behaviour a number of checks were placed on the solution. The forward step was limited to three percent times the spacing between the walls of the annulus. Moreover, the value of turbulent viscosity evaluated at each node for both turbulence models was "diluted" with the value from the corresponding node at the previous step; the most successful ratio of new : old viscosity was 6:4. Finally, the swirl was introduced only gradually by successively increasing the rotational velocity of the core tube at each step until the speed corresponding to experimental conditions was reached. Computations were then carried downstream until the tangential stress ratios on the two walls satisfied within 5% the fully developed flow relation. Computing times per run on a CDC 6600 computer with the mixing length model were typically 250 s, while with the energy-dissipation model they were typically 600 s.

The influence of the Richardson number correction on the predicted flow behaviour is first examined. Figures 15 and 16 show the axial velocity and the angular momentum profiles for the experiment with the largest relative swirl velocity: as before predictions for both models are shown with and without the inclusion of the respective curvature corrections. Evidently in both cases the inclusion of the swirl correction does improve agreement with experiment. Like the measurements, the calculated angular momentum is nearly uniform over the central 80% of the flow; here, therefore, the swirling flow Richardson number is negligible.

Computed behaviour of axial velocity with $\beta = 5$ and $C_C = 0.2$ for nine different conditions is compared with the Kuzay data (52) in Figures 17-19 while Figures 20-21 show the corresponding swirl velocity for the six swirling flow tests. Agreement between the measured and calculated axial velocities is generally satisfactory although for the mixing length model the calculated profile without swirl displays a rather too peaky shape in the region of the velocity maximum. This feature is a peculiar shortcoming of the mixing length hypothesis near velocity maxima or minima, for according to equation (3.4) the turbulent viscosity becomes zero at such stationary points. In contrast, a real turbulent flow exhibits high levels of turbulent transport coefficient on the axis of a pipe or, as here, near the velocity maximum in the annulus. The discrepancy largely disappears when the swirl flow is appreciable because then the non-zero gradient of (V_θ/r) will ensure a substantial level of μ_t even when $\partial U/\partial r$ vanishes. It should however be noted that no such shortcoming is exhibited with the k-ε model of turbulence and the velocity profiles are quite smooth.

Figure 20 shows that the swirling motion displays a quite different behaviour. Although satisfactory agreement is obtained for a swirl ratio ζ of 2.79 the numerical results exhibit nothing like the variation in profile shape that the data do as the swirl ratio is reduced. Indeed the experimental data superficially seem to suggest that as the relative swirl rate falls the effective transport coefficient for angular momentum falls likewise, in almost direct proportion. In other words the transport coefficient associated with swirl is independent of the axial motion. Intuitively this implied result seemed so unacceptable that it was decided to re-examine a selection of the flows in which more attention was given to the "developing flow" regime. Here it must be noted that the computations are not represented as definitive computations of the developing flow situation principally due to the following reasons; (1) the grid is insufficiently fine near the inner tube to resolve the flow accurately near the start of the spinning section; (2) for stability reasons the spin rate was built up, only gradually, over a number of steps to full speed; (3) the mixing length distribution for fully developed flow does not accurately predict the flow development region; (4) the under-relaxation of viscosity may slightly delay the rate of full development. All except (1) would tend to delay the approach of the computed flow to the fully developed state. Nevertheless, one may expect the predictions to display the correct general features of flow development with, perhaps, the axial rate of development not matching precisely the experiment. Figure 21 shows for three experimental conditions the computed profiles of angular momentum at two intermediate stages of development (about 50 and 90 hydraulic diameters after the start of the spinning section) as well as the fully developed profile. It is immediately evident that profiles at 50 hydraulic diameters (exact number about the same with the two turbulence models) are in virtually complete agreement with the experimental data. The predictions bring out clearly that the rate of approach to fully developed flow is dependent on the magnitude of the swirl ratio. It must be said, however, that the present results cannot strictly distinguish the effect of velocity ratio from that of mean axial Reynolds number. The latter parameter is known, however, to exert only a weak effect on development rates in flows without swirl so it is reasonable to expect its effect to be slight here as well. The reason for the rate of approach to fully developed state being dependent on the swirl ratio is that the higher the swirl velocity the larger the turbulence viscosity. The augmentation is especially large early in the development where the effects of swirl are confined near the core tube. The viscosity level is further augmented by virtue of the increase in the modulus of the Richardson number as the swirl rate is increased. The increased viscosity thus raises the rate of radial propagation of angular momentum. With both the turbulence models the "developing" axial velocity profiles at nominally 50 hydraulic diameters were only slightly different from the fully developed ones shown earlier in Figures 17-19 and for that reason are not shown again. Of course, the axial flow had had 14 diameters more of development than the swirling flow and the axial boundary layers grow from both walls of the annulus. Thus, since the coupling of the swirl flow with the axial is relatively weak, the latter displays almost fully developed state in about 50 hydraulic diameters, as nearly required for non-swirling flows.

Finally Figure 22 shows the effect of swirl on the axial pressure gradient, normalized with respect to the value for no swirl. Evidently there is a steady rise in pressure gradient with swirl velocity. For values of ζ below 2 the agreement with predictions for $\beta = 5$ and $C_C = 0.2$ and measurements is close; at the highest swirl rates, however, it appears that the present models somewhat overpredict the influence of swirl. There is a need for further experimental data at higher swirl rates to provide a conclusive test.

In conclusion the numerical study of flow in an annulus with rotating core tube using both the turbulence models has shown that the number of hydraulic diameters needed to reach full development of the swirling flow decreases as the rotational velocity of the core tube increases relative to the mean axial velocity. At low spin rates, where the swirl velocity makes only a minor contribution to the level of turbulent viscosity, the flow requires in excess of 100 hydraulic diameters to attain the fully developed state. Therefore, that of the Kuzay data only experiments at the highest spin rates are near full development.

3.6-5 Concluding remarks

From comparisons of prediction with experiment presented above it is clear that though some discrepancies have emerged the two turbulence models considered here have been quite successful in predicting the overall behaviour of turbulent boundary layers near spinning surfaces. For external flows there is not much to choose between the two turbulence models, both yield nearly identical results. Computing times with the mixing length model are typically about 1/3rd of those required with the energy-dissipation model of turbulence. For internal flows, however, some weaknesses became apparent in the mixing length model. The study of the annulus has shown that despite the success and conceptual simplicity the mixing length model lacks universality, for a different distribution of mixing length was required to predict this flow satisfactorily. Another endemic shortcoming of the mixing length hypothesis near velocity maxima or minima has again been brought to light, for according to the hypothesis the turbulent viscosity vanishes when the velocity gradient is zero. In contrast, real turbulent flows exhibit high levels of turbulent transport coefficients at such stationary points. The energy-dissipation model of turbulence is free from such shortcomings, and required no changes in any of the empirically chosen coefficients listed in Table 2.

CHAPTER 4

TURBULENCE MEASUREMENTS ON A ROTATING CONE

Experimental data for turbulent wall swirling boundary layers are extremely limited. Many of these data have been obtained for Reynolds numbers which are less than fully turbulent and, in consequence, their value to the research effort on the development and testing of the turbulence models is limited. The most useful data, as already mentioned, are probably the measurements of mean velocity near a free spinning disc by Cham and Head (7), and Parr's (8) measurements on a cylinder rotating in a uniform axial air stream. The present measurements are therefore intended to augment the limited available data for the class of axisymmetrical turbulent boundary layers on spinning surfaces.

4.1 Description of the experimental rig

The chosen geometry of the spinning surface here is that of a cone with vertex angle of 80 degrees. The same cone was used by Koosinlin (18) for his velocity measurements by a pitot probe. The cone was machined from four layers of 76 mm aluminium plates, secured together by internal screws. The maximum variation recorded when the cone was slowly rotated and its surface 'clocked' by dial indicator was ±0.025 mm. The cone was driven by a synchronous motor through a timing belt and pulley arrangement offering a wide selection of precise rotational speeds.

The cone half-angle of 40 degrees was sufficiently large to ensure the development of a boundary layer on its surface when rotating in stagnant surroundings. The substantial length of its conical surface of 35.6 cm permitted a significant range of fully turbulent spin Reynolds numbers to be attained. Figure 23 shows the Reynolds numbers provided by the apparatus as a function of surface position and rotational speeds up to the maximum safe speed for the cone of 1500 rpm. The extent of the laminar, transitional and turbulent regimes as established by Kreith *et al.* (30) are indicated on the figure. To avoid spurious air currents and to keep the measurement area free from smoke and dust particles etc. the cone was enclosed in a 10' × 10' × 10' polythene cubical. Photographs 1 and 2 show the conical surface and the cubical respectively.

4.2 Instrumentaion and operating procedure

A simple schematic line diagram of the hot wire signal processing equipment is shown in Figure 24. Two constant temperature series 55A01 DISA anemometers with 5 m type 06A107 cables were used; the transducers were DISA platinum plated tungsten 55A25 straight sensor and 55A29 slanting (45^o) sensor. The signals from the anemometers were linearized using DISA 55D10 linearisers whose transfer function is

$$E_{out} = K(E_{in}^2 - A)^m$$

where E_{out} and E_{in} are respectively the output and input signals. K, A and m depend on the setting; K being dependent on the gain, A on the zero setting and m on the exponent setting, although they are mutually dependent. The mean value of the signal was obtained using DISA 52B30 true integrator connected to a SOLARTRON LM1420.2 digital voltmeter (DVM). The integrator was set to give an output voltage equal to $\frac{1}{T}\int_0^T E_{in}\,dt$. A value of 10-20 seconds for the time of integration, T, was found to be suitable for the near wall region, but considerably longer times were needed for the outer region as there the relative turbulence levels become progressively higher and frequencies lower. The r.m.s. value of the signal was measured with a DISA 55D35 RMS voltmeter with adjustable time constants. The output voltage from RMS voltmeter was measured with a SOLARTRON LM 1420.2 digital voltmeter. The voltage meter built into the RMS voltmeter was not used except to decide when a change in sensitivity was required.

The fluctuating output voltage from the anemometer was continuously displayed on a dual beam oscilloscope during experiments so that any abnormalities in the signal could immediately be detected. Before use the anemometer coils required adjustment. A DISA dummy probe 55A0151 was connected at the end of the 5 m probe cable in place of the probe, and the anemometer adjusted to give the correct readings in the turbulence measurement mode. Fine adjustments were performed using the actual probe and the built-in square wave generator. These adjustments were made to produce optimum frequency response as determined by the output waveform displayed on the oscilloscope. Complete details of this adjustment procedure are given in DISA instruction manual. This adjustment procedure was done only once; the anemometers were left in the stand-by position between all tests. With the anemometer set to the "resistance measurement" position, and all the resistance decades set to zero, the zero level was adjusted with a shorting probe to keep the d.c. motor near zero level. With the actual probe in position, the resistance was measured adjusting the resistance decades until the resistance bridge was in balance. Typical cold resistance values were 3.4-3.48 ohms. For the actual measurements an overheat ratio of 1.8 was used. The anemometers, being of constant temperature type, maintained the resistance of the heated wires at the set value (1.8 × cold resistance) automatically throughout the tests.

The anemometers and probes were linearised and calibrated with the probe in the potential core of a calibration jet using a small on-line Digital PDP8E computer. The turbulence intensity was less than 2% and the velocity could be continuously varied from 0 to 50 m/s by a speed controller connected to the d.c. motor used to drive the fan. The calibration arrangement allowed rotation of the probe around a fixed point on the axis of the jet, one nozzle diameter downstream of the exit. The output from the linearizer was compared with the velocity measured by a pitot probe placed in the same axial plane as the hot wire probe but about 5 mm apart. Velocity was determined from the pitot tube data and the ratio of velocity and linearizer output calculated for several values of velocity between 2 and 25 m/s. Exponent and zero settings of the linearizer were altered until a satisfactory linearization was achieved; some typical linearized values obtained are listed below:

Table 3. Linearization of E and U

U (m/s)	E (from linearizer, volts)	E/U
20.736	3.7935	0.1830
19.077	3.4817	0.1825
18.205	3.3134	0.1821
16.739	3.0430	0.1819
14.642	2.6511	0.1811
12.418	2.2410	0.1805
11.268	2.0342	0.1805
10.140	1.8288	0.1805
9.055	1.6359	0.1806

Two representative linearized plots for the two probes are also shown in Figure 25. After linearization the relation between E and U is

$$E = SU_{eff} \tag{4.1}$$

where $U_{eff} = f(\alpha)U$ with $f(\alpha)$ being dependent only on the yaw angle α. With the cosine law of Champagne and Sleicher (53) the above relation becomes

$$E^2 = S^2U^2(\cos^2\alpha + K^2\sin^2\alpha) \tag{4.2}$$

Thus the calibration determines both the calibration constant S and the yaw factor K. For each value of velocity two values of α are needed to determine S and K. Because the cosine law holds only for a limited range of values of α, angles of 30°, 45°, and 60° were chosen as they are closer to the working values of α for the present-flow situation. For example, for $\alpha = 30^\circ$ and 45° one gets for S^2 and K^2:

$$S^2 = \frac{2E^2(30) - E^2(45)}{U^2} \qquad (4.3)$$

$$K^2 = \frac{3E^2(45) - 2E^2(30)}{2E^2(30) - E^2(45)} \qquad (4.4)$$

Typical values of S^2 and K^2 were found to be 0.05 and 0.04 respectively. The probes were calibrated before and after a set of measurements. A deviation of less than 1.5% in the values of calibration constant S^2 was called satisfactory. The wires were cleaned thoroughly with CCl_4 before and after each run. These precautions resulted in very consistent calibration parameters and reproducible self-consistent results.

A special traversing mechanism permitted the probe to be moved parallel and normal to the conical surface in steps of 0.001 inch, and to be rotated through ±90° with respect to a plane through the cone axis. The probe support holder could also rotate around its axis and had the ball and spring mechanism to be locked exactly on any of the four pairs of holes diametrically opposed; each hole separated from the next one by exactly $\pi/4$ radians. The probe holder also had four lateral internal screws at right angles to the support axis. These screws were used to align the probe support on its centre line. This was accomplished using the straight sensor by adjusting screws until the mean value of the signal was independent of the position of the holder in any pair of holes. The probe support holder had the freedom to be moved vertically upward and downward, to be rotated in a vertical plane around the probe tip as its fixed centre, and to be locked in any fixed position. This enabled the probe support holder to be aligned with the conical surface. The whole assembly of the traversing mechanism was fixed on a platform with four levelling screws. Photographs 3 and 4 show the complete assembly. The traverse was started when the probe support barely touched the conical surface, exact distance from the surface being determined by stainless steel feeler gauges.

Measurements were made for five sets of conditions given in the table below:

Table 4. Measurement parameters

ω (rpm)	x/L	Re
893	0.855	3.67×10^5
1111	0.855	4.55×10^5
1111	0.930	5.44×10^5
1429	0.855	5.88×10^5
1429	0.930	6.95×10^5

The mean flow direction at any location was determined by rotating the 45^0 sensor parallel to the conical surface until the mean value of the signal at two diametrically opposed holes was within one percent of each other. Therefore besides reading the angle θ of the mean flow direction and the perpendicular distance from the conical surface fourteen different readings corresponding to seven different positions of the sensors were taken at each station; twelve (six mean values and six r.m.s. values) with the 45^0 sensor and two (one mean value and one r.m.s. value) with the straight sensor. This information enabled at each location the values of U, $\overline{u^2}$, $\overline{v_\theta^2}$, $\overline{w^2}$, $\overline{uv_\theta}$, $\overline{v_\theta w}$, and $\overline{uw}$ to be obtained as independent as possible of the errors connected with the positioning of the probe. The seven positions of the wire in the streamline oriented co-ordinate system (see Appendix 4) used were:

1. Wire coinciding with the OZ axis; $\theta = 0$ for example

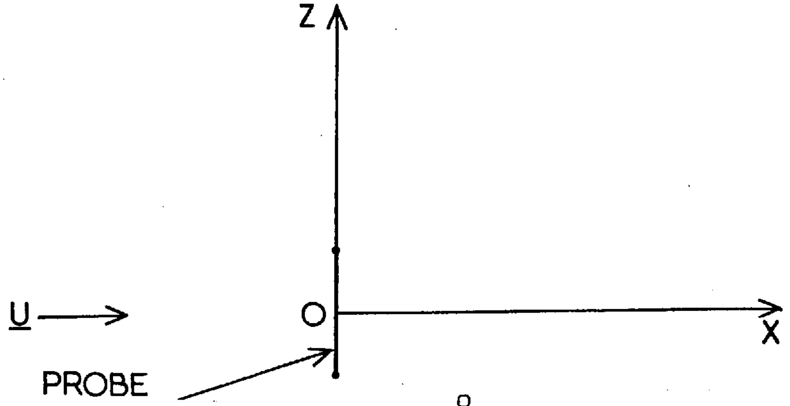

2. Wire in the XOZ plane; $\theta = 45^o$.
3. Wire in the XOZ plane; $\theta = -45^o$.
4. Wire in the XOY plane; $\theta = 45^o$.
5. Wire in the XOY plane; $\theta = -45^o$.
6. Wire in the bisector of XOY plane and XOZ; $\theta = 45^o$.
7. Wire in the bisector of XOY plane and XOZ; $\theta = -45^o$.

These seven positions gave respectively the mean and r.m.s. values of the signal (viz. E1, E2, E3, E4, E5, E6, E7 and e1, e2, e3, e4, e5, e6, e7) at each location. The details of the hot wire data processing analysis are given in Appendix 4.

4.3 Presentation of results

Figures 26-50 represent velocity and turbulence measurement results obtained in the present study. The spin Reynolds number range varies from 3.67×10^5 to 6.95×10^5 corresponding to rotational speed of cone from 893 rpm to 1429 rpm. Figure 23 shows that the dimensions and the speeds of the cone are large enough to ensure a substantial length of fully turbulent flow. At the lowest rotational speed, due to thin boundary layer, the normal distance traversed was only about $z/r/Re^{\frac{1}{2}}$ equal to 20 while at the highest speed it was more than 45. The present hot wire data are therefore limited in the physical distance covered to the range: $5 < z/r/Re^{\frac{1}{2}} < 45$ the lower limit being set by the physical size of the hot wire instrumentation and the upper limit being that beyond which the measured values lose significance due to the large relative turbulence levels in the outer part of the flow.

The measured velocity profiles are compared first with the numerical predictions obtained using the k-ε model of turbulence. At the lowest spin Reynolds number of 3.67×10^5 close agreement is observed between measured and calculated components of axial velocity in Figure 26. The calculated values with $C_C = 0.2$ for value of $z/r/Re^{\frac{1}{2}}$ beyond 10 display progressively higher values and fall to zero more slowly than the predicted values of axial velocity without curvature correction. The measured values follow the latter trend. The agreement between the measured component of swirl velocity and that calculated with curvature correction is, however, satisfactorily close. The velocity profile data measured on the same 80 degree cone at Reynolds number of 4.55×10^5 by Koosinlin (18) and those by the present writer are shown in Figure 31. The former were obtained with a pitot tube, the latter with the hot wire anemometer. The hot wire data in this case are limited in the physical distance covered to the range: $5 < z/r/Re^{\frac{1}{2}} < 30$. As pointed out earlier that beyond this outer limit the measured values lose significance due to the large relative turbulence levels in the outer part of the flow. The pitot tube data are also subject to more uncertainty in this outer region due to small dynamic pressures and the associated difficulty of finding the direction of the resultant mean velocity. The inclusion of the swirl correction term raises the turbulent viscosity in the outer region; consequently the tangential and axial velocities are higher. For the tangential velocity profile inclusion certainly improves the agreement with measurements, both sets of data essentially giving the same variation. For the component of axial velocity the two sets of experiments show differences comparable with the difference between predictions with and without the curvature term included. Somewhat better agreement is displayed closer to the wall, however, by the prediction including curvature effects. Figures 36, 41 and 46 display velocity profiles at higher spin Reynolds numbers of 5.4×10^5, 5.88×10^5 and 6.95×10^5 respectively. It is seen that the inclusion of curvature correction improves the agreement with measurements of the tangential velocity profile. For the component of axial velocity profile, however, the overall agreement between predictions and measurements worsens with higher spin Reynolds numbers. Inclusion of curvature correction term gives satisfactory agreement for $z/r/Re^{\frac{1}{2}}$ greater than about 20. Below this value, however, there seems to be no substantial advantage with this correction. Making this curvature correction term a function of perhaps spin Reynolds number and/or normal distance might give better agreement. The reason for disagreement seems to be the concept of isotropic turbulent viscosity incorporated into the present models, while the flow especially near walls becoming highly non-isotropic as the swirl rate increases. It should be mentioned here that Johnston's (54) three dimensional boundary layer data also implied a strongly non-isotropic viscosity near the wall. As in non-swirling turbulent flows the mean velocity profile data also seem to indicate that very steep velocity gradients occur in the immediate neighbourhood of the wall because stresses there are high and effective viscosities low.

Comparisons of the variations of turbulence kinetic energy for the present set of spin Reynolds numbers are provided in Figures 28, 33, 38, 43 and 48. The measured turbulence energy level is rather higher near the cone surface than either calculated profile but falls more rapidly. Although turbulence energy level decreased with the ordinate $z/r/Re^{\frac{1}{2}}$, the local turbulence level, relative to the local mean velocity, increased substantially with z. At the relatively lower spin Reynolds numbers agreement with predictions is well within the experimental uncertainty. Evidently the inclusion of the swirl correction term in the dissipation rate equation raises the kinetic energy by diminishing ε. The agreement, consequently, with the experimental data at the middle set of spin Reynolds numbers considered here is better up to $z/r/Re^{\frac{1}{2}}$ of approximately equal to 20. Thereafter, however, the data lie in between the predicted values with and without curvature correction. The measured turbulence energy level at the highest spin Reynolds number of 6.95×10^5 is in less satisfactory agreement for $z/r/Re^{\frac{1}{2}}$ up to about 30; thereafter somewhat better agreement with predictions is obtained for $z/r/Re^{\frac{1}{2}}$ to about 45.

The turbulence intensities $\sqrt{\overline{u^2}}/r\omega$, $\sqrt{\overline{v_\theta^2}}/r\omega$, and $\sqrt{\overline{w^2}}/r\omega$ at different spin Reynolds numbers are shown in Figures 30, 35, 40, 45 and 50. Intensities, like the velocity profiles, are normalized with respect to the tangential velocity at the cone-surface. The ordinate as elsewhere is $z/r/Re^{\frac{1}{2}}$. It should be noticed that the intensities of the three velocities differ appreciably from one another over the main inner part of the boundary layer. The degree of anisotropy increases towards the wall and the condition of isotropy seems to approach in the remote regions of the wall. In this swirl induced flow in stagnant surroundings, not unexpectedly, the intensity of the circumferential turbulence velocity component v_θ' has the highest value; that of the radial component perpendicular to the surface w' has the smallest value. Although the components do not show a maximum in the figures it seems that they reach a maximum value in the region very close to the conical surface. Since, due to the physical size of the hot wire instrumentation, the present measurements were taken outside the near wall region no definite quantitative statements about the intensities in the constant stress layer can be made.

But it should be noticed that the intensities measurements shown here are in roughly the same proportion to each other as the relative turbulence intensities data of Klebanoff (55) in a boundary layer along a smooth wall with zero pressure gradient and to the relative turbulence intensities data of Laufer (56) in a pipe flow. It should further be noticed that the present turbulence intensity profiles at various spin Reynolds numbers exhibit reasonable self-consistency.

The shear stress distributions at different spin Reynolds numbers are displayed in Figures 29, 34, 39, 44 and 49. Self consistency of the profiles is again evident. Shear stresses here have been normalized by the square of the conical surface velocity $r\omega$. The shear stress $\overline{v_\theta w}$ has the highest value at the measuring station nearest the wall and then falls smoothly with increasing distance from the wall. Shear stress $\overline{uw}$ has the smallest value at the measuring station nearest the wall and displays some scatter. This also falls of with increasing distance from the wall. Interesting behaviour, however, is exhibited by the stress $\overline{uv_\theta}$. Its value increases for $z/r/Re^{\frac{1}{2}}$ of about 10, thereafter it almost remains constant for $z/r/Re^{\frac{1}{2}}$ of approximately 25, and then falls off with increasing distance from the wall like other shear stresses $\overline{v_\theta w}$ and $\overline{uw}$. Beyond $z/r/Re^{\frac{1}{2}}$ of about 15 the shear stress $\overline{uv_\theta}$ attains relatively higher values than those of the other two components.

Finally, Figures 27, 32, 37, 42 and 47 display the coefficient of correlation $\overline{v_\theta w}/v_\theta' w'$ for the different cases reported here. A roughly constant value of approximately 0.53 may be observed over 75% of the boundary layer with the coefficient tending to go to zero at the wall and at the outer edge of the boundary layer. This result is again similar to that found in high Reynolds number turbulent flow along a smooth wall with zero pressure gradient examined by Klebanoff (55). A value of approximately

0.5 is obtained for the correlation coefficient in the high Reynolds number turbulent boundary layer.

CHAPTER 5

CONCLUSIONS AND RECOMMENDATIONS

5.1 The theoretical contribution

The present research has shown that use of Prandtl mixing length hypothesis and the energy-dissipation model of turbulence lead to generally satisfactory predictions of flow near spinning surfaces provided the respective models are modified to account for the effect of streamline curvature. The results have shown that the swirling flow modification brings great improvement in predictive accuracy over the standard versions of both the turbulence models. For external boundary layers on spinning surfaces there is not much to choose between the two turbulence models, both models producing almost identical results. The mixing length model, however, with its simplicity and being much cheaper to use, is still to be preferred for external flows. For internal flows, however, the study of the annulus with rotating core tube has shown, that as simple a turbulence model as mixing length lacks universality, for a different distribution of mixing length is usually needed for each new geometry considered. Another endemic defect of the mixing length hypothesis near velocity maxima or minima has again been brought to light, for according to the hypothesis the turbulent viscosity vanishes when the velocity gradients are zero. In contrast, real turbulent flows exhibit high levels of turbulent transport coefficients at such stationary points. The energy-dissipation model of turbulence being free from such shortcomings is thus to be preferred for internal flows.

There are some other shortcomings in the predictions with both the turbulence models at high swirling rates that should be noted. It has been shown that at high swirl rates the present models predict too fast a growth rate of axial momentum thickness along the spinning cylinder. The underprediction of the rates of mass transfer from the spinning discs and cones perhaps finds its origin in a similar cause i.e. the effective viscosity becoming highly non-isotropic as the level of swirl progressively increases. It would be valuable to extend present experimental data of high Schmidt numbers to higher swirl rates to help resolve this question.

Finally it may be concluded that to develop a model of turbulence for predicting swirling flows near walls which possess significantly greater universality than the present models one will require the abandonment of the effective viscosity concept. The most promising route seems to be one in which transport equations are solved for each of the non-zero Reynolds stress components. Models of this kind have been presented in references (61) and (62) and by a few other workers. In principle these models are capable of accounting for the non-isotropic features of swirling turbulent flow that have eluded the present models. Because of their much greater complexity however, they have as yet been subject to little testing. Indeed apart from the vortex flow predictions of (57) there seems to have been no calculations made of turbulent flows near spinning surfaces, an omission that ought soon to be remedied.

5.2 The experimental contribution

The experimental data obtained in the present study should supplement the scarce available data for swirling, turbulent boundary layers near walls. Some important points have emerged from the measurements. The measurements of fluctuating quantities yield results which illustrate some similarities between the turbulence structure of swirling boundary layers near walls and that normally found in high Reynolds number turbulent boundary layer flows. The degree of anisotropy increases towards the wall and the condition of isotropy seems to approach in the remote regions of the wall. Anistropy also seems to increase with swirl rate.

The hotwire data of the present study are limited in the physical distance covered to the range: $5 < z/r/Re^{\frac{1}{2}} < 45$ the lower limit being set by the physical size of the hotwire instrumentation and the upper limit being that beyond which the measured values loose significance due to large relative turbulence levels in the outer part of the flow. The experimental difficulties associated with accurate positioning of the probe and its restricted access to the spinning surface suggest the use of perhaps advanced laser-Doppler anemometry techniques for turbulence measurements, especially in the immediate vicinity of the spinning surface.

NOMENCLATURE

Symbol	Meaning
A	constant in the transfer function of linearizer.
a, b, c, d	constants in the linear approximation of the instantaneous response equation of the linearized anemometer.
a	radius of fluid element from centre of eddy.
C_C	parameter in modelled ε equation.
C_M	average drag coefficient for disc and cone, and for cylinder, i.e. $8\pi\int_0^\delta r^2 UV_\theta \sin\alpha \, dz/\omega^2 r^5$; $\int_0^\delta UV_\theta dz/\omega R^2 U_\infty = \delta_{2\theta}/R$ respectively.
C_1, C_2, C_3	empirically chosen coefficients in the modelled ε equation.
C_μ	coefficient in the definition of μ_t.
c_p	specific heat at constant pressure.
D	damping function in the mixing-length formula.
DVM	digital voltmeter.
D_H	hydraulic diameter, $D_o - D_i$.
E	linearised hot wire signal = $\overline{E} + e$.
e	fluctuating component of the electrical signal.
G	mass velocity vector.
H	shape factor, for disc, $\int_0^\delta \frac{V_\theta}{r\omega} dz \Big/ \int_0^\delta \frac{V_\theta}{r\omega}(1 - \frac{V_\theta}{r\omega}) dz$.
h	pitch factor; specific enthalpy.
$\hat{h}$	stagnation enthalpy.

J	diffusional flux.
K	yaw factor; constant in the transfer function of linearizer.
k	turbulence kinetic energy = $\frac{1}{2}(\overline{u^2} + \overline{v_\theta^2} + \overline{w^2})$.
L	length of cone measured in the x-direction.
ℓ	length scale of turbulence (e.g. mixing length); metric coefficient.
MLH	mixing-length hypothesis.
m	constant in the transfer function of linearizer.
m_j	mass fraction of chemical species.
$\dot{m}$	mass flow rate.
n	exponent in the Collis and Williams law.
Nu	local Nusselt number = $\dot{q}''_w \times Pr/c_p(T_w - T_\infty)\mu$.
$\overline{Nu}$	average Nusselt number = $\left[2\int_0^{x_o} r\dot{q}''_w \, dx/r_o x_o\right] x_o Pr/cp(T_w - T_\infty)\mu$.
p	static pressure.
Pr	Prandtl number.
$\dot{q}''$	heat flux.
R	radius of cylinder.
r	radial distance from axis of symmetry.
Re	spin Reynolds number, $\omega rx/\nu$.
Re_t	value of Re at which transition occurs.
Re_∞	free stream Reynolds number, $U_\infty R/\nu$.
Rem	$U_m D_H/\nu$.
Ri	local swirl flow Richardson number.
R_j	rate of generation of chemical species.
R_t	turbulence Reynolds number, $\rho k^2/\mu\varepsilon$.
R_θ	momentum thickness Reynolds number, $V_\theta \theta_{11}/\nu$.

S	calibration constant of the hot wire i.e. constant of proportionality between the cooling velocity and the electrical signal.
s	distance between two points in the general co-ordinate system.
Sc	Schmidt number.
SH	local Sherwood number, $\dot{m}_w \times Sc/\mu(m_{j,w} - m_{j,\infty})$.
$\overline{SH}$	average Sherwood number = $\left[2 \int_0^{x_0} \dot{m} r dx / x_0 r_0\right] x_0 Sc / (m_{j,w} - m_{j,\infty})\mu$.
T	temperature; integral time scale.
$\mathbf{T}$	shear stress.
U	velocity in the x-direction; instantaneous velocity.
U_∞	free stream velocity.
U_m	mean axial velocity.
$\overline{U}$	mean velocity.
u	fluctuating component in the x-direction; also component in the streamwise direction of the fluctuating velocity.
u, v_θ, w	fluctuating velocities in the x, θ, z system.
u'	rms of u.
u, v, w	fluctuating velocities in the x,y,z system.
$\mathbf{V}$	velocity vector.
V_θ	velocity in the circumferential direction.
v_θ	fluctuating component of velocity in the tangential direction.
v'_θ	rms of v_θ.
W	velocity in the z-direction.
w	fluctuating component of velocity in the z-direction.
w'	rms of w.
x	co-ordinate measured along the surface.

z	co-ordinate measured normal to the surface.
x, y, z	co-ordinates of streamline oriented system.

Greek symbols

α	angle made by the x-direction with symmetry axis; yaw angle of the hot wire.
β	parameter in equation (3.8); pitch angle of the hot wire.
Γ	exchange coefficient.
γ	angle of the limiting surface streamline with the main flow direction i.e. $\tan\gamma = \lim\limits_{z\to 0} (U/V_\theta)$.
δ	boundary layer thickness where $U/U_\infty = 0.99$.
δ_2	momentum thickness for disc, $\frac{1}{(r\omega)^2} \int_0^\delta (r\omega - V_\theta)V_\theta \, dz.$
δ_{2x}	momentum thickness in the x-direction for cylinder, $\int_0^\delta \frac{U}{U_\infty} (1 - \frac{U}{U_\infty}) \, dz.$
$\delta_{2\theta}$	swirl momentum thickness for cylinder, $\int_0^\delta UV_\theta \, dz/U_\infty R\omega.$
ε	rate of dissipation of turbulence energy.
θ	angle of revolution about symmetry axis; yaw angle.
θ_{11}	same as δ_2.
κ, λ	mixing-length constants.
μ	dynamic viscosity of fluid.
ν	kinematic viscosity of fluid.
π	3.14159

ρ	density of fluid.
σ	Prandtl or Schmidt number.
σ_t	turbulent Prandtl number for thermal energy.
σ_k	turbulent Prandtl number for turbulence energy.
σ_ε	turbulent Prandtl number for rate of dissipation.
τ	shear stress.
Φ	dependent variable.
ψ	stream function.
ω	rotational speed; dimensionless stream function.
Ω	swirl velocity/free stream velocity.
ζ	tangential velocity of the inner cylinder/mean axial velocity.

Subscripts

eff	effective value.
I, E	inner and outer edges of the boundary layer.
∞	free stream.
i, j, k	indices relating to i, j and k directions.
i	inner
j	chemical species
m	mean
n_1, n_2	normal directions.
O	outer, maximum
Φ	dependent variable.
t	turbulent, tangential direction.
x, z, θ	co-ordinate directions.
+	quantity non-dimensioned by $(\tau_w/\rho)^{\frac{1}{2}}$ and ν.
w	wall value.

Superscripts

—	denotes time average.
'	rms value.
"	per unit area.

REFERENCES

1. Dorfman, L.A., *"Hydrodynamic resistance and the heat loss of rotating solids."* Oliver and Boyd, London (1963).
2. Kreith, F., *"Advances in heat transfer."* 5, Academic Press, New York (1968).
3. Kármán, T. von, "Über laminare und turbulent reibung." Z. angew. Math. Mech. 1, 233 (1921).
4. Goldstein, S., "On the resistance to the rotation of a disc immersed in a fluid." Proceedings Camb. Phil. Soc., 31, 232 (1935).
5. Dorfman, L.A., "Calculation of the boundary layer on an arbitrary axisymmetric surface rotating in a still medium." J. Appl. Mech. and Tech. Phys. 3, 62 (1965).
6. Kreith, F., "Frictional drag and convection heat transfer on rotating cones in mixed and turbulent flow." Proc. of the Heat Transfer and Fluid Mechanics Institute, Stanford University Press (1966).
7. Cham, T.S. and Head, M.R., "Turbulent boundary layer on a rotating disc." J. Fluid Mech. 37, 129 (1969).
8. Parr, von O., "Untersuchungen der dreidimensionalen Grenzschicht an rotierenden Drehkörpern bei axialer Anströmung." Ing. Arch. 32, 393 (1963).
9. Cham, T.S. and Head, M.R., "The turbulent boundary layer on a rotating cylinder in an axial stream." J. Fluid Mech. 42, 1 (1970).
10. Furuya, Y., Nakamura, I. and Kawachi, H., "The experiment on the skewed boundary layer on a rotating body." Bull. JSME 9, 702 (1966).
11. Bayley, F.J. and Owen, J.M., "Flow between a rotating and a stationary disc." Aeronautical Quarterly, 20, 333 (1969).

12. Bayley, F.J. and Owen, J.M., "The fluid dynamics of a shrouded disc system with a radial outflow of coolant." J. Eng. Power, Trans. ASME, 92, 335 (1970).

13. Owen, J.M., "Flow between a rotating disc and a stationary disc." Ph.D. Thesis, U. of Sussex, England (1969).

14. Patankar, S.V. and Spalding, D.B., "*Heat and mass transfer in boundary layers*." Intertext Books, London (1970).

15. Prandtl, L., "Bericht über Untersuchungen zur ausgebildeten Turbulenz." Z. angew. Math. Mech. 5, 136 (1925).

16. Van Driest, E.R., "On turbulent flow near a wall." J. Aeronautical Sciences, 23, 1007 (1956).

17. Cooper, P., "Turbulent boundary layer on a rotating disc calculated with an effective viscosity." AIAA Journal, 9, 255 (1971).

18. Koosinlin, M.L., "Turbulent transport properties in swirling two-dimensional boundary layers." Ph.D. Thesis, U. of London, England (1974).

19. Kolmogorov, A.N., "Equations of turbulent motion in an incompressible fluid." Izv. Academy of Sciences, USSR, Physics, 6, 56 (1942).

20. Cham, T.S. and Head, M.R., "Turbulent boundary layer flows on a rotating disc." J. Fluid Mech. 37, 129 (1969).

21. Davies, D.B., "On the calculation of eddy viscosity and heat transfer in a turbulent boundary layer near a rapidly rotating disc." Quart. J. of Mech. and Appl. Math. 12, 211 (1959).

22. Hartnett, J.P., Tsai, S. and Jantscher, H.N., "Heat transfer to a nonisothermal rotating disc with a turbulent boundary layer." J. Heat Transfer, 87, 362 (1965).

23. Tien, C.L., "Heat transfer by the induced flow about a rotating cone of non-uniform surface temperature." Int. J. Heat Mass Transfer, 8, 411 (1965).

24. Kreith, F., "Frictional drag and convective heat transfer on rotating cones in mixed and turbulent flow." Proc. of the Heat Transfer and Fluid Mechanics Institute, Stanford University Press (1966).

25. Kreith, F., Taylor, J.H. and Chong, J.P., "Heat and mass transfer from a rotating disc." J. Heat Transfer, 8, 95 (1959).

26. Theodorsen, T. and Regier, A., "Experiments on drag of revolving discs, cylinders, and streamline rods at high speed." NACA Rep. 793 (1944).

27. Gregory, N., Stuart, J.T. and Walker, W.S., "On the stability of three dimensional boundary layers with application to the flow due to a rotating disc." Phil. Trans. Royal Soc., A248, 155 (1956).

28. Cochran, W.G., "The flow due to a rotating disc." Proc. Camb. Phil. Soc. 30, 365 (1934).

29. Erian, F.F. and Tong, Y.H., "Turbulent flow due to a rotating disc." The Physics of Fluids, 14, 2588 (1971).

30. Kreith, F., Ellis, D. and Geising, J., "Boundary layer and transition characteristics of a rotating cone." ASME Paper No. 62-WA-105 (1962).

31. Cobb, E.C. and Saunders, O.A., "Heat transfer from a rotating disc." Proc. Royal Soc. A236, 343 (1956).

32. McComas, S.T. and Hartnett, J.P., "Temperature profiles and heat transfer associated with a single disc rotating in still air." Fourth Int. Heat Transfer Conference, Paris-Versailles, III, FC7.7 (1970).

33. Dennis, R.W., Newstead, C. and Ede, A.J., "The heat transfer from a rotating disc in an air cross flow." Fourth Int. Heat Transfer Conference, Paris-Versailles, III, FC7.1 (1970).

34. Kreith, F., Taylor, J.H. and Chong, J.P., "Heat and mass transfer from a rotating disc." J. Heat Transfer, 81, 95 (1959).

35. Tien, C.L. and Campbell, D.T., "Heat and mass transfer from rotating cones." J. Fluid Mechanics, 17, 105 (1963).

36. Ellison, B.T., "Mass transfer to a rotating disc." Ph.D. Thesis, U. of California, Berkeley (1969).

37. Daguenet, M., "Etude du transport de matière en solution, a l'aide des èlectrodes à disque et à anneau tournants." Int. J. Heat Mass Transfer, 11, 1581 (1968).

38. Popiel, Cz. O. and Boguslawski, L., "Local heat transfer coefficients on the rotating disc in still air." Int. J. Heat Mass Transfer, 18, 167 (1975).

39. Kestin, J. and Richardson, P.D., "Heat transfer across turbulent, incompressible boundary layers." Int. J. Heat Mass Transfer, 6, 147 (1963).

40. Sparrow, E.M. and Gregg, J.L., "Heat transfer from a rotating disc to fluids of any Prandtl number." J. Heat Transfer, 81, 249 (1959).

41. Koosinlin, M.L. and Lockwood, F.C., "The prediction of boundary layers on rotating axially symmetrical bodies." Imperial College, Mech. Eng. Dept. Rep. BL/TN/B/42 (1971).

42. Lilley, D.G. and Chigier, N.A., "Non-isotropic turbulent stress distribution in swirling flows from mean value distributions." Int. J. Heat Mass Transfer, 14, 573 (1971).

43. Launder, B.E. and Priddin, C.H., "A comparison of some proposals for the mixing length near a wall." Int. J. Heat Mass Transfer, 16, 700 (1972).

44. Bradshaw, P., "The effects of streamline curvature on turbulent flow." AGARDograph No. 169 (1973).

45. Bradshaw, P., "The analogy between streamline curvature and buoyancy in turbulent shear flow." J. Fluid Mech. 36, 177 (1971).

46. Launder, B.E. and Spalding, D.B., *"Mathematical models of turbulence."* Academic Press, London and New York (1972).

47. Jones, W.P. and Launder, B.E., "The prediction of laminarization with a two-equation model of turbulence." Int. J. Heat Mass Transfer, 15, 301 (1972).

48. Launder, B.E., Morse, A.P., Rodi, W. and Spalding, D.B., "The prediction of free shear flows - a comparison of the performance of six turbulence models." Proc. Langley Free Shear Flows Conference, July 20-21 (1972).

49. Launder, B.E. and Spalding, D.B., "The numerical computation of turbulent flow." Comp. Meth. in Appl. Mech. and Eng. 3, 269 (1974).

50. Jones, W.P. and Renz, V., "Condensation from a turbulent stream onto a vertical surface." Int. J. Heat Mass Transfer, 17, 1019 (1974).

51. Jones, W.P. and Launder, B.E., "The calculation of low Reynolds number phenomena with a two-equation model of turbulence." Int. J. Heat Mass Transfer, 16, 1189 (1973).

52. Kuzay, T., "Turbulent heat and momentum transfer studies in an annulus with rotating inner cylinder." Ph.D. Thesis, U. of Minnesota (1973).

53. Champagne, F.H., Sleicher, C.A. and Wehrmann, O.H., "Turbulence measurements with inclined hot wire." J. Fluid Mech. 28, 153 (1967).

54. Johnston, J.P., "Measurements in a three-dimensional turbulent boundary layer induced by a swept forward facing step." J. Fluid Mech. 42, 823 (1970).

55. Klebanoff, P.S., "Characteristics of turbulence in a boundary layer with zero pressure gradient." NACA TN3178 (1954).

56. Laufer, J., "The structure of turbulence in fully developed pipe." NACA Rep. 1174 (1954).

57. Donaldson, C. du P., "Calculation of turbulent shear flows for atmospheric and vortex motions." AIAA J.10 (1972).

58. Launder, B.E., Reece, G.J. and Rodi, W., "Progress in the development of a Reynolds-stress turbulence closure." J. Fluid Mech., 68, 537 (1975).

59. Gosman, A.D., Pun, W.M., Runchal, A.K., Spalding, D.B. and Wolfshtein, M., *"Heat and mass transfer in recirculating flows."* Academic Press, London (1969).

60. Launder, B.E. and Whitelaw, J.H., Imperial College, Mech. Eng. Dept. Rep. ON/G/12 (1972).

61. Jones, W.P., "Laminarisation in strongly accelerated boundary layers." Ph.D. Thesis, U. of London (1971).

62. Prandtl, L. and Wieghardt, K., "Uber ein neues Formelsystem für die ausgebildete turbulenz." Nach. Akad. Wiss. Göttingen, Math-Phys (1945).

63. Emmons, H.W., "Shear flow turbulence." Proc. 2nd U.S. Nat. Cong. Appl. Mech. ASME (1954).

64. Priddin, C.H., "The behaviour of the turbulent boundary layer on curved, porous walls." Ph.D. Thesis, U. of London (1974).

65. Launder, B.E., Priddin, C.H. and Sharma, B.I., "The calculation of turbulent boundary layers on spinning and curved surfaces." J. Fluid Mech. To be published.

66. Ribeiro, M.M.C., "Turbulent mixing of coaxial jets." M.Sc.Thesis, U. of London (1972).

67. Ribeiro, M.M.C., "Statistical characteristics of a turbulent jet." Imperial College, Mech. Eng. Dept. Rep. HTS/74/19 (1974).

68. Collis, D.C. and Williams, M.J., "Two dimensional convection from heated wires at low Reynolds number." J. Fluid Mech. 6, 357 (1959).

69. Rodi, W., "A new method of analysing hot wire signals in highly turbulent flow, and its evaluation in a round jet." Imperial College, Mech. Eng. Dept. Rep. ET/TN/B/10 (1971).

70. Ribeiro, M.M.C., Private communication (1975).

71. Durst, F. and Rodi, W., "Evaluation of hot wire signals in highly turbulent flows." Fluid Dynamic Measurements in the Industrial and Medical Environment Proc., Leicester, England, Paper II.4-5, 160 (1972).

72. Kovasznay, L.S.G., "The hot wire anemometer in supersonic flow." Proc. Roy. Soc. A198, 174 (1949).

73. Corrsin, S., "*Experimental methods handbuch der physics; Turbulence.*" Springer-Verlag VIII/2 (1963).

74. Champagne, F.H. and Sleicher, C.A., "Turbulence measurements with inclined hot wires, part 2." J. Fluid Mech. 28, 177 (1967).

75. Hinze, J.O., "*Turbulence.*" McGraw-Hill, New York (1959).

APPENDIX I

DERIVATION OF THE CONSERVATION EQUATIONS

A general axisymmetrical co-ordinate system is illustrated in the figure below. The co-ordinates x and z designate the members of two orthogonal families of surfaces of revolution while θ represents the angle of revolution about the symmetry axis from a reference plane.

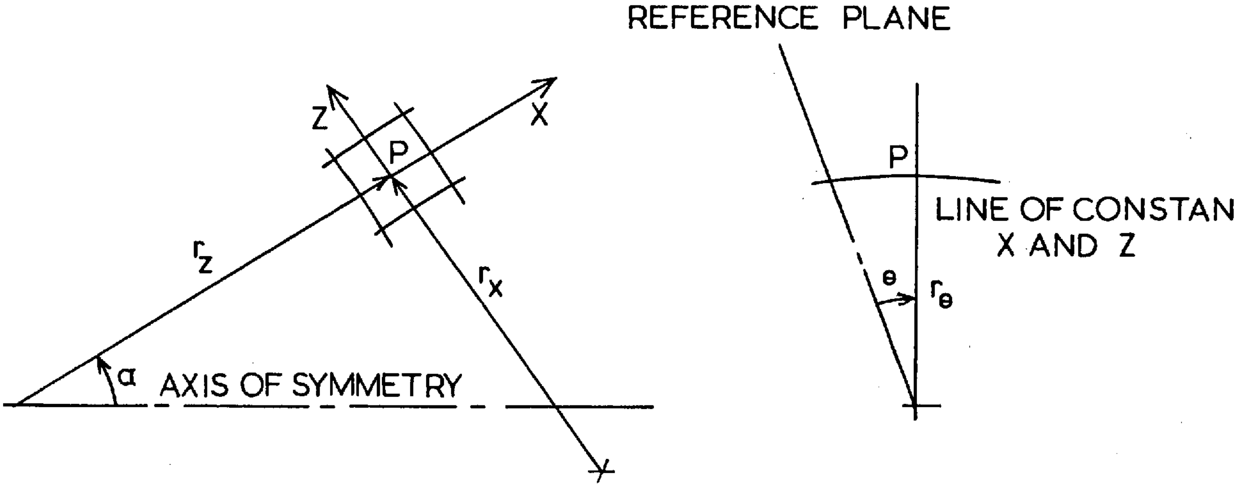

THE AXI-SYMMETRICAL CO-ORDINATE SYSTEM.

The distance ds between two neighbouring points in the field is related to the increments in x, z and θ by:

$$(ds)^2 = (\ell_x dx)^2 + (\ell_z dz)^2 + (\ell_\theta d\theta)^2 \tag{A1.1}$$

where ℓ_x, ℓ_z and ℓ_θ are "metric coefficients". If θ is measured in radians, ℓ_θ is then identical with the radius of curvature r_θ. For axisymmetrical flows considered here $\partial/\partial\theta$ terms will vanish, but not the differentials with respect to x and z.

The radii r_x and r_z can be related to α, ℓ_x and ℓ_z as follows:

$$\frac{1}{r_x} = -\frac{\partial\alpha}{\ell_x \partial x} = \frac{1}{\ell_x \ell_z}\frac{\partial \ell_x}{\partial z} \tag{A1.2}$$

and

$$\frac{1}{r_z} = \frac{\partial\alpha}{\ell_z \partial z} = \frac{1}{\ell_x \ell_z} \frac{\partial \ell_z}{\partial x} \tag{A1.3}$$

The radius r_θ can also be written in terms of α and ℓ's

$$dr_\theta = (\sin\alpha)\ell_x dx + (\cos\alpha)\ell_z dz \tag{A1.4}$$

For the present axisymmetric flows, $\ell_x = \ell_z = 1$, $\ell_\theta = r$ and $r_x = r_z = \infty$.

The Conservation Equations

The general elliptic forms of the conservation equations for mass, momentum, stagnation enthalpy and chemical species for the class of axisymmetrical flows considered here are presented below in vector notation. The complete details are provided in Gosman *et al.* (59). The massive amount of algebra has been left out in the following and all symbols are defined in the Nomenclature.

The continuity equation:

$$\text{div } G = 0 \tag{A1.5}$$

The momentum equation for each of the three directions:

$$G.\text{grad } U = \text{div } T_x + (UG - T_x).\text{grad } \alpha + (V_\theta G_\theta - T_{\theta,\theta}) \frac{\sin\alpha}{r_\theta} - \frac{1}{\ell_x} \frac{\partial p}{\partial x} \tag{A1.6}$$

$$G.\text{grad } W = \text{div } T_z - (WG - T_z).\text{grad } \alpha + (V_\theta G_\theta - T_{\theta,\theta}) \frac{\cos\alpha}{r_\theta} - \frac{1}{\ell_z} \frac{\partial p}{\partial z} \tag{A1.7}$$

$$G.\text{grad } (\ell_\theta V_\theta) = \text{div } (\ell_\theta T_\theta) \tag{A1.8}$$

$$G.\text{grad } \hat{h} = -\text{div}[J_h + \Sigma_j h_j J_j + J_k - (UT_x + WT_z + V_\theta T_\theta)] \tag{A1.9}$$

and

$$\mathbf{G}.\mathrm{grad}\ m_j = -\mathrm{div}\ \mathbf{J}_j + R_j \qquad \text{(A1.10)}$$

Equations (A1.6-A1.10) possess the common form:

$$\mathbf{G}.\mathrm{grad}\ \Phi = -\mathrm{div}\ \mathbf{J}_\Phi + d \qquad \text{(A1.11)}$$

where Φ represents the dependent variable and d is the source term. $\mathbf{J}_\Phi$ stands for the diffusive fluxes of enthalpy or mass; for laminar flows the following gradient-type laws hold

$$\mathbf{J}_h = -\Gamma_h C_p\ \mathrm{grad}\ T \qquad \text{(A1.12)}$$

$$\mathbf{J}_j = -\Gamma_j\ \mathrm{grad}\ m_j \qquad \text{(A1.13)}$$

For momentum equations (A1.6-A1.8), the diffusive fluxes correspond to the shear stresses and are represented by the symbol $\mathbf{T}$. For laminar flow, the components of the shear stresses are connected with the various components of the gradient of velocity, viz.

$$T_{x,x} = \mu\left[\frac{2}{\ell_x}\frac{\partial U}{\partial x} + \frac{2W}{r_x} - \frac{2}{3}\,\mathrm{div}\ \mathbf{V}\right]$$

$$T_{z,z} = \mu\left[\frac{2}{\ell_z}\frac{\partial W}{\partial z} + \frac{2U}{r_z} - \frac{2}{3}\,\mathrm{div}\ \mathbf{V}\right]$$

$$T_{\theta,\theta} = \mu\left[\frac{2}{\ell_\theta}(U\sin\alpha + W\cos\alpha) - \frac{2}{3}\,\mathrm{div}\ \mathbf{V}\right]$$

$$T_{x,z} = T_{z,x} = \mu\left[\frac{\ell_x}{\ell_z}\frac{\partial}{\partial z}\left(\frac{U}{\ell_x}\right) + \frac{\ell_z}{\ell_x}\frac{\partial}{\partial x}\left(\frac{W}{\ell_z}\right)\right]$$

$$T_{x,\theta} = T_{\theta,x} = \mu\left[\frac{\ell_\theta}{\ell_x}\frac{\partial}{\partial x}\left(\frac{V_\theta}{\ell_\theta}\right)\right]$$

$$T_{z,\theta} = T_{\theta,z} = \mu\left[\frac{\ell_\theta}{\ell_z}\frac{\partial}{\partial z}\left(\frac{V_\theta}{\ell_\theta}\right)\right]$$

In terms of the co-ordinates x, z and θ, equation (A1.11) takes the form

$$\frac{G_x}{\ell_x}\frac{\partial\Phi}{\partial x} + \frac{G_z}{\ell_z}\frac{\partial\Phi}{\partial z} = -\frac{1}{\ell_x\ell_z\ell_\theta}\left[\frac{\partial}{\partial x}(\ell_z\ell_\theta J_{\Phi,x}) + \frac{\partial}{\partial z}(\ell_x\ell_\theta J_{\Phi,z})\right] + d \qquad (A1.14)$$

Parabolic Forms of the Equations

The general elliptic form of the conservation equations presented above may be considerably simplified for the special case of boundary layer flows where there is a single predominant direction of flow and the diffusive fluxes are significant only at right-angles to this direction. Thus, regions of recirculation are absent in boundary layer flows.

Direction x is chosen to be the predominant direction of flow here. Diffusive fluxes therefore are negligible in the x direction. The equation for the conservation of momentum in the cross-stream direction (A1.7) is normally ignored for non-swirling boundary layer flows unless the surface curvature is large. For swirl velocities common in engineering practice, however, the last term in this equation is not negligible except for the special case of a spinning disc where it is zero since $\cos\alpha = 0$. The convection terms are most probably negligible and the diffusion term is certainly negligible as W is small everywhere. The following approximations are therefore valid:

$$G.\text{grad}\ W \simeq 0\ ,$$

$$(UG - T_x).\text{grad}\ \alpha \simeq \frac{UG_x}{\ell_x}\frac{\partial\alpha}{\partial x}$$

$$(WG - T_z).\text{grad}\ \alpha \simeq \frac{WG_x}{\ell_x}\frac{\partial\alpha}{\partial x}$$

With these relations equations (A1.5 to A1.10) reduce to

$$\frac{\partial}{\partial x}(\ell_z\ell_\theta G_x) + \frac{\partial}{\partial z}(\ell_x\ell_\theta G_z) = 0 \qquad (A1.15)$$

$$\frac{G_x}{\ell_x}\frac{\partial U}{\partial x} + \frac{G_z}{\ell_z}\frac{\partial U}{\partial z} = \frac{1}{\ell_x\ell_z\ell_\theta}\frac{\partial}{\partial z}\left[\frac{\ell_x\ell_\theta}{\ell_z}\,\Gamma_{x,z}\,\frac{\partial U}{\partial z}\right] - \frac{1}{\ell_x}\frac{\partial p}{\partial x} + \frac{WG_x}{\ell_x}\frac{\partial \alpha}{\partial x} + \frac{V_\theta G_\theta}{\ell_\theta}\sin\alpha \tag{A1.16}$$

$$0 = -\frac{1}{\ell_z}\frac{\partial p}{\partial z} - \frac{UG_x}{\ell_x}\frac{\partial \alpha}{\partial x} + \frac{V_\theta G_\theta}{\ell_\theta}\cos\alpha \tag{A1.17}$$

$$\frac{G_x\partial(\ell_\theta V_\theta)}{\ell_x\partial x} + \frac{G_z\partial(\ell_\theta V_\theta)}{\ell_z\partial z} = \frac{1}{\ell_x\ell_z\ell_\theta}\frac{\partial}{\partial z}\left[\frac{\ell_x\ell_\theta}{\ell_z}\,\Gamma_{\theta,z}\,\frac{\partial(\ell_\theta V_\theta)}{\partial z} - 2\Gamma_{\theta,z}\,\ell_x\ell_\theta V_\theta\cos\alpha\right] \tag{A1.18}$$

$$\frac{G_x}{\ell_x}\frac{\partial \hat{h}}{\partial x} + \frac{G_z}{\ell_z}\frac{\partial \hat{h}}{\partial z} = -\frac{1}{\ell_x\ell_z\ell_\theta}\frac{\partial}{\partial z}\left[\ell_x\ell_\theta\left(J_h + \sum_j h_jJ_j - UT_{x,z} - V_\theta T_{\theta,z}\right)\right] \tag{A1.19}$$

$$\frac{G_x}{\ell_x}\frac{\partial m_j}{\partial x} + \frac{G_z}{\ell_z}\frac{\partial m_j}{\partial z} = -\frac{1}{\ell_x\ell_z\ell_\theta}\frac{\partial}{\partial z}[\ell_x\ell_\theta J_j] + R_j \tag{A1.20}$$

Equations A1.16, A1.18, A1.19 and A1.20 possess the common form:

$$\frac{G_x}{\ell_x}\frac{\partial \Phi}{\partial x} + \frac{G_z}{\ell_z}\frac{\partial \Phi}{\partial z} = -\frac{1}{\ell_x\ell_z\ell_\theta}\frac{\partial}{\partial z}[\ell_x\ell_\theta J_{\Phi,z}] + d \tag{A1.21}$$

For the tangential momentum equation the dependent variable $\ell_\theta V_\theta$ preserved the common form of the equations. However, as pointed out earlier in Chapter 2 it is numerically simpler and convenient to employ V_θ/ℓ_θ as the dependent variable on the right-hand side, the diffusion and source term are replaced by a single diffusion term:

$$\frac{G_x}{\ell_x}\frac{\partial(\ell_\theta V_\theta)}{\partial x} + \frac{G_z}{\ell_z}\frac{\partial(\ell_\theta V_\theta)}{\partial z} = \frac{1}{\ell_x\ell_z\ell_\theta}\frac{\partial}{\partial z}\left[\frac{\ell_x\ell_\theta^3}{\ell_z}\,\Gamma_{z,\theta}\,\frac{\partial(V_\theta/\ell_\theta)}{\partial z}\right] \tag{A1.22}$$

For the present class of axisymmetrical swirling boundary layers the angle α in the general orthogonal co-ordinate system has a constant value. The metric coefficients ℓ_x and ℓ_z are both equal to unity whereas $\ell_\theta = r_\theta = r$. Radii r_x and r_z extend to infinity. With these simplifications the above equations reduce to the familiar forms presented in Chapter 2.

$$\frac{\partial U}{\partial x} + \frac{U}{r}\sin\alpha + \frac{\partial W}{\partial z} + \frac{W}{r}\cos\alpha = 0 \tag{A1.23}$$

$$\rho U \frac{\partial U}{\partial x} + \rho W \frac{\partial U}{\partial z} = -\frac{\partial p}{\partial x} + \frac{1}{r}\frac{\partial}{\partial z}[r\Gamma_{x,z}\frac{\partial U}{\partial z}] + \rho\frac{V_\theta^2}{r}\sin\alpha \tag{A1.24}$$

$$\frac{\partial p}{\partial z} = \rho\frac{V_\theta^2}{r}\cos\alpha \tag{A1.25}$$

$$\rho U \frac{\partial (rV_\theta)}{\partial x} + \rho W \frac{\partial (rV_\theta)}{\partial z} = \frac{1}{r}\frac{\partial}{\partial z}[r^3\Gamma_{z,\theta}\frac{\partial (V_\theta/r)}{\partial z}] \tag{A1.26}$$

$$\rho U \frac{\partial \hat{h}}{\partial x} + \rho W \frac{\partial \hat{h}}{\partial z} = \frac{1}{r}\frac{\partial}{\partial z}[r(\Gamma_h\frac{\partial h}{\partial z} + UT_{x,z} + V_\theta T_{\theta,z})] \tag{A1.27}$$

$$\rho U \frac{\partial m}{\partial x} + \rho W \frac{\partial m}{\partial z} = \frac{1}{r}\frac{\partial}{\partial z}[r\Gamma_j\frac{\partial m}{\partial z}] \tag{A1.28}$$

The generation term R_j in the absence of chemical reaction is zero in equation (A1.20), and the contribution $\Sigma h_j J_j$ of the chemical components in the stagnation enthalpy equation is neglected.

For laminar flows $\Gamma_{x,z}$ and $\Gamma_{z,\theta}$ simply represent the molecular viscosity μ while Γ_h and Γ_j are equal to μ/σ; σ is the Prandtl or Schmidt number of the fluid.

For turbulent flows $\Gamma_{x,z}$ and $\Gamma_{z,\theta}$ are the effective viscosity μ_{eff}, and Γ_h and Γ_j are the effective Prandtl or Schmidt number described in detail in Chapters 2 and 3. Except for the inclusion of μ_{eff} and σ_{eff} the components of the mean velocity satisfy the same equations as those which are described by the corresponding velocity components in laminar flows.

APPENDIX 2

DERIVATION OF κ AND ε EQUATIONS

The general conservation equations for axisymmetric flows presented in Appendix 1 form the starting point for the derivation of the turbulence energy equation. Steps outlined in (60) by Launder and Whitelaw are closely followed in the derivation and modelling of different terms.

The continuity equation in vector notation, presented in Appendix 1, can be written:

$$\mathrm{div}\,\mathbf{G} = 0 \tag{A2.1}$$

expanding and using relations (A1.2) and (A1.3) one gets

$$\frac{1}{\ell_x \ell_\theta \ell_\theta}\left[\frac{\partial}{\partial x}(\ell_z \ell_\theta G_x) + \frac{\partial}{\partial z}(\ell_x \ell_\theta G_z)\right] = 0 \tag{A2.2}$$

$$\frac{\partial G_x}{\partial x} + \frac{G_x}{r_z} + \frac{G_x}{r_\theta}\sin\alpha + \frac{\partial G_z}{\partial z} + \frac{G_z}{r_x} + \frac{G_z}{r_\theta}\cos\alpha = 0 \tag{A2.3}$$

Now the instantaneous values are decomposed into a time average and a fluctuating quantity, e.g.

$$\mathbf{G} = \overline{\mathbf{G}} + \mathbf{G}' \tag{A2.4}$$

$$\mathbf{V} = \overline{\mathbf{V}} + \mathbf{V}' \tag{A2.5}$$

$$\mathbf{p} = \overline{p} + p' \tag{A2.6}$$

For simplicity overscore — is omitted in the following and the time average is simply represented as $\mathbf{G}$, $\mathbf{V}$ or $\mathbf{p}$. Substituting (A2.4) and (A2.5) into (A2.3) yields

$$\frac{\partial G_x}{\partial x} + \frac{G_x}{r_z} + \frac{G_x}{r_\theta}\sin\alpha + \frac{\partial G_z}{\partial z} + \frac{G_z}{r_x} + \frac{G_z}{r_\theta}\cos\alpha +$$

$$\frac{\partial G'_x}{\partial x} + \frac{G'_x}{r_z} + \frac{G'_x}{r_\theta}\sin\alpha + \frac{\partial G'_z}{\partial z} + \frac{G'_z}{r_x} + \frac{G'_z}{r_\theta}\cos\alpha = 0 \tag{A2.7}$$

Time averaging (A2.7) and employing the usual properties of fluctuating quantities gives

$$\frac{\partial G_x}{\partial x} + \frac{G_x}{r_z} + \frac{G_x}{r_\theta} \sin\alpha + \frac{\partial G_z}{\partial z} + \frac{G_z}{r_x} + \frac{G_z}{r_\theta} \cos\alpha = 0 \qquad \text{(A2.8)}$$

Substracting (A2.8) from (A2.7) one gets

$$\frac{\partial G'_x}{\partial x} + \frac{G'_x}{r_z} + \frac{G'_x}{r_\theta} \sin\alpha + \frac{\partial G_z}{\partial z} + \frac{G'_z}{r_x} + \frac{G'_z}{r_\theta} \cos\alpha = 0 \qquad \text{(A2.9)}$$

The streamwise momentum equation in direction x is written as (Ref.59):

$$\frac{1}{\ell_x} \operatorname{div} \left[\ell_x (\mathbf{G}U - \mathbf{T}_x)\right] - \frac{\rho W^2 - T_{z,z}}{r_z} - \frac{\rho V_\theta^2 - T_{\theta,\theta}}{r_\theta} \sin\alpha - \frac{G_x U - T_{x,x}}{\ell_x^2} \frac{\partial \ell_x}{\partial x}$$

$$+ \frac{1}{\ell_x} \frac{\partial p}{\partial x} = 0 \qquad \text{(A2.10)}$$

The first term on the left-hand side can be written as

$$\frac{1}{\ell_x} \operatorname{div} \left[\ell_x (\mathbf{G}U - \mathbf{T}_x)\right] = \frac{1}{\ell_x} \frac{1}{\ell_x \ell_z \ell_\theta} \left\{ \frac{\partial}{\partial x} \left[\ell_x \ell_z \ell_\theta (G_x U - T_{x,x})\right] \right.$$

$$\left. + \frac{\partial}{\partial z} \left[\ell_x^2 \ell_\theta (G_z U - T_{x,z})\right] \right\}$$

or

$$= \frac{\partial}{\partial x} (G_x U - T_{x,x}) + \left(\frac{G_x U - T_{x,x}}{\ell_x^2} \right) \frac{\partial \ell_x}{\partial x}$$

$$+ \frac{G_x U - T_{x,x}}{r_z} + \frac{(G_x U_x - T_{x,x})}{r_\theta} \sin\alpha + \frac{\partial}{\partial z} (G_z U - T_{x,z})$$

$$+ \frac{2(G_z U - T_{x,z})}{r_x} + \frac{(G_z U - T_{x,z})}{r_\theta} \cos\alpha \qquad \text{(A2.11)}$$

Substituting (A2.11) into (A2.10) gives

$$\frac{\partial}{\partial x}(G_x U - T_{x,x}) + \frac{G_x U - T_{x,x}}{r_z} + \frac{G_x U_x - T_{x,x}}{r_\theta} \sin\alpha + \frac{\partial}{\partial z}(G_z U - T_{x,z})$$

$$+ \frac{2(G_z U - T_{x,z})}{r_x} + \frac{(G_z U - T_{x,z})}{r_\theta} \cos\alpha - \frac{G_z W - T_{z,z}}{r_z}$$

$$- \frac{G_\theta V_\theta - T_{\theta,\theta}}{r_\theta} \sin\alpha + \frac{\partial p}{\partial x} = 0 \qquad \text{(A2.12)}$$

Substituting relations (A2.4-A2.6) into the above equation yields

$$\frac{\partial}{\partial x}\left[(G_x+G'_x)(U+U') - (T_{x,x}+T'_{x,x})\right] + \frac{(G_x+G'_x)(U+U') - (T_{x,x}+T'_{x,x})}{r_2}$$

$$+ \frac{(G_x+G'_x)(U+U') - (T_{x,x}+T'_{x,x})}{r_\theta}\sin\alpha + \frac{\partial}{\partial z}\left[(G_z+G'_z)(U+U) - (T_{x,z}+T'_{x,z})\right]$$

$$+ \frac{2[(G_z+G'_z)(U+U')] - (T_{x,z}+T'_{x,z})}{r_x} + \frac{(G_z+G'_z)(U+U') - (T_{x,z}+T_{x,z})}{r_\theta}\cos\alpha$$

$$- \frac{(G_z+G'_z)(W+W') - (T_{z,z}+T'_{z,z})}{r_z} - \frac{(G_\theta+G'_\theta)(V_\theta+V'_\theta) - (T_{\theta,\theta}+T'_{\theta,\theta})}{r_\theta}\sin\alpha$$

$$+ \frac{\partial}{\partial x}(p+p') = 0 \qquad \text{(A2.13)}$$

Multiplying equation (A2.13) by U' and rearranging yields

$$\frac{\partial}{\partial x}\left[G_xUU'+G_xU'^2+G'_xUU'+G'_xU'U'-T_{x,x}U'-T'_{x,x}U'\right] - \left[(G_x+G'_x)(U+U')\right.$$

$$\left.- (T_{x,x}+T'_{x,x})\right]\frac{\partial U'}{\partial x} + \frac{G_xUU'+G_xU'^2+G'_xUU'+G'_xU'U'-T_{x,x}U'-T'_{x,x}U'}{r_z}$$

$$+ \frac{G_xUU'+G_xU'^2+G'_xUU'+G'_xU'U'-T_{x,x}U'-T'_{x,x}U'}{r_\theta}\sin\alpha$$

$$+ \frac{\partial}{\partial z}\left[G_zUU'+G_zU'^2+G'_2UU'+G'_2UU'+G'U'^2-T_{x,z}U'-T'_{x,z}U'\right]$$

$$- \left[G_zU+G_zU'+G'_zU+G'_zU'-T_{x,z}-T'_{x,z}\right]\frac{\partial U'}{\partial z}$$

$$+ 2\,\frac{G_zUU'+G_zU'^2+G'_2UU'+G'_2U'^2-T_{x,z}U'-T'_{x,z}U'}{r_x}$$

$$+ \frac{G_zUU'+G_zU'^2G_zUU'+G'_zU'^2-T_{x,z}U'-T_{x,z}U'}{r_\theta}\cos\alpha$$

$$- \frac{G_zWU'+G_zU'W'+G'_2WU'+G'_zW'U'}{r_z} - \frac{T_{z,z}U'-T'_{z,z}U'}{r_z}$$

$$- \frac{G_\theta V_\theta U'+G_\theta V'_\theta U'+G'_\theta V'_\theta U'G'_\theta V'_\theta U'-T_{\theta,\theta}U'-T'_{\theta,\theta}U'}{r_\theta}\sin\alpha$$

$$+ U'\frac{\partial p}{\partial x} + U'\frac{\partial p'}{\partial x} = 0 \qquad \text{(A2.14)}$$

The conservation equation in the cross-stream direction z is written as

$$\frac{1}{\ell_z}\,\mathrm{div}\,[\ell_z(GW-T_z)] - \frac{\rho U^2-T_{x,x}}{r_x} - \frac{\rho V_\theta^2-T_{\theta,\theta}}{r_\theta}\cos\alpha$$

$$- \frac{G_zW-T_{z,z}}{\ell_z^2}\,\frac{\partial \ell_z}{\partial z} + \frac{1}{\ell_z}\,\frac{\partial p}{\partial z} = 0 \qquad \text{(A2.15)}$$

The first term on the left-hand side can be expanded i.e.

$$\frac{1}{\ell_z}\,\mathrm{div}\,[\ell_z(GW-T_z)] = \frac{1}{\ell_z}\,\frac{1}{\ell_x\ell_z\ell_\theta}\left\{\frac{\partial}{\partial x}[\ell_z\ell_z\ell_\theta(G_xW-T_{z,x})]\right.$$

$$\left. + \frac{\partial}{\partial z}\,[\ell_z\ell_x\ell_\theta(G_zW-T_{z,z})]\right\}$$

or

$$= \frac{\partial}{\partial x}(G_xW-T_{z,x}) + 2\,\frac{G_xW-T_{z,x}}{r_z} + \frac{G_xW-T_{z,x}}{r_\theta}\sin\alpha$$

$$+ \frac{\partial}{\partial z}\,(G_zW-T_{z,z}) + \frac{G_zW-T_{z,z}}{\ell_z^2}\,\frac{\partial \ell_z}{\partial z} + \frac{G_zW-T_{z,z}}{r_\theta}\cos\alpha$$

$$+ \frac{G_zW-T_{z,z}}{r_x}$$

Therefore equation (A2.15) becomes

$$\frac{\partial}{\partial x}(G_xW-T_{z,x}) + 2\,\frac{G_xW-T_{z,x}}{r_z} + \frac{G_xW-T_{z,x}}{r_\theta}\sin\alpha$$

$$+ \frac{\partial}{\partial z}(G_zW-T_{z,z}) + \frac{G_zW-T_{z,z}}{r_\theta}\cos\alpha + \frac{G_zW-T_{z,z}}{r_x}$$

$$- \frac{G_xU-T_{x,x}}{r_x} - \frac{G_\theta V_\theta-T_{\theta,\theta}}{r_\theta}\cos\alpha + \frac{\partial p}{\partial z} = 0 \qquad \text{(A2.16)}$$

Again substituting the relations (A2.4-A2.6) into (A2.16) and multiplying by W' yields:

$$\frac{\partial}{\partial x}(G_xWW'+G_xW'^2+G'_xWW'+G'_xW'W'-T_{z,x}W'_z-T'_{z,x}W')$$

$$-\ (G_xW+G_xW'+G'_xW+G'_xW'-T_{z,x}-T'_{z,x})\ \frac{\partial W'}{\partial x}$$

$$+\ 2\ \frac{G_xWW'+G_xW'^2G'_xWW'+G'_xW'Wp-T_{z,x}-T'_{z,x}W'}{r_z}$$

$$+\ \frac{G_xWW'+G_xW'^2+G_xWW'+G'_xW'W'-T_{z,x}W'-T'_{z,x}W'}{r_\theta}\ \sin\alpha$$

$$+\ \frac{\partial}{\partial z}(G_zWW'+G_zW'^2+G'_zWW'+G'_zW'W'-T_{z,z}W'-T'_{z,z}W')$$

$$-\ (G_zW+G_zW'+G'_zW+G'_zW'-T_{z,z}-T'_{z,z})\ \frac{\partial W'}{\partial z}$$

$$+\ \frac{G_zWW'+G_zW'^2+G'_zWW'+G'_zW'W'-T_{z,z}W'-T'_{z,z}W'}{r_\theta}\ \cos\alpha$$

$$-\ \frac{G_xUW'+G_xU'W'+G'_xUW'+G'_xU'W'-T_{x,x}W'-T'_{x,x}W'}{r_x}$$

$$-\ \frac{G_\theta V_\theta W'+G_\theta V'_\theta W'+G'_\theta V_\theta W'+G'_\theta V'_\theta W'-T_{\theta,\theta}W'+T'_{\theta,\theta}W'}{r_\theta}\ \cos\alpha$$

$$+\ \frac{G_zWW'+G_zW'^2+G'_zWW'+G'_zW'W'-T_{z,z}W'-T'_{z,z}W'}{r_x}\ +\ W'\ \frac{\partial p}{\partial z}\ +\ W'\ \frac{\partial p'}{\partial z}\ =\ 0 \qquad \text{(A2.17)}$$

The conservation equation for tangential momentum is written as:

$$\frac{1}{\ell_\theta}\,\mathrm{div}[\ell_\theta(GV_\theta-T_\theta)]\ =\ 0 \qquad \text{(A2.18)}$$

or

$$\frac{1}{\ell_\theta}\ \frac{1}{\ell_x\ell_z\ell_\theta}\ \ \frac{\partial}{\partial x}[\ell_z\ell_\theta\ell_\theta(G_xV_\theta-T_{x,\theta})]\ +\ \frac{\partial}{\partial z}[\ell_x\ell_\theta\ell_\theta(G_zV_\theta-T_{\theta,z})]\ =\ 0$$

or

$$\frac{\partial}{\partial x}(G_xV_\theta-T_{x,\theta})\ +\ \frac{G_xV_\theta-T_{x,\theta}}{r_z}\ +\ 2\ \frac{G_xV_\theta-T_{x,\theta}}{r_\theta}\ \sin\alpha$$

$$+\ \frac{\partial}{\partial z}(G_zV_\theta-T_{\theta,z})\ +\ \frac{G_zV_\theta-T_{\theta,z}}{r_x}\ +\ 2\ \frac{G_zV_\theta-T_{z,\theta}}{r_\theta}\ \cos\alpha\ =\ 0 \qquad \text{(A2.19)}$$

Substituting relations (A2.4-A2.6) into (A2.19) and multiplying by V'_θ gives:

$$
\begin{aligned}
& \frac{\partial}{\partial x}(G_x V_\theta V'_\theta + G_x V'^2_\theta + G'_x V_\theta V'_\theta + G'_x V'_\theta V'_\theta - T_{x,\theta} V'_\theta - T_{x,\theta} V'_\theta) \\
- \quad & (G_x V_\theta + G_x V'_\theta + G'_x V'_\theta - T_{x,\theta} - T'_{x,\theta}) \frac{\partial V'_\theta}{\partial x} \\
+ \quad & (G_x V_\theta V'_\theta + G_x V'^2_\theta + G'_x V_\theta V'_\theta + G'_x V'_\theta V'_\theta - T_{x,\theta} V'_\theta - T_{x,\theta} V'_\theta)/r_z \\
+ \quad & 2(G_x V_\theta V'_\theta + G_x V'^2_\theta + G'_x V_\theta V'_\theta + G'_x V'_\theta V'_\theta - T_{x,\theta} V'_\theta - T'_{x,\theta} V'_\theta) \sin\alpha/r_\theta \\
+ \quad & \frac{\partial}{\partial z}(G_z V_\theta V'_\theta + G_z V'^2_\theta + G'_z V_\theta V'_\theta + G'_z V'_\theta V'_\theta - T_{\theta,z} V'_\theta - T'_{\theta,z} V'_\theta) \\
- \quad & (G_z V_\theta + G_z V'_\theta + G'_z V_\theta + G'_z V'_\theta - T_{\theta,z} - T'_{\theta,z}) \frac{\partial V'_\theta}{\partial z} \\
+ \quad & (G_z V_\theta V'_\theta + G_z V'^2_\theta + G_z V_\theta V'_\theta + G'_z V'_\theta V'_\theta - T_{\theta,z} V'_\theta - T'_{\theta,z} V'_\theta)/r_x \\
+ \quad & 2(G_z V_\theta V'_\theta + G_z V'^2_\theta + G'_z V_\theta V'_\theta + G'_z V'_\theta V'_\theta + T_{z,\theta} V'_\theta - T'_{z,\theta} V'_\theta)\cos\alpha/r_\theta = 0 \qquad \text{(A2.20)}
\end{aligned}
$$

Equations (A2.14), (A2.17) and (A2.20) are now added together. Convective, diffusive, productive and dissipative terms are explicitly written out below:

Convective terms

$$
\begin{aligned}
& \frac{\partial}{\partial x}(G_x U'^2) + G_x U'^2/r_z + G_x U'^2 \sin\alpha/r_\theta + \frac{\partial}{\partial z}(G_z U'^2) + 2G_z U'^2/r_x \\
+ \quad & G_z U'^2 \sin\alpha/r_\theta + \frac{\partial}{\partial x}(G_x W'^2) + 2G_x W'^2/r_z + G_x W'^2 \sin\alpha/r_\theta \\
+ \quad & \frac{\partial}{\partial z}(G_z W'^2) + G_z W'^2/r_x + G_z W'^2 \cos\alpha/r_\theta + \frac{\partial}{\partial x}(G_x V'^2_\theta) \\
+ \quad & G_x V'^2_\theta/r_z + 2G_x V'^2_\theta \sin\alpha/r_\theta + \frac{\partial}{\partial z}(G_z V'^2_\theta) + G_z V'^2_\theta/r_x \\
+ \quad & 2G_z V'^2_\theta \cos\alpha/r_\theta
\end{aligned}
$$

If k' is set equal to $(U'^2 + W'^2 + V'^2_\theta)/2$ the above terms can be simply written as

$$2\frac{\partial}{\partial x}(G_x k') + 2G_x k'/r_z + G_x W'/r_z + 2G_x k' \sin\alpha/r_\theta + 2\frac{\partial}{\partial z}(G_z k')$$

$$+ 2G_z k'/r_x + G_z U'^2/r_x + 2G_z k' \cos\alpha/r_\theta + G_z V_\theta'^2 \cos\alpha/r_\theta$$

$$- G_x \frac{\partial k'}{\partial x} - G_z \frac{\partial k'}{\partial z}$$

These can be further written as

$$= 2k' \left(\frac{\partial G_x}{\partial x} + G_x/r_z + G_x \sin\alpha/r_\theta + \frac{\partial G_z}{\partial z} + G_z/r_x + G_z \cos\alpha/r_\theta\right)$$

$$+ \left(G_x \frac{\partial k'}{\partial x} + G_z \frac{\partial k'}{\partial z}\right) + G_x W'^2/r_z + G_z U'^2/r_x$$

$$+ G_z V_\theta'^2 \cos\alpha/r_\theta + G_x V_\theta'^2 \sin\alpha/r_\theta$$

Productive and diffusive terms

These terms are grouped as follows:

$$UU' \frac{\partial G_x'}{\partial x} + G_x' U' \frac{\partial U}{\partial x} + G_x' U \frac{\partial U'}{\partial x} - G_x' U \frac{\partial U'}{\partial x} + U' \frac{\partial}{\partial x}(G'U') + G_z' U \frac{\partial U'}{\partial z}$$

$$+ G_z' U' \frac{\partial U}{\partial z} + G_x' W \frac{\partial W'}{\partial x} + G_x' W' \frac{\partial W}{\partial x} + WW' \frac{\partial G_x'}{\partial x}$$

$$- G_x' W \frac{\partial W'}{\partial x} + W' \frac{\partial}{\partial x}(G_x' W') + G_z' W \frac{\partial W'}{\partial z} + G_z' W' \frac{\partial W}{\partial z} + WW' \frac{\partial G_z'}{\partial z}$$

$$- G_z' W \frac{\partial W'}{\partial z} + W' \frac{\partial}{\partial z}(G_z' W') + G_x' V_\theta \frac{\partial V_\theta'}{\partial x} + G_x' V_\theta' \frac{\partial V_\theta}{\partial x} + V_\theta V_\theta' \frac{\partial G_x'}{\partial x} - G_x' V_\theta \frac{\partial V_\theta'}{\partial x}$$

$$+ V_\theta' \frac{\partial}{\partial x}(G_x' V_\theta') + G_z' V_\theta \frac{\partial V_\theta'}{\partial z} \quad G_z' V_\theta' \frac{\partial V}{\partial z} + V_\theta V_\theta' \frac{\partial G_z'}{\partial z} - G_z' V_\theta \frac{\partial V_\theta'}{\partial z} + V_\theta' \frac{\partial}{\partial z}(G_z' V_\theta')$$

$$+ U' \frac{\partial p'}{\partial x} + W' \frac{\partial p'}{\partial z} + G_z' U'^2/r_x + G_z' U'^2/r_x + G_z' UU'/r_x \quad G_z' UU' \cos\alpha/r_\theta$$

$$+ G_z' U'^2 \cos\alpha/r_\theta + G_x' UU'/r_z + G_x' U'^2/r_z \quad G_x' UU' \sin\alpha/r_\theta + G_x' U'^2 \sin\alpha/r_\theta$$

$$- G_z' U'W'/r_z - G_z' U'W/r_z - G_z' W'U'/r_z - G_\theta' V_\theta' U' \sin\alpha/r_\theta - G_\theta' V_\theta U' \sin\alpha/r_\theta$$

$$- G_\theta' V_\theta' U' \sin\alpha/r_\theta + G_x' WW'/r_z + G_x' WW'/r_z + G_x' W'^2/r_z + G_x' W'^2/r_z$$

$$+ G_x' WW' \sin\alpha/r_\theta + G_x' W'^2 \sin\alpha/r_\theta + G_z' WW' \cos\alpha/r_\theta + G_z' W'^2 \cos\alpha/r_\theta$$

$$+ G_z' WW'/r_x + G_z' W'^2/r_x - G_x' UW'/r_x - G_x' U'W'/r_x - G_\theta' V_\theta W' \cos\alpha/r_\theta$$

$$- G'_\theta V'_\theta W' \cos\alpha / r_\theta + G'_x V_\theta V'_\theta / r_z + G'_x V'^2_\theta / r_z + G'_x V_\theta V'_\theta \sin\alpha / r_\theta + G'_x V_\theta V'_\theta \sin\alpha / r_\theta$$

$$+ G'_x V'^2_\theta \sin\alpha / r_\theta + G'_z V_\theta V'_\theta / r_x + G'_z V'^2_\theta / r_x + G'_z V_\theta V'_\theta \cos\alpha / r_\theta + G'_z V'_\theta V_\theta \cos\alpha / r_\theta$$

$$+ G'_z V'^2_\theta \cos\alpha / r_\theta + G'_z V'^2_\theta \cos\alpha / r_\theta .$$

For the present class of axisymmetric boundary layers r_x and r_z approach infinity and $r_\theta = r$. Therefore the above terms can be simplified as:

Production and diffusion

$$G'_x \frac{\partial k'}{\partial x} + G'_z \frac{\partial k'}{\partial z} + G'_z U' \left(\frac{\partial U}{\partial z}\right) + G'_z V'_\theta \left(\frac{\partial V_\theta}{\partial z} - \frac{V_\theta}{r} \cos\alpha\right) - G'_\theta U' V_\theta \sin\alpha / r$$

$$- G'_\theta W' V_\theta \cos\alpha / r + G'_x V'_\theta V_\theta \sin\alpha / r + G'_z V'_\theta V_\theta \cos\alpha / r - G_\theta V'_\theta U' \sin\alpha / r$$

$$- G'_\theta U' V'_\theta \sin\alpha / r - G'_\theta V'_\theta W' \cos\alpha / r + G'_x V'^2_\theta \sin\alpha / r + G'_z V'^2_\theta \cos\alpha / r$$

$$+ U' \frac{\partial p'}{\partial x} + W' \frac{\partial p'}{\partial z}$$

or

$$= G'_x \frac{\partial k'}{\partial x} + G'_z \frac{\partial k'}{\partial z} + G'_z U' \left(\frac{\partial U}{\partial z}\right) + G'_z V'_\theta \left(\frac{\partial V_\theta}{\partial z} - \frac{V_\theta}{r} \cos\alpha\right)$$

$$- \rho V'_\theta U' \frac{V_\theta}{r} \sin\alpha + U' \frac{\partial p'}{\partial x} + W' \frac{\partial p'}{\partial z} .$$

Dissipative terms

$$-U' \frac{\partial T'_{x,x}}{\partial x} - T'_{x,x} U' \sin\alpha / r - U' \frac{\partial T'_{x,z}}{\partial z} - T'_{x,z} U' \cos\alpha / r + T'_{\theta,\theta} U' \cos\alpha / r$$

$$- W' \frac{\partial T'_{z,x}}{\partial x} - T'_{z,x} W' \sin\alpha / r - W' \frac{\partial T_{z,z}}{\partial z} - T'_{z,z} W' \sin\alpha / r + T'_{\theta,\theta} W' \cos\alpha$$

$$- V'_\theta \frac{\partial T'_{x,\theta}}{\partial x} - 2T'_{x,\theta} V'_\theta \sin\alpha / r - V'_\theta \frac{\partial T'_{\theta,z}}{\partial z} - 2T'_{z,\theta} V'_\theta \cos\alpha / r .$$

Now time averaging all the above terms yields

$$\rho\frac{Dk}{Dt} = -\overline{G_z'U'}\left(\frac{\partial U}{\partial z}\right) - \overline{G_z'V_\theta'}\left(\frac{\partial V_\theta}{\partial z} - \frac{V_\theta}{r}\cos\alpha\right) - \overline{G_z'\frac{\partial k'}{\partial z}}$$

$$- \overline{W'\frac{\partial p'}{\partial z}} \quad - \text{Dissipation} \qquad \text{(A2.21)}$$

The complete discussion on modelling of different terms in the above equation appears in (60) and (61). The interaction between the mean and fluctuating motion leads to transfer of energy from the mean to the fluctuating motion, thus, representing production of turbulence energy by the first two terms on the right-hand side. Now the following approximations are made:

$$-\overline{G_z'U'} = \mu_t\left(\frac{\partial U}{\partial z}\right) \qquad \text{(A2.22)}$$

$$-\overline{G_z'V_\theta'} = \mu_t\left(\frac{\partial V_\theta}{\partial z} - \frac{V_\theta}{r}\cos\alpha\right)$$

$$= \mu_t\left(r\frac{\partial(V_\theta/r)}{\partial z}\right) \qquad \text{(A2.23)}$$

The group of dissipation terms ε is modelled as $\sim k^{3/2}/\ell$. Following the practice for non-swirling flows it is presumed that the diffusion of k by turbulent motions and pressure fluctuations obeys the gradient type law i.e.

$$\text{Diffusion of } k = \frac{1}{r}\frac{\partial}{\partial z}\left(r\frac{\mu_t}{\sigma_k}\frac{\partial k}{\partial z}\right) \qquad \text{(A2.24)}$$

where σ_k is a 'turbulent Prandtl number' for the turbulence energy, which is assumed to have a constant value. Such an approximation has previously been proposed independently by a number of workers, e.g. Prandtl (62), Emmons (63).

With the above relations the complete turbulence energy equation for the present class of flows can be written:

$$\rho U\frac{\partial k}{\partial x} + \rho W\frac{\partial k}{\partial z} = \frac{1}{r}\frac{\partial}{\partial z}\left[r\left(\mu + \frac{\mu_t}{\sigma_k}\right)\frac{\partial k}{\partial z}\right]$$

$$+ \mu_t\left[\left(\frac{\partial U}{\partial z}\right)^2 + \left(r\frac{\partial V_\theta/r}{\partial z}\right)^2\right] - \rho\varepsilon - 2\mu\left(\frac{\partial k^{\frac{1}{2}}}{\partial z}\right)^2 \qquad \text{(A2.25)}$$

The reasons for the inclusion of the extra term $2\mu(\frac{\partial k^{\frac{1}{2}}}{\partial z})$ in the above equation have been pointed out in Chapter 3 and in references (47) and (61).

Mixing length viscosity formulation

It is interesting to note that if a local balance between the production and dissipation of turbulence energy is assumed (i.e. convection and diffusion of k negligible, sometimes called the condition of 'local-equilibrium') equation (A2.25) reduces to:

$$\mu_t \left[(\frac{\partial U}{\partial z})^2 + (r \frac{\partial V_\theta / r}{\partial z})^2 \right] = \rho\varepsilon \qquad \text{(A2.26)}$$

From relations

$$\varepsilon = k^{3/2}/\ell \qquad \text{and} \qquad \mu_t = \rho k^{\frac{1}{2}} \ell$$

it can be seen that

$$\mu_t = \rho \ell^{4/3} \varepsilon^{1/3} \qquad \text{(A2.27)}$$

ℓ here has the dimensions of a length scale. Equations (A2.26) and (A2.27) can be combined to give the final form of the mixing-length viscosity formula presented in Chapter 3, i.e.

$$\mu_t = \rho \ell^2 \left[(\frac{\partial U}{\partial z})^2 + (r \frac{\partial V_\theta / r}{\partial z})^2 \right]^{\frac{1}{2}} \qquad \text{(A2.28)}$$

The equation for the dissipation-rate of turbulence energy

The exact equation for ε in the general co-ordinate system considered earlier is a little more difficult to derive. The derivation in general tensor notation and in cartesian form has been provided by Priddin (64) and Jones (61) respectively. The formal derivation of the ε-equation is therefore not included here. The modification of the Jones ε-equation to the present axisymmetric co-ordinate system is, however, presented below. The equation for the dissipation-rate of turbulence kinetic energy may be derived by manipulation of the Navier-Stokes equations. In cartesian tensor notation this may be achieved by first differentiating the momentum equation for u_i with respect to x_j, multiplying by $(2\nu\, \partial u_i/\partial x_j)$ and finally averaging. The result is:

$$\begin{aligned}
\frac{D\varepsilon}{Dt} = {} & \nu \frac{\partial^2 \varepsilon}{\partial x_j \partial x_j} - 2\nu\, \overline{u_m \frac{\partial u_j}{\partial x_i}}\, \frac{\partial^2 U_j}{\partial x_i \partial x_m} \\
& - 2\nu \frac{\partial U_j}{\partial x_m} \left[\overline{\frac{\partial u_j}{\partial x_i} \frac{\partial u_m}{\partial x_i}} + \overline{\frac{\partial u_i}{\partial x_j} \frac{\partial u_i}{\partial x_m}} \right] \\
& - 2\nu\, \overline{\frac{\partial u_j}{\partial x_i} \frac{\partial u_m}{\partial x_i} \frac{\partial u_j}{\partial x_m}} - 2\nu^2\, \overline{\left(\frac{\partial^2 u_j}{\partial x_m \partial x_i} \right)^2} \\
& - \frac{\partial}{\partial x_m} \left[\nu\, \overline{u_m \frac{\partial u_j}{\partial x_i}} + \nu\, \overline{\frac{\partial u_m}{\partial x_i} \frac{\partial p}{\partial x_i}} \right]
\end{aligned} \qquad \text{(A2.29)}$$

The terms on the right-hand side (except first) of the above equation require closure assumptions to close the equation. There is no direct experimental evidence about any of the terms and closure therefore involves a substantial amount of speculation. The proposed approximations for the different terms are detailed in (61), (64) and by several other workers. Here, the final form of the ε-equation is written, i.e.

$$\begin{aligned}
\rho \frac{D\varepsilon}{Dt} = {} & \frac{\partial}{\partial x_j} \left[(\mu + \frac{\mu_t}{\sigma_\varepsilon}) \frac{\partial \varepsilon}{\partial x_j} \right] + C_1 \mu_t \frac{\varepsilon}{k} \frac{\partial U_i}{\partial x_j} \left(\frac{\partial U_i}{\partial x_j} + \frac{\partial U_j}{\partial x_i} \right) \\
& - C_2 \frac{\rho \varepsilon^2}{k} + C_3 \nu \mu_t \left(\frac{\partial^2 U_i}{\partial x_k \partial x_j} \right)^2
\end{aligned} \qquad \text{(A2.30)}$$

The empirical coefficients have been assigned the forms and values given in Chapter 3.

When the above dissipation rate equation is specialized to plane boundary layer conditions it reduces to:

$$\rho \frac{D\varepsilon}{Dt} = \frac{\partial}{\partial z}\left[(\mu + \frac{\mu_t}{\sigma_\varepsilon}) \frac{\partial \varepsilon}{\partial z}\right] + C_1 \mu_t \frac{\varepsilon}{k} (\frac{\partial U}{\partial z})^2 - C_2 \frac{\rho \varepsilon^2}{k}$$

$$+ C_3 \nu \mu_t (\frac{\partial^2 U}{\partial z^2})^2 \qquad (A2.31)$$

When the above equation is used for axisymmetric boundary layers the second and last term clearly need modification, which is as follows.

The exact term in equation (A2.29) which requires modification is

$$2\nu \overline{u_m \frac{\partial u_j}{\partial x_i} \frac{\partial^2 U_j}{\partial x_i \partial x_m}}$$

which is approximated to $= -C_3 \nu \nu_t \left[\frac{\partial^2 U_j}{\partial x_i \partial x_m}\right]^2$ or

$$2\nu \overline{u_m \frac{\partial u_j}{\partial x_i} \frac{\partial U_j}{\partial x_i \partial x_m}} = -C_3 \nu \nu_t \left[\frac{\partial}{\partial x_i} (\frac{\partial U_j}{\partial x_m})\right]^2 \qquad (A2.32)$$

For plane boundary layers the right-hand side simply reduces to

$$-C_3 \nu \nu_t \left[\frac{\partial}{\partial z} (\frac{\partial U}{\partial z})\right]^2$$

For axisymmetric boundary layers considered here it has been shown earlier that

$$\frac{\partial U_j}{\partial x_m} = \left[(\frac{\partial U}{\partial z})^2 + (r \frac{\partial V_\theta / r}{\partial z})^2\right]^{\frac{1}{2}} \qquad (A2.33)$$

Therefore equation (A2.32) becomes

$$2\nu \overline{u_m \frac{\partial u_j}{\partial x_i} \frac{\partial^2 U_j}{\partial x_i \partial x_m}} = -C_3 \nu \nu_t \left\{\frac{\partial}{\partial z}\left[(\frac{\partial U}{\partial z})^2 + (r \frac{\partial V_\theta / r}{\partial z})^2\right]^{\frac{1}{2}}\right\}^2 \qquad (A2.34)$$

Finally, substituting relations (A2.33) and (A2.34) into equation (A2.31) yields the ε-equation for the present axisymmetric, swirling boundary layer flows, i.e.

$$\rho U \frac{\partial \varepsilon}{\partial x} + \rho W \frac{\partial \varepsilon}{\partial z} = \frac{1}{r}\frac{\partial}{\partial z}\left[r(\mu + \frac{\mu_t}{\sigma_\varepsilon}) \frac{\partial \varepsilon}{\partial z} \right]$$

$$+ C_1 \frac{\varepsilon}{k} \mu_t \left[(\frac{\partial U}{\partial z})^2 + (r \frac{\partial V_\theta / r}{\partial z})^2 \right]$$

$$- C_2 \frac{\rho \varepsilon^2}{k} + C_3 \nu \mu_t \left\{ \frac{\partial}{\partial z} \left[(\frac{\partial U}{\partial z})^2 + (r \frac{\partial V_\theta / r}{\partial z})^2 \right]^{\frac{1}{2}} \right\}^2 \qquad \text{(A2.35)}$$

It should be noticed that the k-ε equations presented here also possess the common form of equation (A2.21) i.e.

$$\frac{G_x}{\ell_x}\frac{\partial \Phi}{\partial x} + \frac{G_z}{\ell_z}\frac{\partial \Phi}{\partial z} = - \frac{1}{\ell_x \ell_z \ell_\theta} \frac{\partial}{\partial z} [\ell_x \ell_\theta \, J_{\Phi,z}] + d$$

APPENDIX 3

MODIFICATION IN k-ε TURBULENCE MODEL FOR STREAMLINE CURVATURE

When the k-ε turbulence model as represented by equations (3.12), (3.13) and (3.14) was applied to the calculation of turbulent flows on spinning surfaces it was found that the strong influence of curvature was not well reproduced. This shortcoming in the model was corrected, as shown by equation (3.15), by the introduction of a "source" term in the transport equation for ε. Physical support for the inclusion of such a term may now be inferred formally by the argument developed below. More pertinent details also appear in (64) and (65).

Consider an idealised turbulent eddy circular in cross-section in the plane of rotation following a curved mean streamline as indicated in the Figure below. It is assumed that the eddy has length scale ℓ, velocity scale $k^{\frac{1}{2}}$ and is undergoing an infinitesimal rotation of $\delta\phi$, during which a fluid element at 1, radius a from the eddy centre, moves to point 2. The effect of shear forces on the eddy development for the moment is neglected and the eddy is assumed to be small (i.e. $\ell << r$) and hence no influence of the eddy on the mean centrifugal pressure field is allowed. Although the mean flow will follow the

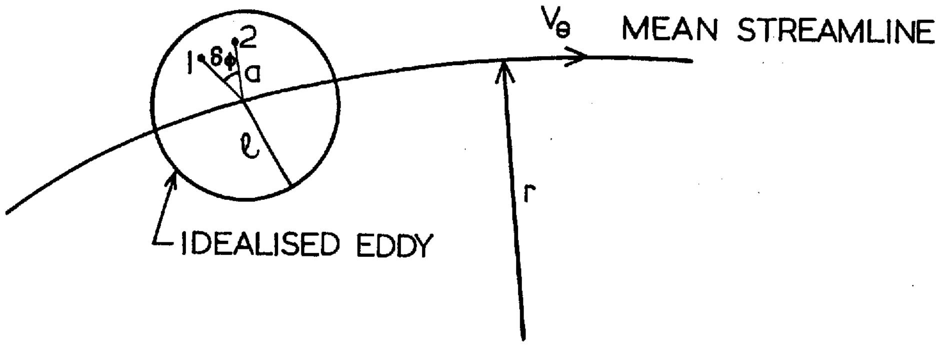

curved streamline pattern indicated in the Figure above there will be migration across the mean streamlines due to rotation of the body. In line with the idealisations mentioned above, it is assumed that the total pressure of the eddy fluid remains constant during translation. Thus

$$p_2 + \tfrac{1}{2}\rho V_{\theta,2}^2 = p_1 + \tfrac{1}{2}\rho V_\theta^2 \tag{A3.1}$$

The radial distance travelled by the fluid element during rotation $\delta\phi$ is $a \sin\phi\,\delta\phi$. The static pressure at 2, p_2 is therefore given by

$$p_2 = p_1 + a \sin\phi\,\delta\phi \,\frac{\partial p}{\partial r} \tag{A3.2}$$

Thus, if the total pressure of the fluid element remains constant, substituting relation (A3.2) into (A3.1) yields

$$\rho V_{\theta,2}^2 = \rho V_\theta^2 - 2\, a \sin\phi\,\delta\phi \,\frac{\partial p}{\partial r} \tag{A3.3}$$

Now, in general, $V_{\theta,2}$ will be different from the value of V_θ of the neighbouring fluid at the same radius. Therefore the centrifugal force per unit area will differ from that of the surrounding fluid by an amount Δp_2 given by

$$\Delta p_2 = \frac{\rho V_{\theta,2}^2}{r} \quad \frac{\rho\left(V_\theta + \frac{\partial V_\theta}{\partial r}\, a \sin\phi\,\delta\phi\right)^2}{r} \tag{A3.4}$$

Substituting from (A3.3) and neglecting terms of the order $\delta\phi^2$ yields

$$\Delta p_2 = \frac{\rho V_\theta^2}{r} - \frac{2}{r}\, a \sin\phi\,\delta\phi \,\frac{\partial p}{\partial r} - \frac{\rho V_\theta^2}{r} - \frac{2\rho V_\theta}{r}\,\frac{\partial V_\theta}{\partial r}\, a \sin\phi\,\delta\phi$$

or

$$\Delta p_2 = -2a \sin\phi\,\delta\phi \left[\frac{1}{r}\frac{\partial p}{\partial r} + \frac{\rho V_\theta}{r}\frac{\partial V_\theta}{\partial r}\right] \tag{A3.5}$$

On assuming that the mean flow is in radial equilibrium i.e. $\frac{\partial p}{\partial r} = \rho V_\theta^2/r$ it is thus readily seen that the centrifugal pressure differential acting on the element at 2 is

$$\Delta p_2 = -2a\ \sin\phi\delta\phi \left[\frac{\rho V_\theta^2}{r^2} + \frac{\rho V_\theta}{r}\frac{\partial V_\theta}{\partial r}\right] \qquad \text{(A3.6)}$$

in the radially outward direction. The torque acting on a turbulent eddy about its centre is therefore given by

$$\delta M = -2a\ \sin\phi\delta\phi \left[\frac{\rho V_\theta^2}{r} + \frac{\rho V_\theta}{r}\frac{\partial V_\theta}{\partial r}\right] a\ \sin\phi\delta a$$

Likewise, for all other elements in the eddy, the displacement by the turbulent motion will disturb the particles from their state of centrifugal pressure equilibrium. Thus, integrating for the whole eddy the net torque acting on it due to the mean flow curvature is

$$M = -2\frac{\rho V_\theta}{r^2}\left[V_\theta + r\frac{\partial V_\theta}{\partial r}\right]\int_{\phi=0}^{2\pi}\int_{a=0}^{\ell} \sin^2\phi d\phi a^2 da \qquad \text{(A3.7)}$$

It is assumed that for small eddy size V_θ does not vary greatly over the eddy. Formal integration yields

$$M = -\frac{2\pi}{3}\ell^3\left(\frac{\rho V_\theta}{r^2}\right)\left(V_\theta + r\frac{\partial V_\theta}{\partial r}\right)$$

or

$$M = -\frac{2\pi}{3}\rho\ell^3\frac{V_\theta}{r^2}\frac{\partial(rV_\theta)}{\partial r} \qquad \text{(A3.8)}$$

or simply

$$M \propto \rho\ell^3\frac{V_\theta}{r^2}\frac{\partial(rV_\theta)}{\partial r}$$

Now, the average angular momentum of the energy containing turbulent motions is proportional to $\rho k^{\frac{1}{2}}\ell^2$. So if, in addition to a transport equation for k, the turbulence model also provided one for $k^{\frac{1}{2}}\ell^2$ one should expect this equation to be of the form:

$$\frac{D(k^{\frac{1}{2}}\ell^2)}{Dt} = C'\ell^3\frac{V_\theta}{r^2}\frac{\partial(rV_\theta)}{\partial r} + \ldots \qquad \text{(A3.9)}$$

where coefficient C' would be determined from experiment and the dots denote the terms that would be present in a uni-directional form of the equation.

In the present work the 'second' turbulence transport equation is one for the dissipation rate, ε, not for $k^{\frac{1}{2}}\ell^2$. It is, however, easy to transform from one variable to the other by noting that

$$\varepsilon \propto k^{3/2}/\ell$$

Therefore equation (A3.9) becomes

$$\frac{D(k^{\frac{1}{2}}\frac{k^3}{\varepsilon^2})}{Dt} = C\,\frac{k^{9/2}}{\varepsilon^3}\,\frac{V_\theta}{r^2}\,\frac{\partial(rV_\theta)}{\partial r} + \ldots$$

or

$$\frac{k^{7/2}}{\varepsilon^3}\,\frac{D\varepsilon}{Dt} = C\,\frac{k^{9/2}}{\varepsilon^3}\,\frac{V_\theta}{r^2}\,\frac{\partial(rV_\theta)}{\partial r} + \ldots \qquad \text{(A3.10)}$$

The constant C is adjusted as necessary at each stage in the derivation. After further simplifying equation (A3.10) it is thus deduced that the transport equation for flows with significant curvature should run

$$\frac{D\varepsilon}{Dt} = C\,\frac{kV_\theta^2}{r}\,\frac{\partial(rV_\theta)}{\partial r} + \ldots \qquad \text{(A3.11)}$$

In practice it is convenient to link the new 'source' term with the main decay term in the ε equation. That term then becomes $C_2\,\frac{\varepsilon^2}{k}\,(1-C_c Ri)$, and the complete dissipation rate equation may then be written

$$\rho\,\frac{D\varepsilon}{Dt} = \frac{\partial}{\partial x_j}\left[(\mu + \frac{\mu_t}{\sigma_\varepsilon})\,\frac{\partial\varepsilon}{\partial x_j}\right] + C_1\frac{\mu_t\varepsilon}{k}\,\frac{\partial U_i}{\partial x_j}\,(\frac{\partial U_i}{\partial x_j} + \frac{\partial U_j}{\partial x_i})$$

$$-C_2\frac{\rho\varepsilon^2}{k}\,(1-C_c Ri) + C_3\nu\mu_t\,(\frac{\partial^2 U_i}{\partial x_k \partial x_j})^2 \qquad \text{(A3.12)}$$

where Ri is the dimensionless parameter

$$\frac{k^2}{\varepsilon^2}\,\frac{V_\theta}{r^2}\,\frac{\partial(rV_\theta)}{\partial r}\,.$$

which may be regarded as a Richardson number wherein the time scale of turbulence k/ε now replaces the mean-flow time scale appearing in equation (3.9). All the coefficients in equation (A3.12) retain the values assigned to them in Chapter 3 and the additional coefficient of the Richardson number term, C_c, is taken as 0.2 on the basis of extensive computer optimisation. It should be noted that flows in which $\frac{\partial(rV_\theta)}{\partial r}$ is positive are relatively more stable, and when $\frac{\partial(rV_\theta)}{\partial r}$ is negative, relatively less stable than the corresponding flow with straight streamlines.

APPENDIX 4

HOT WIRE SIGNAL ANALYSIS

A method of analysing hot wire signals by a linearized set up to obtain mean and fluctuating quantities is described and evaluated. The material presented here draws heavily on references (66) and (67). It has been pointed out in Chapter 4 that the transfer function of a DISA 55D10 linearizer is

$$E_{out} = K(E_{in}^2 - A)^m \qquad (A4.1)$$

where E_{out} and E_{in} are respectively the output and input signals; K, A and m depend on gain, zero and exponent setting respectively. The use of such a linearizer implies that the law of Collis and Williams (68) is to be employed for the anemometer transfer function, i.e.

$$E_{an} = b_1 U_{eff}^n + b_2 \qquad (A4.2)$$

Substituting the above relation into equation (A4.1), the relation for the linearizer becomes

$$E = E_{out} = K b_1 U_{eff}^{m/n} + b_2 - A \qquad (A4.3)$$

By manipulating the setting of the linearizer to obtain $m = n$, $A = b_2$ and calling $S = 1/Kb_1$ yields the linearized relation

$$U_{eff} = SE \qquad (A4.4)$$

The velocities acting on a hot wire are shown in the Figure below. α here is the yaw angle and β the pitch angle. If the wire were infinitely long, only the normal components U_{n1} and U_{n2} would contribute to heat transfer. The cooling would also be independent of the pitch angle. In practice, however, finite length (about 200 to 300 diameter long) to diameter ratio and the wire supports give rise to non-zero tangential cooling and U_{n1} acts differently from U_{n2} (69). This can be incorporated into Champagne *et al.* (53) relation such that

$$U_{eff}^2 = U_{n1}^2 + h^2U_{n2}^2 + K^2U_t^2 \qquad (A4.5)$$

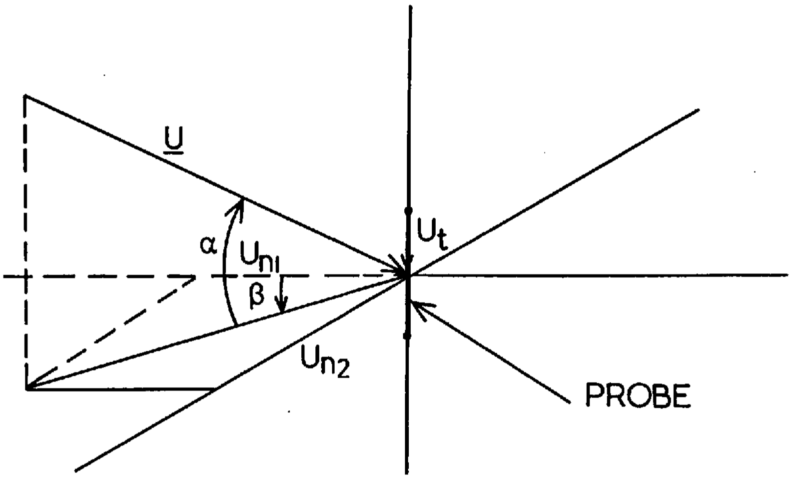

HOT WIRE IN GENERAL VELOCITY FIELD

where K is the yaw factor and h the pitch factor. U_{eff}, the effective cooling velocity described by relation (A4.5) as indicated earlier is proportional to the electrical signal for a linearized system. Therefore combining equations (A4.4) and (A4.5) gives

$$\begin{aligned} U_{eff}^2 &= U^2[\cos^2\alpha(\cos^2\beta + h^2\sin^2\beta) + K^2\sin^2\alpha] \\ &= E^2S^2 \qquad (A4.6) \end{aligned}$$

In order to separate the influence of yaw and pitch one can write:

$$U_{eff}(\alpha) = U^2(\cos^2\alpha + K^2\sin^2\alpha) \quad \text{for } \beta = 0 \qquad (A4.7)$$

and

$$U_{eff}(\beta) = U^2(\cos^2\beta + h^2\sin^2\beta) \quad \text{for } \alpha = 0 \qquad (A4.8)$$

Equation (A4.6) allows experimental determination of the value of S, h, and K by measuring electrical signal for different velocities in a very low turbulent field and the corresponding velocity with a pitot probe in three different spatial positions at the same location, i.e. $\alpha = 0$, $\beta = 0$; $\alpha = 0$, $\beta = \pi/4$; $\alpha = \pi/4$, $\beta = 0$.

The response equation

The Figure below shows a wire placed in an xoz plane. α is the angle between the mean flow direction and the normal to the wire. Expressing the instantaneous velocity U in terms of mean velocity $\overline{U}$

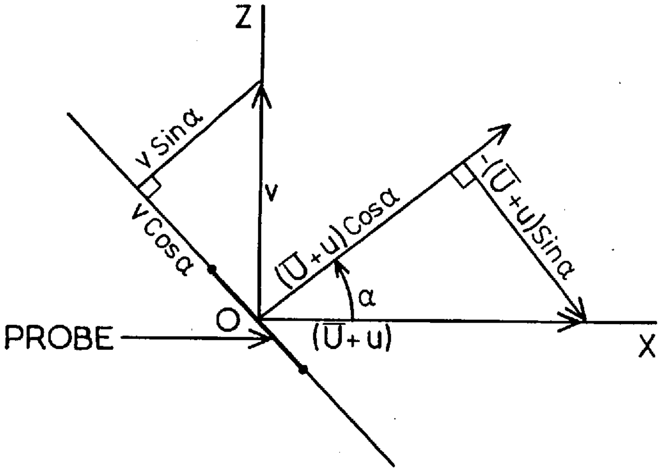

HOT WIRE IN THE XOZ PLANE

and the fluctuating components u, v, and w the normal and tangential components of the cooling velocities are:

$$U_{n1} = (\overline{U} + u)\cos\alpha + v\sin\alpha$$

$$U_{n2} = w$$

$$U_t = -(\overline{U} + u)\sin\alpha + v\cos\alpha$$

Substituting the above relations into equation (A4.5) yields the response equation as:

$$U_{eff} = SE = \Big\{[(\overline{U} + u)\cos\alpha + v\sin\alpha]^2 + h^2w^2 + K^2[v\cos\alpha - (\overline{U} + u)\sin\alpha]^2\Big\}^{\frac{1}{2}} \qquad (A4.9)$$

The mean velocity $\overline{U}$ is obtained from the signal $\overline{E}$ whereas the fluctuating velocities are obtained from the signal $\overline{e^2} = \overline{(E - \overline{E})^2}$. Different methods to obtain these two signals from the above non-linear equation have been discussed in (66). The method outlined below follows the same path with some modifications introduced here (70).

Equation (A4.9) can be rearranged to give

$$SE = \bar{U}\cos\alpha\left(1 + \frac{u}{\bar{U}} + \frac{v}{\bar{U}}\tan\alpha\right)$$

$$\left[1 + \frac{\dfrac{h^2}{\cos^2\alpha}\left(\dfrac{w}{\bar{U}}\right)^2 - K^2\left(\dfrac{v}{\bar{U}} - \tan\alpha - \dfrac{u}{\bar{U}}\tan\alpha\right)^2}{\left(1 + \dfrac{u}{\bar{U}} + \dfrac{v}{\bar{U}}\tan\alpha\right)^2}\right]^{\frac{1}{2}} \tag{A4.10}$$

The above equation is linearized by recasting it into the following form:

$$SE = \bar{U}\cos\alpha\left(1 + \frac{u}{\bar{U}} + \frac{v}{\bar{U}}\tan\alpha\right)$$

$$\left\{a + b\left[\frac{h^2}{\cos^2\alpha}\,\frac{w^2}{\bar{U}^2} + K^2\left(\frac{v}{\bar{U}} - \tan\alpha - \frac{u}{\bar{U}}\tan\alpha\right)^2\right]\right.$$

$$\left.\left[c + d\left(\frac{u}{\bar{U}} + \frac{v}{\bar{U}}\tan\alpha\right)\right]\right\} \tag{A4.11}$$

the coefficients a, b, c and d are calculated by the least squares approximation such that

$$\left[1 + \frac{\dfrac{h^2}{\cos^2\alpha}\,\dfrac{w^2}{\bar{U}^2} + K^2\left(\dfrac{v}{\bar{U}} - \tan\alpha - \dfrac{u}{\bar{U}}\tan\alpha\right)^2}{\left(1 + \dfrac{u}{\bar{U}} + \dfrac{v}{\bar{U}}\tan\alpha\right)^2}\right]^{\frac{1}{2}}$$

$$= \left[a + b\,\frac{\dfrac{h^2}{\cos^2\alpha}\,\dfrac{w^2}{\bar{U}^2} + K^2\left(\dfrac{v}{\bar{U}} - \tan\alpha - \dfrac{u}{\bar{U}}\tan\alpha\right)^2}{\left(1 + \dfrac{u}{\bar{U}} + \dfrac{v}{\bar{U}}\tan\alpha\right)^2}\right]$$

and

$$\left(1 + \frac{u}{\bar{U}} + \frac{v}{\bar{U}}\tan\alpha\right)^{-2} = c + d\left(\frac{u}{\bar{U}} + \frac{v}{\bar{U}}\tan\alpha\right)$$

are satisfied for the actual range of working values for the present variables.

Equation (A4.11) is expanded to give

$$
\begin{aligned}
SE = {} & \bar{U}\cos\alpha[(a+bcK^2\tan^2\alpha) + \frac{u}{\bar{U}}(a + 3bcK^2\tan^2\alpha + bdK^2\tan^2\alpha) \\
& + \frac{v}{\bar{U}}(a\tan\alpha - 2bcK^2\tan^2\alpha + bcK^2\tan^3\alpha + bdK^2\tan^3\alpha) \\
& + \frac{u^2}{\bar{U}^2}(3bcK^2\tan^2\alpha + 3bdK^2\tan^2\alpha) \\
& + \frac{v^2}{U^2}(bcK^2 - 2bcK^2\tan^2\alpha - 2bdK^2\tan^2\alpha + bdK^2\tan^4\alpha) \\
& + \frac{w^2}{\bar{U}^2}(bdh^2/\cos^2\alpha) + \frac{uv}{U^2}(-4bcK^2\tan\alpha - 2bdK^2\tan\alpha + 2bcK^2\tan^3\alpha\ 4bdK^2\tan^3\alpha) \\
& + \frac{u^3}{\bar{U}^3}(bcK^2\tan^2\alpha + 3bdK^2\tan^2\alpha) + \frac{v^3}{\bar{U}^3}(bcK^2\tan\alpha + bdK^2\tan\alpha - 2bdK^2\tan^3\alpha) \\
& + \frac{uv^3}{\bar{U}^3}(bcK^2 + bdK^2 - 2bcK^2\tan^2\alpha - 6bdK^2\tan^2\alpha + 2bdK^2\tan^4\alpha) \\
& + \frac{u^2v}{\bar{U}^3}(-2bcK^2\tan\alpha - 4bdK^2\tan\alpha + bcK^2\tan^3\alpha + 5bdK^2\tan^3\alpha) \\
& + \frac{uw^2}{\bar{U}^3}(bch^2/\cos^2\alpha + bdh^2/\cos^2\alpha) + \frac{vw^2}{\bar{U}^3}(bch^2\tan\alpha/\cos^2\alpha + bdh^2\tan\alpha/\cos^2\alpha) \\
& + \frac{u^4}{\bar{U}^4}(bdK^2\tan^2\alpha) + \frac{v^4}{\bar{U}^4}(bdK^2\tan^2\alpha) + \frac{uv^3}{\bar{U}^4}(2bdK^2\tan\alpha - 2bdK^2\tan^3\alpha) \\
& + \frac{u^3v}{\bar{U}^4}(-2bdK^2\tan\alpha + 2bdK^2\tan^3\alpha) + \frac{u^2v^2}{\bar{U}^4}(bdK^2 - 4bdK^2\tan^2\alpha + bdK^2\tan^4\alpha) \\
& + \frac{u^2w^2}{\bar{U}^4}(bdh^2/\cos^2\alpha) + \frac{v^2w^2}{\bar{U}^4}(bdh^2\tan^2\alpha/\cos^2\alpha) \\
& + \frac{uvw^2}{\bar{U}^4}(2bdh^2\tan\alpha/\cos^2\alpha)]
\end{aligned}
\qquad (A4.12)
$$

Now the response equations to get $\bar{U}$, $\overline{u^2}$, $\overline{v^2}$, $\overline{w^2}$, $\overline{uv}$, $\overline{uw}$ and $\overline{vw}$ by placing the hot wire in different positions are presented below. For instance, the response equation (A4.12) for $\alpha = 0$ in plane xoz after time averaging reduces to

$$S\bar{E} = \bar{U}\,[a + \frac{\overline{v^2}}{\bar{U}}(bcK^2) + \frac{\overline{w^2}}{\bar{U}^2}(bch^2) + \frac{\overline{u^2}}{\bar{U}^2}\frac{\overline{w^2}}{\bar{U}^2}(bdh^2)$$

$$+ \frac{\overline{uw}}{\bar{U}^2}\frac{\overline{uw}}{\bar{U}^2}(2bdh^2) + R] \qquad (A4.13)$$

where

$$R = \frac{\overline{uv^2}}{\bar{U}^3}(bcK^2 + bdK^2) + \frac{\overline{uw^2}}{\bar{U}^3}(bch^2 + bdh^2) + \frac{\overline{u^2v^2}}{\bar{U}^4}(bdK^2)$$

and it can be shown (70) that R representing the remaining terms in equation (A4.13) is negligible, being of the order ~ 0.002. It has been mentioned earlier that rms values are evaluated from the relation $\overline{e^2} = \overline{E^2} - \bar{E}^2$. The final set of equations for different wire positions to obtain the desired quantities is presented below. E_1, e_1 etc. refer to the mean and rms value of the signal in different wire positions.

a. Wire in the xoz plane; $\alpha = 0$

$$S\bar{E}_1 = \bar{U}\,[a + \frac{\overline{v^2}}{\bar{U}^2}(bcK^2) + \frac{\overline{w^2}}{\bar{U}^2}(bch^2) + \frac{\overline{u^2}}{\bar{U}^2}\frac{\overline{w^2}}{\bar{U}^2}(bdh^2)$$

$$+ \frac{\overline{uw}}{\bar{U}^2}\frac{\overline{uw}}{\bar{U}^2}(2bdh^2)] \qquad (A4.14)$$

and

$$S^2\overline{e_1^2} = \bar{U}^2\,[(1-a^2) + \frac{\overline{u^2}}{\bar{U}^2} + \frac{\overline{v^2}}{\bar{U}^2}(K^2 - 2abcK^2) + \frac{\overline{w^2}}{\bar{U}^2}(h^2 - 2abch^2)$$

$$+ \frac{\overline{u^2}}{\bar{U}^2}\frac{\overline{v^2}}{\bar{U}^2}(-2abdK^2) + \frac{\overline{u^2}}{\bar{U}^2}\frac{\overline{w^2}}{\bar{U}^2}(-2abdh^2) + \frac{\overline{v^2}}{\bar{U}^2}\frac{\overline{w^2}}{\bar{U}^2}(-2bcK^2bch^2)$$

$$+ \frac{\overline{w^2}}{\bar{U}^2}\frac{\overline{w^2}}{\bar{U}^2}(-bch^2bch^2) + \frac{\overline{uv}}{\bar{U}^2}\frac{\overline{uv}}{\bar{U}^2}(-2abdK^2) + \frac{\overline{uw}}{\bar{U}^2}\frac{\overline{uw}}{\bar{U}^2}(-4abdh^2)$$

$$+ \frac{\overline{u^2}}{\bar{U}^2}\frac{\overline{w^2}}{\bar{U}^2}\frac{\overline{w^2}}{\bar{U}^2}(-2bch^2bdh^2) + \frac{\overline{w^2}}{\bar{U}^2}\frac{\overline{uw}}{\bar{U}^2}\frac{\overline{uw}}{\bar{U}^2}(-4bch^2bdh^2)$$

$$+ \frac{\overline{u^2}}{\bar{U}^2}\frac{\overline{w^2}}{\bar{U}^2}\frac{\overline{u^2}}{\bar{U}^2}\frac{\overline{w^2}}{\bar{U}^2}(-bdh^2bdh^2) + \frac{\overline{uw}}{\bar{U}^2}\frac{\overline{uw}}{\bar{U}^2}\frac{\overline{uw}}{\bar{U}^2}\frac{\overline{uw}}{\bar{U}^2}(-4bdh^2bdh^2)$$

$$+ \frac{\overline{u^2}}{\bar{U}^2}\frac{\overline{w^2}}{\bar{U}^2}\frac{\overline{uw}}{\bar{U}^2}\frac{\overline{uw}}{\bar{U}^2}(-4bdh^2bdh^2)] \qquad (A4.15)$$

b. Wire in the xoz plane; α = 45° and α = -45°

$$\overline{(e_2^2 + e_3^2)S^2} = \bar{U}^2 \{ [1 + K^2 - (a + bcK^2)(a + bcK^2]$$

$$+ \frac{\overline{u^2}}{\bar{U}^2}[1 + K^2 - 2(a + bcK^2)(3bcK^2 + 3bdK^2)]$$

$$+ \frac{\overline{v^2}}{\bar{U}^2}[1 + K^2 - 2(a + bcK^2)(-bcK^2 - bdK^2)]$$

$$+ \frac{\overline{w^2}}{\bar{U}^2}[2h^2 - 2(2bch^2)(a + bcK^2)]$$

$$+ \frac{\overline{u^2}}{\bar{U}^2}\frac{\overline{w^2}}{\bar{U}^2}[-2(a + bcK^2)(2bdh^2) - 2(2bch^2)(3bK^2c + 3bK^2d)]$$

$$+ \frac{\overline{v^2}}{\bar{U}^2}\frac{\overline{w^2}}{\bar{U}^2}[-2(a + bcK^2)(2bdh^2) - 2(-bcK^2 - bdK^2)(2bch^2)]$$

$$+ \frac{\overline{w^2}}{\bar{U}^2}\frac{\overline{w^2}}{\bar{U}^2}(-4bch^2bch^2) + \frac{\overline{uw}}{\bar{U}^2}\frac{\overline{uw}}{\bar{U}^2}[-4(a + bcK^2)(2bdh^2)]$$

$$+ \frac{\overline{vw}}{\bar{U}^2}\frac{\overline{vw}}{\bar{U}^2}[-4(a + bcK^2)(2bdh^2)] \} \qquad (A4.16)$$

$$\overline{(e_2^2 - e_3^2)S^2} = \bar{U}^2 \{ \frac{\overline{uv}}{\bar{U}^2}[2 - 2K^2 - 2(a + bcK^2)(2bdK^2 - 2bcK^2)]$$

$$+ \frac{\overline{uv}}{\bar{U}^2}\frac{\overline{w^2}}{\bar{U}^2}[-2(a + bcK^2)(4bdh^2)] \} \qquad (A4.17)$$

c. Wire in the xoy plane; $\alpha = 45^{0}$ and $\alpha = -45^{0}$.

$$\overline{(e_4^2 + e_5^2)S^2} = \bar{U}^2 \Big\{ [1 + K^2 - (a + bcK^2)(a + bcK^2)]$$

$$+ \frac{\overline{u^2}}{\bar{U}^2} [1 + K^2 - 2(a + bcK^2)(3bcK^2 + 3bdK^2)]$$

$$+ \frac{\overline{w^2}}{\bar{U}^2} [1 + K^2 - 2(a + bcK^2)(-bcK^2 - bdK^2)]$$

$$+ \frac{\overline{v^2}}{\bar{U}^2} [2h^2 - 2(2bch^2)(a + bcK^2)]$$

$$+ \frac{\overline{u^2}}{\bar{U}^2} \frac{\overline{v^2}}{\bar{U}^2} [-2(a + bcK^2)(2bdh^2) - 2(2bch^2)(3bcK^2 + 3bdK^2)]$$

$$+ \frac{\overline{v^2}}{\bar{U}^2} \frac{\overline{w^2}}{\bar{U}^2} [-2(a + bcK^2)(2bdh^2) - 2(-bcK^2 - bdK^2)(2bch^2)]$$

$$+ \frac{\overline{v^2}}{\bar{U}^2} \frac{\overline{v^2}}{\bar{U}^2} (-4bch^2bch^2) + \frac{\overline{uv}}{\bar{U}^2} \frac{\overline{uv}}{\bar{U}^2} -4(a + bcK^2)(2bdh^2)$$

$$+ \frac{\overline{vw}}{\bar{U}^2} \frac{\overline{vw}}{\bar{U}^2} [-4(a + bcK^2)(2bdh^2)] \Big\} \qquad (A4.18)$$

$$\overline{(e_4^2 - e_5^2)S^2} = \bar{U}^2 \Big\{ \frac{\overline{uw}}{\bar{U}^2} [2 - 2K^2 - 2(a + bcK^2)(2bdK^2 - 2bcK^2)]$$

$$+ \frac{\overline{uw}}{\bar{U}^2} \frac{\overline{v^2}}{\bar{U}^2} [- 2(a + bcK^2)(4bdh^2)] \Big\} \qquad (A4.19)$$

d. Wire in the plane bisector of xoy and xoz, $\alpha = 45^{0}$ and $\alpha = -45^{0}$ (i.e. wire parallel to the bisector of the 1st and 3rd quadrants of the xoz plane).

$$\overline{(e_6^2 + e_7^2)S^2} = \bar{U}^2 \Big\{ [1 + K^2 - (a + bcK^2)(a + bcK^2)]$$

$$+ \frac{\overline{u^2}}{\bar{U}^2} [1 + K^2 - 2(a + bcK^2)(3bcK^2 + 3bdK^2)]$$

$$+ \frac{\overline{v^2}}{2\bar{U}^2} [1 + K^2 - 2(a + bcK^2)(-bcK^2 - bdK^2)][2h^2 - 2(2bch^2)(a+bcK^2)]$$

$$+ \frac{\overline{w^2}}{2\bar{U}^2} [1 + K^2 - 2(a + bcK^2)(-bcK^2 - bdK^2)][2h^2 - 2(2bch^2)(a+bcK^2)]$$

$$+ \frac{\overline{vw}}{\bar{U}^2} [1 + K^2 - 2(a + bcK^2)(-bcK^2 - bdK^2) - 2h^2 + 2(2bch^2)(a + bcK^2)]$$

$$+ \frac{\overline{u^2}}{2\bar{U}^2} \frac{\overline{v^2}}{\bar{U}^2} [-2(a + bcK^2)(1bdh^2) - 2(2bch^2)(3bK^2c + 3bK^2d)]$$

$$+ \frac{\overline{u^2}}{2\bar{U}^2} \frac{\overline{w^2}}{\bar{U}^2} [-2(a + bcK^2)(1bdh^2) - 2(2bch^2)(3bK^2c + 3bK^2d)]$$

$$+ \frac{\overline{v^2}}{4\bar{U}^2} \frac{\overline{v^2}}{\bar{U}^2} [-2(a + bcK^2)(2bdh^2) - 2(-bcK^2 - bdK^2)(2bch^2) - 4bch^2bch^2$$

$$- 4(a + bcK^2)(2bdh^2)]$$

$$+ \frac{\overline{w^2}}{4\bar{U}^2} \frac{\overline{w^2}}{\bar{U}^2} [-2(a + bcK^2)(2bdh^2) - 2(-bcK^2 - bdK^2)(2bch^2)$$

$$- 4bch^2bch^2 - 4(a + bcK^2)(2bdh^2)]$$

$$+ \frac{\overline{v^2}}{2\bar{U}^2} \frac{\overline{w^2}}{\bar{U}^2} [-2(a + bcK^2)(2bdh^2) - 2(-bcK^2 - bdK^2)(2bch^2) - 4bch^2bch^2$$

$$+ 4(a + bcK^2)(2bdh^2)]$$

$$+ \frac{\overline{u^2}}{\bar{U}^2} \frac{\overline{vw}}{\bar{U}^2} [-2(a + bcK^2)(2bdh^2) - 2(2bch^2)(3bK^2c + 3bK^2d)]$$

$$+ \frac{\overline{vw}}{\bar{U}^2} \frac{\overline{vw}}{\bar{U}^2} [2(a + bcK^2)(2bdh^2) + 2(-bcK^2 - bdK^2)(2bch^2)$$

$$- 4bch^2bch^2]$$

$$+ \frac{\overline{v^2}}{\bar{U}^2} \frac{\overline{vw}}{\bar{U}^2} [4bch^2bch^2] + \frac{\overline{w^2}}{\bar{U}^2} \frac{\overline{vw}}{\bar{U}^2} [4bch^2bch^2]$$

$$+ \frac{\overline{uv}}{2\bar{U}^2}\,\frac{\overline{uv}}{2\bar{U}^2}\,[-4(a + bcK^2)(2bdh^2)]$$

$$+ \frac{\overline{uv}}{\bar{U}^2}\,\frac{\overline{uw}}{\bar{U}^2}\,[4(a + bcK^2)(2bdh^2)]$$

$$+ \frac{\overline{uw}}{2\bar{U}^2}\,\frac{\overline{uw}}{\bar{U}^2}\,[-4(a + bcK^2)(2bdh^2)] \qquad (A4.20)$$

Equations (A4.14) to (A4.20) were solved by Gauss-Siedel (successive approximations) method to yield the desired quantities, $\bar{U}$, $\overline{u^2}$, $\overline{v^2}$, $\overline{w^2}$, $\overline{uv}$, $\overline{uw}$ and $\overline{vw}$, in the streamline oriented system. Finally these quantities are transformed to the fixed co-ordinate system by simple trigonometric relations given in (69).

Analysis of the propagation of error in measurement

An analysis of the propagation of the random error is not difficult because the quantities to determine are of the same order of magnitude as, and are strongly linked with, the measured quantities provided, at each location a suitable set of orientations of the probe is chosen.

It has been shown earlier that equation (A4.10) is linearized by a least squares approximation to the form given by equation (A4.11). Another approach suggested by Rodi (69) and Durst and Rodi (71) is to square the equation (A4.10) and then take the time average. Here the two methods are briefly compared. The complete step by step details can be found in (66). To keep the analysis brief only $\bar{U}$, $\overline{u^2}$, $\overline{v^2}$, $\overline{w^2}$ and $\overline{uv}$ are evaluated. Final results, however, are tabulated for all quantities measured here. To simplify the analysis further it will be assumed that no error is associated with the calculation of the pitch and yaw factors and that they are zero and 1 respectively.

For the squared method of (69) the time mean response equation with the above simplifications reduces to

$$\overline{E^2S^2} = \overline{v^2} + \overline{w^2} + \cos^2\alpha(\overline{U}^2 + \overline{u^2} - \overline{v^2}) + \sin 2\alpha\,\overline{uv} \tag{A4.21}$$

for a wire located in the xoy plane.

To extract $\overline{U}$. $\overline{u^2}$, $\overline{v^2}$, $\overline{w^2}$ and $\overline{uv}$ only four wire positions are sufficient, namely

1. plane xoz; $\alpha = 0$
2. plane xoz; $\alpha = \pi/4$
3. plane xoy; $\alpha = \pi/4$
4. plane xoy; $\alpha = -\pi/4$

Substituting these values into equation (A4.21) gives the set:

$$\begin{aligned}
\overline{E_1^2S_1^2} &= (\overline{U}^2 + \overline{u^2}) + \overline{v^2} \\
\overline{E_2^2S_2^2} &= \tfrac{1}{2}(\overline{U}^2 + \overline{u^2}) + \overline{v^2} + \tfrac{1}{2}\overline{w^2} \\
\overline{E_3^2S_3^2} &= \tfrac{1}{2}(\overline{U}^2 + \overline{u^2}) + \tfrac{1}{2}\overline{v^2} + \overline{w^2} + \overline{uv} \\
\overline{E_4^2S_4} &= \tfrac{1}{2}(\overline{U}^2 + \overline{u^2}) + \tfrac{1}{2}\overline{v^2} + \overline{w^2} - \overline{uv}
\end{aligned} \tag{A4.22}$$

where $\overline{E_i^2}$ is the mean value of the squared signal from the linearized anemometer and S_i is the calibration constant determined from the relationship $\overline{U} = \overline{E}S$ in a very low turbulence level flow field. For simplicity let $M_i = \overline{E_i^2S_i}$; $x_i = \overline{U}^2 + \overline{u^2}$; $x_j = \overline{u_j^2}$ where $j = 1 = v$, $j = 2 = w$; and $x_4 = \overline{uv}$. The equation set (A4.22) then becomes:

$$\begin{aligned}
x_1 &= \tfrac{1}{2}(3M_1 - 4M_2 + M_3 + M_4) \\
x_2 &= \tfrac{1}{2}(-M_1 + 4M_2 - M_3 - M_4) \\
x_3 &= \tfrac{1}{2}(-M_1 + M_3 + M_4) \\
x_4 &= \tfrac{1}{2}(M_3 - M_4)
\end{aligned} \tag{A4.33}$$

and the variation δx_i associated with the variation δM_j is:

$$\begin{aligned}
\delta x_1 &= \tfrac{1}{2}(3\delta M_1 - 4\delta M_2 + \delta M_3 + \delta M_4) \\
\delta x_2 &= \tfrac{1}{2}(-\delta M_1 + 4\delta M_2 - \delta M_3 - \delta M_4) \\
\delta x_3 &= \tfrac{1}{2}(-\delta M_1 + \delta M_3 + \delta M_4) \\
\delta x_4 &= \tfrac{1}{2}(\delta M_3 - \delta M_4)
\end{aligned} \qquad (A4.24)$$

Expressing this in terms of fraction variation e.g.

$$\frac{\delta x_1}{x_1} = \frac{1}{3M_1 - 4M_2 + M_3 + M_4}\left[3M_1\frac{\delta M_1}{M_1} - 4M_2\frac{\delta M_2}{M_2} + M_3\frac{\delta M_3}{M_3} + M_4\frac{\delta M_4}{M_4}\right]$$

and finally the limits of confidence interval will be:

$$\frac{|\delta x_1|}{x_1} = \frac{1}{|3M_1 - 4M_2 + M_3 + M_4|}\left[3M_1\frac{|\delta M_1|}{M_1} - 4M_2\frac{|\delta M_2|}{M_2} + M_3\frac{|\delta M_3|}{M_3} + M_4\frac{|\delta M_4|}{M_4}\right]$$

Now it is assumed that the measurement error is always the same i.e.

$$\frac{|\delta M_i|}{M_i} = \frac{|\delta M|}{M}$$

and therefore

$$\frac{\delta x_1}{x_1} = \frac{3M_1 - 4M_2 + M_3 + M_4}{|3M_1 - 4M_2 + M_3 + M_4|}\,\frac{\delta M}{M} \qquad (A4.25)$$

Similarly for the other components (dropping the absolute sign for simplicity)

$$\frac{\delta x_2}{x_1} = \frac{M_1 + 4M_2 + M_3 + M_4}{|-M_1 + 4M_2 - M_3 - M_4|}\,\frac{\delta M}{M} \qquad (A4.26)$$

$$\frac{\delta x_3}{x_3} = \frac{M_1 + M_3 + M_4}{|-M_1 + M_3 + M_4|}\,\frac{\delta M}{M} \qquad (A4.27)$$

$$\frac{\delta x_4}{x_4} = \frac{M_3 + M_4}{|M_3 - M_4|}\,\frac{\delta M}{M} \qquad (A4.28)$$

From equation (A4.28) it can be seen that if $M_3 = M_4$ the fractional error is infinite. This is because in this situation the value of the shear stress is zero and even for small values the fractional error will be infinite. Now, $\overline{u^2} = x_1 - \overline{U}^2$; therefore

$$\frac{\delta\overline{u^2}}{\overline{u^2}} = \frac{\delta x_1}{\overline{u^2}} - \frac{\delta\overline{U}^2}{\overline{u^2}}$$

or rewriting

$$\frac{\delta\overline{u^2}}{\overline{u^2}} = \frac{\delta x_1'}{x_1}\left(1 + \frac{1}{\overline{u^2}/\overline{U}^2}\right) + \frac{\delta\overline{U}^2}{\overline{U}^2}\,\frac{1}{\overline{u^2}/\overline{U}^2} \qquad \text{(A4.29)}$$

Since $\overline{U}^2$ and $\overline{u^2}$ appear always linked, the information about $\overline{U}$ is obtained by linearizing the response equation by Champagne's (53) series development when a wire is located in the xoz plane with $\alpha = 0$; the resulting equation when third order terms are neglected is:

$$S\overline{E} = \overline{U}(1 + \tfrac{1}{2}\overline{u^2}/\overline{U}^2)$$

and following the above procedure it can be deduced that

$$\frac{\delta\overline{E}S}{\overline{E}S} = \frac{\delta\overline{U}}{\overline{U}}$$

if the second order term like $\overline{U}\delta(x_2/\overline{U}^2)$ is neglected. Assuming $\overline{E^2} = \overline{E}^2$ and $\overline{E}S = M^{\frac{1}{2}}$ one gets

$$\frac{1}{2}\,\frac{\delta M}{M} = \frac{\delta\overline{U}}{\overline{U}}$$

substituting the above relation into equation (A4.29) yields

$$\frac{\delta\overline{u^2}}{\overline{u^2}} = \left[\left(1 + \frac{1}{\overline{u^2}/\overline{U}^2}\right)\frac{3M_1 + 4M_2 + M_3 + M_4}{|3M_1 - 4M_2 + M_3 + M_4|} + \frac{1}{\overline{u^2}/\overline{U}^2}\right]\frac{\delta M}{M}$$

Finally, if the turbulence intensity $\frac{\sqrt{\overline{u^2}}}{\overline{U}}$ is denoted by T the complete set for the evaluation of the confidence interval of the calculated values is:

$$\frac{\delta\overline{U}}{\overline{U}} = \frac{1}{2}\,\frac{\delta M}{M} \tag{A4.30}$$

$$\frac{\delta\overline{u^2}}{\overline{u^2}} = \left[(1 + \frac{1}{T^2})\,\frac{3M_1 + 4M_2 + M_3 + M_4}{|3M_1 - 4M_2 + M_3 + M_4|} + \frac{1}{T^2}\right]\frac{\delta M}{M} \tag{A4.31}$$

$$\frac{\delta\overline{v^2}}{\overline{v^2}} = \frac{M_1 + 4M_2 + M_3 + M_4}{|-M_1 + 4M_3 - M_3 - M_4|}\;\frac{\delta M}{M} \tag{A4.32}$$

$$\frac{\delta\overline{w^2}}{\overline{w^2}} = \frac{M_1 + M_3 + M_4}{|-M_1 + M_3 + M_4|}\;\frac{\delta M}{M} \tag{A4.33}$$

$$\frac{\delta\overline{uv}}{\overline{uv}} = \frac{M_3 + M_4}{|M_3 - M_4|}\;\frac{\delta M}{M} \tag{A4.34}$$

Following exactly the above procedure the corresponding set for the present method (equations A4.14 - A4.19) is

$$\frac{\delta\overline{U}}{\overline{U}} = \frac{1}{2}\,\frac{\delta M}{M} \tag{A4.35}$$

$$\frac{\delta\overline{u^2}}{\overline{u^2}} = \frac{\delta M}{M} \tag{A4.36}$$

$$\frac{\delta\overline{v^2}}{\overline{v^2}} = \frac{2M_2 + M_1}{|2M_2 - M_1|}\;\frac{\delta M}{M} \tag{A4.37}$$

$$\frac{\delta\overline{w^2}}{\overline{w^2}} = \frac{2M_3 + M_1}{|2M_3 - M_1|}\;\frac{\delta M}{M} \tag{A4.38}$$

$$\frac{\delta\overline{uv}}{\overline{uv}} = \frac{M_3 + M_4}{|M_3 - M_4|}\;\frac{\delta M}{M} \tag{A4.39}$$

where it should be noted that $M_i = \overline{e_i^2}\, s_i^2$. In order to determine $\delta M/M$, it was assumed that each measurement carries an error of 1%. Therefore for the calibration rig

$$U = ES$$

$$\frac{|\delta S|}{S} = \frac{|\delta E|}{E} + \frac{|\delta U|}{U} = 0.02$$

and since $M = \overline{E^2}S^2 = \overline{e^2}S^2$

$$\frac{\delta M}{M} = \frac{|\delta \overline{E^2}|}{\overline{E^2}} + 2\frac{|\delta S}{S}$$

$$= \frac{|\delta \overline{e^2}|}{\overline{e^2}} + 2\frac{|\delta S|}{S} = 0.05$$

The values of M_i with the above assumptions for the squared method are determined from the equation set (A4.22) whereas for the present method they are obtained from equations (A4.14-A4.19). The results obtained are shown in the following Table. The values for the stresses $\overline{uw}$ and $\overline{vw}$ for the squared method are of the same order of magnitude as those for $\overline{uv}$. More detailed results are given in (66).

The present method has also been compared with the series development of Champagne *et al.* (53) in (66), where for a turbulence level of 50% it has been concluded that the present method is much superior to the series method. The accuracy of the series development method progressively becomes worse as the turbulence level rises.

TABLE. Comparison of random error in the measurements.

Turb. level	Squared method ($\frac{\delta x}{x}$ * 100)					Present method ($\frac{\delta x}{x}$ * 100)						
	$\overline{U}$	$\overline{u^2}$	$\overline{v^2}$	$\overline{w^2}$	$\overline{uv}$	$\overline{U}$	$\overline{u^2}$	$\overline{v^2}$	$\overline{w^2}$	$\overline{uv}$	$\overline{uw}$	$\overline{vw}$
20%	2.5	544	285	140	72	2.5	5	15	15	15	15	15
25	"	365	195	95	50	"	"	"	"	"	"	"
30	"	267	146	70	37	"	"	"	"	"	"	"
35	"	208	116	55	30	"	"	"	"	"	"	"
40	"	169	97	46	25	"	"	"	"	"	"	"
45	"	143	84	39	22	"	"	"	"	"	"	"
50	"	125	75	35	20	"	"	"	"	"	"	"
55	"	111	68	31	18	"	"	"	"	"	"	"
60	"	100	62	28	16	"	"	"	"	"	"	"
65	"	92	58	26	15	"	"	"	"	"	"	"
70	"	85	55	25	15	"	"	"	"	"	"	"

Systematic errors in the approximated form of the response equation

For simplicity the quantity inside square brackets of equation (A4.10) is represented by (1+A). The quantity A is always positive since all the terms are squared and the denominator is generally higher than the numerator either due to the quantity 1 or because K^2 is very small ($\sim$0.02). This quantity A has been approximated by Champagne *et al.* (53) by the first two terms of the MacLaurin series expansion. When the best linear fit is compared with the true value it is found that the maximum deviation for $0 \leq A \leq 1$ is 1.09% whereas with the series approach it is 6.06%, and for $0 \leq A \leq 1.5$ (corresponding to turbulence level of about 50%) the two values are 1.95% and 10.95% respectively.

The denominator inside square brackets may be for simplicity written as $(1+B)^{-2}$. When B approaches -1 the expression between brackets increases very rapidly, there an approximation of the quadratic type is poor representation in such regions. However, the term under the square root is weighted by (1+B) that tends to zero as rapidly as the denominator in the square root term. Therefore the influence of a bad representation is damped down. Ribeiro (70) has shown that with these approximations turbulence intensities above 50% could be treated. However, the occurrence of the reversion of the velocity direction will influence the probe to distort the flow field. Therefore measurement results with turbulence intensities in excess of 50% should be carefully interpreted because of the inability of the wire to handle reverse flow.

Effect of finite size of the wire

When an infinitely long cylindrical wire of resistance R is located in a flow field the heat balance equation reads:

$$c_m \frac{dT_w}{dt} = RI^2 - s = \frac{E^2}{R} - s \qquad \text{(A4.40)}$$

where c_m is the heat capacity of the wire, I is the current passing through the wire and S represents a sink term expressing the heat removed by the flow field. If the wire is maintained at a constant temperature through adequate control of I equation (A4.40) simply reduces to

$$\frac{E^2}{R} = s \qquad \text{(A4.41)}$$

R, now being a constant as it is only dependent on the temperature. Thus in order to determine the transferfunction of a hot wire of infinite length s has to be determined. The dimensionless groups that affect the steady heat transfer (expressed in terms of Nusselt number) are the Reynolds number, the Prandtl number, the Grashof number and the dimensionless overheat ratio of the wire $(T_w-T_a)/T_a$, T_w being the wire temperature and T_a the flow temperature. In most practical situations where hot wire anemometry is used the buoyant effects are negligible. Thus

$$Nu = Nu[Re, Pr, (T_w - T_a)/T_a]$$

Several forms of the above relation have been suggested according to the type of fluid; for steady flow of air Collis and Williams (68) found that the experimental values are well correlated by the empirical equation

$$Nu = [A + B(\frac{Ud}{\nu})^n]\left[1 + \frac{T_w - T_a}{T_a}\right]^m \qquad (A4.42)$$

d being the wire diameter. The coefficients A, B, n and m are independent of the Reynolds number inside the limited range of Reynolds number, e.g. for $0.02 < Re < 44$, $A = 0.24$, $B = 0.56$, $n = 0.45$ and $m = 0.17$; and for $44 < Re < 140$, $A = 0$, $B = 0.48$, $n = 0.51$ and $m = 0.17$. The discontinuity at $Re = 44$ has been explained as due to the occurrence of vortex shedding (72). In actual situations the flow is unsteady. However following Corrsin (73) and Ribeiro (70) the steady flow approach is justified in the present situation.

Equations (A4.41) and (A4.42) are only applicable to infinite wires. In practice their finite size makes the temperature distribution non-uniform. If x is a co-ordinate along the wire and radial temperature gradients are neglected the conduction term changes the form of the equation (A4.40)

$$\frac{\pi d^2}{4}\frac{d}{x}(k_w \frac{d\theta}{dx}) = RI^2 - s \qquad (A4.43)$$

θ is the local overheat $(T_w - T_a)$ now, R and s are local values dependent on θ. In order to integrate the above equation the two source terms must be expressed in terms of θ. Champagne *et al.* expressing the sources to be quadratic expressions in terms of the overheat ratio proposed a solution of the form:

$$\frac{\theta}{\theta_o} = f_1[f_2\sinh f_2x - \cosh f_2x] + (f_1 + 1) \qquad \text{(A4.44)}$$

where f_1 and f_2 are functions of the velocity field, the current through the wire and the dimensions and electrical properties of the wire. Their measurements of temperature distribution agree within 10% of equation (A4.44). Champagne *et al.*'s results indicate that for typical probes with $\ell/d \simeq 200$ operating in typical conditions of overheat ratio of .8 the temperature is kept within 2% in a central region of 100 diameters for velocities as low as 5 m/s. Another very important conclusion from their measurements is that for wires not perpendicular with the velocity the temperature distribution changes only slightly near the prongs. Thus the cooling that arises in such circumstances is not due to dependence on α of the end conduction losses but is due to cooling by the tangential component of the velocity. It is therefore for this reason that effective cooling velocity is written as

$$U_{eff} = U_{eff}(U_n, U_t)$$

Hinze (75) has suggested above relation of the form

$$U_{eff} = U(\cos^2\alpha + K^2\sin^2\alpha)^{\frac{1}{2}} \; (U_n^2 + K^2U_t^2)^{\frac{1}{2}}$$

The above equation is still not satisfactory because of the influence of the shape and dimensions of the probe. The form of the equation which reasonably accounts-for these effects and used here has been suggested in (69) as equation (A4.6) i.e.

$$U_{eff} = U[\cos^2\alpha(\cos^2\beta + h^2\sin^2\alpha) + K^2\sin^2\alpha]^{\frac{1}{2}}$$

or

$$U_{eff} = [U_{n1}^2 + h^2U_{n2}^2 + K^2U_t^2]^{\frac{1}{2}}$$

The symbols appearing in the above equation have already been explained at the beginning of this Appendix.

APPENDIX 5

COMPUTER PROGRAM MODIFICATIONS

This Appendix describes the changes made to the original program GENMIX of Patankar and Spalding (14). Minor changes (such as changes in the specification of total number of steps etc.) are not pointed ou explicitly; these, as the exact programming of other changes, may be seen from the complete program listing following this guide.

Chapter 0

Extra variables added to the subroutine MAIN are: DUDY, PML, REPRDF, REYT and RTU. DUDY simply indicates dU/dy. PML stands for Prandtl mixing length. REPRDF indicates the value of spin Reynolds nu bers at which profiles are desired. REYT and RTU represent turbulence Reynolds number in Chapter 6 of MAIN program.

Apart from these additions, the other changes were to increase th dimension of the profile quantities from 43 to 100. The common block GM4 was deleted, and in its place common blocks SWFT4, SOURCE, VISCO, VISC and AVER were inserted. The quantities in these blocks following the general scheme of GENMIX are self explanatory. For instance EMUTU stands for turbulent viscosity while EMULAM is laminar viscosity. An additional common block, DATA, specified the values of REPRDF.

Chapter 1-2

These chapters are essentially the same as in the original MAIN. Comment cards have been inserted to explain any changes. It should be noted that for geometries considered here the index KRAD takes the val 1.

Chapter 3

This chapter contains the dependent variables used in the program. Two new dependent variables F(3,I) and F(4,I), respectively representing the turbulence kinetic energy and its local rate of dissipation, have been introduced here. It should be noted that F(1,I) array here represents the product of circumferential velocity and radius. Other variables, with comment cards, are self-explanatory.

Chapter 4

This chapter lists the values of the material constants used in the calculations. EMU(I), EMULAM(I), EMUTUR(I), EMUEFF(I), RHO(I) and REYT(I) are also initialized here.

Chapter 5

In this chapter initial values of all the dependent variables are prescribed. W here stands for the angular velocity and RETRAN is the transition Reynolds number. XU and XULAST for the calculations are calculated from the relation

$$Re = \frac{x^2 \sin\alpha\omega}{\nu}$$

Simple initial profiles for U, V_θ and $\hat{h}$ are introduced here. Initial profiles of k and ε are specified in the next chapter.

Chapter 6

This chapter differs from the one in the GENMIX version. The reader is introduced to Prandtl's mixing length model of turbulence here. Mixing length constants κ and λ are assigned the values 0.42 and 0.085 respectively. The formulation of the turbulence model is given in Chapter 3. FORTRAN statements appearing here are straightforward. The initial profiles of turbulence energy and its local rate of dissipation are also calculated here. The initial profile of k is specified as a parabolic function of the boundary layer thickness, modified by a damping function near the wall, viz.

$$k = k_{max} \, [1 - \exp(-z^{+}/11)^{2}][1 - 2Az^{*} + Az^{*2}]$$

where $z^{*} = z/z_{edge}$; $k_{max} = \frac{\tau}{\rho C_{\mu}^{\frac{1}{2}}}$ and $A = \frac{1 - k_{edge}}{k_{max}}$

For the initial profile of dissipation rate it was assumed that

$$\varepsilon = C_{\mu}\rho k^{2}/\mu_{t}$$

where C_{μ} was taken as 0.09. It has been mentioned already that in all the cases examined here the predicted flow behaviour was negligibly dependent upon uncertainties in the prescribed initial profiles.

It should be noted that the values given to k and ε for wall and external boundary nodes are very small, i.e. F(3,1) = F(4,1) = 1.E-20 and F(3,NP3) = F(4,NP3) = 1.E-20. FORTRAN statements to print the initial profiles of k and ε are also included here.

Chapter 7

Here the size of the forward step DX is simply calculated as

DX = FRADX*Y(N)

where FRADX is assigned some value (0.06 in this case) in Chapter 2 of MAIN. There is another criterion listed here to control the step size, i.e.

$$dx^{+} = (\rho\tau)^{\frac{1}{2}} \frac{dx}{\mu} = 100$$

but in all the calculations presented here the first criterion was sufficient to control the step size changes.

Chapter 8

This chapter is much shorter than that of GENMIX, because the variety of boundary conditions are not required for the present case. The I-boundary is always taken to be a wall - the E-boundary may be a wall or a free boundary. TAUI, TAUE, RMI, RME, INDI, INDE, AJI(J) and AJE are set here. FORTRAN statements expressing the formulation of cross-stream pressure gradient also appear here in array SU(1,I). It is recalled that

$$\frac{\partial p}{\partial z} = \frac{\rho V_\theta^2}{r} \cos\alpha$$

If the value of $\partial p/\partial x$ is known along the I boundary, the value along any line is simply

$$\left(\frac{\partial p}{\partial x}\right)_i = \left(\frac{\partial p}{\partial x}\right)_I + \frac{\partial}{\partial x} \int_0^{z_i} \frac{\rho V_\theta^2}{r} \cos\alpha \, dz$$

To overcome the difficulty of not knowing the changes in V_θ/r at the grid point where $\partial p/\partial x$ is to be evaluated the rate of change appropriate to the previous interval was taken, not merely as a first guess but as the final value. Simple trapezoidal integration scheme is used to formulate the above expression into FORTRAN statements.

Chapter 9

This chapter is considerably shorter than that of GENMIX, and contains nothing new. A criterion to control step size by a simple entrainment formulation appears here but was never used in the present calculations.

Chapter 10

Chapter 10 provides the output from the program. Self-explanatory expressions for the station variables such as Reynolds number and Nusselt number are given here. Subroutine PROFIL to print profiles of the dependent variables is also called from here.

Chapter 11-12

The operation of these chapters is similar to that of GENMIX except the program termination statements of Chapter 11 have been absorbed into Chapter 12. The statement CALL STRIDE(3) also appears here.

Subroutine AUX

This subroutine lists all the steps in the calculation of turbulent viscosity μ_t by the k-ε model of turbulence. Source term arrays SU, SD, SUU and SDU for the variables are also filled in this subroutine. The operation of this subroutine is as follows.

The first sequence of statements (1-10) gives the values of all the constants used in the k-ε model. The formulation of turbulent viscosity is presented next as:

$$\mu_t = C_\mu \rho k^2/\varepsilon$$

where $$C_\mu = 0.09 \exp[-3.4/(1 + R_t(50)^2]$$

The FORTRAN statements expressing these expressions are straightforward. The value of turbulent viscosity calculated at cell boundaries is then added to the laminar value already in array EMULAM. The effective Prandtl numbers are calculated next. For later use μ_{eff} is modified by multiplying it by $r/\delta y$.

The entrainment rate $\dot{\text{RME}}$ is calculated next in the same way as in GENMIX, except it is controlled by the circumferential velocity here.

The remaining sections of the subroutine calculates source terms for all the dependent variables. The DD loop 84 calculates the source term $-dp/dx + \frac{\rho V_\theta^2}{r} \sin\alpha$ for the streamwise momentum equation. Statements 220 to 242 fill source term arrays for the $\hat{h}$ and m equations. Source terms for k and ε equations are calculated next. The source term arrays SU(3,I) and SU(4,I) are set to zero first. The variable DUDY is used to represent dU/dz while DVDY is $\frac{dV_\theta/r}{dz}$. D2UDY and D2VDY similarly represent second derivatives. DKDY represents $dk^{\frac{1}{2}}/dz$. The values of these derivatives are calculated separately for mid regions (3 to NP1) and I and E boundaries. The FORTRAN formulation of these expressions is straightforward and needs no further elaboration here. The DO loop 100 actually calculates source terms. The source term, for instance, for the k-equation is

$$\underbrace{\mu_t\left[\left(\frac{\partial U}{\partial z}\right)^2 + \left(r\,\frac{\partial V_\theta/r}{\partial z}\right)^2\right]}_{PJ3} - \underbrace{\rho\varepsilon - 2\mu\left(\frac{\partial k^{\frac{1}{2}}}{\partial z}\right)^2}_{DJ3}$$

Rate of production of turbulence energy by mean strain is calculated as PJ3. Similarly DJ3 represents dissipation of energy terms in the k-equation. Similar notation (PJ4 and DJ4) is used to evaluate expressions in the ε-equation. The streamline curvature correction is included in the final calculation of DJ4 as

```
DJ4 = DJ4*(1 - AR*RCHSDN)
```

where AR is the coefficient C_c and RCHSDN stands for Richardson number. Both the source terms are subject to a stabilising procedure, whereby the total source for ϕ, $S_u + S_D \cdot \phi_D$ is set to either $S_u\phi_D/\phi_u$ or $2S_u - S_u\phi_D/\phi_u$ depending on the sign of S_u (= PJ-DJ). Finally, the sources are multiplied by $r\delta y$ for the axisymmetric case.

Subroutine PROFIL

This subroutine is used to print the desired output. First sequence of statement (10-11) defines the station variables. WRITE statement 23 prints quantities like x, Reynolds number, Nusselt number and friction factor etc. The second part of this subroutine is concerned with the print out of profile variables like $z(\omega/\nu)^{\frac{1}{2}}$, U and V_θ etc. There is nothing fancy about the FORTRAN statements appearing here and are easy to understand.

Subroutine WF

This subroutine provides "wall functions" required by the Patankar-Spalding procedure. Near the wall, since fluxes of momentum, mass and energy are significant only in the normal direction and the transport of these quantities by convection is negligible, the partial differential equations of Chapter 2-3 reduce to ordinary ones. In this Couette flow region these equations can be solved to yield simple algebraic relations which relate the fluxes of these quantities at the wall to conditions at the grid node adjacent to the wall. These algebraic relations are called "wall-functions". For example for the streamwise momentum equation it can be easily shown that

$$\frac{\tau_{x,w}}{\rho U^2} = \frac{\mu}{\rho U z} - \frac{z}{2\rho U^2}\left(\frac{\partial p}{\partial x} - \rho \frac{V_\theta^2}{r} \sin\alpha\right)$$

Similar relations for the other variables V_θ, $\hat{h}$ and m can be readily derived. The flux of k is zero, and for ε it is given by

$$\frac{1}{\sigma_\varepsilon Re} - 0.5*A3(1.-B3)*\varepsilon z/Uk$$

where A3 and B3 are equal to 1.92 and 0.3 respectively.

Subroutine STRIDE

This subroutine is the core of the Patankar-Spalding solution procedure, and as such has been left unchanged for the most part. Minor changes due to the elimination of the source term from the equation for swirl velocity, V_θ, are, however, outlined below.

The momentum equation for the swirl direction as explained in (14) may be expressed as

$$\frac{\partial(rV_\theta)}{\partial x} + (a + b\omega)\frac{\partial(rV_\theta)}{\partial\omega} = \frac{\partial}{\partial\omega}\left[cr^2\frac{\partial(V_\theta/r)}{\partial\omega}\right]$$

It should be noticed that this equation differs from the standard form, in that rV_θ is the operand of the differentiations on the left and V_θ/r is that on the right. This necessitates some modifications to the expressions for the finite-difference coefficients. The complete details are given in (14); here, the sequences of statements altered in STRIDE are listed. First attention is drawn to the mid-region coefficients AD, BD, and DF in DO loop 3004. According to the procedure described in (14) T^*_+ in FORTRAN statement for AD is multiplied by $(r_+/r_{++})^2$. T^*_- and T^*_+ are similarly modified in FORTRAN statements for BD and DF. For grid point 2, the modified ADF, BDF and DF appear after statement 8005; for NP2 they follow statement 2318. These modifications are straightforward and follow the procedure outlined in reference (14).

```
      PROGRAM DISCON(INPUT,OUTPUT,TAPE5=INPUT,TAPE6=OUTPUT)
CHAPTER 0 .----------------------------------------------DIMENSIONS AN
      DIMENSION DUDY(100),PML(100),REPROF(5),REYT(100),RTU(100)
      COMMON/GENERAL/AJE(10),AJI(10),CSALFA,DPDX(100),DX,EMU(100),
     1F(5,100),FS(5,100),H,IFIN,INDE(10),INDI(10),ISTEP,ITEST,IUTRAP,
     2KEX,KIN,KRAD,N,NEQ,NPH,NP1,NP2,NP3,OM(100),PET,PR(3),PREF(5,100),
     3PSIE,PSII,R(100),RHO(100),RME,RMI,RN15,RU(100),R25,SD(5,100),
     4SU(5,100),TAUE,TAUI,U(100),XD,XU,Y(100),YE,YI

      COMMON/SWFT4/AK,ALMG,IPRINT,IPROF,ITR,ITURB,W,SNALFA,RENOLD
      COMMON/SOURCE/SUU(100),SDU(100),P(100),PP(100),OMD(100),OMP(100)
      COMMON/VISCO/EMULAM(100),EMUTUR(100),EMUT(100),EMUEFF(100)
      COMMON/VISC/RATIO(100)
      COMMON/AVER/ENUR,ENSQRE
      DATA REPROF/2.E5,9.93E5,2.E6/

C
C     UNSHROUDED DISCS AND CONES IN STILL AIR.
C
C     TURBULENCE MODELS
C    1 MIXING LENGTH HYPOTHESIS.
C    2  LOW RE ENERGY-DISSIPATION
C
C     PROGRAM                      BHARAT I SHARMA
C     JULY 1975
C
C
CHAPTER 1 ---------------------------------------------------------CONTRO
      IFIN=0
      ITEST=0
      IUTRAP=0
      IPROF=1
      IPRINT=50
C     HEAT TRANSFER,ITR=1... MASS TRANSFER,ITR=2...
      ITR=1
      ITR=2
C     LAMINAR FLOW,ITURB=1   TURBULENT FLOW,ITURB=2
      ITURB=1
      IPASS=0
CHAPTER 2 -------------------------------------------------------GRID AND
      FRADX=0.06
      N=90
      N=40
      N=70
      NP1=N+1
      NP2=N+2
      NP3=N+3
      OM(1)=0.0
      OM(NP3)=1.0
      POWER=1.0
      POWER=2.0
      DO 10 I=2,NP2
   10 OM(I)=(FLOAT(I-2)/FLOAT(N))**(1.+POWER)
      DO 11 I=2,NP2
      OMD(I)=OM(I+1)-OM(I)
   11 OMP(I)=OM(I+1)-OM(I-1)
      ISTEP=0
      LASTEP=5000
      CSALFA=0.5
```

```
      CSALFA=0.86603
      CSALFA=0.0
      SNALFA=SQRT(1.0-CSALFA*CSALFA)

      KRAD=1
      KIN=1
      KEX=2
CHAPTER 3 -----------------------------------------------DEPENDENT VARIABLES SE
C     U(I)=RADIAL OR AXIAL VELOCITY
C     F(1,I)=CIRCUMFERENTIAL VELOCITY*RADIUS
C     F(2,I)=STAGNATION ENTHALPY
C     F(3,I)=TURBULENCE KINETIC ENERGY
C     F(4,I)=RATE OF DISSIPATION
C     FS(1,I)=CIRCUMFERENTIAL VELOCITY.
C     FS(2,I)=TEMPERATURE
      NEQ=3
      NPH=NEQ-1
CHAPTER 4-------------MATERIAL CONSTANTS(S I UNITS)
      CP=6012.4
      EMUNP3=1.225E-5
      RHONP3=0.075
      EMUKIN=EMUNP3/RHONP3
      ALMG=0.085
      PR(1)=1.0
      PR(2)=0.72
      H=PR(2)
      IF(ITR.EQ.2) PR(2)=2.4
      IF(ITR.EQ.2) H=1.0
      DO 40 I=1,NP3
      PREF(1,I)=PR(1)
      PREF(2,I)=PR(2)
      RHO(I)=RHONP3
      EMU(I)=EMUNP3
      EMULAM(I)=EMUNP3
      EMUTUR(I)=0.
      EMUEFF(I)=EMULAM(I)
      EMUT(I)=0.
      RATIO(I)=0.
C-------------------TURBULENCE MODEL CONSTANTS
      PR(3)=1.0
      PR(4)=1.0
      PREF(3,I)=PR(4)
      PREF(4,I)=PR(4)
      REYT(I)=0.
   40 CONTINUE
CHAPTER 5 ----------------------------------------------------------INITIAL CO
      TWALL=100.0


C
      W=3500.0*6.284/60.0
      W=288.
      XU    =SQRT(REPROF(1)*EMUKIN/SNALFA/W)
      XULAST=SQRT(REPROF(3)*EMUKIN/SNALFA/W)
      R(1)=XU*SNALFA

      XI=0.955
      XI=0.93
      XI=XI*0.356*3.2808

C     RETRAN IS TRANSITION REYNOLDS NUMBER.
      RETRAN=3.E5
```

```
      RETRAN=2.8E5
      RETRAN=2.4E5
      DO 51 I=1,NP3
      R(I)=R(1)
      DPDX(I)=0.0
      IF(OM(I).LT..2)  GO TO 52
      U(I)=0.25*(1.0-OM(I))*R(1)*W
      GO TO 53
   52 U(I)=OM(I)*R(1)*W
   53 CONTINUE
      F(1,I)=(1.-OM(I)**.535)*W*R(1)*R(I)
      SU(1,I)=0.0
      SD(1,I)=0.0
      SUU(I)=0.0
      SDU(I)=0.0
      SU(2,I)=0.0
      SD(2,I)=0.0
      FS(2,I)=TWALL*(1.0-OM(I))
      F(2,I)=CP*FS(2,I)+.5*(U(I)*U(I)+(F(1,I)/R(I))**2)
      IF(ITR.EQ.2) F(2,I)=1.0-OM(I)

C     INITIAL SOURCE TERMS FOR K-E
      SU(3,I)=0.
      SD(3,I)=0.
      SU(4,I)=0.
      SD(4,I)=0.
      F(3,I)=1.E-15
      F(4,I)=1.E-15

   51 CONTINUE
      U(2)=0.25*U(3)
      U(2)=0.5*U(3)
      U(NP2)=0.5*U(NP1)
      RESQ=SQRT(REPROF(1))
      DELTA=4.43*R(1)/RESQ
      PEI=.443*RHO(NP3)*W*R(1)**3/RESQ
      PSII=0.0
      PSIE=PSII+PEI
      RENOLD=W*R(1)*XU/EMUKIN
C     WRITE STARTING CONDITIONS.
      WRITE(6,59)RHO(NP3),EMU(NP3),DELTA,PEI,XU,R(1),CSALFA,RENOLD,W
   59 FORMAT(6H INPUT,12E10.3)
CHAPTER 6 -------------------------------------------------THERMODYNAMIC PR

   60 CONTINUE
      ABSU2=ABS(U(2))
      IF(ABSU2.GT. U(3))U(2)=U(2)/ABSU2*0.9*U(3)
   65 CONTINUE
      DO 61 I=1,NP3
      EMU(I)=EMUNP3
      EMUEFF(I)=EMUTUR(I)+EMULAM(I)
   61 FS(1,I)=F(1,I)/R(I)
   63 CONTINUE


C------------TRANSITION  FROM  LAMINAR  TO  TURBULENT
      IF(RENOLD .LT. RETRAN)GO TO 69
      IPASS=IPASS+1

C     PRANDTL MIXING LENGTH MODEL OF TURBULENCE.
      DO 62 I=1,NP3
      IYL=NP3-I
```

```
      IF(F(1,IYL) .GE. .01*F(1,1))GO TO 64
   62 CONTINUE
   64 I2=IYL
      I1=I2-1
      YL=Y(I1)+(Y(I2)-Y(I1))*(.01*F(1,1)-F(1,I1))/(F(1,I2)-F(1,I1))
      AKK=0.42
      ALMG=0.085
      ALMGYL=ALMG*YL
      EMUNP3=EMU(NP3)
      RHONP3=RHO(NP3)
      APLUS=EMUNP3*26./SQRT(RHONP3)

      DO 55 I=3,NP1
      YD=Y(I+1)-Y(I)
      YM=.5*(Y(I)+Y(I+1))
      RM=.5*(R(I)+R(I+1))
      DV1DY=(U(I+1)-U(I))/YD
      DV3DY=RM*(FS(1,I+1)/R(I+1)-FS(1,I)/R(I))/YD
      DUDY(I)=SQRT(DV1DY**2+DV3DY**2/PREF(1,I))
      YPLUS=SQRT(EMUEFF(I)*DUDY(I))*YM/APLUS
      T2=1.-EXP(-YPLUS)
      PML(I)=AKK*YM*T2
      IF(PML(I) .GT. ALMGYL)PML(I)=ALMGYL
      EMUT(I)=RHONP3*PML(I)*PML(I)*DUDY(I)
      IF(EMUT(I) .LT. 1.E-30)EMUT(I)=1.E-30
      RATIO(I)=EMUT(I)/EMULAM(I)

C--------------CALCULATION  OF  INITIAL  K-E  PROFILES
      IF(ITURB .EQ. 2)GO TO 66
       IF(ISTEP .LE. 5000)GO TO 66
      NEQ=5
       NPH=NEQ-1
      RENP3=10.0
      AK=3.4
      BK=50.
       CM=0.09
      F(3,1)=0.
      F(4,1)=0.
      F(3,NP3)=1.E-20
      F(4,NP3)=1.E-20
      J=0
      TAUS=AJI(1)/R(1)
      TAUR=(TAUS*TAUS+TAUI*TAUI)**0.5
      FMX=TAUR/(RHONP3*SQRT(CM))
      CK2=1.-F(3,NP3)/FMX
      CK1=-2.*CK2
      Z=Y(I)/Y(NP3)
      SKINUS=ABS(TAUR/RHONP3)
      SKINU=SQRT(SKINUS)
        YPLUS=Y(I)*SKINU/EMUKIN
      F(3,I)=(1.-EXP(-(YPLUS/11.)**2))*FMX
      F(3,I)=F(3,I)*(1.+CK1*Z+CK2*Z*Z)
        IF(EMUT(I) .LT. 0.)REYT(I)=0.
   57 CONTINUE
      IF(EMUT(I) .LE. 0.)GO TO 58
      J=J+1
      T=EXP(-AK/(1.+REYT(I)/BK)**2)
      RTU(I)=REYT(I)
      REYT(I)=EMUT(I)/(CM*T*EMULAM(I))
      IF(ABS(RTU(I)/REYT(I)-1.) .GT. 1.E-5 .AND. J .LT. 50)GO TO 57
   58 CONTINUE
      IF(YPLUS .GT. 50. .AND. REYT(I) .LT. RENP3)REYT(I)=RENP3
```

```
      IF(REYT(I) .GT. 0.)F(4,I)=RHO(I)*F(3,I)**2/(EMULAM(I)*REYT(I))
      IF(F(4,I) .EQ. 0.)F(4,I)=F(4,I-1)
      SKINUS=ABS(TAUR/RHONP3)
      SKINU=SQRT(SKINUS)
      AA=F(3,I)/SKINU**2
      AAA=F(4,I)*EMUKIN/(SKINU**4)
      WRITE(6,56)I,Z,YPLUS,AA,AAA,RATIO(I),REYT(I)
   56 FORMAT(I5,6E10.3)
   66 CONTINUE
   55 CONTINUE

   54 CONTINUE
   69 CONTINUE
      R(1)=XU*SNALFA
      CALL STRIDE(1)
CHAPTER 7 -----------------------------------------------------------FORWAR
      IF(ISTEP .EQ. 0)DX=FRADX*Y(N)
      DX=FRADX*Y(N)
      IF(ISTEP .EQ. 0)GO TO 70
       TAUS=AJI(1)/R(1)
      TAUR=(TAUS*TAUS+TAUI*TAUI)**0.5
      DXPLUS=150
      DXPLUS=200.
      DDX=EMUNP3/SQRT(TAUR*RHONP3)*DXPLUS
      IF(DX .GT. DDX)DX=DDX
      IF(DX .LT. XULAST-XU)GO TO 70
      DX=XULAST-XU
       IF(DX .LT. 1.E-30)DX=1.E-30
   70 CONTINUE
      XN=XU+DX
CHAPTER 8 --------------------------------------------ADJUST LONGITUDINAL CON
      IF(ISTEP.GT.0)   GO TO 80
      TAUI=0.0
      TAUE=0.0
      RMI=0.0
      RME=0.0
      DO 81 J=1,5
      INDI(J)=1
      INDE(J)=1
      AJI(J)=0.0
      AJE(J)=0.0
   81 CONTINUE
   80 CONTINUE

C     CROSS STREAM PRESSURE GRADIENT TERM, PRESSURE AT E BOUNDARY KNOWN.
      IF(CSALFA.EQ.0.0)   GO TO 85
      DO 82 I=1,NP3
   82 SU(1,I)=RHO(I)*FS(1,I)*FS(1,I)/R(I)*CSALFA
      P(NP3)=0.0
      P(NP2)=P(NP3)
      DO 83 I=2,NP1
      L=NP3-I
      L1=L+1
   83 P(L)=P(L1)-.5*(SU(1,L)+SU(1,L1))*(Y(L1)-Y(L))
      DO 84 L=2,NP2
      IF(ISTEP.EQ.0)   PP(L)=P(L)
      DPDX(L)=(P(L)-PP(L))/DX
   84 PP(L)=P(L)
   85 CONTINUE

CHAPTER 9 -----------------------------------------TRANSPORT AND ENTRAINMENT PRO
      CALL AUX
```

```
C                                    ADJUSTMENT OF FORWARD STEP
      IF(RMI .EQ. 0. .AND. RME .EQ. 0.)GO TO 86
      FRA=0.05
      DDX=FRA*PEI/ABS(RMI-RME)
      IF(DX .LT. DDX)GO TO 86
      DX=DDX
      XD=XU+DX
   86 CONTINUE

      CALL STRIDE(2)
      U(1)=0.0
      U(NP3)=0.0
      F(1,NP3)=0.0
      F(1,1)=W*R(1)*R(1)
      F(2,1)=CP*FS(2,1)+.5*FS(1,1)*FS(1,1)
      IF(ITR.EQ.2)F(2,1)=1.0
      F(2,NP3)=CP*FS(2,NP3)
      IF(ITR.EQ.2) F(2,NP3)=0.0

      F(3,1)=0.0
      F(3,NP3)=0.0
      F(4,1)=0.0
      F(4,NP3)=0.0
CHAPTER 10 ------------------------------------------------------------------
      RENOLD=W*R(1)*XU/EMUKIN
      IF(ISTEP .EQ. 0)QSUM=0.0
      QWALL=AJI(2)-(F(1,1)/R(1))*(AJI(1)/R(1))/PR(2)
      IF(ITR .EQ. 2)QWALL=AJI(2)
      RQWALL=XU*QWALL
      IF(RENOLD .GT. RETRAN)QSUM=QSUM+RQWALL*DX
C 110-119 ---------------------------------------------------------------P
      IF(RENOLD.LT.REPROF(IPROF)) GO TO 120
  111 CONTINUE
      IPROF=IPROF+1
      CALL PROFIL(1)
C 120-129 --------------------------------------------------------------ST
  120 IF(ISTEP/IPRINT*IPRINT.NE.ISTEP) GO TO 130
      IF(RENOLD .GT. RETRAN)GO TO 123
      QSUM=0.0
      ENUR=RQWALL*PR(2)/(CP*TWALL*EMULAM(NP3))
      IF(ITR .EQ. 2)ENUR=RQWALL*PR(5)/(F(2,1)*EMULAM(NP3))
      ENSQRE=ENUR/SQRT(RENOLD)
      QLAM=RQWALL*XU
      GO TO 129
  123 CONTINUE
      QMEAN=(QLAM+2.*QSUM)/XU**2
      ENUR=QMEAN*XU*PR(2)/(CP*TWALL*EMULAM(NP3))
      IF(ITR .EQ. 2)ENUR=QMEAN*XU*PR(2)/(F(2,1)*EMULAM(NP3))
      ENSQRE=ENUR/RENOLD**0.8
  129 CALL PROFIL(2)
  130 CONTINUE
CHAPTER 12 ------------------------------------------------------------------
      IF(RENOLD .GT. 1.9E6)IFIN=1
      IF(ISTEP.GT.LASTEP) IFIN=1
      IF(XU.GT.XULAST) IFIN=1
      IF(IFIN.EQ.1) GO TO 150
      CALL STRIDE(3)

      GO TO 60
  150 CONTINUE
```

```
      STOP
      END



      SUBROUTINE AUX
      DIMENSION DUDY(100),D2UDY(100),DVDY(100),D2VDY(100),DKDY(100),
     1F3(100),RDY(100),REYT(100)
      COMMON/GENERAL/AJE(10),AJI(10),CSALFA,DPDX(100),DX,EMU(100),
     1F(5,100),FS(5,100),H,IFIN,INDE(10),INDI(10),ISTEP,ITEST,IUTRAP,
     2KEX,KIN,KRAD,N,NEQ,NPH,NP1,NP2,NP3,OM(100),PEI,PR(5),PREF(5,100),
     3PSIE,PSII,R(100),RHO(100),RME,RMI,RN15,RU(100),R25,SD(5,100),
     4SU(5,100),TAUE,TAUI,U(100),XD,XU,Y(100),YE,YI
      COMMON/SWFT4/AK,ALMG,IPRINT,IPROF,ITR,ITURB,W,SNALFA,RENOLD
      COMMON/SOURCE/SUU(100),SDU(100),P(100),PP(100),OMD(100),OMP(100)
      COMMON/VISCO/EMULAM(100),EMUTUR(100),EMUT(100),EMUEFF(100)
      COMMON/AVER/ENUR,ENSQRE

C     FOR UNSHROUDED ROTATING SURFACES.
C     THE CIRCUMFERENTIAL VELOCITY DETERMINES THE LAYER THICKNESS
C     AND CONTROLS THE ENTRAINMENT.
C 1-10 -----------------------------------------------------------LOCA
      IF(ISTEP .GT. 0)GO TO 10
      CM=0.09
      AK=3.4
       BK=50.0
       CK=2.0
      A1=1.44
      A2=2.0
      A3=1.92
      B3=0.3
      C3=1.0
      PRT=0.9
      PRTK=1.0
      PRTE=1.3
      IPASS=0
   10 CONTINUE

C 21-30 ----------------------------------------------------------MOD
      IF(ISTEP .LE. 5000)GO TO 12
      IF(ITURB .EQ. 1)GO TO 21
      DO 15 I=3,NP1
      F(3,I)=AMAX1(F(3,I),0.0)
      F(4,I)=AMAX1(F(4,I),1.E-15)
      IF(F(4,I) .EQ. 1.E-15)F(3,I)=0.
   15 CONTINUE
      IPASS=IPASS+1
      DO 18 I=3,NP1
      REYT(I)=RHO(I)*F(3,I)**2/(F(4,I)*EMULAM(I))
      T=EXP(-AK/(1.+REYT(I)/BK)**2)
      Z=EMUTUR(I)
      EMUT(I)=CM*T*RHO(I)*F(3,I)**2/F(4,I)
   18 CONTINUE
   12 CONTINUE
C     ----------EFFECTIVE VISCOSITY AT MID POINTS

      DO 19 I=2,NP2
      EMUTUR(I)=EMUT(I)
      EMULAM(I)=0.5*(EMULAM(I+1)+EMULAM(I))
      EMUEFF(I)=EMUT(I)+EMULAM(I)
```

```
   19 EMU(I)=EMUEFF(I)
      EMU(NP2)=EMUT(NP2)+EMULAM(NP2)
      EMU(1)=EMULAM(1)
      DO 20 I=2,NP2
      IF(NEQ .EQ. 2)GO TO 20
      PREF(2,I)=EMU(I)/(EMULAM(I)/PR(2)+EMUT(I)/PRT)
      PREF(3,I)=EMU(I)/(EMULAM(I)/PR(3)+EMUT(I)/PRTK)
       PREF(4,I)=EMU(I)/(EMULAM(I)/PR(4)+EMUT(I)/PRTE)
   20 CONTINUE
C 21-30 --------------MODIFICATION OF EMU ARRAY
   21 DO 22 I=2,NP1
   22 EMU(I)=EMU(I)/(Y(I+1)-Y(I))
      EMU(NP2)=EMU(NP2)/YE
      DO 23 I=2,NP1
   23 EMU(I)=EMU(I)*0.5*(R(I)+R(I+1))
C-----------------------------------------------------------------------
C     ------------------------------------------------------ENTRAINMENT
      ULIM=0.01
      RAT=ABS(F(1,NP1)-F(1,NP2))/F(1,1)
      IF(RAT.LT.ULIM) EMU(NP1)=EMU(NP1)*RAT/ULIM
      RME=-2.*EM U(NP1)

CHAPTER 2 --------------------------------------------------------------
      DO 84 I=2,NP2
   84 F(5,I)=(-DPDX(I)+RHO(I)*FS(1,I)*FS(1,I)/R(I)*SNALFA)/(RHO(I)*U(I))
      PD8=PEI/8.0
      SUU(2)=PD8*(3.*F(5,2)+F(5,3))*OM(3)
      DO 86 I=3,NP1
   86 SUU(I)=PD8*(3.*F(5,I)*OMP(I)+F(5,I-1)*OMD(I-1)+F(5,I+1)*OMD(I))
      SUU(NP2)=PD8*(3.*F(5,NP2)+F(5,NP1))*OMD(NP1)

C     -----------------------------------------------------------------
      IF(NEQ.EQ.2) GO TO 235
      IF(ITR .EQ. 2) GO TO 241
      DO 220 I=1,NP3
      SD(1,I)=U(I)*U(I)
  220 SD(2,I)=FS(1,I)*FS(1,I)
      DO 230 I=2,NP1
      SD(3,I)=SD(1,I+1)-SD(1,I)+SD(2,I+1)-SD(2,I)
      SD(3,I)=EM U(I)*SD(3,I)*.5*(1.-1./PREF(2,I))
      F5=.5*(FS(1,I)+FS(1,I+1))
  230 SU(3,I)=SD(3,I)-EMUEFF(I)*F5*F5*CSALFA
      SU(3,1)=0.0
      SU(3,NP2)=0.0
      DO 240 I=2,NP2
      SD(2,I)=0.0
  240 SU(2,I)=SU(3,I)-SU(3,I-1)
      GO TO 235
  241 DO 243 I=2,NP2
      SU(2,I)=0.0
  243 SD(2,I)=0.0
  235 CONTINUE
      DO 242 I=1,NP3
      SDU(I)=0.0
      SU(1,I)=0.0
      SD(1,I)=0.0
  242 CONTINUE

      IF(ITURB .EQ. 1)GO TO 120
      IF(ISTEP .LE. 5000)GO TO 120

C     PRELIMINARIES FOR SOURCE TERMS FOR K-E
```

```
      DO 1 I=2,NP2
       EMUT(I)=EMUTUR(I)
      F3(I)=0.
      IF(F(3,I) .NE. 0.)F3(I)=F(3,I)*SQRT(ABS(F(3,I)))/ABS(F(3,I))
      SU(3,I)=0.
      SD(3,I)=0.
      SU(4,I)=0.
      SD(4,I)=0.
    1 CONTINUE
      RDY(NP3)=0.
         DUDY(NP3)=0.
      D2UDY(NP3)=0.
      DVDY(NP3)=0.
      D2VDY(NP3)=0.
      DKDY(NP3)=0.
      DO 2 I=3,NP1
      RM=0.5*(R(I)+R(I+1))
      BYP=Y(I+1)-Y(I)
      BYM=Y(I)-Y(I-1)
      BY=BYP+BYM
      T1=BYM/(BY*BYP)
      T2=BYP/(BY*BYM)
      RDY(I)=0.5*R(I)*(Y(I+1)-Y(I-1))
      DUDY(I)=T1*(U(I+1)-U(I))+T2*(U(I)-U(I-1))
      D2UDY(I)=((U(I+1)-U(I))/(Y(I+1)-Y(I))-(U(I)-U(I-1))/(Y(I)-Y(I-1)))
     1/(0.5*BY)
      DVDY(I)=RM*(T1*(FS(1,I+1)/R(I+1)-FS(1,I)/R(I))+T2*(FS(1,I)/R(I)
     1-FS(1,I-1)/R(I-1)))
      D2VDY(I)=RM*(((FS(1,I+1)/R(I+1)-FS(1,I)/R(I))/(Y(I+1)-Y(I))-(
     1FS(1,I)/R(I)-FS(1,I-1)/R(I-1))/(Y(I)-Y(I-1)))/(0.5*BY))
      DKDY(I)=T1*(F3(I+1)-F3(I))+T2*(F3(I)-F3(I-1))
    2 CONTINUE
C
C     SPECIAL TREATMENT OF HALF INTERVALS AT I AND E BOUNDARIES
C-----------------------------------I    BOUNDARY
      IF(ABS(F(3,2)) .GE. F(3,3) .OR. ABS(F(4,2)).GE. F(4,3))GO TO 5
      RDY(2)=0.5*(R(2)+R25)*YI
      RI=0.5*(R(1)+R25)
      DUDY(2)=(0.5*(U(2)+U(3))-U(1))/YI
      D2UDY(2)=((U(3)-U(2))/(Y(3)-Y(2))-TAUI/EMULAM(1))/YI
      DVDY(2)=RI* (0.5*(FS(1,2)/R(2)+FS(1,3)/R(3))-FS(1,1)/R(1))/YI
      TAUS=AJI(1)/R(1)
      D2VDY(2)=(RI*(FS(1,3)/R(3)-FS(1,2)/R(2))/(Y(3)-Y(2))+TAUS/
     1EMULAM(1))/YI
      DKDY(2)=(SQRT(0.5*(F(3,2)+F(3,3)))-SQRT(F(3,1)))/YI
C     ------------------------------E  BOUNDARY
    5 CONTINUE
      IF(ABS(F(3,NP2)) .GE. F(3,NP1) .OR. ABS(F(4,NP2)) .GE. F(4,NP1))
     1GO TO 6
      RDY(NP2)=0.5*(R(NP2)+RN15)*YE
      RE=0.5*(RN15+R(NP3))
      DUDY(NP2)=(U(NP3)-0.5*(U(NP1)+U(NP2)))/YE
      D2UDY(NP2)=((U(NP2)-U(NP1))/(Y(NP2)-Y(NP1)))/YE
      DVDY(NP2)=RE  *(0.5*(FS(1,NP1)/R(NP1)+FS(1,NP2)/R(NP2))-
     1FS(1,NP3)/R(NP3))/YE
      D2VDY(NP2)=RE*(FS(1,NP3)/R(NP3)-(FS(1,NP2)/R(NP2)-FS(1,NP1)/R(NP
     11))/(Y(NP2)-Y(NP1))))/YE
      DKDY(NP2)=(SQRT(F(3,NP3))-SQRT(.5*(F(3,NP1)+F(3,NP2))))/YE
C--------------------------------------J=4
    6 CONTINUE
      EMUT(2)=0.25*EMUT(3)
      EMUT(NP2)=0.25*EMUT(NP1)
```

```
      F(3,2)=0.25*(3.*F(3,2)+F(3,3))
      F(3,NP2)=0.25*(3.*F(3,NP2)+F(3,NP1))
      F(4,2)=0.25*(3.*F(4,2)+F(4,3))
      F(4,NP2)=0.25*(3.*F(4,NP2)+F(4,NP1))
C-----------------------------------------J=3
C     PJ3-----------------------------PRODUCTION
C     DJ3----------------------------DISSIPATION
      DO 100 I=2,NP2
      IF(F(3,I) .LE.0. .OR. F(4,I) .LE. 0.)GO TO 100
      PJ3=EMUT(I)*(DUDY(I)*DUDY(I)+DVDY(I)*DVDY(I))
      DJ3=RHO(I)*F(4,I)+CK*EMULAM(I)*DKDY(I)**2
      SU(3,I)=PJ3-DJ3
      SD(3,I)=-ABS(SU(3,I))/F(3,I)
      SU(3,I)=SU(3,I)+ABS(SU(3,I))


      PJ4=A1*F(4,I)/F(3,I)*PJ3+A2*EMULAM(I)*EMUT(I)*(DUDY(I)*D2UDY(I)+
     1DVDY(I)*(D2VDY(I)+DVDY(I)/RM*(R(I+1)-R(I))/(Y(I+1)-Y(I)))))**2/
     2(DUDY(I)**2+DVDY(I)**2)/RHO(I)
      REYT(I)=RHO(I)*F(3,I)**2/(F(4,I)*EMULAM(I))
      FN3=1.-B3*EXP(-(REYT(I)/C3)**2)
      DJ4=A3*F(4,I)**2*RHO(I)*FN3/F(3,I)
       RCHSON=0.

      AR=0.
      DJ4=DJ4*(1.-AR*RCHSON)
      SU(4,I)=PJ4-DJ4
      SD(4,I)=-ABS(SU(4,I))/F(4,I)
      SU(4,I)=SU(4,I)+ABS(SU(4,I))
  100 CONTINUE
      DO 110 J=3,NPH
      DO 110 I=2,NP2
      SU(J,I)=SU(J,I)*RDY(I)
      SD(J,I)=SD(J,I)*RDY(I)
  110 CONTINUE
C-------REDEFINITION OF VARIABLES BACK TO POINTS 2 AND NP2
      DO 111 J=3,NPH
      F(J,2)=(4.*F(J,2)-F(J,3))/3.
  111 F(J,NP2)=(4.*F(J,NP2)-F(J,NP1))/3.
  120 CONTINUE
      RETURN
      END




      SUBROUTINE PROFIL(IP)
      DIMENSION REYT(100)
      COMMON/GENERAL/AJE(10),AJI(10),CSALFA,DPDX(100),DX,EMU(100),
     1F(5,100),FS(5,100),H,IFIN,INDE(10),INDI(10),ISTEP,ITEST,IUTRAP,
     2KEX,KIN,KRAD,N,NEQ,NPH,NP1,NP2,NP3,OM(100),PEI,PR(5),PREF(5,100),
     3PSIE,PSII,R(100),RHO(100),RME,RMI,RN15,RU(100),R25,SD(5,100),
     4SU(5,100),TAUE,TAUI,U(100),XD,XU,Y(100),YE,YI
      COMMON/SWFT4/AK,ALMG,IPRINT,IPROF,ITR,ITURB,W,SNALFA,RENOLD
      COMMON/SOURCE/SUU(100),SDU(100),P(100),PP(100),OMD(100),OMP(100)
      COMMON/VISCO/EMULAM(100),EMUTUR(100),EMUT(100),EMUEFF(100)
      COMMON/VISC/RATIO(100)
      COMMON/AVER/ENUP,ENSQRE
C     --------------  ---------------  -----------  ---------------
      EMUKIN=EMU(NP3)/RHO(NP3)
      CF=0.0
```

```
      DO 10 I=2,NP2
   10 CF=CF+(F(1,I)+F(1,I+1))*OMD(I)
      CF=.5*CF*PEI*25.136/(RHO(NP3)*W*W*R(1)**5) * SNALFA
      EN=2.*PEI/(RHO(NP3)*W*R(1)**3)
      THETA=0.0
      DELTA=0.0
      F11=FS(1,1)
      DM=FS(1,2)/U(2)
      F1M=(F11-FS(1,2))*DM
      DO 11 I=3,NP2
      F1I=FS(1,I)
      DP=F1I/U(I)
      F1P=(F11-F1I)*DP
      THETA=THETA+(F1M+F1P)*OMD(I-1)
      DELTA=DELTA+(DM +DP )*OMD(I-1)
      DM=DP
   11 F1M=F1P
      THETA=.5*PEI*THETA/(RHO(NP3)*R(1)*F11*F11)
      DELTA=.5*PEI*DELTA/(RHO(NP3)*R(1)*F11)
      RTHETA=W*R(1)*THETA/EMUKIN
      HFORM=THETA/DELTA
      TAUS=AJI(1)/R(1)
      WRITE(6,23)ISTEP,XU,R(1),RENOLD,EN,HFORM,CF,PEI,TAUI,TAUS,
     1ENUR,ENSQRE,F11
C     ----------------------------      ------------------------------
      IF(IP.EQ.2) GO TO 100
      CP=6012.4
      TWALL=FS(2,1)

      WRITE(6,24)
      UR=SQRT(TAUI/RHO(NP3))
      UT=SQRT(TAUS/RHO(NP3))
      YR=UR/EMUKIN
      YT=UT/EMUKIN
      WW=SQRT(W/EMUKIN)
      WP2=FS(1,1)*FS(1,1)
      DO 12 I=1,NP3
      W1=Y(I)
      W1=W1*WW


      W2=W1*WW
      W3=W1/THETA
      W4=U(I)/F11
      W5=FS(1,I)/F11
      W6=W1*YR
      W6=SQRT(U(I)*U(I)+FS(1,I)*FS(1,I))
       W6=W6/F11
      W7=U(I)/UR
      W8=W1*YT
      F1I=F11-FS(1,I)
      W9=F1I/UT
      URES=(TAUI*TAUI+TAUS*TAUS)**.25/RHO(NP3)**.5
      YRES=URES/EMUKIN
      W10=W1*YRES
      W11=SQRT(F1I*F1I+U(I)*U(I))/URES
      TRL=(F(2,I)-0.5*(U(I)*U(I)+(F(1,I)/R(I))**2))/CP
      W12=TRL/TWALL
      IF(ITR .EQ. 2)W12=F(2,I)/F(2,1)
      VRATIO=F1I/(U(I)+1.E-10)
      IF(I.EQ.NP3) GO TO 14
      TAURES=(FS(1,I+1)-FS(1,I))**2  +  (U(I+1)-U(I))**2
```

```
      TAURES=TAURES**0.5/(Y(I+1)-Y(I))*EMUEFF(I)
      TRATIO=(FS(1,I+1)-FS(1,I))/(U(I+1)-U(I)+1.E-10)
   14 CONTINUE
      WRITE(6,23)I,W1,W4,W5,W6,W7,W8,W9,W10,W11,TAURES,VRATIO,W12
   12 CONTINUE
      IF(ITURB.EQ.1) GO TO 16
C     ---------------------------------------------------------------------
      WRITE(6,28)
      DO 18 I=3,NP1
      W1=Y(I)*WW
      W1=Y(I)/(R(1)/SQRT(RENOLD))
      W2=EMUTUR(I)/EMULAM(I)
      W2=EMUT(I)/EMULAM(I)
      W3=EMUEFF(I)/EMULAM(I)
      TAUS=AJI(1)/R(1)
      TAUR=(TAUI*TAUI+TAUS*TAUS)**0.5
      SKINUS=ABS(TAUR/RHO(I))
      SKINU=SQRT(SKINUS)
      W4=F(3,I)/SKINU**2
      W4=F(3,I)/(F11*F11)
      W5=F(4,I)*EMUKIN/(SKINU**4)
      W6=RATIO(I)
      W7=RHO(I)*F(3,I)**2/(F(4,I)*EMULAM(I))
      WRITE(6,29)I,W1,W2,W3,W4,W5,W6,W7
   18 CONTINUE
C     ---------------------------------------------------------------
   17 CONTINUE
   16 CONTINUE
      WRITE(6,26)

   23 FORMAT(I5,12E10.3)
   24 FORMAT(* GRID      Y        V1/WR      V3/WR       Y1+        V1+
     1 Y3+        V3+       YRES+      URES+      TAURES    VRATIO    TAURAT
     2IO *)
   26 FORMAT(*  STEP     XU       R       RE.NO       ENTRAIN        H-FORM
     1    CF        PEI       TAUI       TAUS        NU/SHR      C=NU/RE   WR *
     2)
   28 FORMAT(*  GRID  Y.SQ(W/V)  EMUT/L  EMUE/L   F(3,I)  F(4,I)
     1 RATIO  REYT  *)
   29 FORMAT(I5,7E10.3)
  100 CONTINUE
      RETURN
      END




      SUBROUTINE WF(J,I1,I2,I3,OUT1.OUT2,OUT3)
      COMMON/GENERAL/AJE(10),AJI(10),CSALFA,DPDX(100),DX,EMU(100),
     1F(5,100),FS(5,100),H,IFIN,INDE(10),INDI(10),ISTEP,ITEST,IUTRAP,
     2KEX,KIN,KRAD,N,NEQ,NPH,NP1,NP2,NP3,OM(100),PEI,PR(5),PREF(5,100).
     3PSIE,PSII,R(100).RHO(100),RME,RMI,RN15,RU(100),R25,SD(5,100),
     4SU(5,100),TAUE,TAUI,U(100),XD,XU,Y(100),YE,YI
      COMMON/SWFT4/AK,ALMG,IPRINT,IPROF,ITR,ITURB,W,SNALFA,RENOLD
      COMMON/SOURCE/SUU(100),SDU(100),P(100),PP(100),OMD(100),OMP(100)
      COMMON/VISCO/EMULAM(100),EMUTUR(100),EMUT(100),EMUEFF(100)
C     GENERAL WALL FUNCTIONS FOR LAMINAR SWIRLING FLOWS.
C     FOR AXIAL AND TANGENTIAL VELOCITIES,FOR STAGNATION ENTHALPY.
C     FOR MASS TRANSFER.     FOR SHROUDED AND UNSHROUDED GEOMETRIES.
C     ---------------------------------------------------------------------
      I25=I3-1/I1
```

```
      JDASH=J+1
      GO TO (100,200,300,400,400),JDASH

CHAPTER 1 ----------------------------------------RADIAL VELOCITY. NO MAS
  100 UREF=.5*(U(I2)+U(I3))
      RHOREF=.5*(RHO(I2)+RHO(I3))
      RREF=.5*(R(I2)+R(I3))
      RRUREF=RREF*RU(I25)
      YREF=YI+(YE-YI)*OM(I1)
      VREF=.5*(EMULAM(I2)+EMULAM(I3))
      RE=UREF*RHOREF*YREF/VREF
      F11=F(1,I1)/R(I1)
      F25=.5*(F(1,I2)/R(I2)+F(1,I3)/R(I3))
      DPXREF=.5*(DPDX(I2)+DPDX(I3))
      FP=YREF/(RU(I25)*UREF)*(DPXREF-RHOREF*F25*F25*SNALFA/RREF)
      S=1.0/RE-FP/2.0
      OUT1=.5-FP*RE/12.0
      OUT2=S*RRUREF
      OUT3=OUT2*UREF/RREF
      EMU(I25)=VREF*RREF/ABS(Y(I3)-Y(I2))
      RETURN
CHAPTER 2 -----------------------------------CIRCUMFERENTIAL VELOCITY.
  200 CONTINUE
      FP=F25*YREF*SNALFA      /2./RREF/(F25-F11)
      OUT1=0.0
      GO TO 210
  300 CONTINUE
CHAPTER 3-------------------STAGNATION  ENTHALPY
      FP=0.0
      OUT1=(H-1.)*.5*(UREF*UREF+F25*F25)/6012.4
      IF(ITR .EQ. 2)OUT1=0.0
  210 CONTINUE
      S=1./RE/PR(J)-FP
      OUT2=S*RRUREF
      OUT3=OUT2/RREF
      RETURN
CHAPTER  4 ------------------------------K--E
  400 S=0.
      A3=1.92
      B3=0.3
      RMREF=RMI+(RME-RMI)*OM(I1)
      BM=RMREF/RRUREF
      F3REF=0.5*(F(3,I2)+F(3,I3))
      F4REF=0.5*(F(4,I2)+F(4,I3))
      FSO=-A3*(1.-B3)*F4REF*YREF/(UREF*RHOREF*F3REF)
      FSO=FSO*RHOREF
      IF(J .EQ. 3)GO TO 410
      S=1./(PR(J)*RE)+0.5*FSO
      IF(J .EQ. 4)GO TO 410
      S=1./(PR(J)*RE)
      IF(BM .EQ. 0)GO TO 410
      S=BM/(PR(J)*(EXP(BM*RE)-1.))
  410 OUT1=0.
      OUT2=S*RRUREF
      OUT3=OUT2/RREF
      PREF(J,I25)=PR(J)
      RETURN
      END
```

```
      SUBROUTINE STRIDE(ISW)
      DIMENSION A(5,100),AU(100),B(5,100),BU(100),C(5,100),CU(100),
     1FDIFE(5),FDIFI(5),GE(5),GI(5),TTPF(5)
      COMMON/GENERAL/AJE(10),AJI(10),CSALFA,DPDX(100),DX,EMU(100),
     1F(5,100),FS(5,100),H,IFIN,INDE(10),INDI(10),ISTEP,ITEST,IUTRAP,
     2KEX,KIN,KRAD,N,NEQ,NPH,NP1,NP2,NP3,OM(100),PEI,PR(5),PREF(5,100),
     3PSIE,PSII,R(100),RHO(100),RME,RMI,RN15,RU(100),R25,SD(5,100),
     4SU(5,100),TAUE,TAUI,U(100),XD,XU,Y(100),YE,YI
      COMMON/SOURCE/SUU(100),SDU(100),P(100),PP(100),OMD(100),OMP(100)
      COMMON/VISCO/EMULAM(100),EMUTUR(100),EMUT(100),EMUEFF(100)
      GO TO (1000,2000,3000), ISW

C     FOR...KRAD=1...KIN=1...KEX=2...R(1).GT.0.....

C*************************************  S T R I D E 1  *****************
 1000 IF(ISTEP.GT.0) GO TO 1100
      OM(1)=0.
      OM(2)=0.
      OM(NP2)=1.
      OM(NP3)=1.0
      OMI=.5*OM(3)
      OME=.5*(1.-OM(NP1))
      BPI=0.5
      BPE=1.0
      Y(1)=0.
C-------------------------  CALCULATION OF RHO*U 'S  ----------------
 1100 DO 1101 I=1,NP3
 1101 RU(I)=RHO(I)*U(I)
      RU3=RU(3)
      RUN1=RU(NP1)
      DO 1102 I=2,NP1
      RU(I)=.5*(RU(I)+RU(I+1))
      IF(RU(2) .LE. 0.)RU(2)=1.E-20
      IF(RU(I).GT.0.)GO TO 1102
      IF(ITEST.EQ.0) WRITE(6,1200)
 1200 FORMAT(25HAN RU IS ZERO OR NEGATIVE)
     1,SU(3,I),SD(3,I),SU(4,I),SD(4,I)
*********************** STRIDE
 1250 FORMAT(I5,12E10.3)
      WRITE(6,1250)I,Y(I),RU(I),U(I),F(1,I),F(2,I),F(3,I),F(4,I),EMUT(I)
      ITEST=1
      IFIN=1
 1102 CONTINUE
C-------------------------  CALCULATION OF Y 'S AND R 'S  -----------
C  -----------------------------------------  Y'S FOR PLANE GEOMETRY
      YI=PEI*OMI/(BPI*RU(2))
      Y(3)=YI+PEI*OM(3)/(RU(2)+RU3)
      Y(2)=2.0*YI-Y(3)
      DO 1103 I=4,NP1
 1103 Y(I)=Y(I-1)+PEI*(OM(I)-OM(I-1))/RU(I-1)
      YN15=Y(NP1)+PEI*(1.-OM(NP1))/(RU(NP1)+RUN1)
      YE=PEI*OME/(BPE*RU(NP1))
      Y(NP3)=YN15+YE
      Y(NP2)=2.0*YN15-Y(NP1)
C  ---------------------  Y'S AND R'S FOR AXISYMMETRICAL GEOMETRY
      IF(CSALFA.EQ.0.) GO TO 1110
C  -----------------------------------------  CSALFA NE ZERO
      COSD2=.5*CSALFA
 1105 R1D2=.5*R(1)
      R1D2SQ=R1D2*R1D2
      DO 1104 I=2,NP3
      Y(I)=Y(I)/(R1D2+SQRT(ABS(R1D2SQ+COSD2*Y(I))))
```

```
 1104 R(I)=R(1)+Y(I)*CSALFA
      YI=YI/(R1D2+SQRT(ABS(R1D2SQ+COSD2*YI)))
      YN15=YN15/(R1D2+SQRT(ABS(R1D2SQ+COSD2*YN15)))
 1107 R25=R(1)+YI*CSALFA
      RN15=R(1)+YN15*CSALFA
      YF=Y(NP3)-YN15
      RETURN
 1110 DO 1111 I=2,NP3
      Y(I)=Y(I)/R(1)
 1111 R(I)=R(1)
      YI=YI/R(1)
      YN15=YN15/R(1)
      R25=R(1)
      RN15=R(1)
      YF=Y(NP3)-YN15
      RETURN
C************************************  S T R I D E 2  ***************
 2000 PX=PEI/DX
            G=RMI-RME
      PD4=.25*PX
            PG=PX+G
      PGD4=.25*PG
            RMID2=.5*RMI
            GD4=.25*G
            BOMP=OM(3)-OM(2)
      PGOMP=PGD4*BOMP
      P4OMP=PD4*BOMP
C  --------------------------------------------  GRID POINT 2
C---------------------------------------------  TAUI, BPI, T1
      CALL WF(0,1,2,3,BPI,T1,TAUI)
C  ---------------------  BOUNDARY COEFFICIENTS FOR VELOCITY
 2002       HLP=RMID2-GD4*(OM(2)+OM(3))
            AHLP=ABS(HLP)
      THLP=HLP+HLP
            TP=EM U(2)
      TTP=TP+AHLP+ABS(TP-AHLP)
      AD=TTP-THLP-T1-PGOMP+.5*SDU(2)
      BD=2.*(T1+RMI)
      CD=P4OMP*(3.*U(2)+U(3))+2.*SUU(2)
      DU=AD+BD+PX*BOMP-2.*SDU(2)
      AU(2)=AD/DU
      BU(2)=BD/DU
      CU(2)=CD/DU
C  -----------------------------  BOUNDARY COEFFICIENTS FOR FIS
      IF(NEQ.EQ.1) GO TO 2304
      DO 2300 J=1,NPH
      TPF2=TP/PREF(J,2)
      TTPF(J)=TPF2+AHLP+ABS(TPF2-AHLP)
      CALL WF(J,1,2,3,FDIFI(J),T1F,GI(J))
      IF(INDI(J).EQ.2) GO TO 2303
      AJI(J)=GI(J)*(F(J,1)-.5*(F(J,2)+F(J,3))-FDIFI(J))
C  ---------------------------------------  COEFFICIENTS
 8005 IF(J.NE.1)  GO TO 2302
      ADF=TTPF(J)*R25*R25/R(3)/R(3)-THLP-T1F*R(1)*R(1)/R(3)/R(3)-PGOMP
      BDF=2.*(T1F+RMI)
      DF=3.*PGOMP+THLP+TTPF(J)*R25*R25/R(2)/R(2)+T1F*R(1)*R(1)/R(2)/R(2)
      GO TO 8110
 2302 ADF=TTPF(J)-THLP-T1F-PGOMP+.5*SD(J,2)
      BDF=2.*(T1F+RMI)
      DF=ADF+BDF+PX*BOMP-2.*SD(J,2)
 8110 CONTINUE
      T=-T1F*FDIFI(J)
```

```
      GO TO 2305
 2303 ADF=TTPF(J)-THLP-PGOMP+.5*SD(J,2)
      BDF=0.
      DF=ADF+PX*BOMP-2.*SD(J,2)+RMI*2.
      T=RMI*F(J,1)+AJI(J)*R(1)
 2305 TT=3.*F(J,2)+F(J,3)
      CDF=P4OMP*TT+2.*(T+SU(J,2))
      A(J,2)=ADF/DF
      B(J,2)=BDF/DF
 2300 C(J,2)=CDF/DF
C  -----------------------------------------  GRID POINT NP2
C-----------------------------------------  TAUE, BPE, TNP3
 2304 IF(KEX.NE.1) GO TO 2003
 2003 TNP3=0.
      IF(KRAD.EQ.1) BPE=(R(NP3)*(5.*RU(NP3)+RU(NP1))+3.*RN15*
     1              (RU(NP3)+RU(NP1)))/6./(R(NP3)+ RN15)/RU(NP1)
C  -------------------  BOUNDARY COEFFICIENTS FOR VELOCITY
 2310 BOMM=OM(NP2)-OM(NP1)
      HLM=RMID2-GD4*(OM(NP1)+OM(NP2))
      AHLM=ABS(HLM)
      THLM=HLM+HLM
      TM=EM U(NP1)
      TTM=TM+AHLM+ABS(TM-AHLM)
      PGOMM=PGD4*BOMM
      P4OMM=PD4*BOMM
      AD=2.*(TNP3-RME)
      BD=TTM+THLM-TNP3-PGOMM +.5*SDU(NP2)
      CD=P4OMM*(3.*U(NP2)+U(NP1))      +2.0*SUU(NP2)
      DU=AD+BD+PX*BOMM  -2.*SDU(NP2)
      AU(NP2)=AD/DU
      BU(NP2)=BD/DU
      CU(NP2)=CD/DU
      IF(NEQ.EQ.1) RETURN
C  ---------------------  BOUNDARY COEFFICIENTS FOR F'S
      DO 2320 J=1,NPH
      TMF=TM/PREF(J,NP1)
      TTMF=TMF+AHLM+ABS(TMF-AHLM)
 2311 TNP3F=0.
      FDIFE(J)=0.
C  -----------------------------------------  COEFFICIENTS
 2318 IF(J.NE.1)  GO TO 2312
      ADF=2.*(TNP3F-RMF)
      BDF=TTMF*RN15*RN15/R(NP2)/R(NP2)+THLM-TNP3F*R(NP3)*R(NP3)/R(NP1)/
     1      R(NP1)-PGOMM
      DF=3.*PGOMM-THLM+TTMF*RN15*RN15/R(NP2)/R(NP2)+TNP3F*R(NP3)*R(NP3)
     1     /R(NP2)/R(NP2)
      GO TO 8003
 2312 ADF=2.*(TNP3F-RMF)
      BDF=TTMF+THLM-TNP3F-PGOMM+.5*SD(J,NP2)
      DF=ADF+BDF+PX*BOMM-2.*SD(J,NP2)
 8003 CONTINUE
      T=-TNP3F*FDIFE(J)
      GO TO 2315
2313  ADF=0.
      BDF=TTMF+THLM-PGOMM+.5*SD(J,NP2)
      DF=BDF+PX*BOMM-2.*SD(J,NP2)-RME*2.
      T=-RMF*F(J,NP3)-AJE(J)*R(NP3)
 2315 TT=3.*F(J,NP2)+F(J,NP1)
      CDF=P4OMM*TT+2.*(T+SU(J,NP2))
      A(J,NP2)=ADF/DF
      B(J,NP2)=BDF/DF
 2320 C(J,NP2)=CDF/DF
```

```
      RETURN
C*************************************  S T R I D E 3  ****************
 3000 DO 3005 I=3,NP1
            BOMM=BOMP
            BOMP=OM(I+1)-OM(I)
            BOM=BOMM+BOMP
            BOMT3=BOM*3.
            PGOMM=PGOMP
      PGOMP=PGD4*BOMP
      PBOM=PX*BOM
      THLM=THLP
            HLP=RMID2-GD4*(OM(I+1)+OM(I))
      THLP=HLP+HLP
            AHLP=ABS(HLP)
      TTM=TTP
            TP=EM U(I)
      TTP=TP+AHLP+ABS(TP-AHLP)
      AD=TTP-THLP-PGOMP
      BD=TTM+THLM-PGOMM
      CD=PD4*(BOMT3*U(I)+BOMP*U(I+1)+BOMM*U(I-1))      +2.*SUU(I)
      DU=AD+BD+PBOM     -2.*SDU(I)
            AU(I)=AD/DU
            BU(I)=BD/DU
            CU(I)=CD/DU
C ----------------------------------------  START OF J LOOP
            IF(NEQ.EQ.1) GO TO 3005
            DO 3004 J=1,NPH
3002  TTMF=TTPF(J)
 3003 TPF=EM U(I)/PREF(J,I)
      TTPF(J)=TPF+AHLP+ABS(TPF-AHLP)
      IF(J.NE.1)  GO TO 8008
      RP=.5*(R(I)+R(I+1))
      RM=.5*(R(I)+R(I-1))
      AD=TTPF(J)*RP*RP/R(I+1)/R(I+1)-THLP-PGOMP
      BD=TTMF*RM*RM/R(I-1)/R(I-1)+THLM-PGOMM
      DF=PGD4*BOMT3+THLP-THLM+    (TTPF(J)*RP*RP+TTMF*RM*RM)/R(I)/R(I)
      GO TO 8009
 8008 CONTINUE
      AD=TTPF(J)-THLP-PGOMP
      BD=TTMF+THLM-PGOMM
      DF=AD+BD+PBOM-2.*SD(J,I)
 8009 CONTINUE
      CD=PD4*(BOMT3*F(J,I)+BOMP*F(J,I+1)+BOMM*F(J,I-1))+2.*SU(J,I)
            A(J,I)=AD/DF
            B(J,I)=BD/DF
 3004       C(J,I)=CD/DF
 3005 CONTINUE
      IF(KEX.EQ.2.AND.RU(NP3).NE.0.)U(NP3)=U(NP3)-DPDX(NP3)*DX/RU(NP3)
C---------------------------  SOLVE FOR DOWNSTREAM U 'S  ------------
3047  BU(2)=BU(2)*U(1)+CU(2)
      DO 3048 I=3,NP2
      T=1.-BU(I)*AU(I-1)
      AU(I)=AU(I)/T
 3048 BU(I)=(BU(I)*BU(I-1)+CU(I))/T
      DO 3050 IDASH=2,NP2
      I=N+4-IDASH
      U(I)=AU(I)*U(I+1)+BU(I)
 3050 CONTINUE
      IF(NEQ.EQ.1) GO TO 3060
C---------------------------  SOLVE FOR DOWNSTREAM F 'S  ------------
      DO 3320 J=1,NPH
      B(J,2)=B(J,2)*F(J,1)+C(J,2)
```

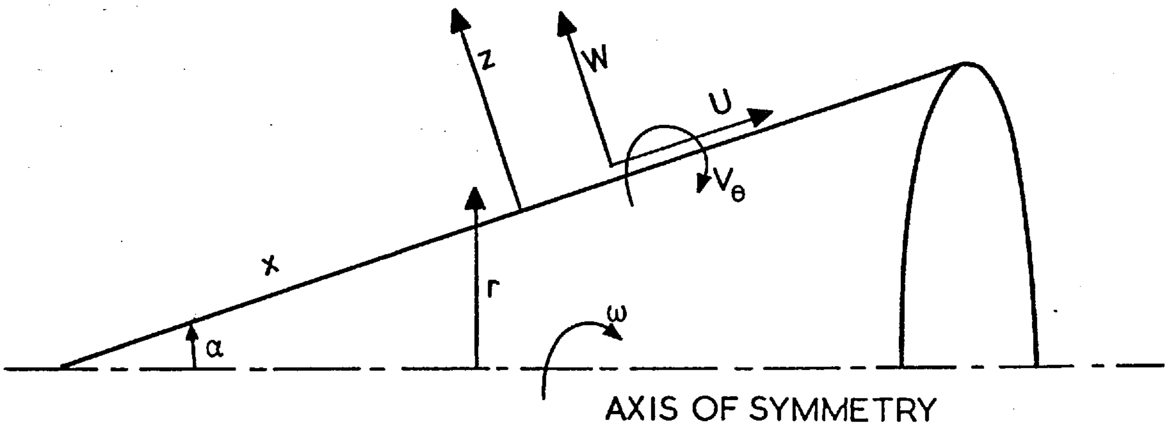

Fig. I GEOMETRY AND NOMENCLATURE FOR SWIRLING FLOWS.

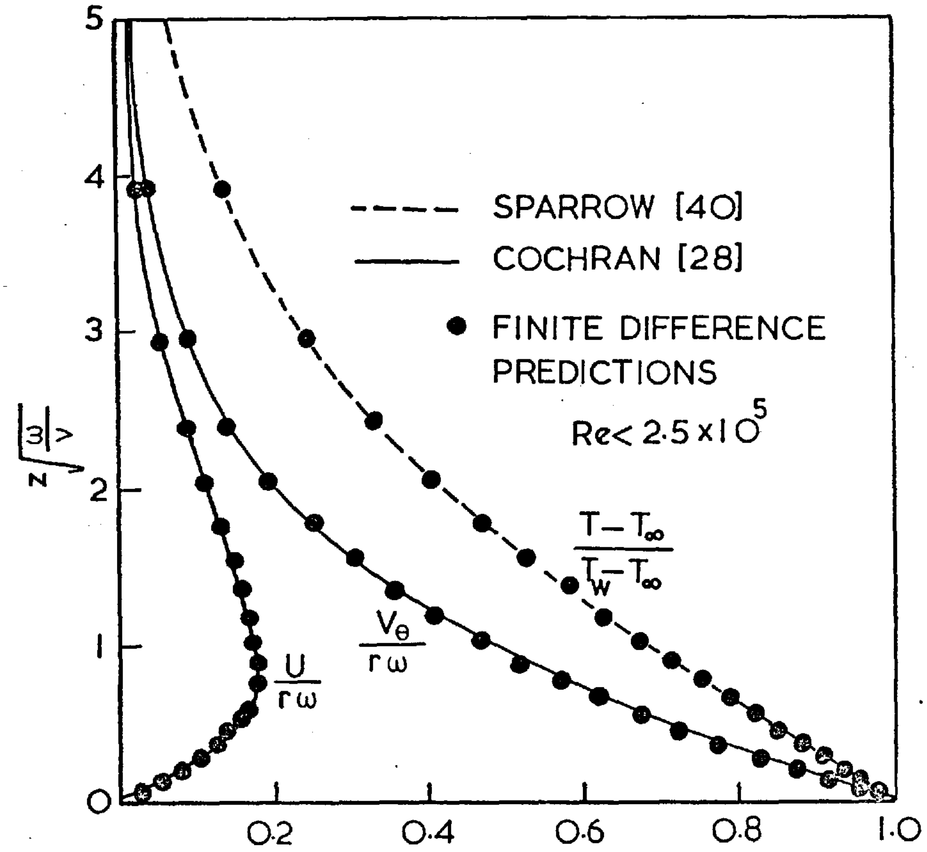

Fig. 2 LAMINAR FLOW NEAR A SWIRLING DISC: VELOCITY AND TEMPERATURE PROFILES.

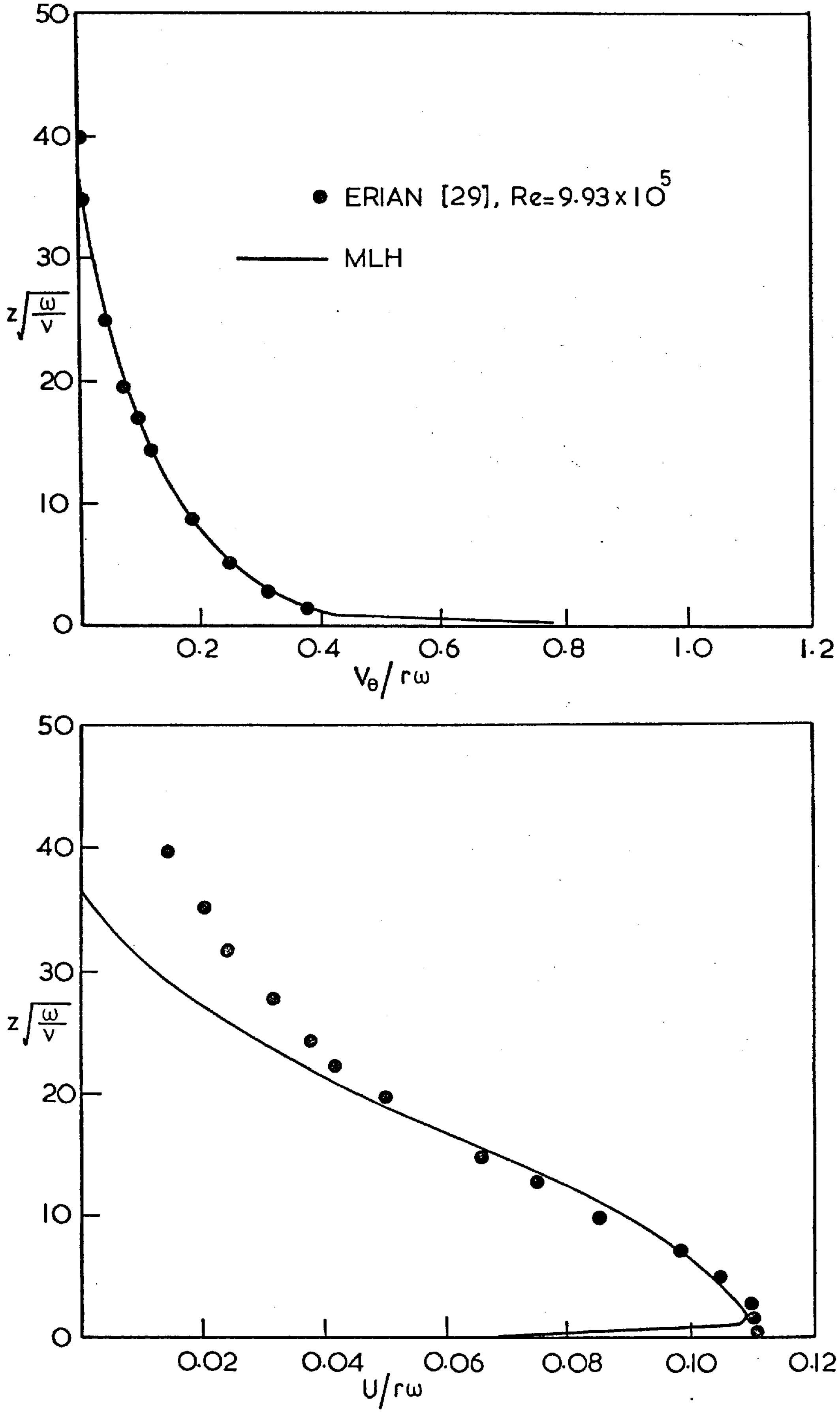

Fig. 3(a) TURBULENT FLOW VELOCITY PROFILES NEAR A SPINNING DISC.

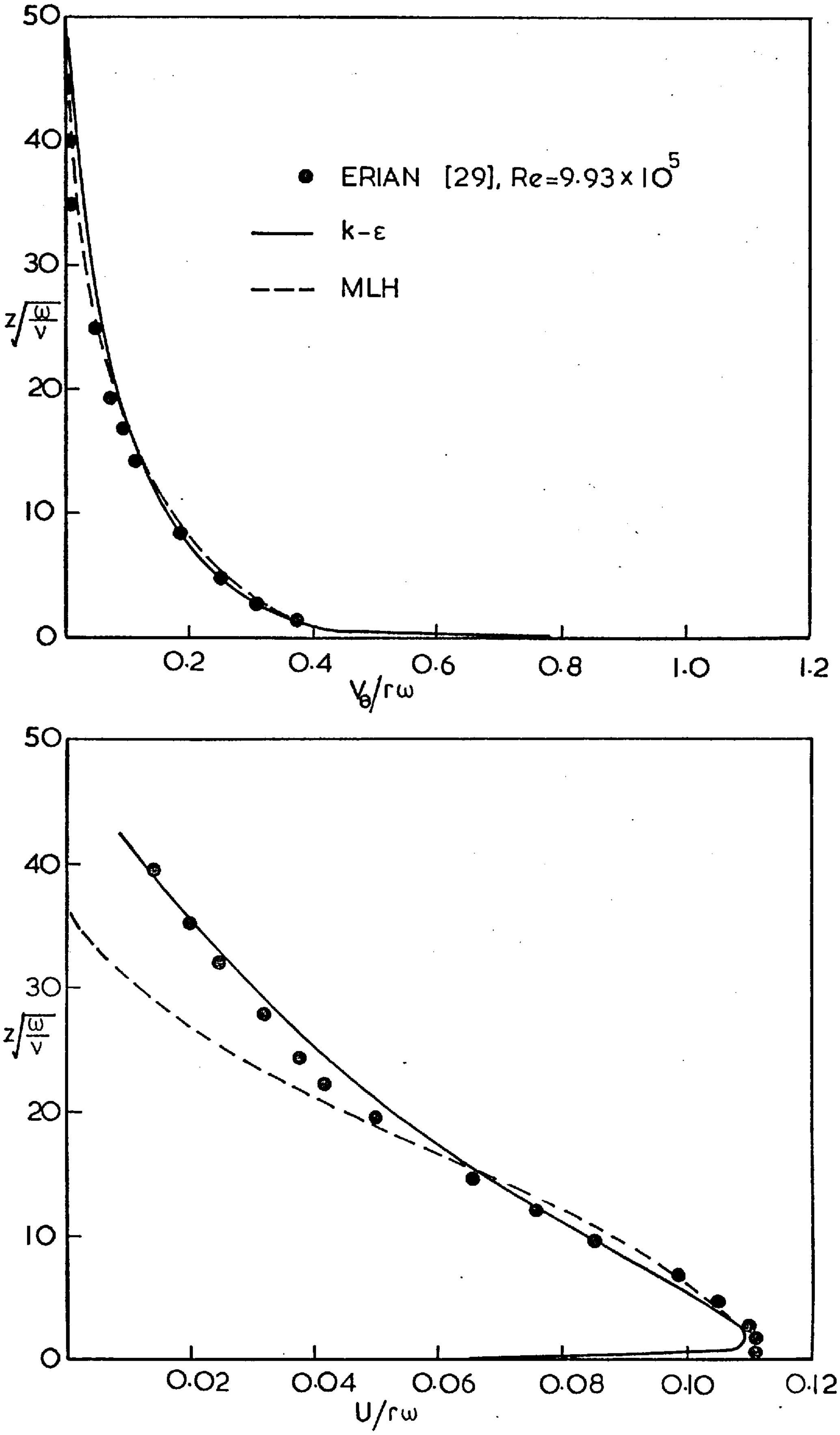

Fig. 3(b) TURBULENT FLOW VELOCITY PROFILES NEAR A SPINNING DISC.

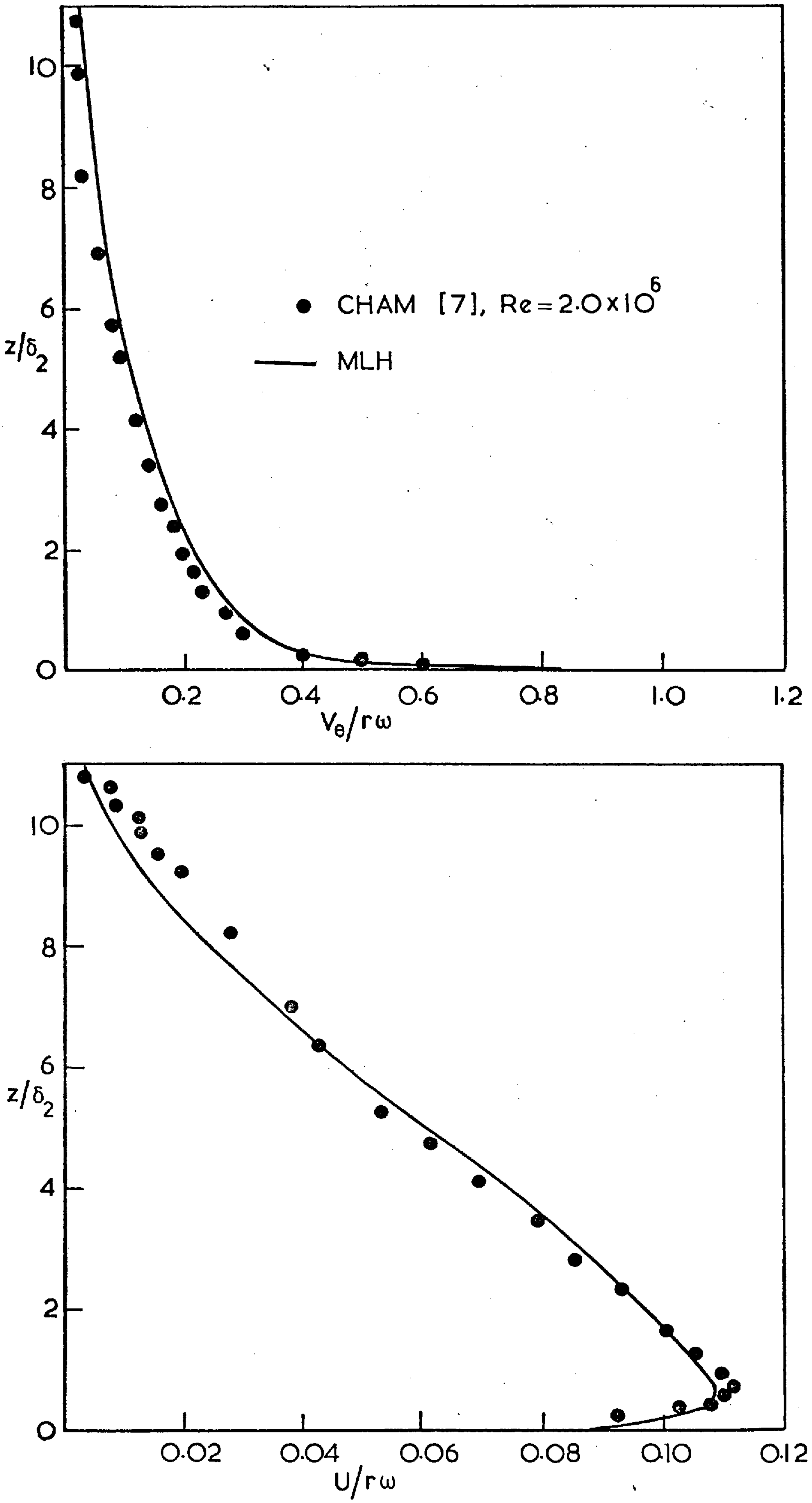

Fig. 4(a) TURBULENT FLOW VELOCITY PROFILES NEAR A SPINNING DISC.

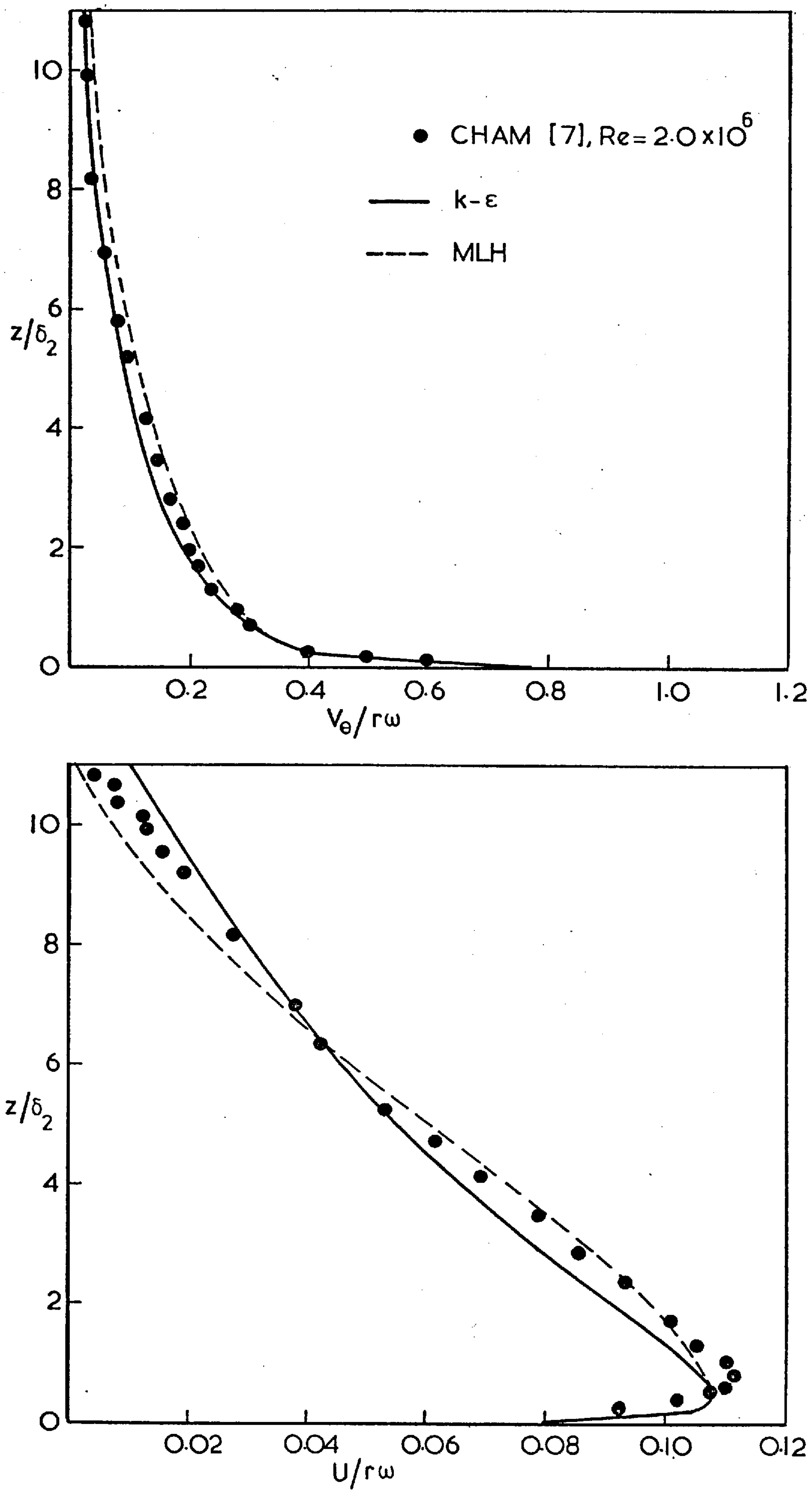

Fig. 4(b) TURBULENT FLOW VELOCITY PROFILES NEAR A SPINNING DISC.

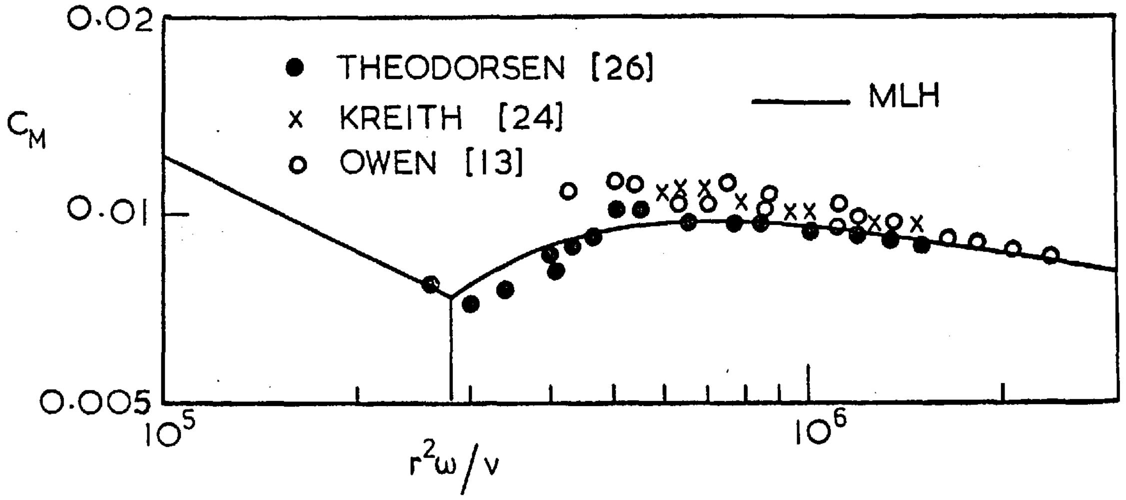

Fig. 5(a) TORQUE COEFFICIENT FOR SPINNING DISC.

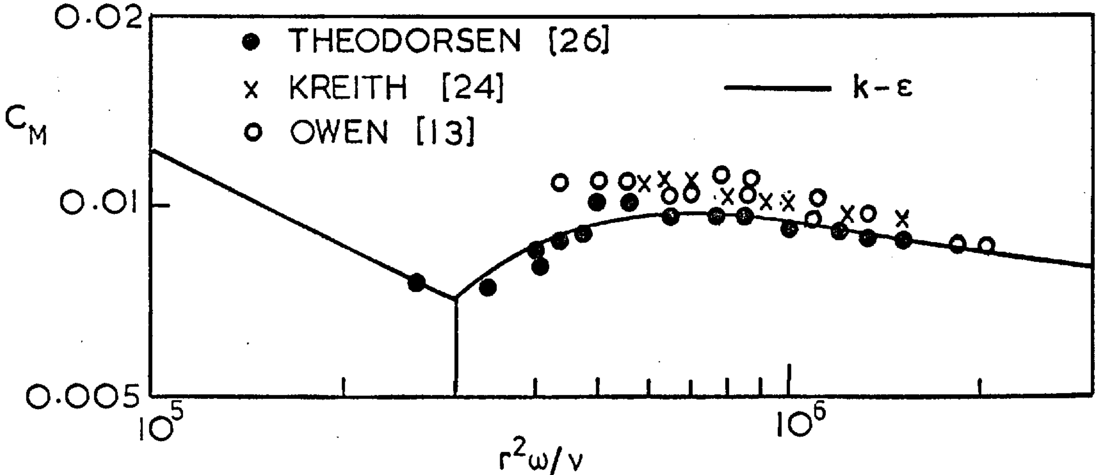

Fig. 5(b) TORQUE COEFFICIENT FOR SPINNING DISC.

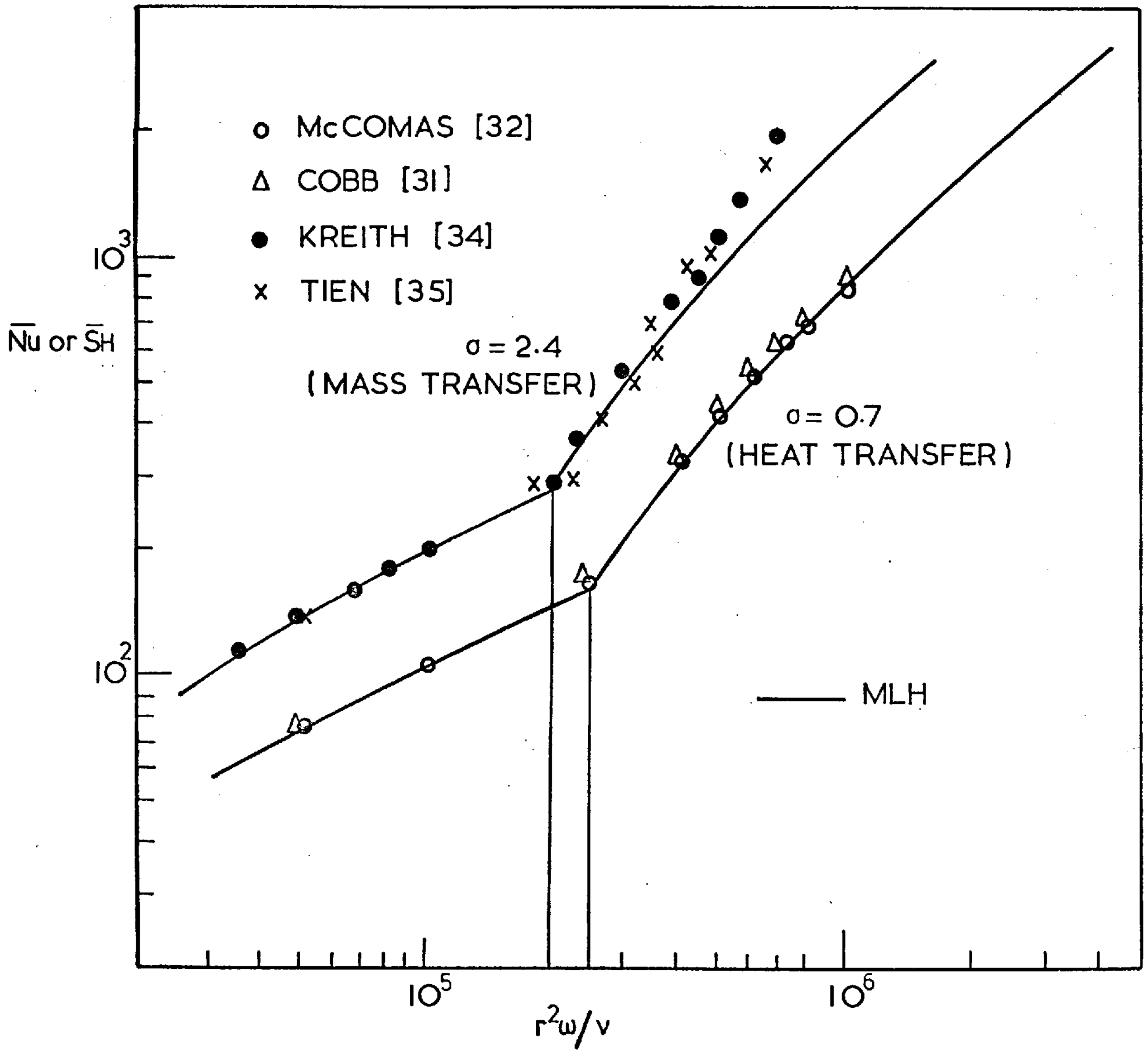

Fig. 6(a) AVERAGE HEAT AND MASS TRANSFER RATES FROM SPINNING DISC.

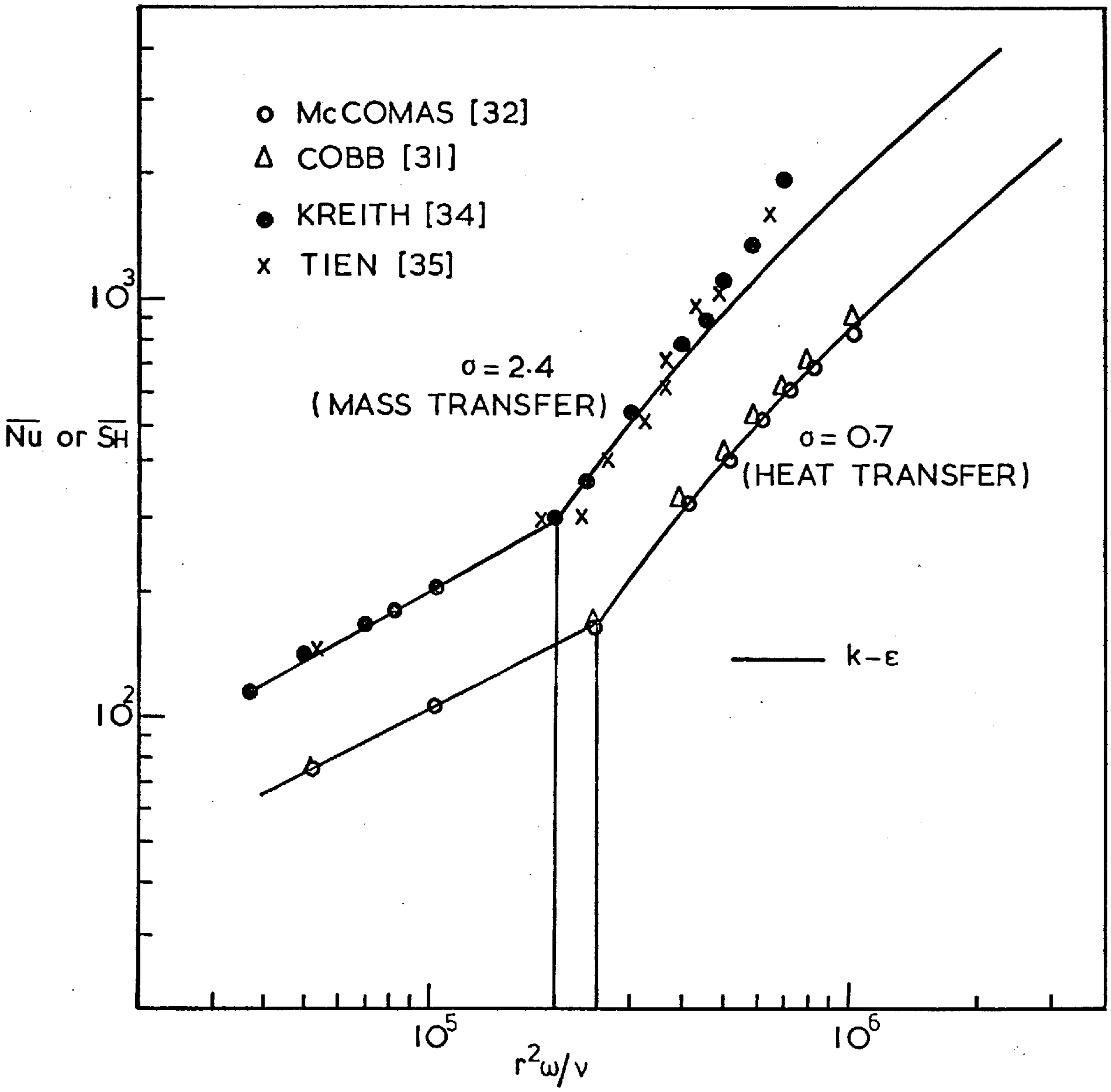

Fig. 6(b) AVERAGE HEAT AND MASS TRANSFER FROM A DISC ROTATING IN STILL AIR.

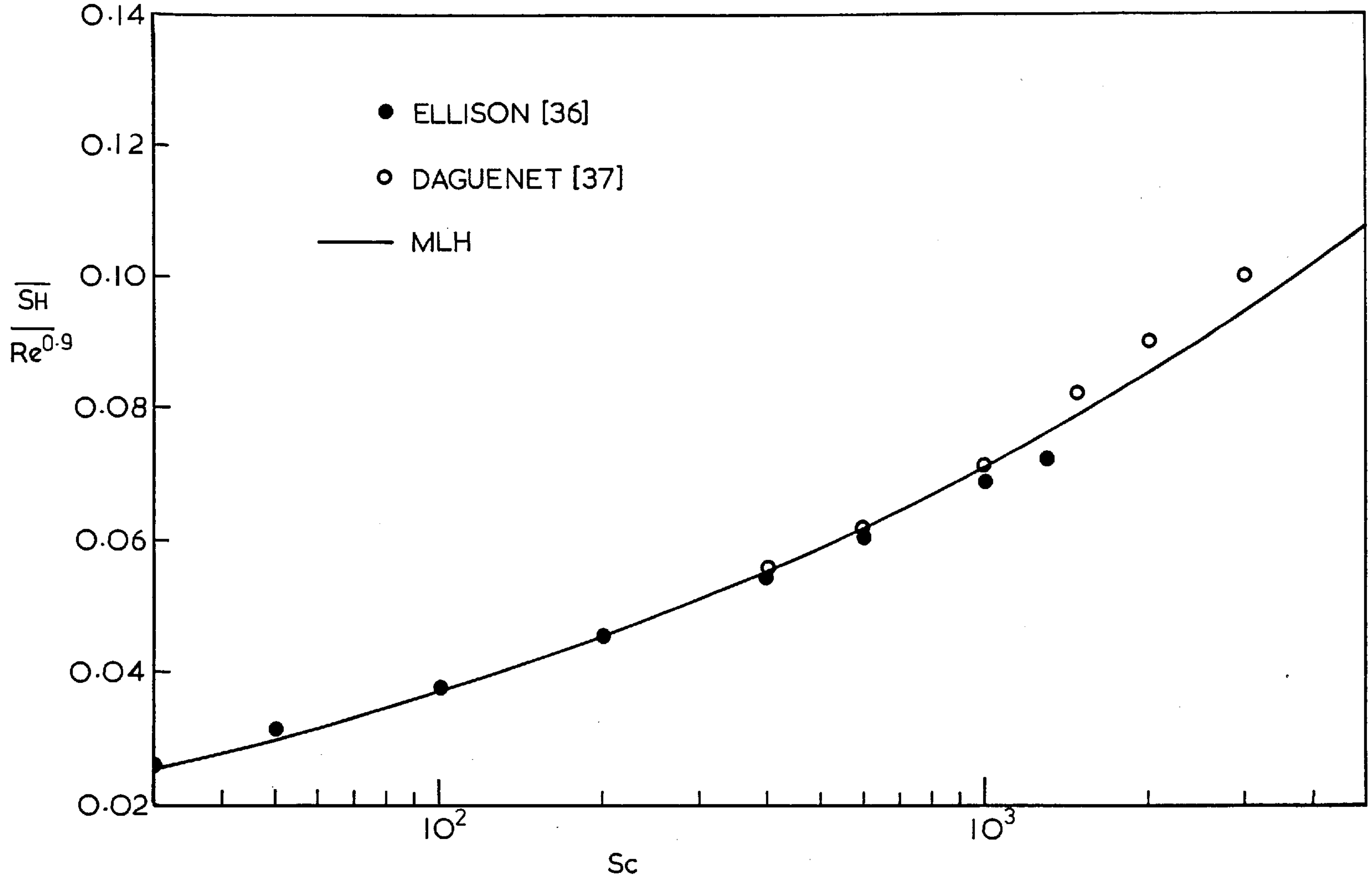

Fig. 7(a) AVERAGE MASS TRANSFER FROM A SPINNING DISC AT HIGH SCHMIDT NUMBERS.

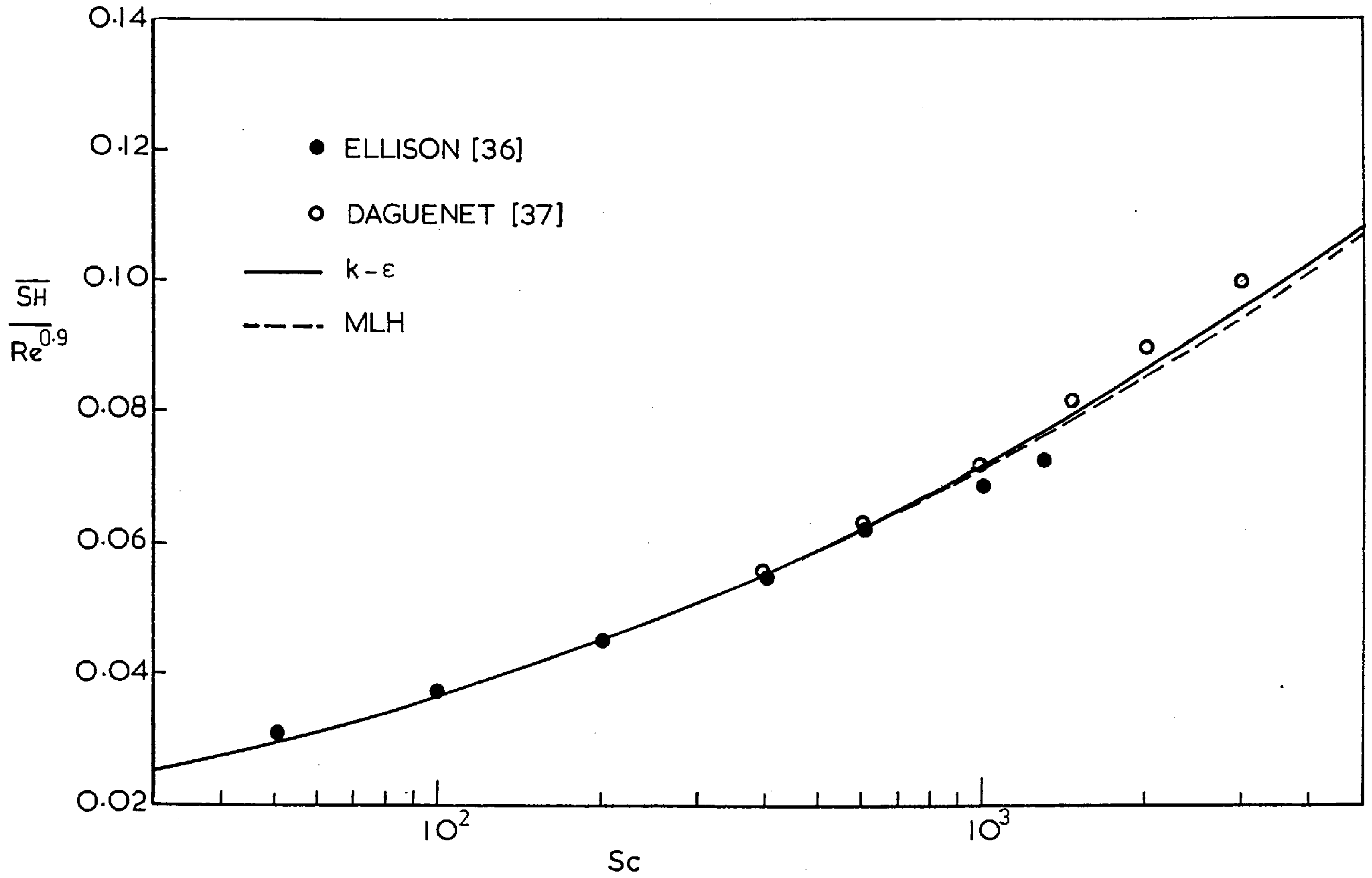

Fig. 7(b) AVERAGE MASS TRANSFER FROM A SPINNING DISC AT HIGH SCHMIDT NUMBERS.

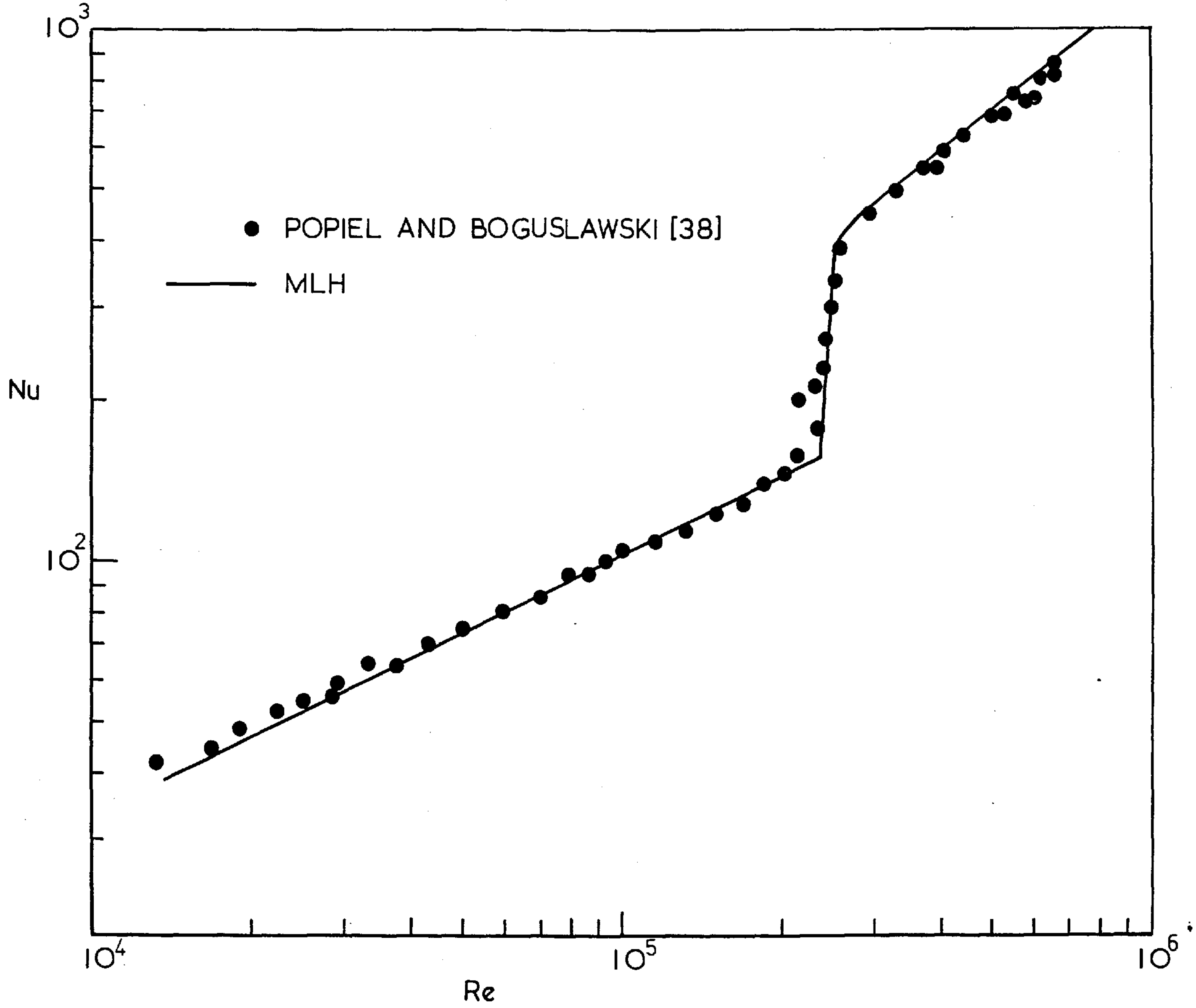

Fig. 8(a) LOCAL HEAT TRANSFER FROM A SPINNING DISC IN STILL AIR.

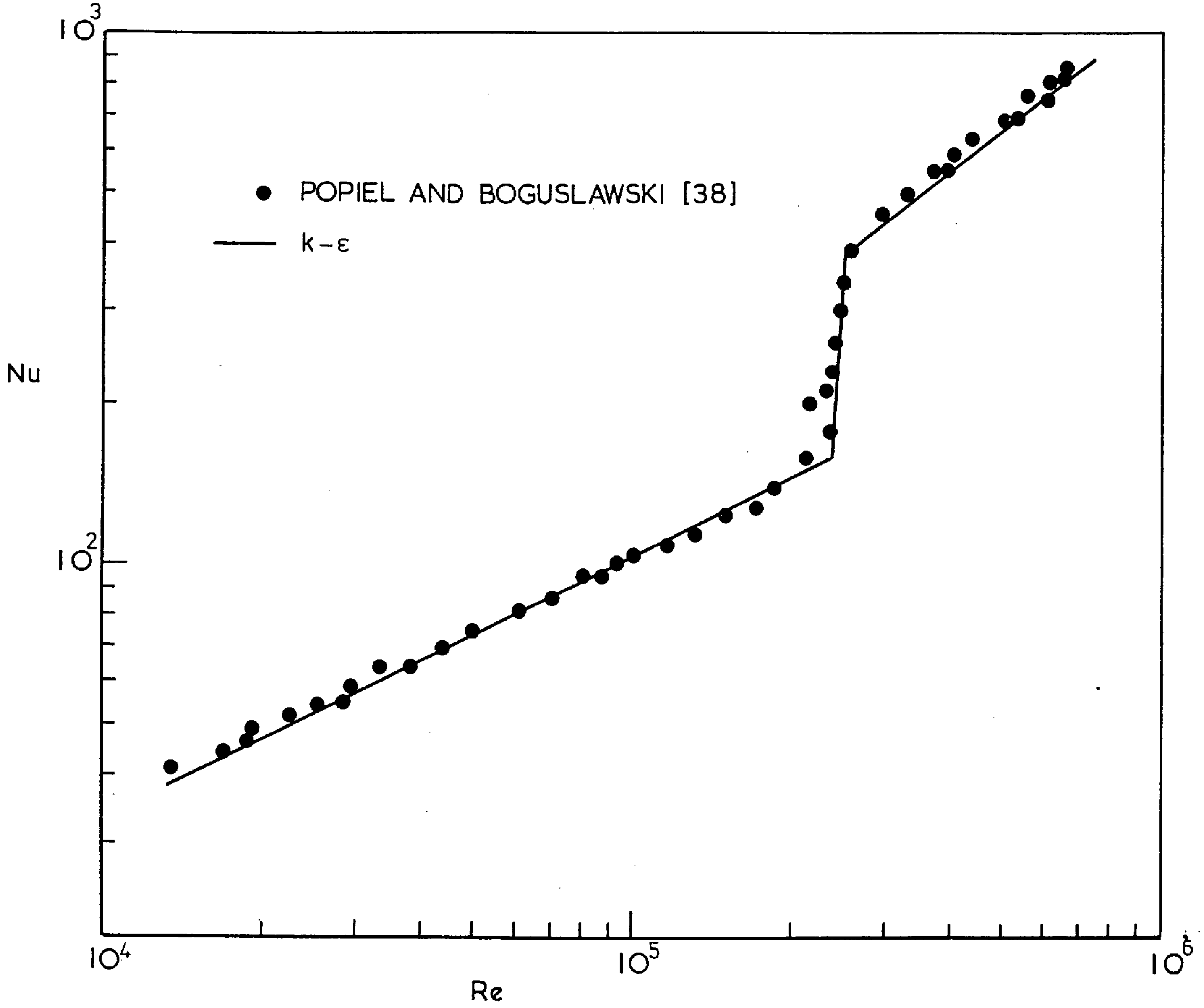

Fig. 8(b) LOCAL HEAT TRANSFER FROM A SPINNING DISC IN STILL AIR.

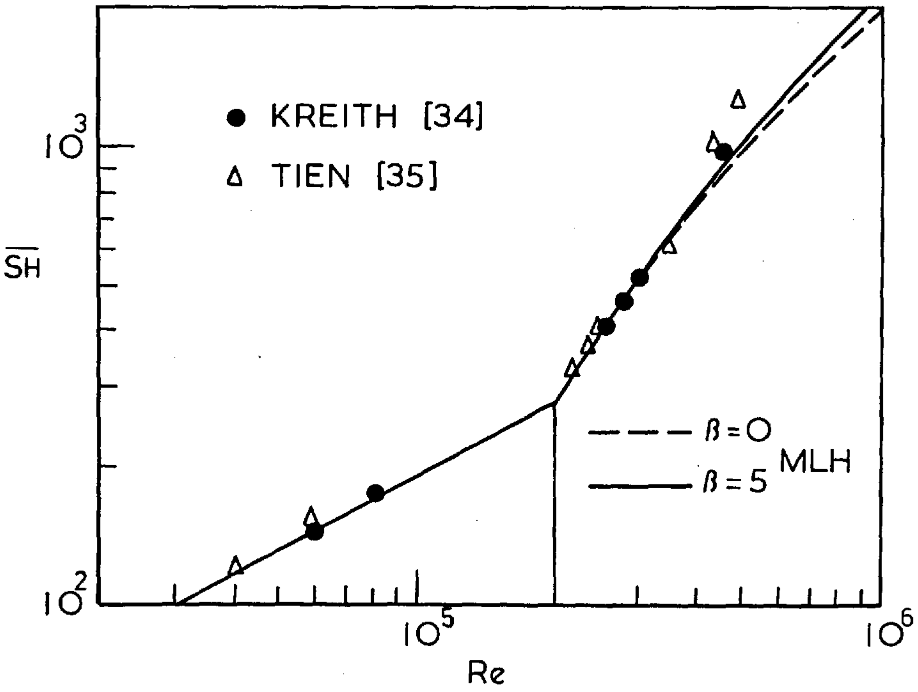

Fig. 9(a) MASS TRANSFER FROM SPINNING 120° CONE IN STILL AIR.

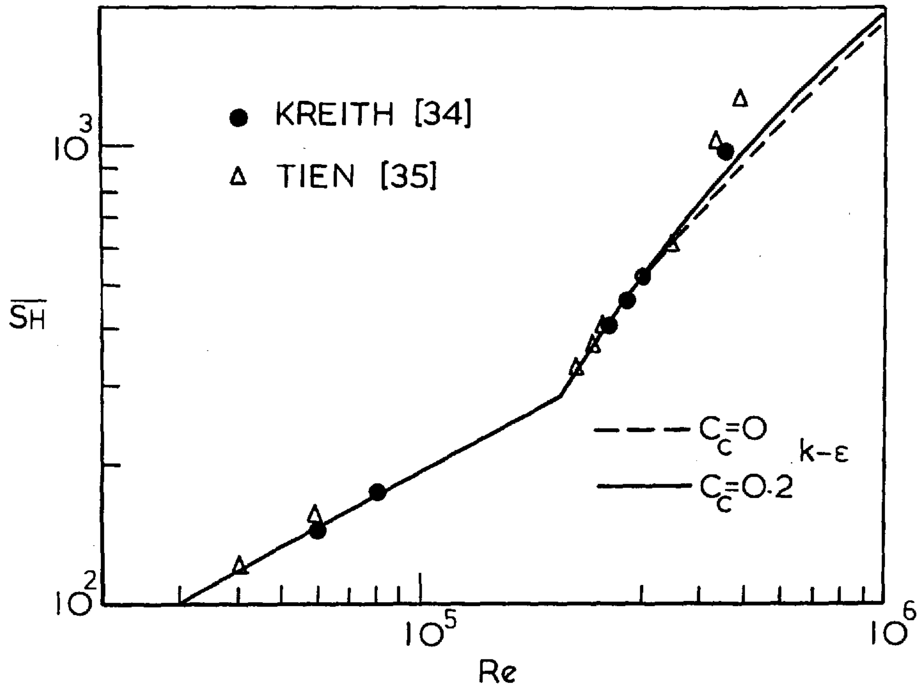

Fig 9(b) MASS TRNSFER FROM SPINNING 120° CONE IN STILL AIR.

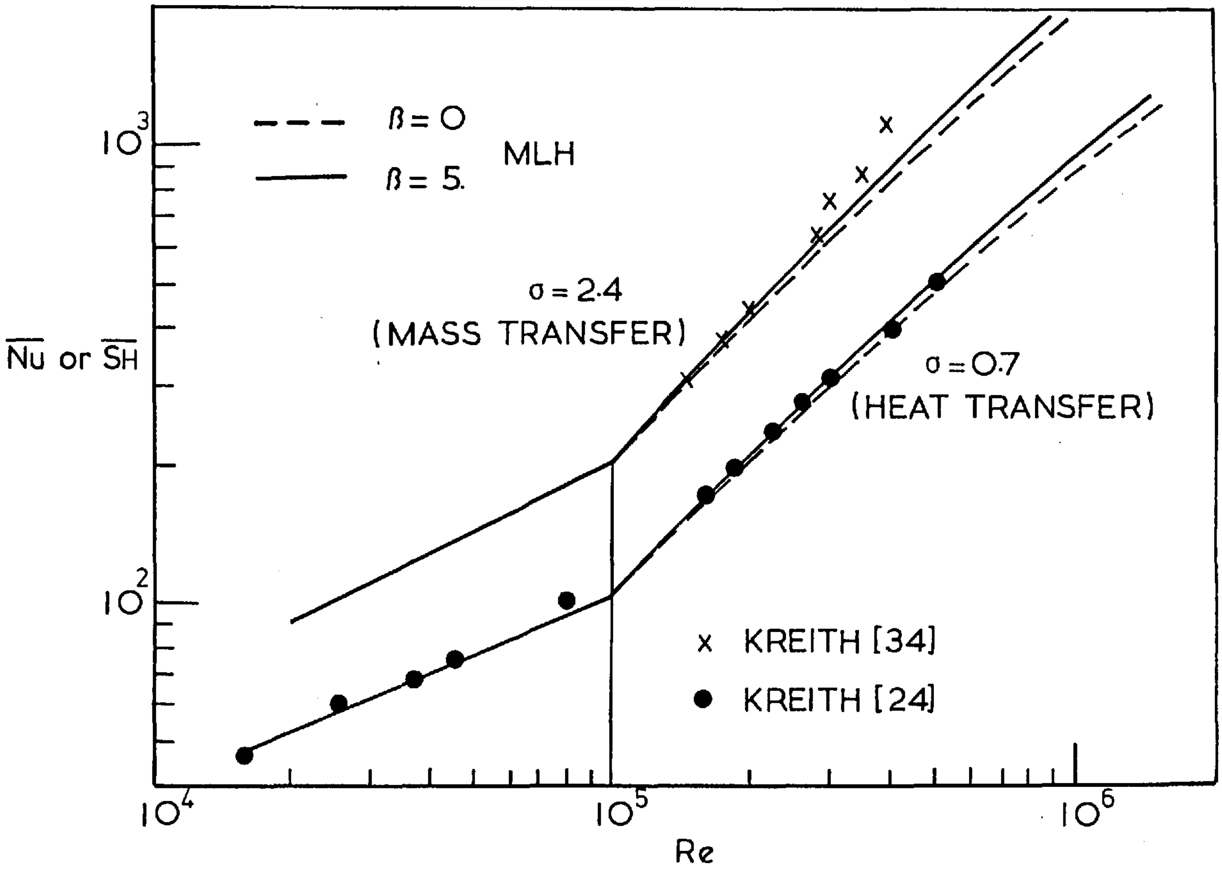

Fig. 10(a) HEAT AND MASS TRANSFER FROM SPINNING 60° CONE IN STILL AIR.

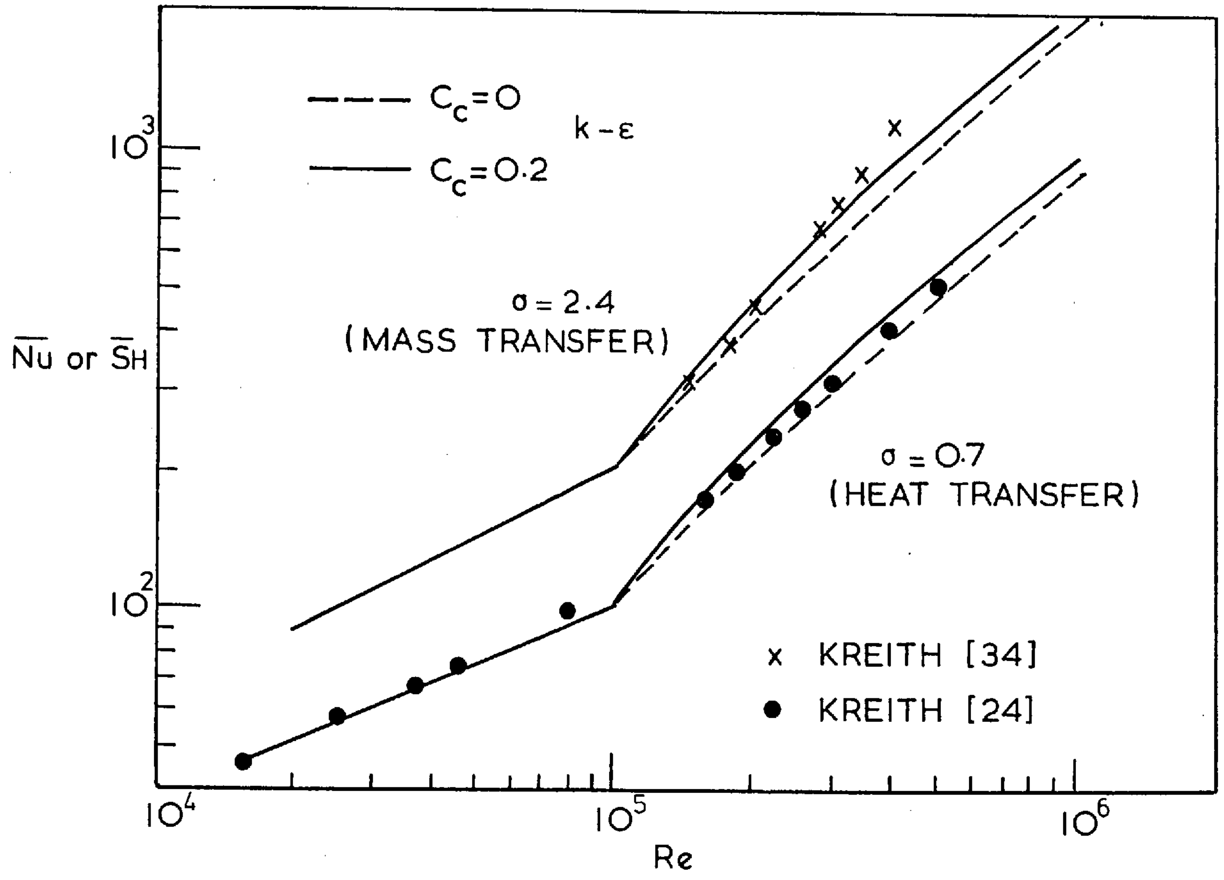

Fig. 10(b) HEAT AND MASS TRANSFER FROM SPINNING 60° CONE IN STILL AIR.

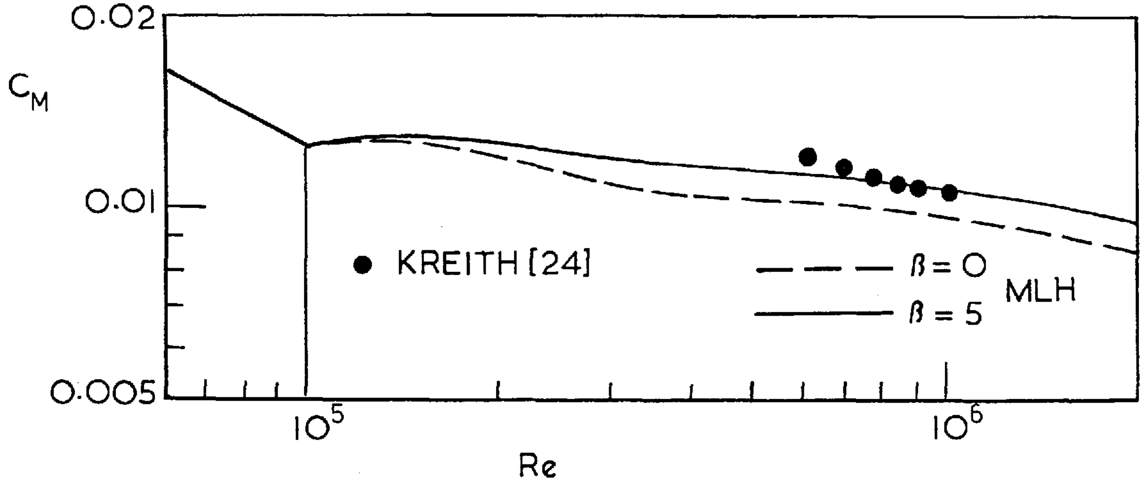

Fig. 11(a) TORQUE COEFFICIENT FOR SPINNING 60° CONE IN STILL AIR.

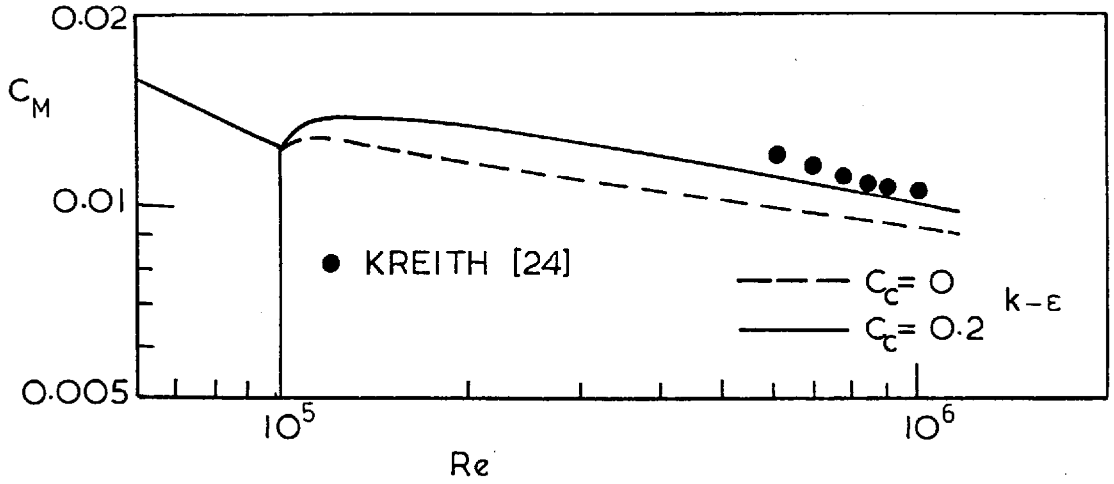

Fig. 11(b) TORQUE COEFFICIENT FOR SPINNING 60° CONE IN STILL AIR.

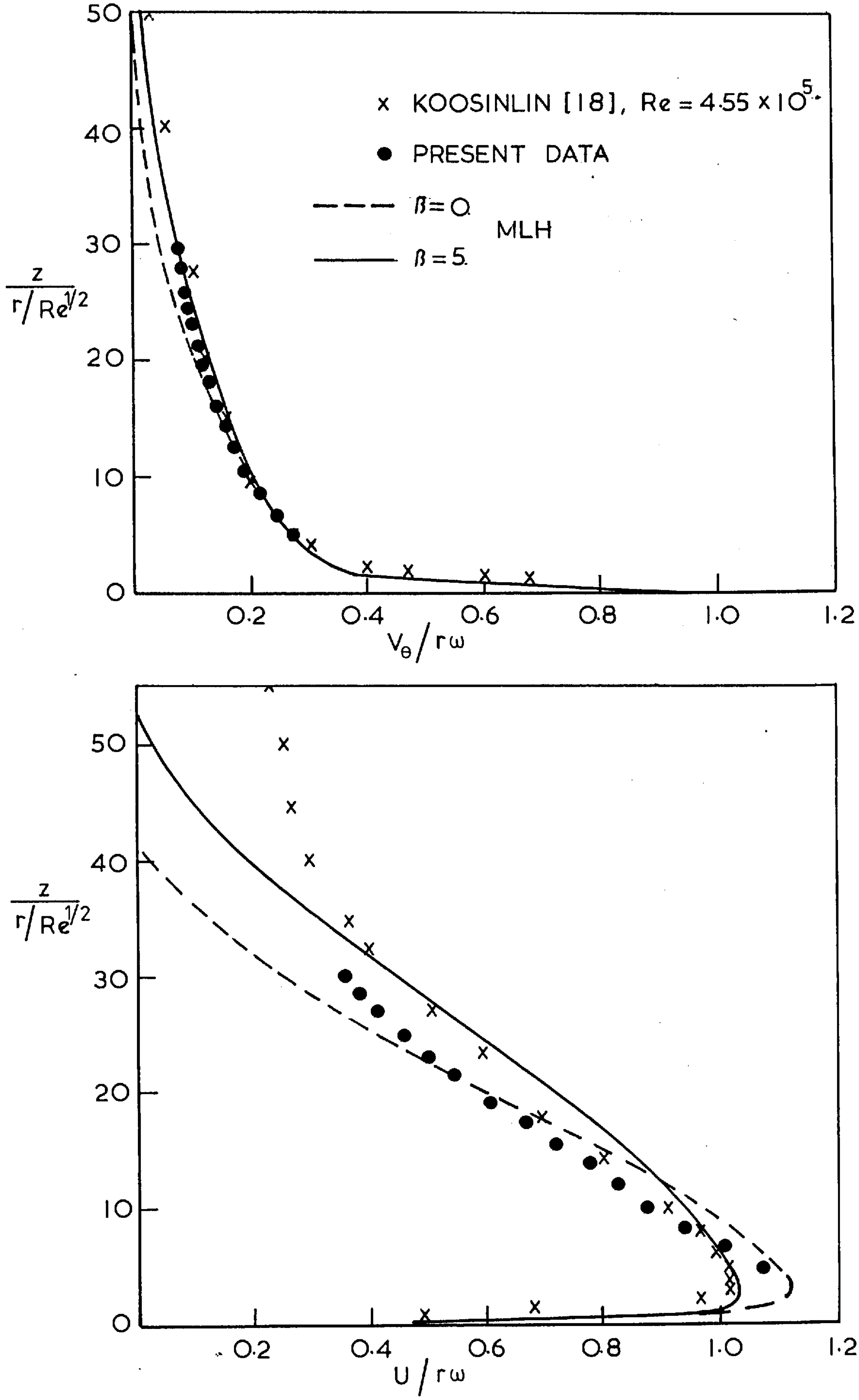

Fig. 12(a) TURBULENT VELOCITY PROFILES NEAR AN 80° SPINNING CONE IN STILL AIR.

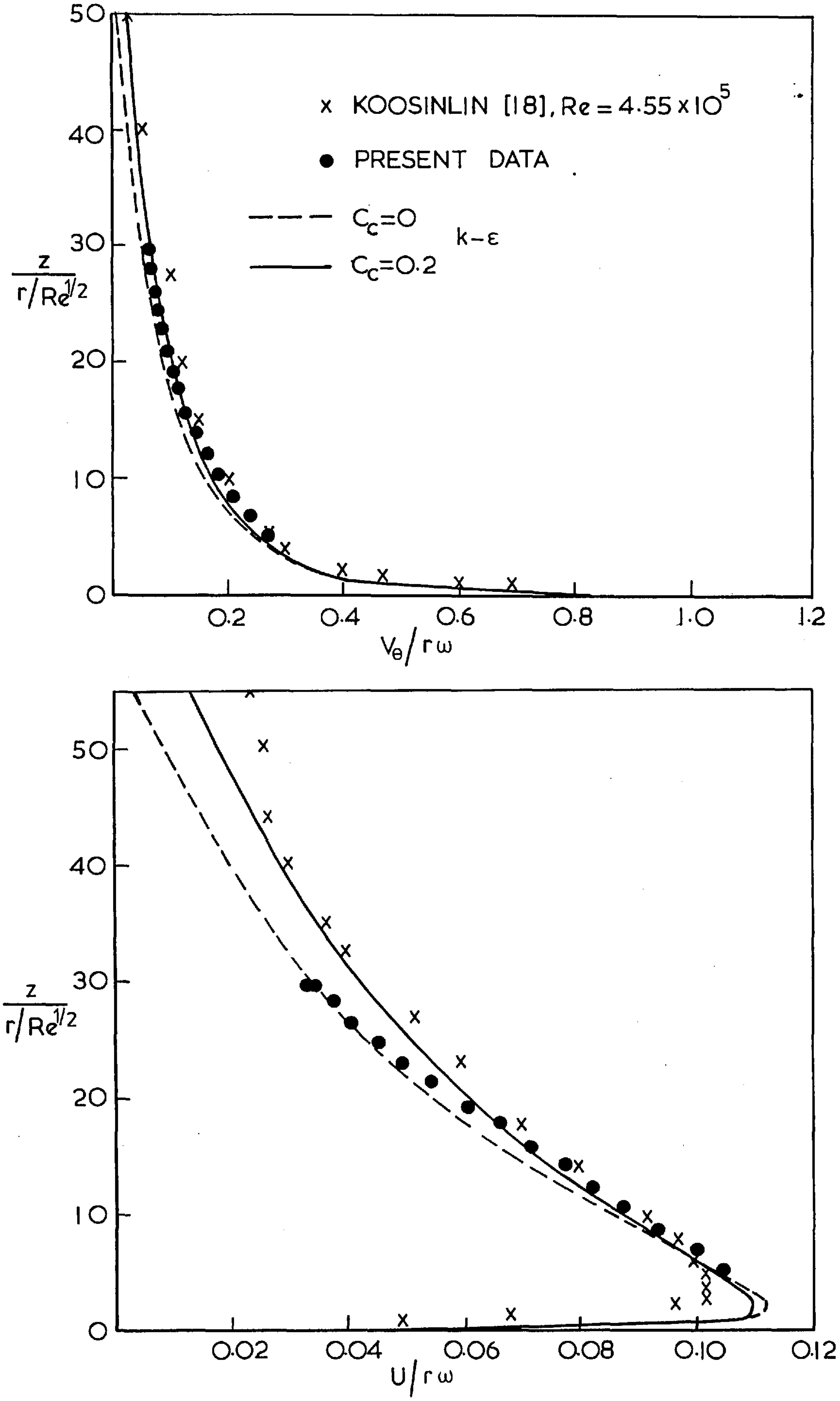

Fig. 12(b) TURBULENT VELOCITY PROFILES NEAR AN 80° SPINNING CONE IN STILL AIR.

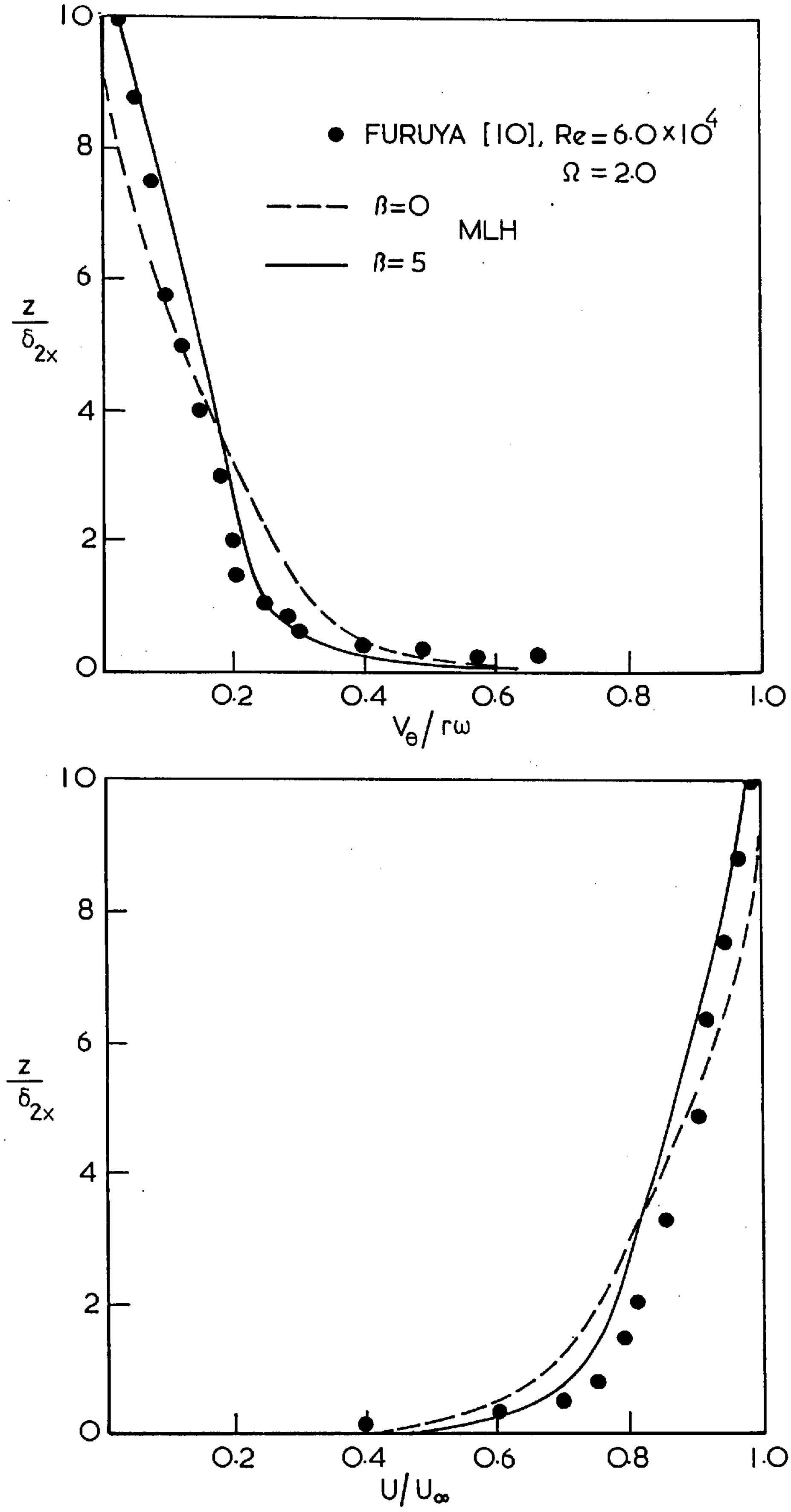

Fig. 13(a) VELOCITY PROFILES IN FLOW PAST SPINNING CYLINDER.

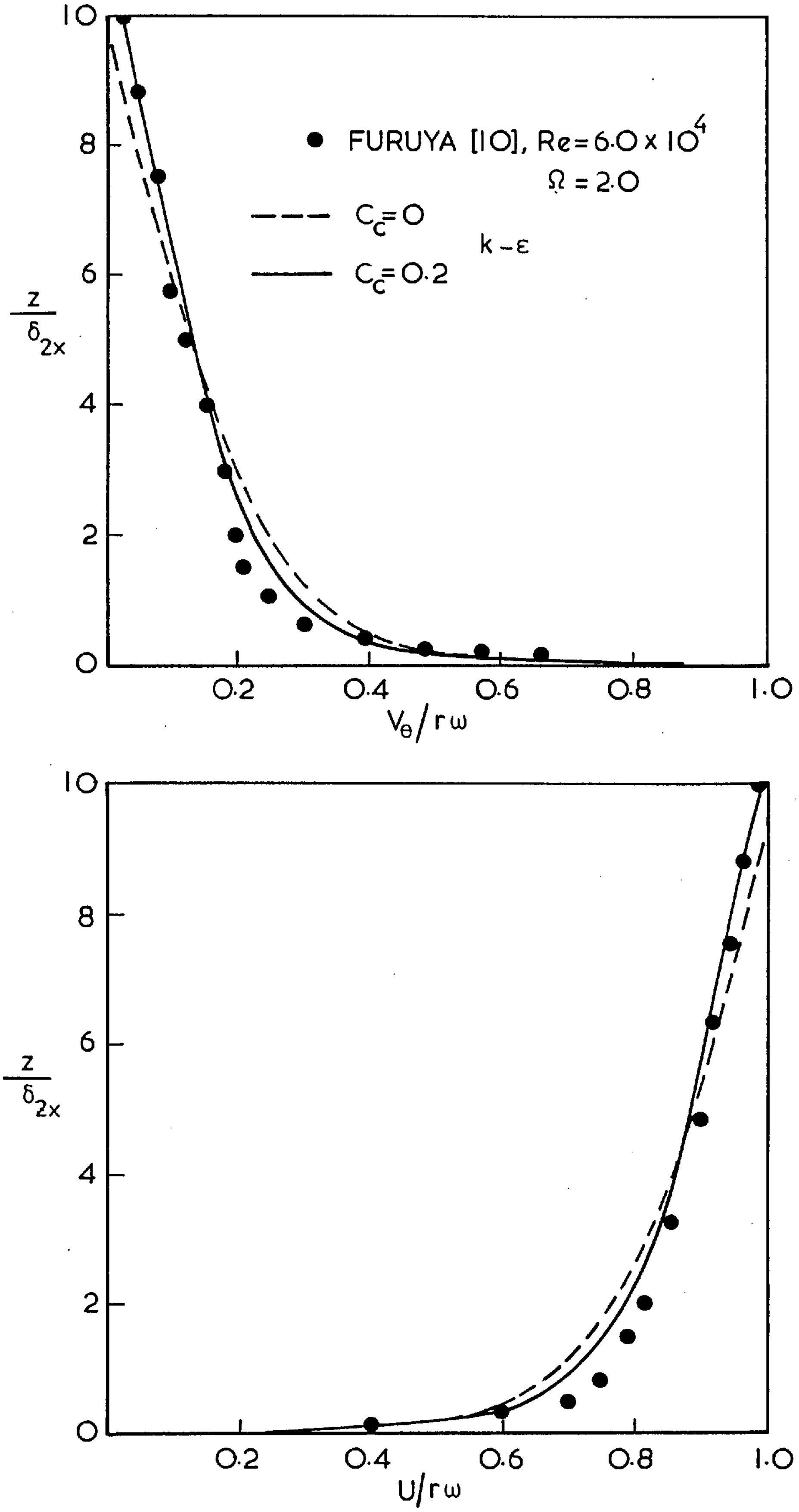

Fig. 13(b) VELOCITY PROFILES IN FLOW PAST SPINNING CYLINDER.

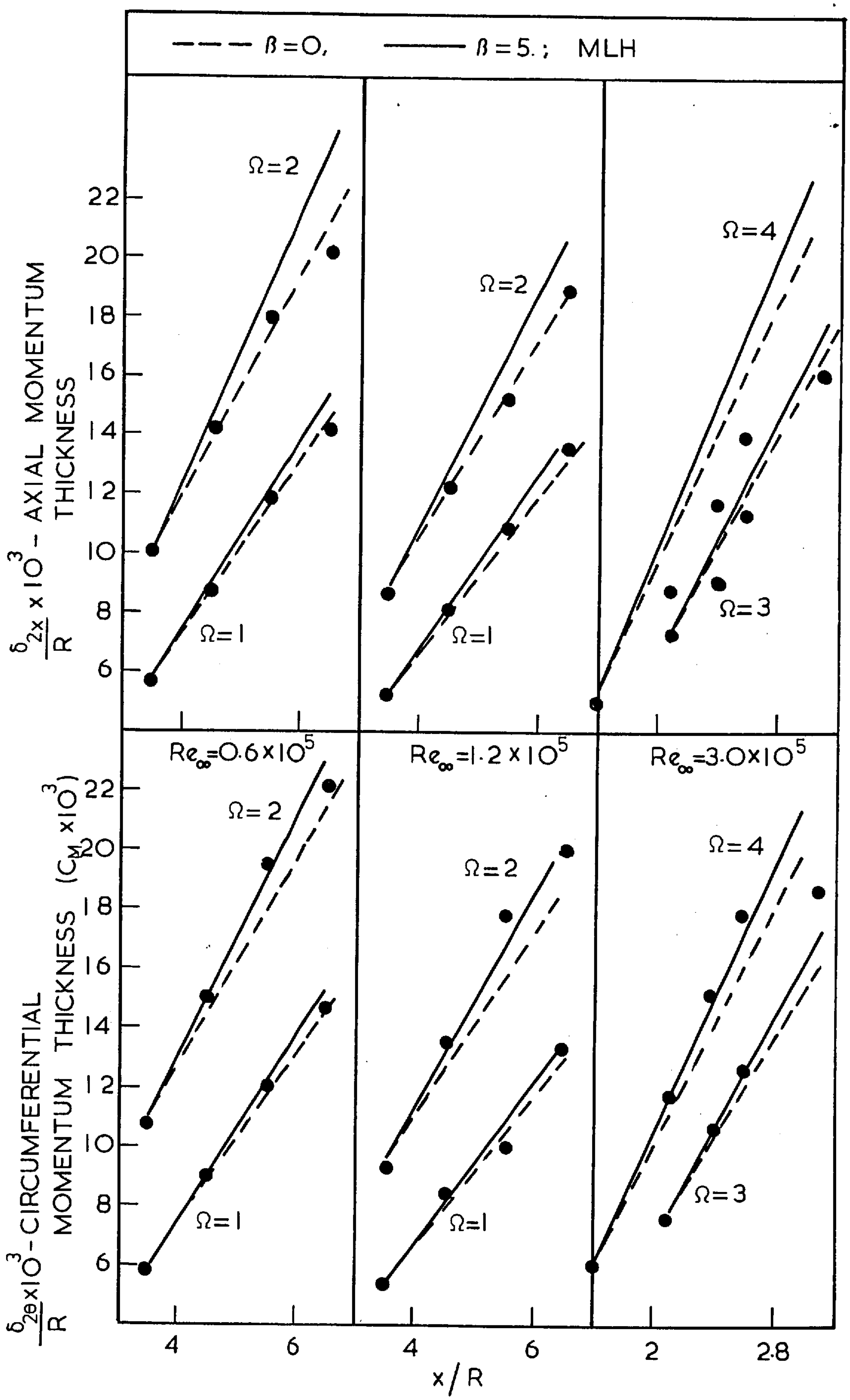

Fig. 14(a) MOMENTUM THICKNESS DEVELOPMENT FOR FLOW PAST SPINNING CYLINDER.

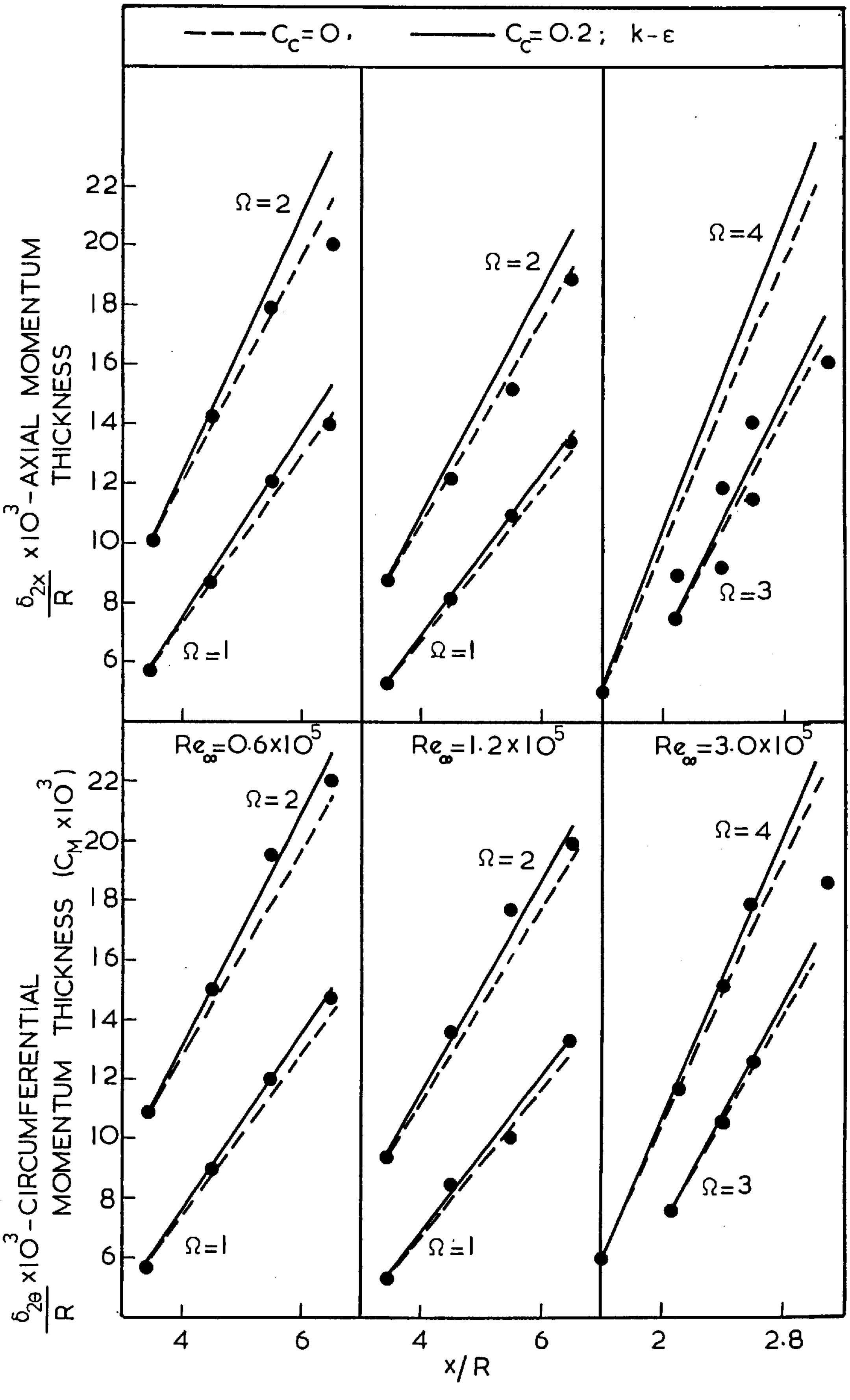

Fig. 14(b) MOMENTUM THICKNESS DEVELOPMENT FOR FLOW PAST SPINNING CYLINDER.

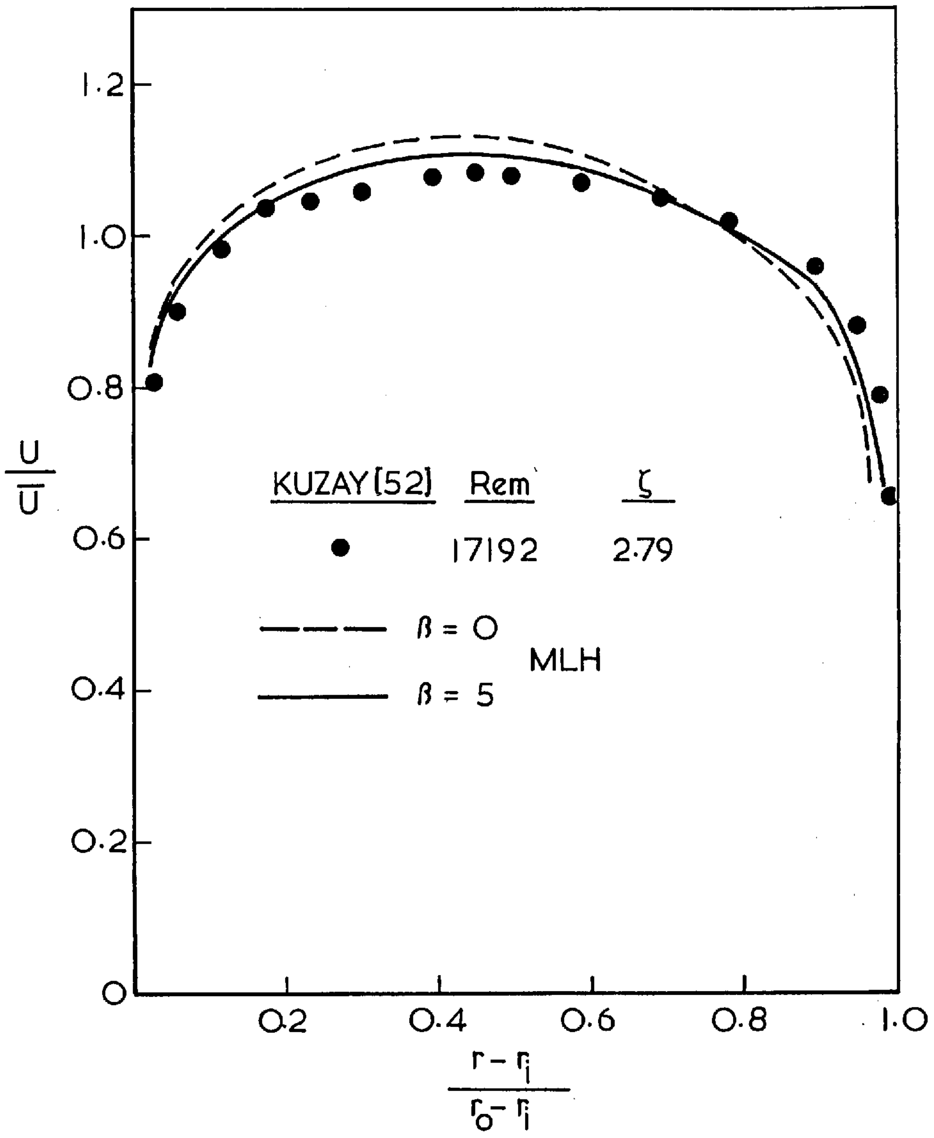

Fig.15(a) INFLUENCE OF CURVATURE CORRECTION (β=5) ON AXIAL VELOCITY PROFILE.

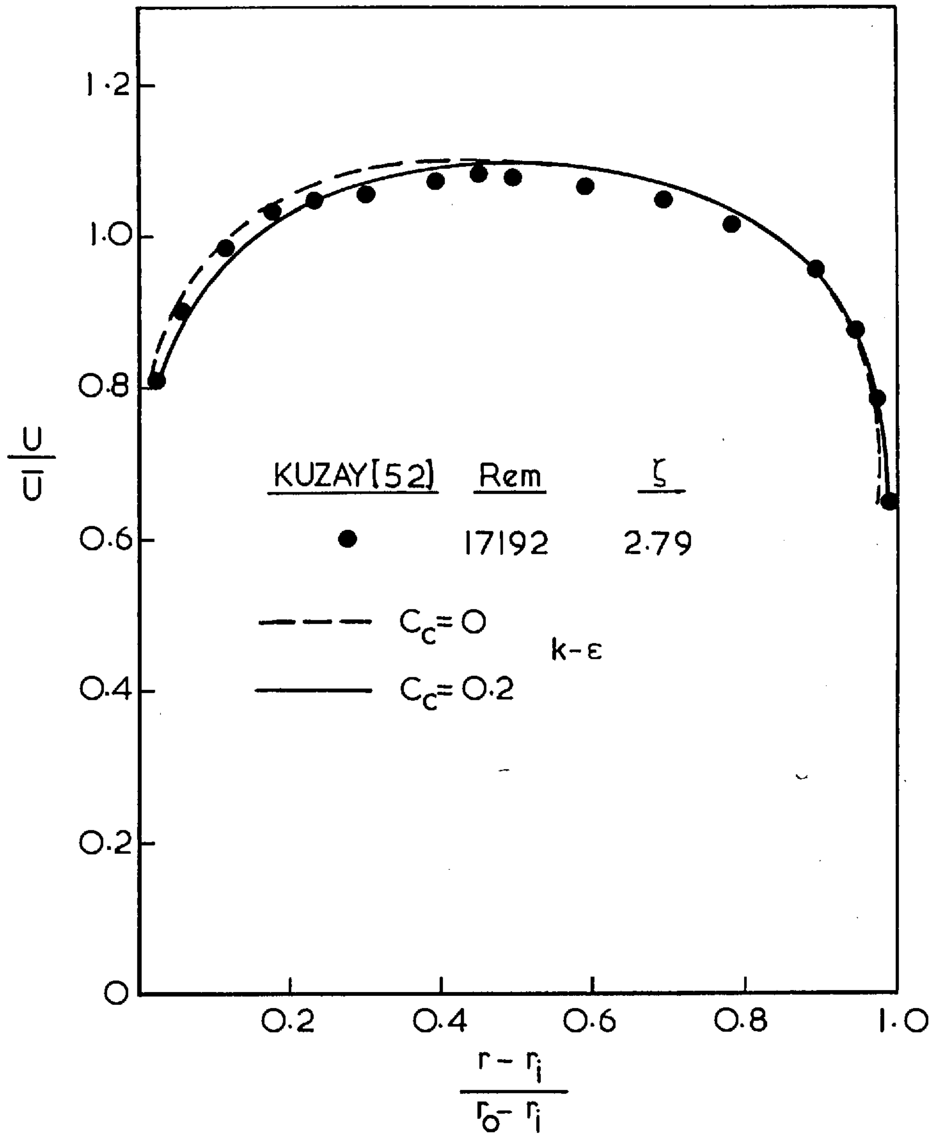

Fig. 15(b) INFLUENCE OF CURVATURE CORRECTION (C_c=0·2) ON AXIAL VELOCITY PROFILE.

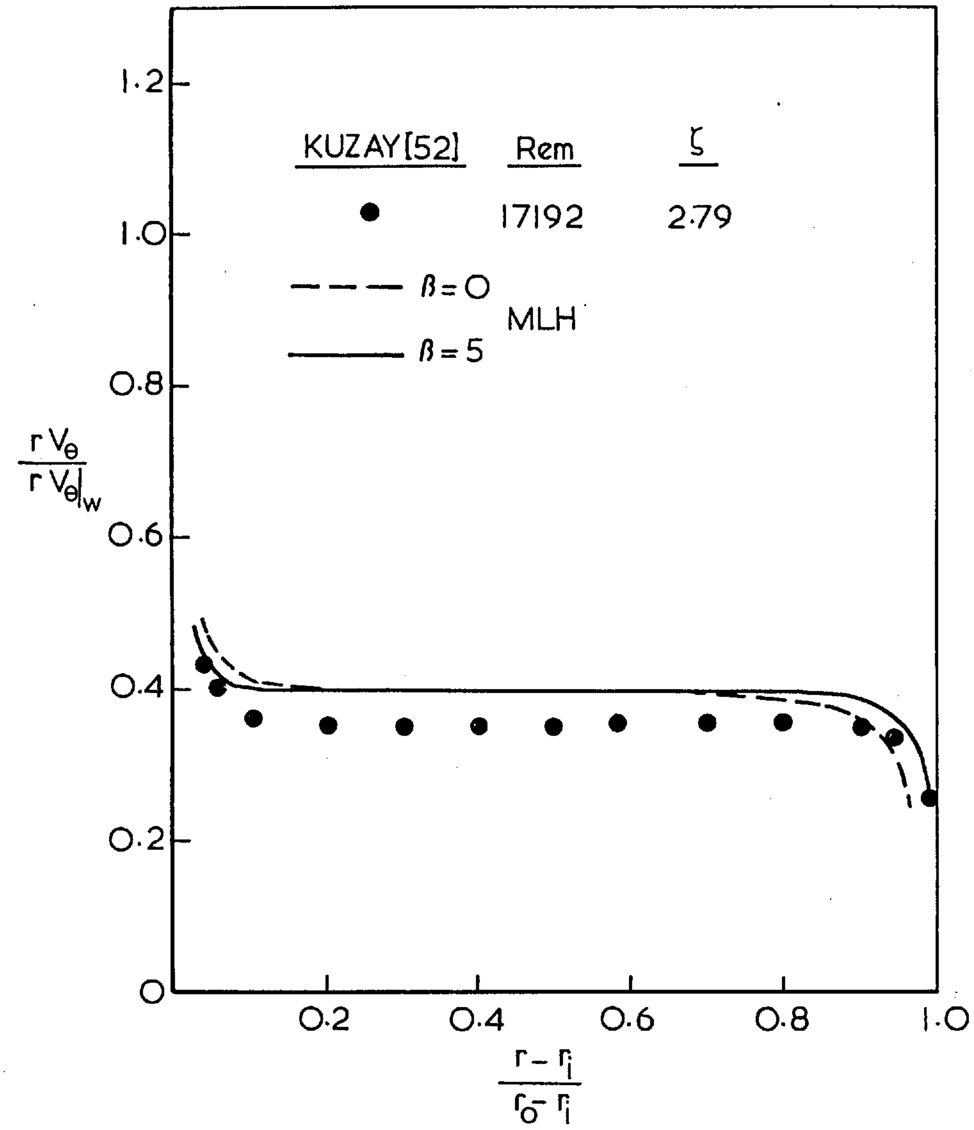

Fig. 16(a) INFLUENCE OF CURVATURE CORRECTION (β=5) ON ANGULAR MOMENTUM PROFILE.

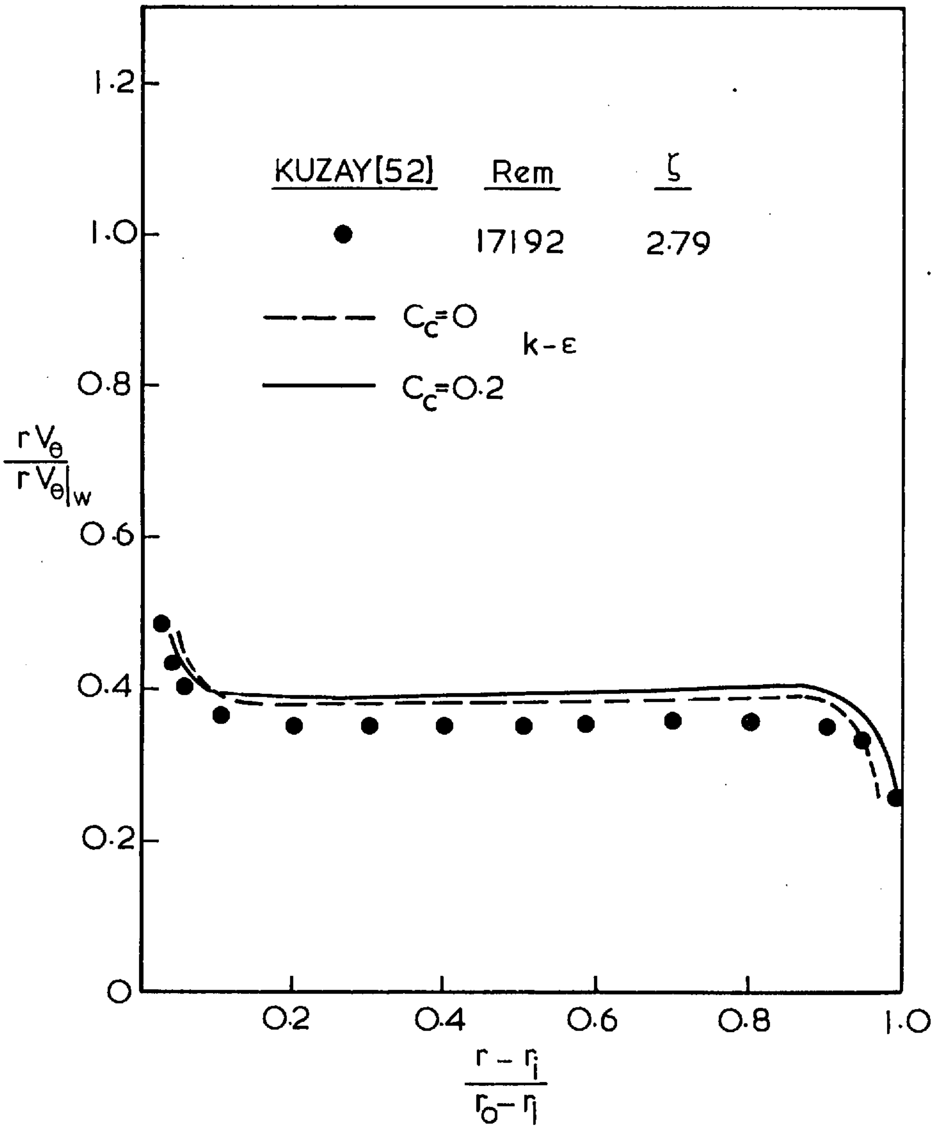

Fig. 16(b) INFLUENCE OF CURVATURE CORRECTION (C_c=0·2) ON ANGULAR MOMENTUM PROFILE.

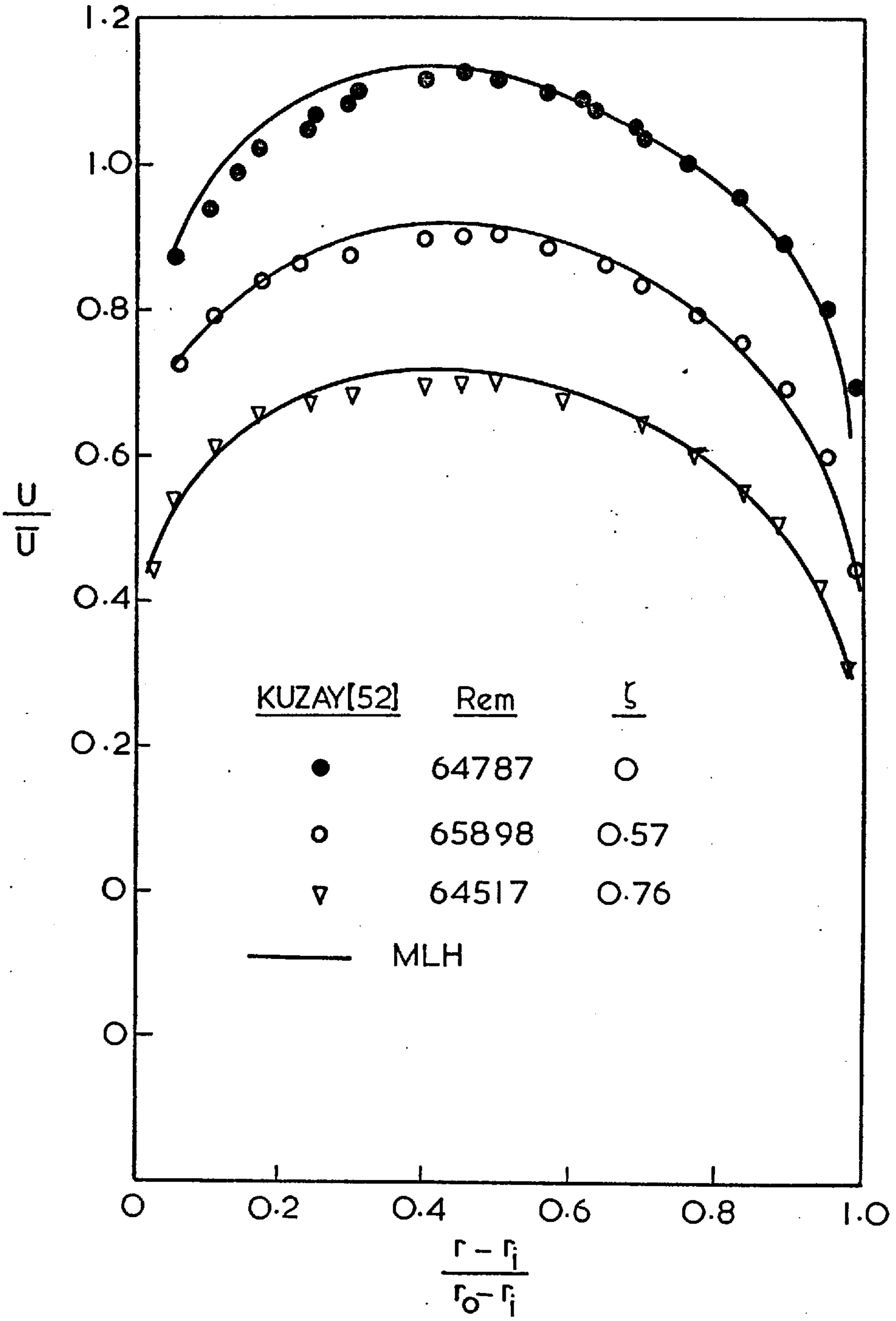

Fig. 17(a) AXIAL VELOCITY PROFILES IN AN ANNULUS WITH ROTATING CORE TUBE.

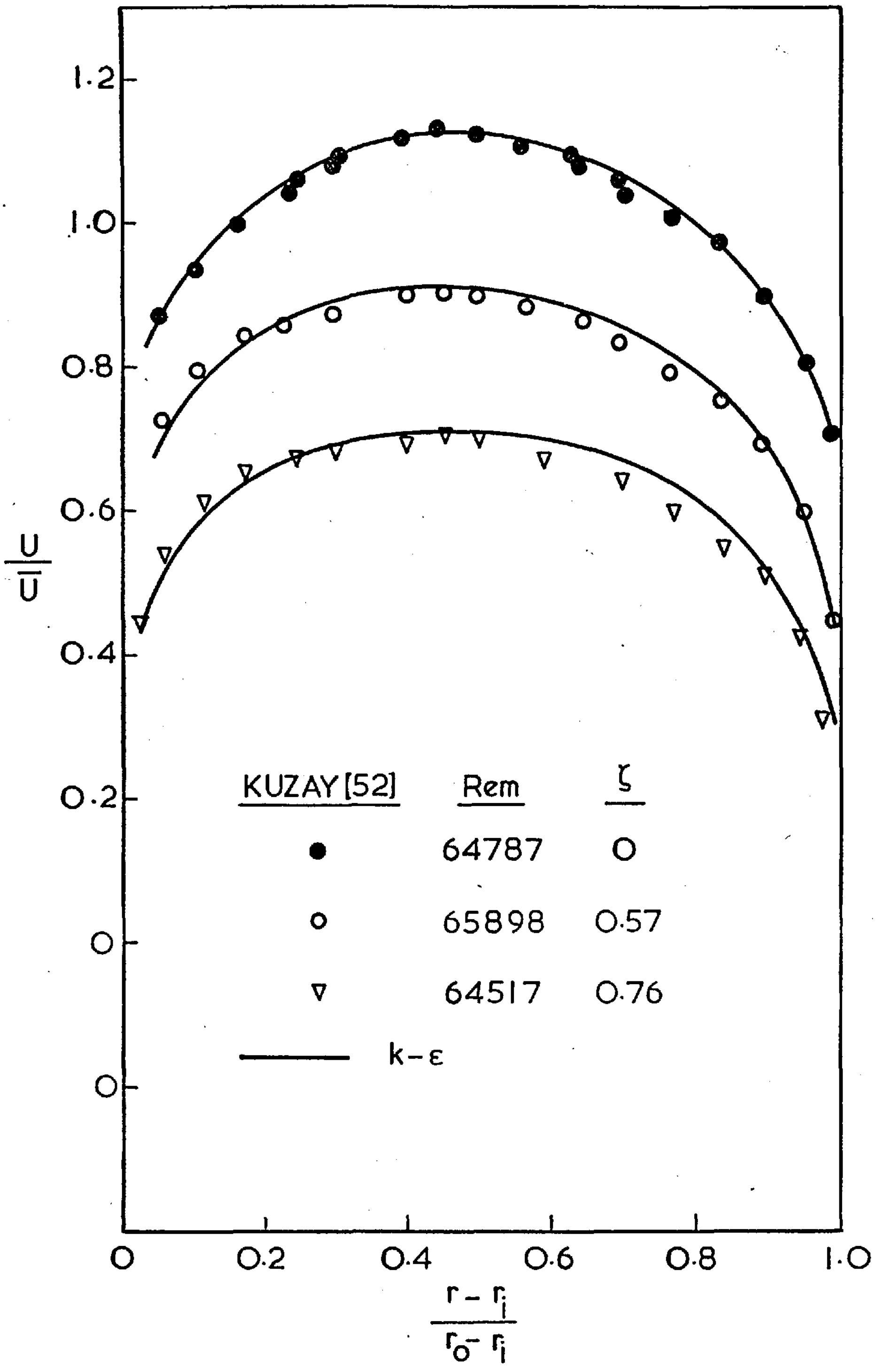

Fig. 17(b) AXIAL VELOCITY PROFILES IN AN ANNULUS WITH ROTATING CORE TUBE.

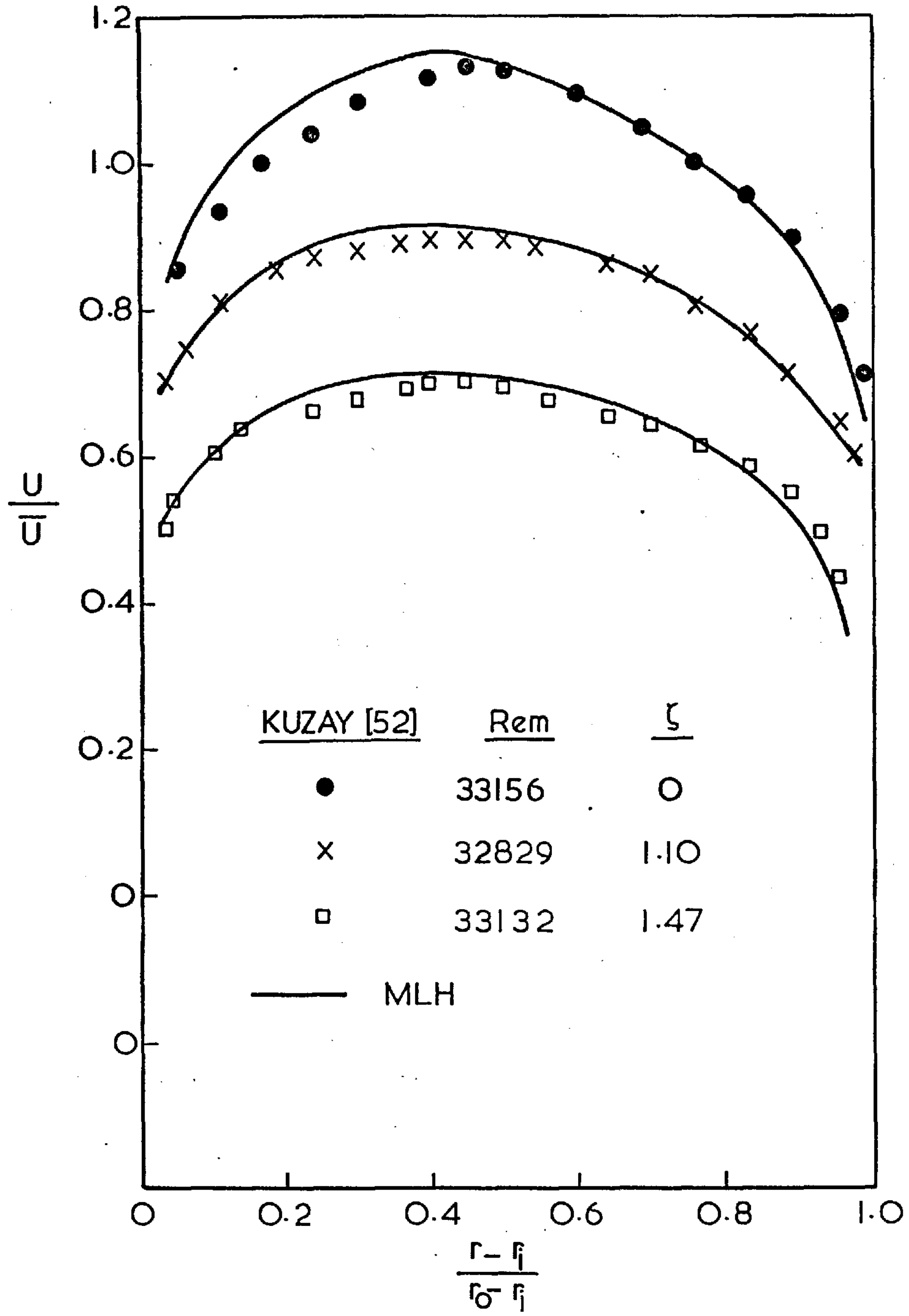

Fig.18(a) AXIAL VELOCITY PROFILES IN AN ANNULUS WITH ROTATING CORE TUBE.

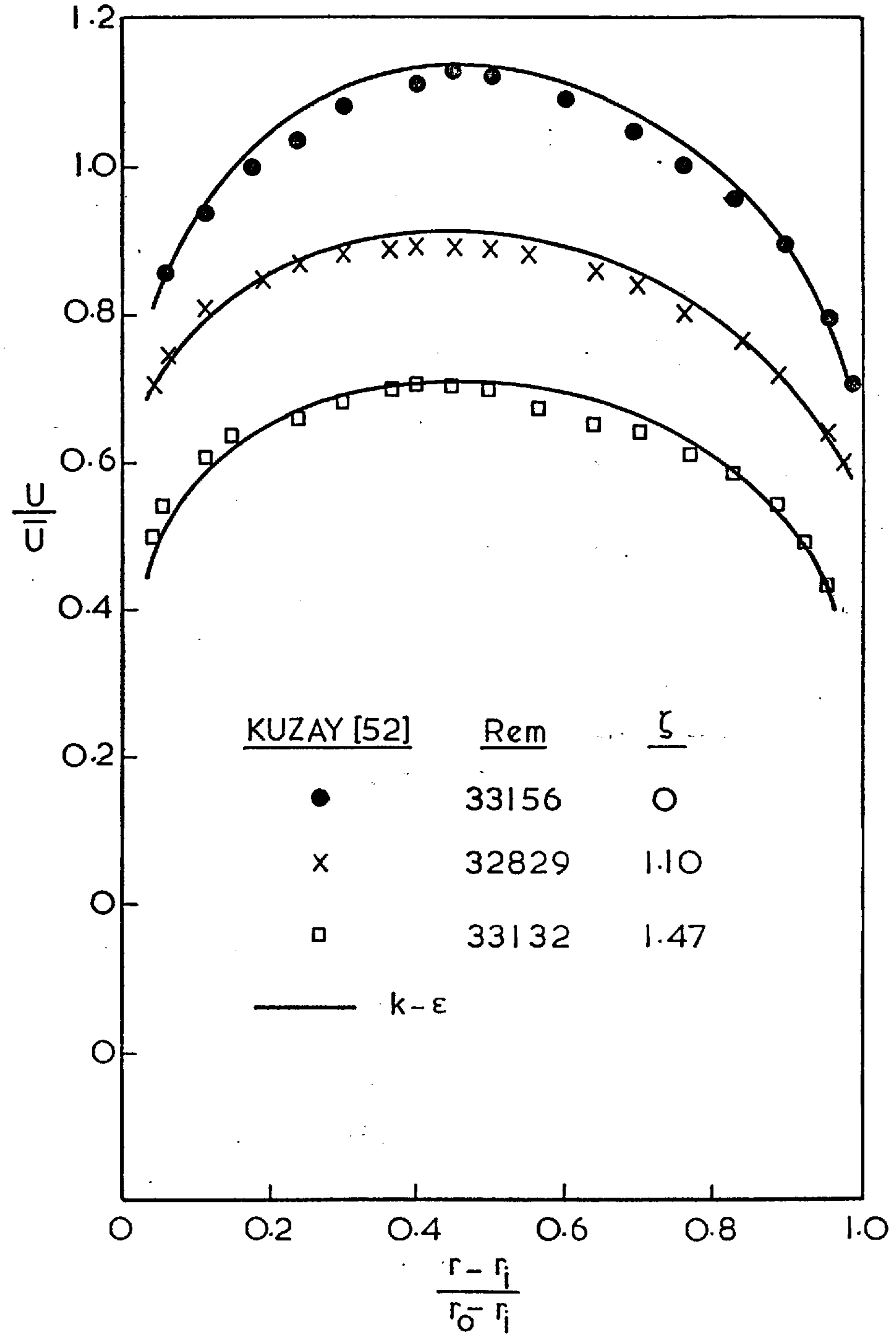

Fig. 18(b) AXIAL VELOCITY PROFILES IN AN ANNULUS WITH ROTATING CORE TUBE.

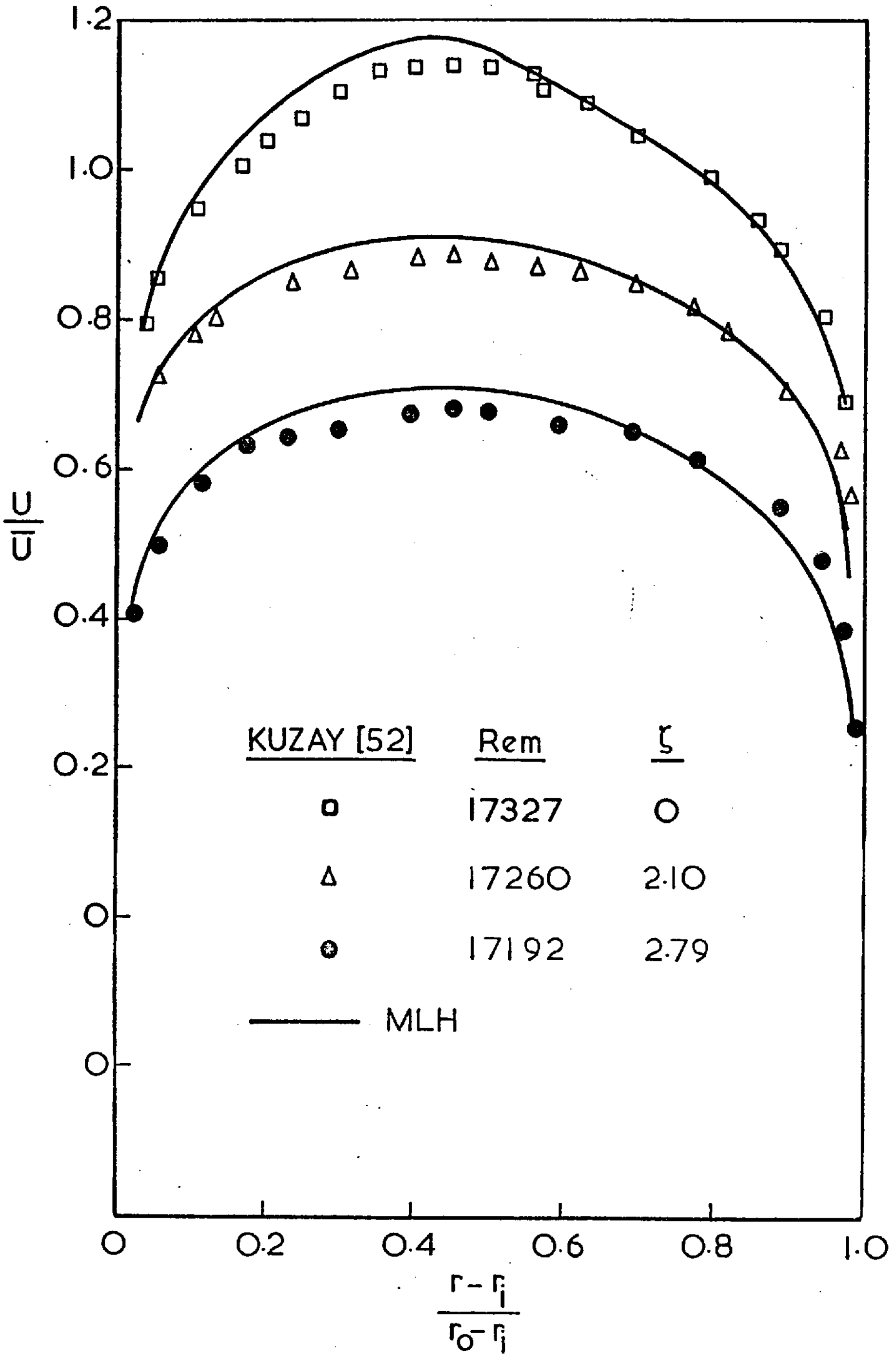

Fig. 19(a) AXIAL VELOCITY PROFILES IN AN ANNULUS WITH ROTATING CORE TUBE.

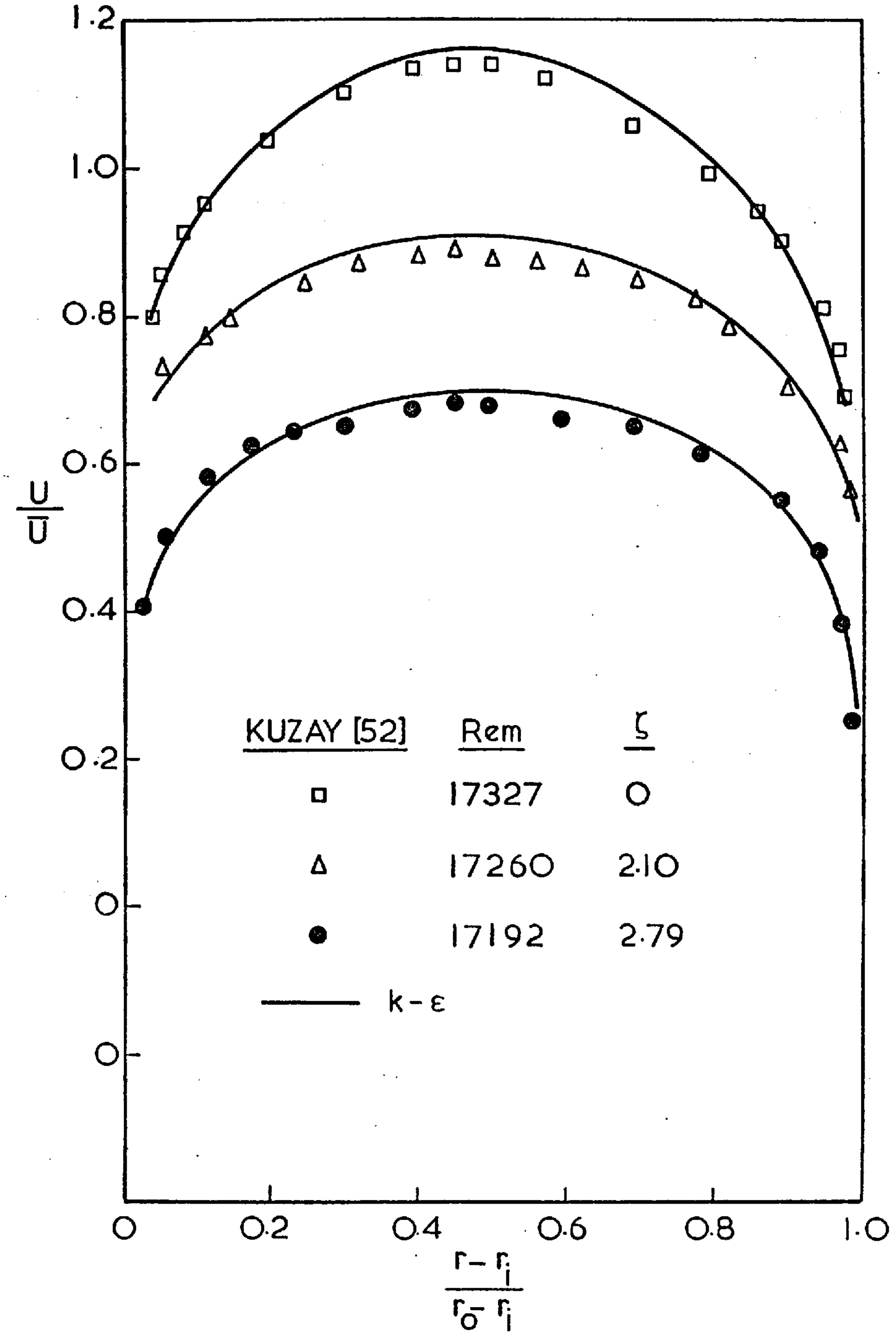

Fig. 19(b) AXIAL VELOCITY PROFILES IN AN ANNULUS WITH ROTATING CORE TUBE.

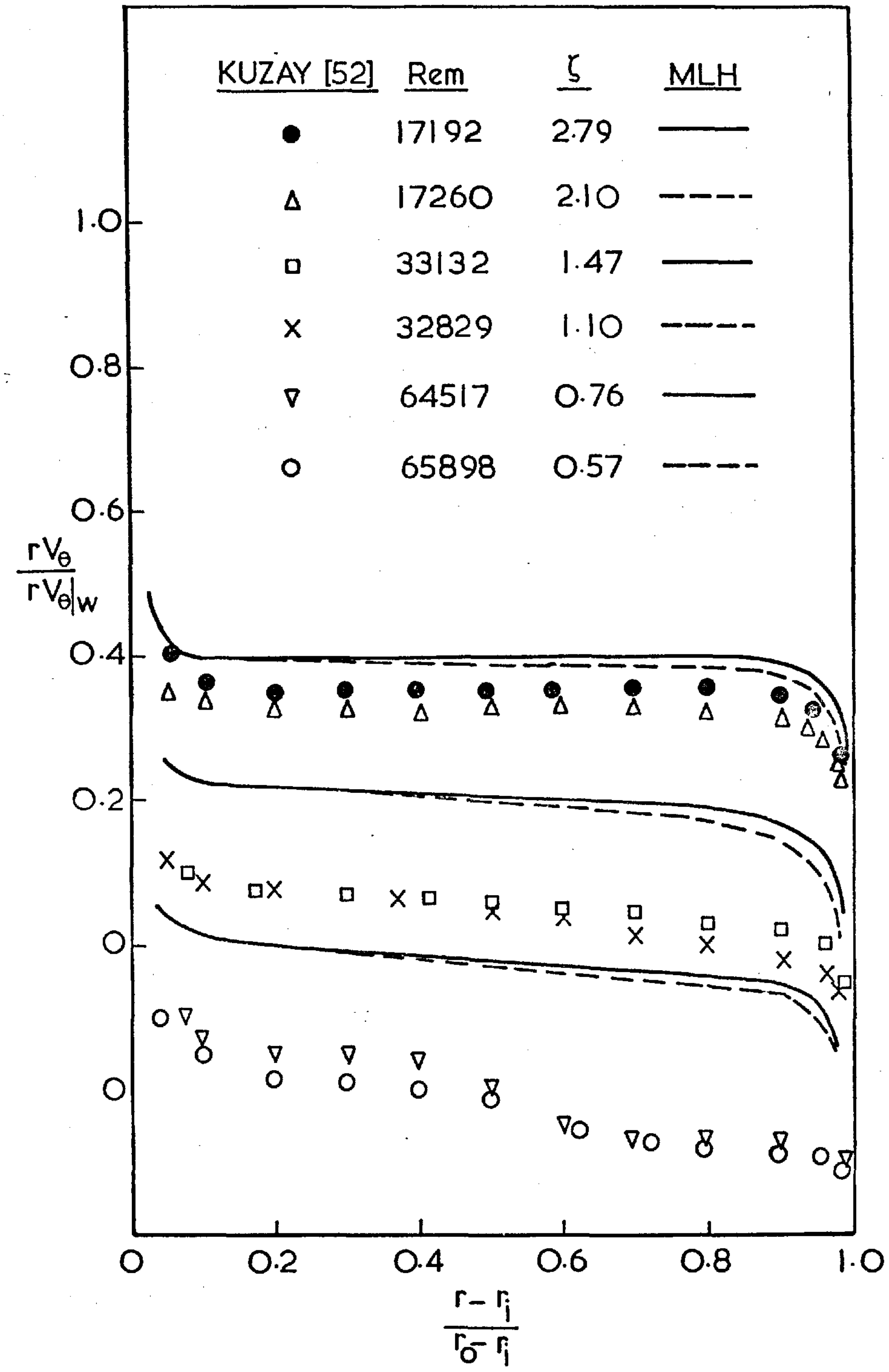

Fig. 20(a) ANGULAR MOMENTUM PROFILES IN AN ANNULUS WITH ROTATING CORE TUBE.

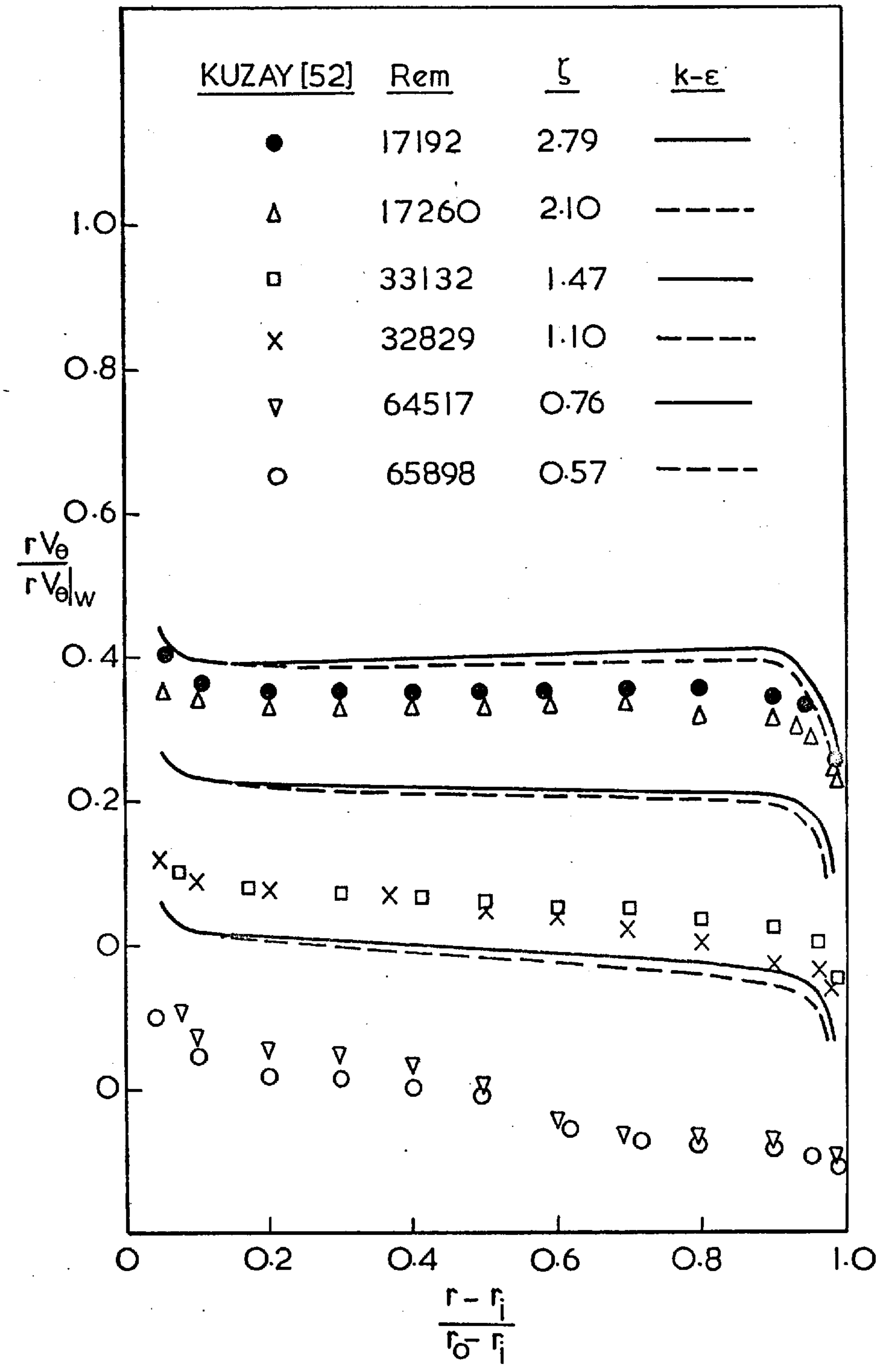

Fig. 20(b) ANGULAR MOMENTUM PROFILES IN AN ANNULUS WITH ROTATING CORE TUBE.

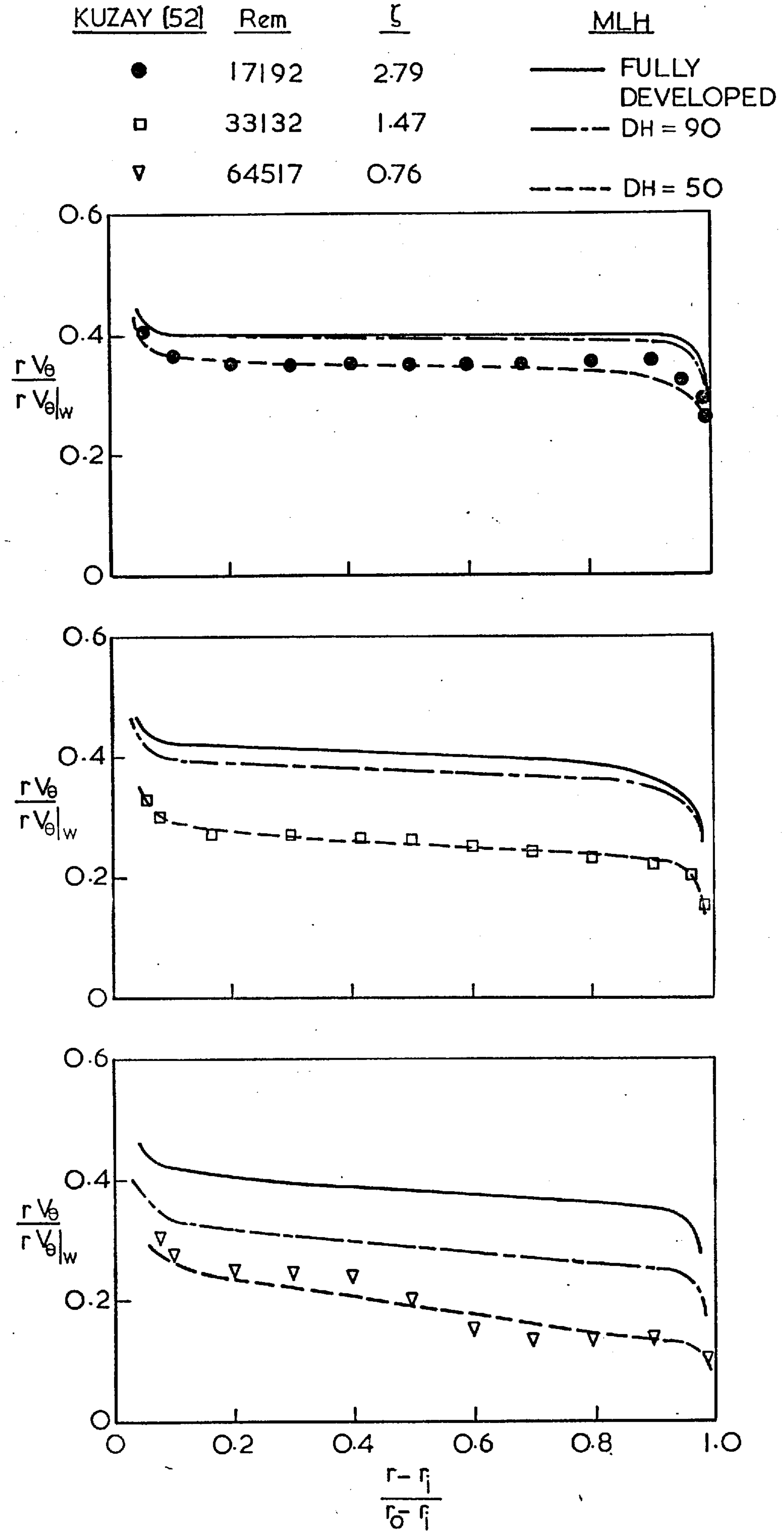

Fig. 21(a) ANGULAR MOMENTUM PROFILES IN AN ANNULUS WITH ROTATING CORE TUBE.

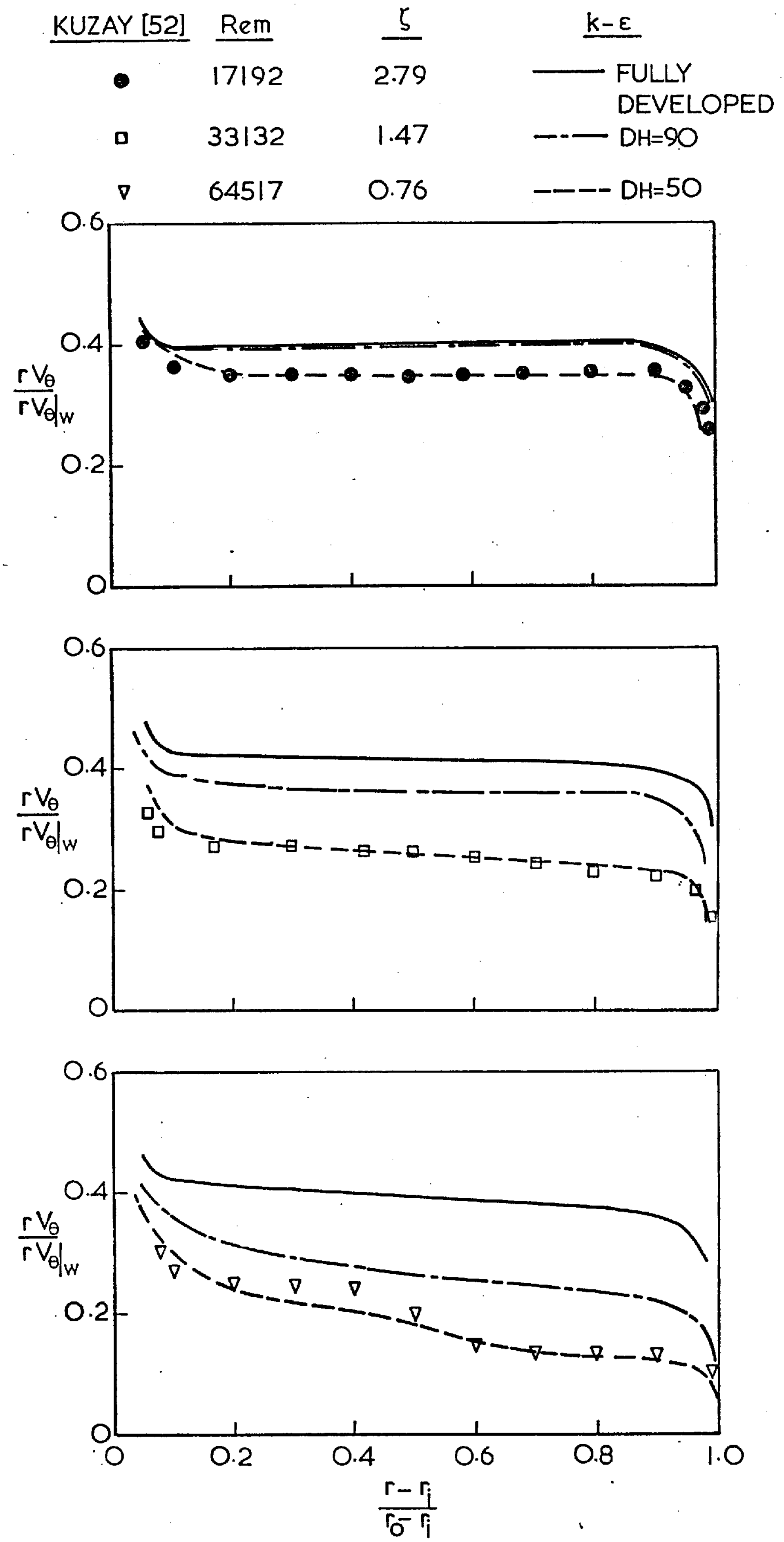

Fig. 21(b) ANGULAR MOMENTUM PROFILES IN AN ANNULUS WITH ROTATING CORE TUBE.

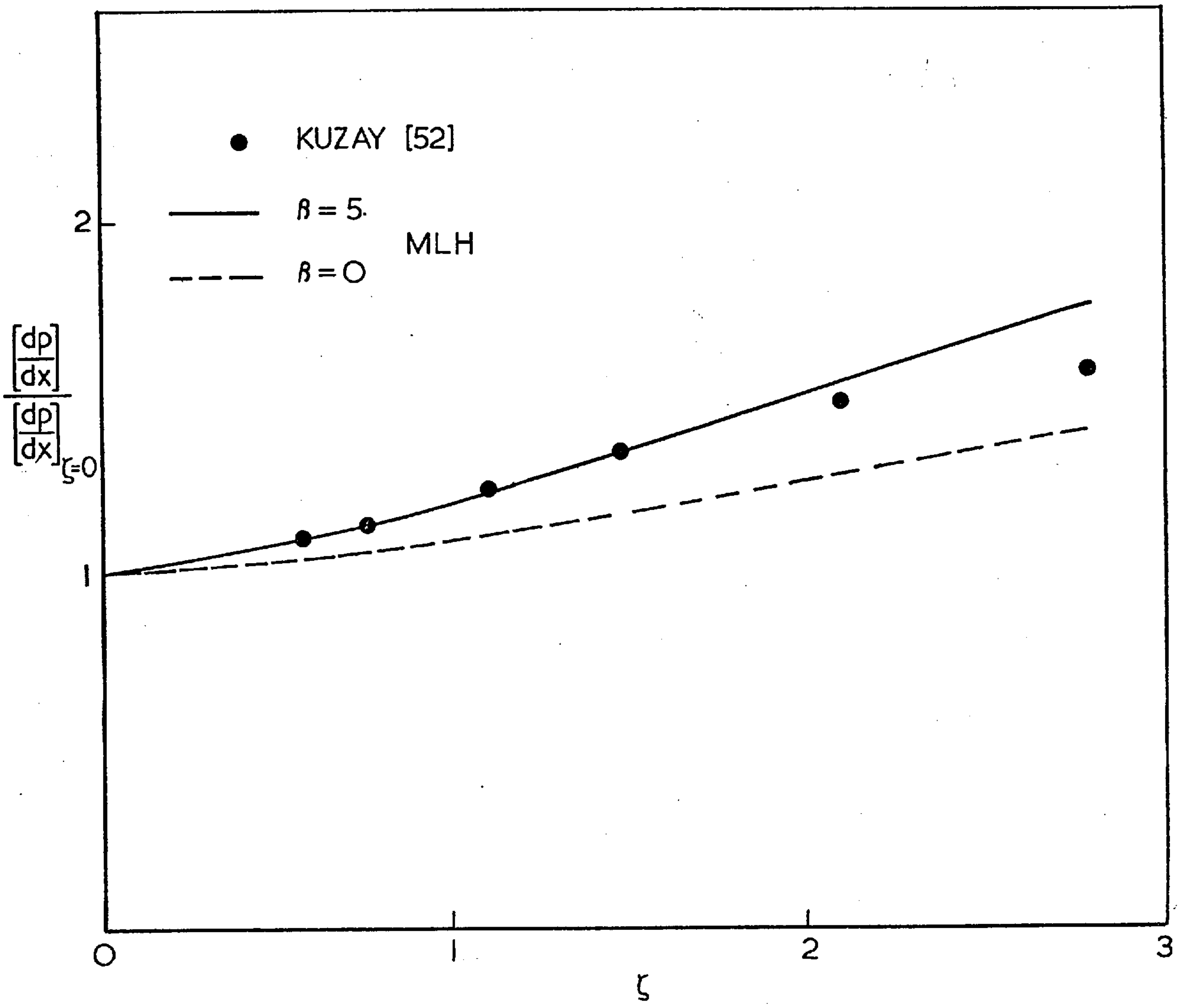

Fig. 22(a) EFFECT OF SWIRL ON THE AXIAL PRESSURE GRADIENT.

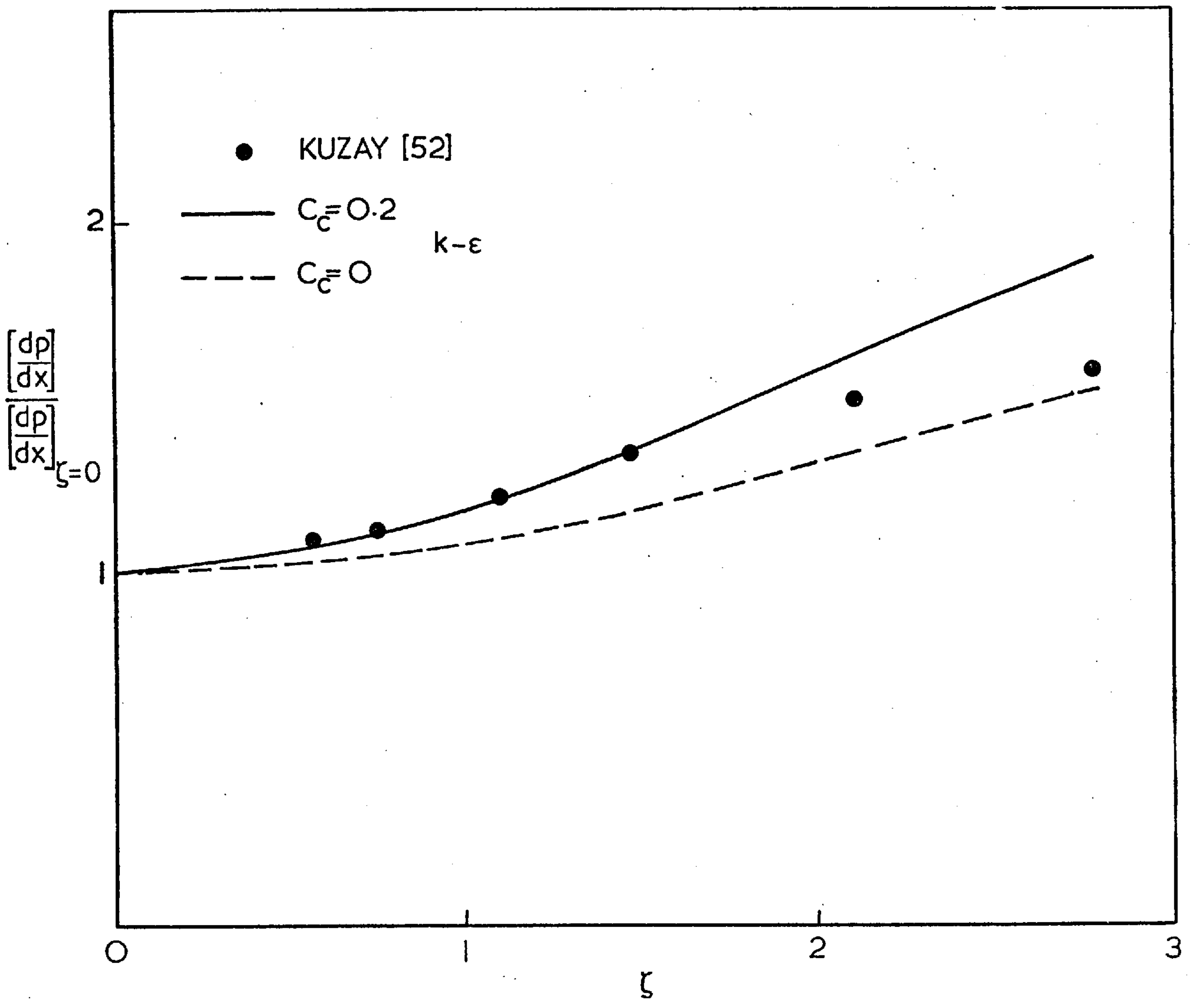

Fig. 22(b) EFFECT OF SWIRL ON THE AXIAL PRESSURE GRADIENT.

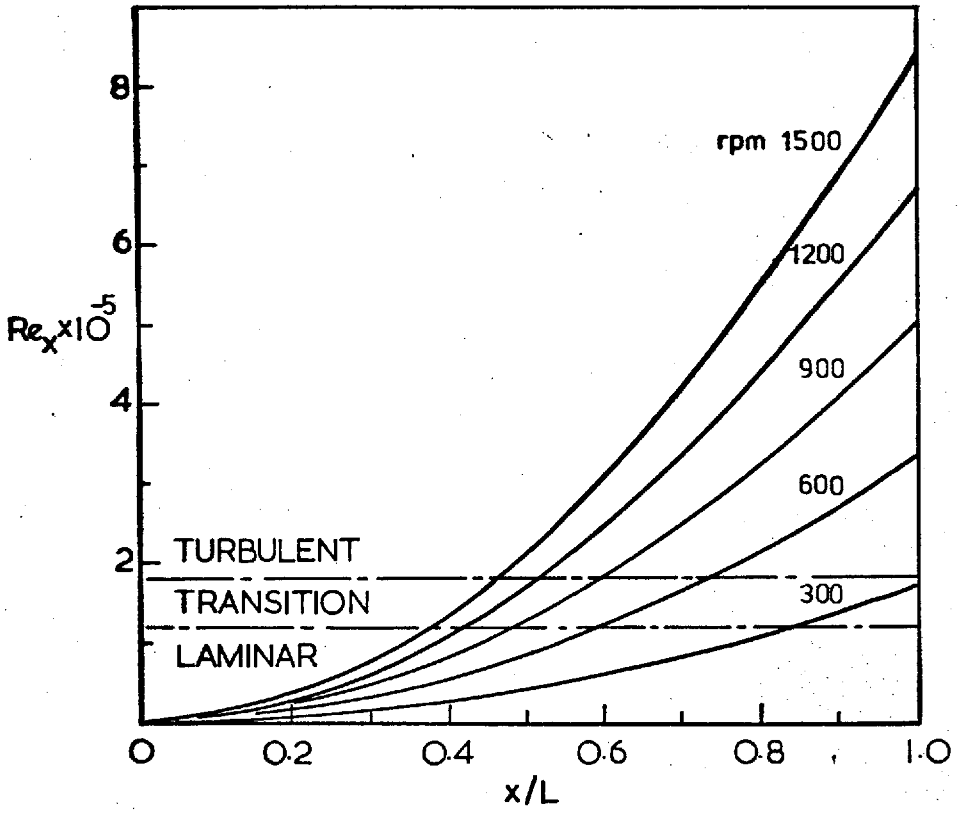

Fig. 23 FLOW REGIMES AND REYNOLDS NUMBERS ATTAINABLE WITH THE APPARATUS.

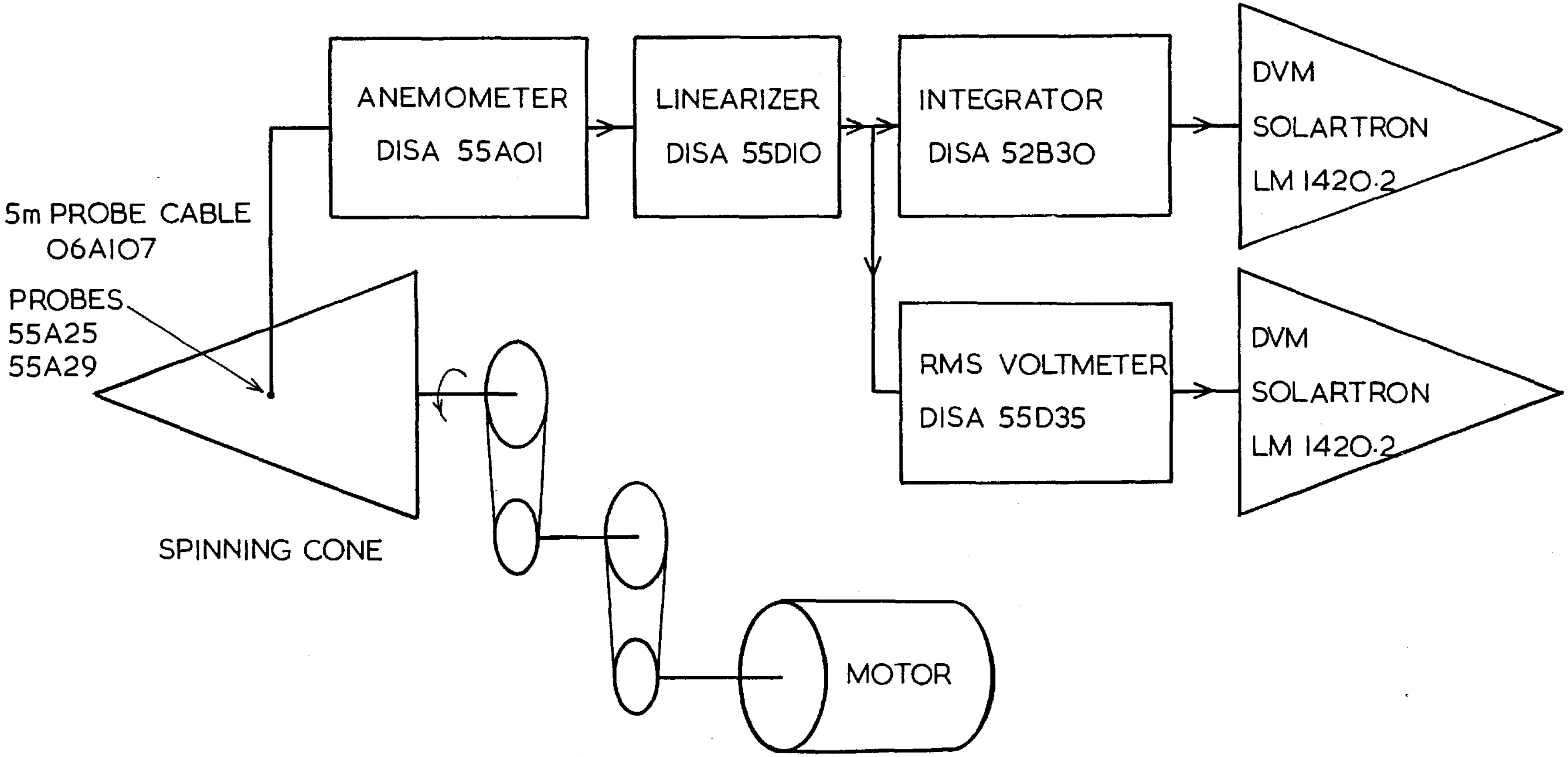

Fig. 24 SCHEMATIC LINE DIAGRAM OF CONE-PULLEY ARRANGEMENT AND HOT WIRE SIGNAL PROCESSING EQUIPMENT.

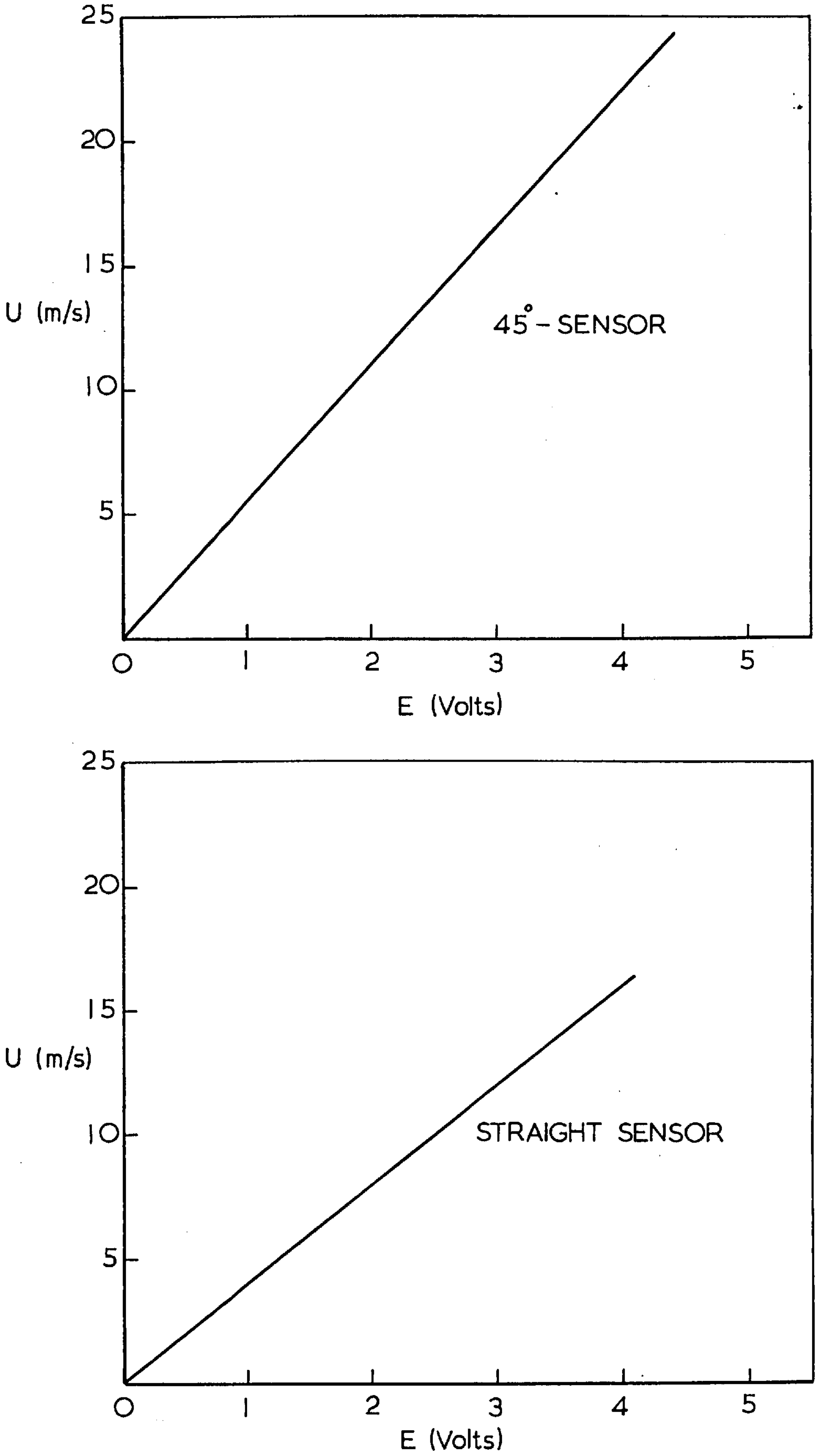

Fig. 25 SAMPLE LINEARISED PLOTS OF U Vs. E.

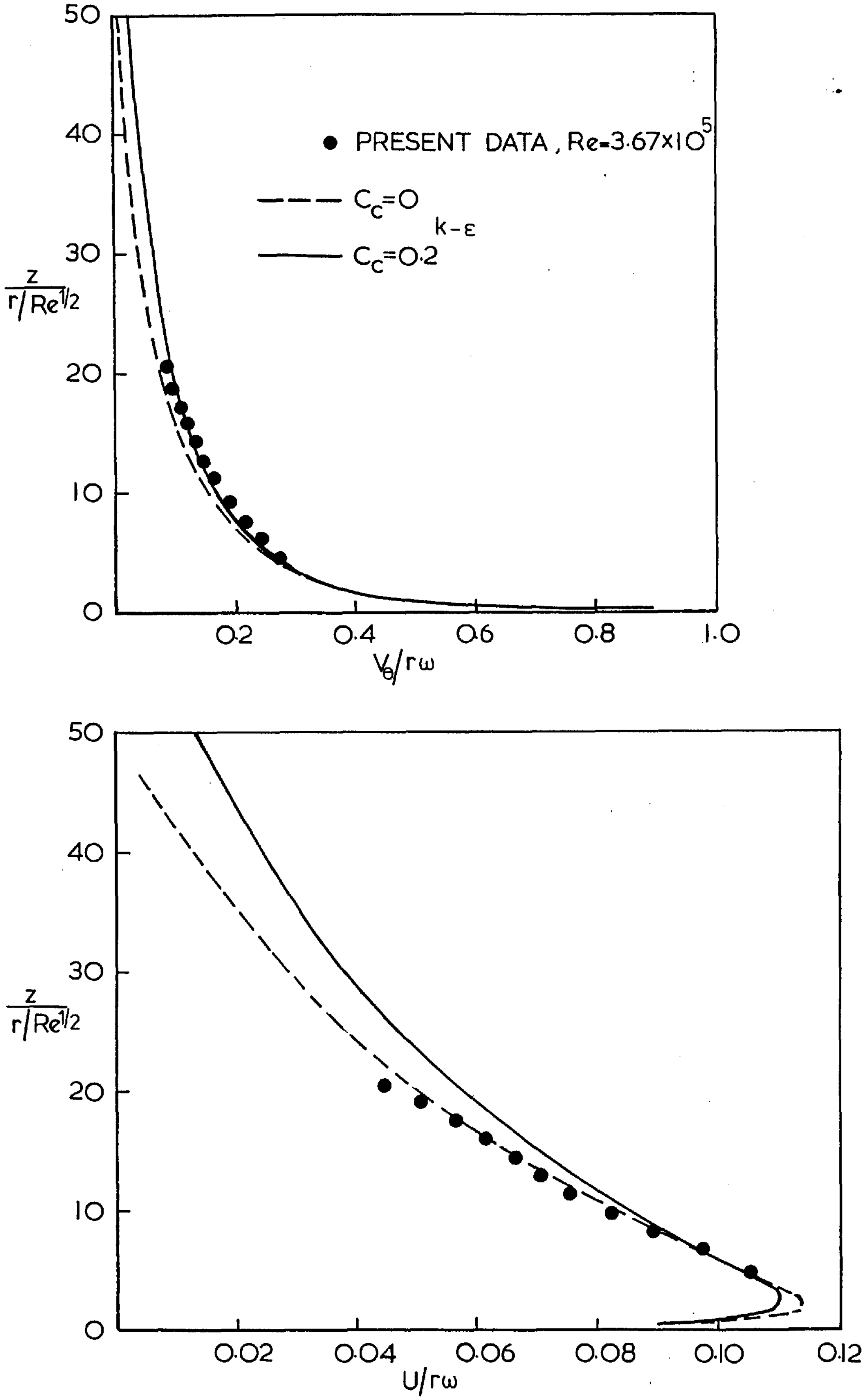

Fig. 26 VELOCITY PROFILES NEAR AN 80° SPINNING CONE, $\omega = 893$ rpm.

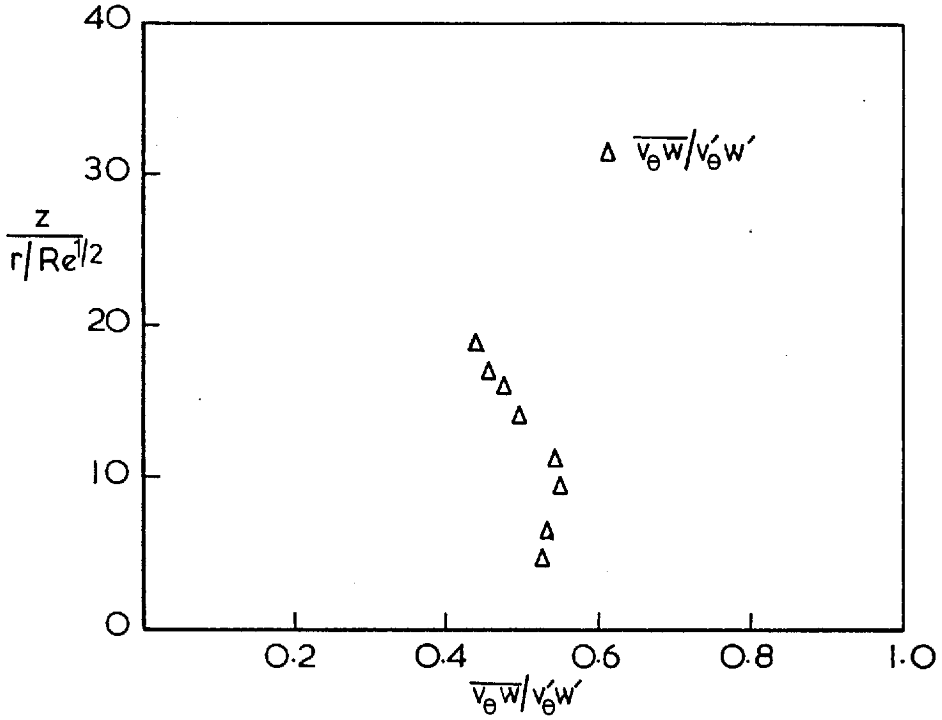

Fig. 27 COEFFICIENT OF CORRELATION ACROSS THE LAYER.

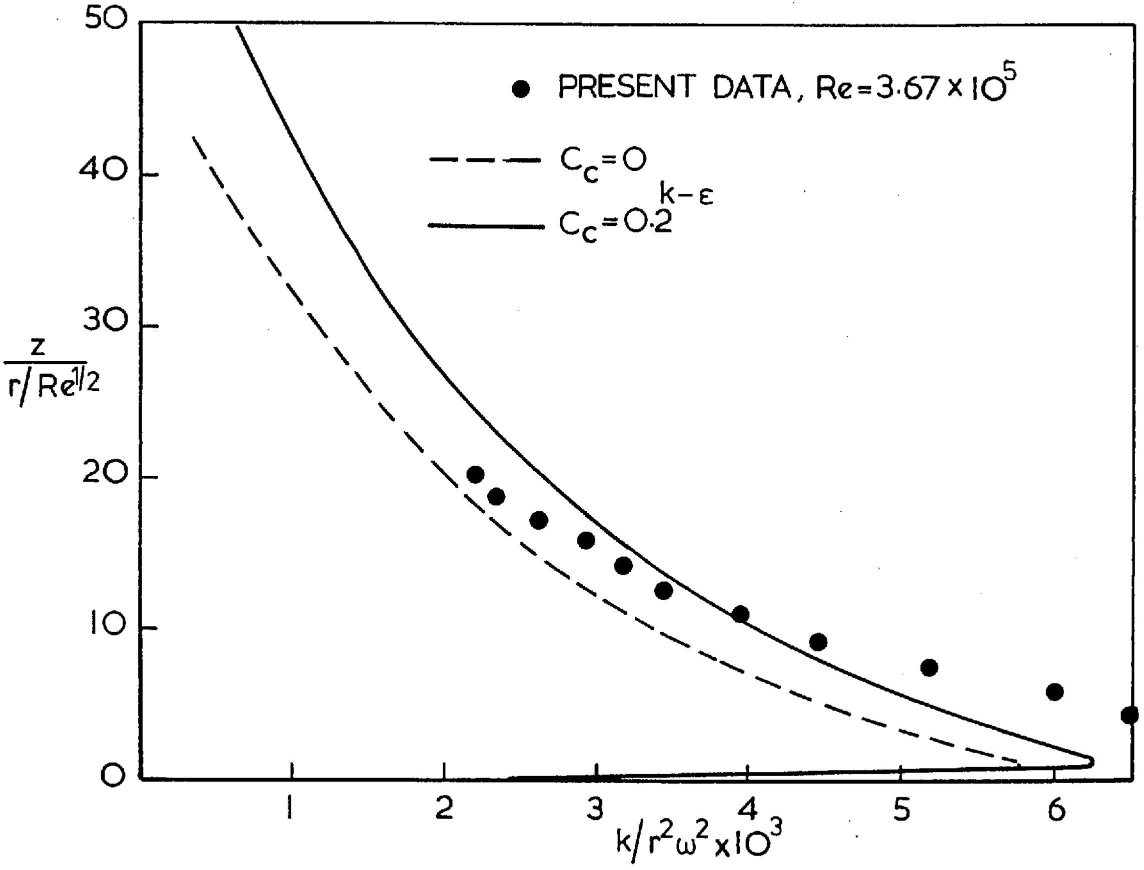

Fig. 28 TURBULENCE ENERGY PROFILES NEAR AN 80° SPINNING CONE.

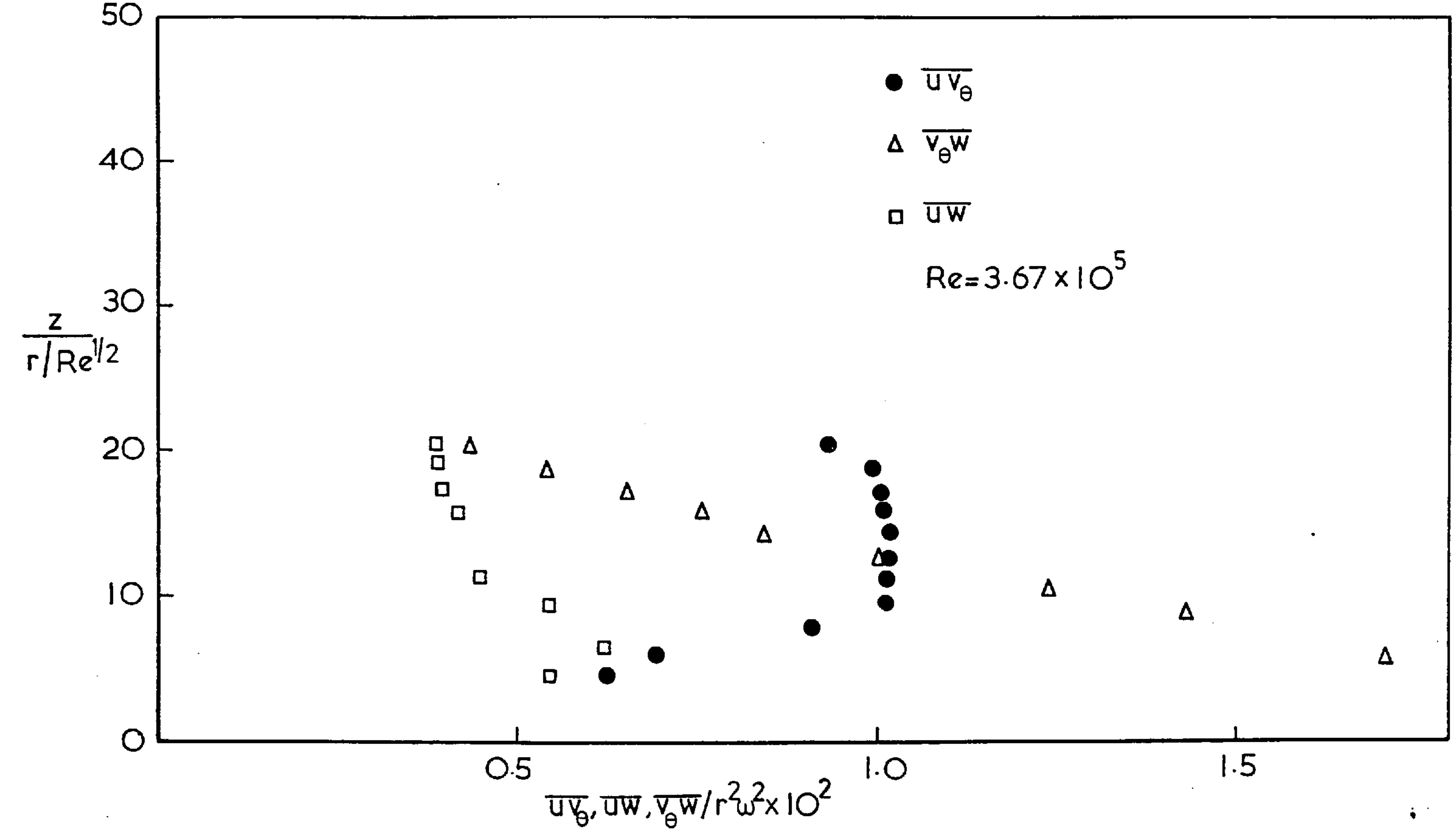

Fig. 29 SHEAR STRESS PROFILES NEAR AN 80° SPINNING CONE.

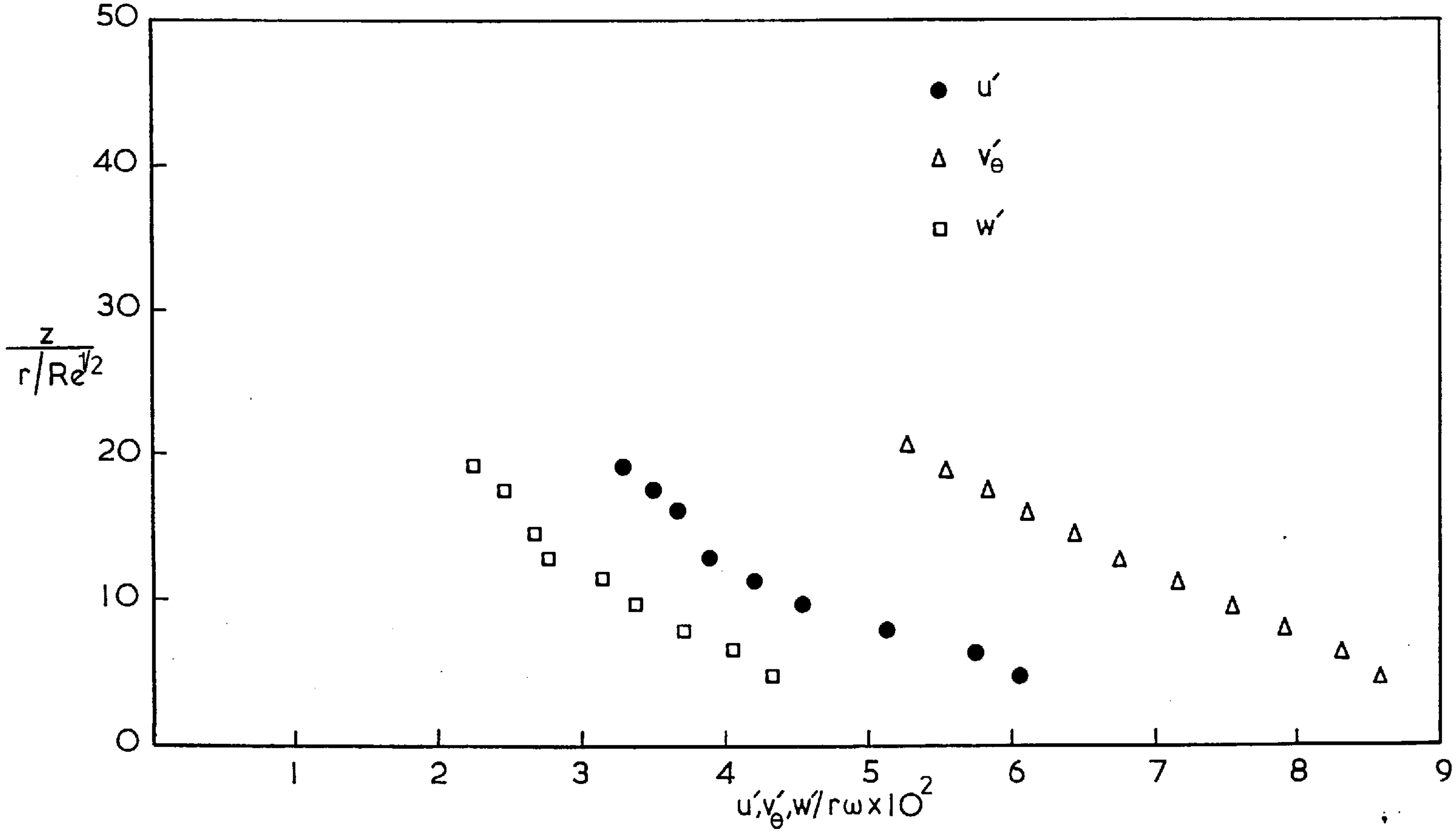

Fig. 30 RELATIVE TURBULENCE INTENSITY PROFILES NEAR AN 80° SPINNING CONE.

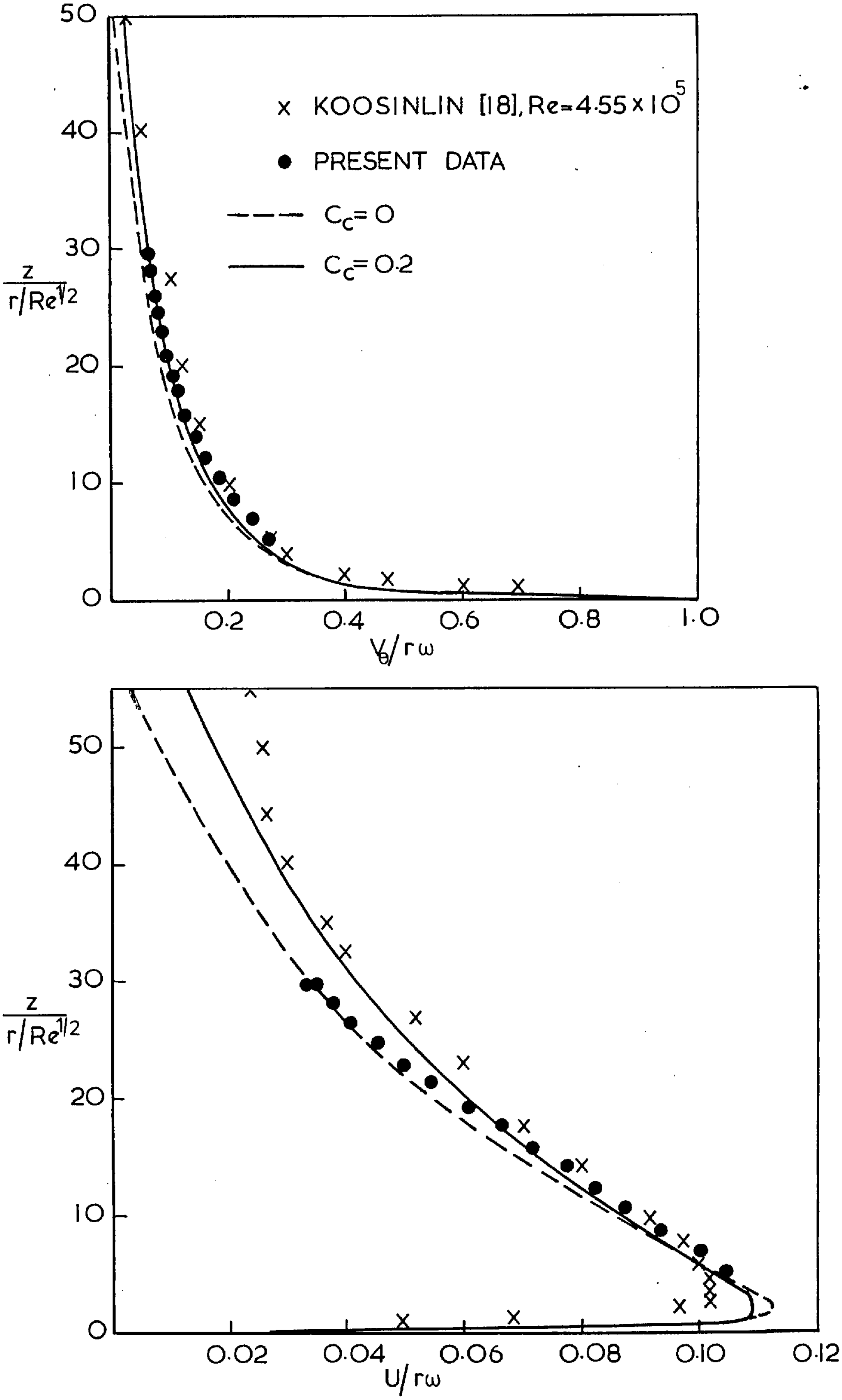

Fig. 31 VELOCITY PROFILES NEAR AN 80° SPINNING CONE, ω = 1111 rpm.

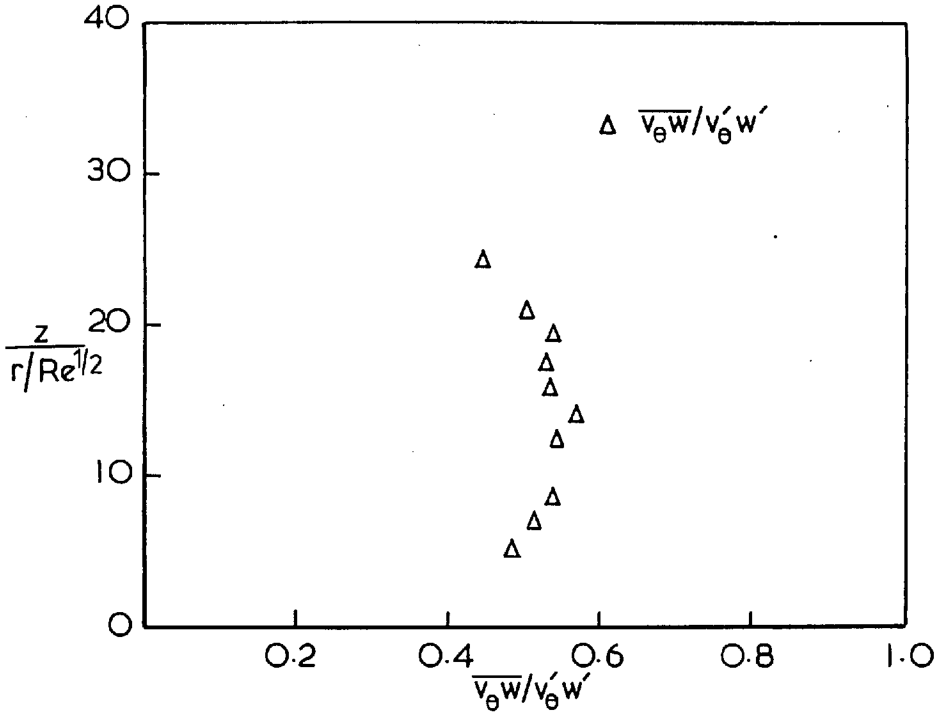

Fig. 32 COEFFICIENT OF CORRELATION ACROSS THE LAYER.

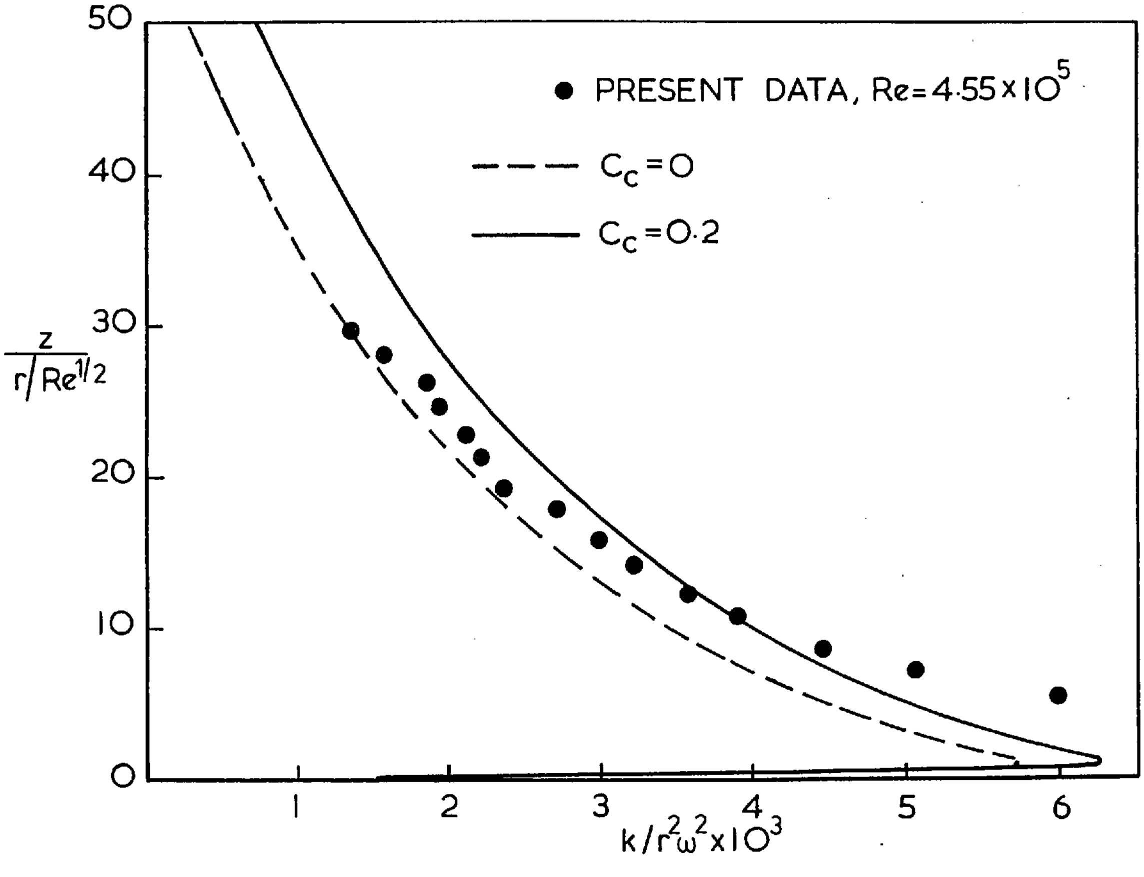

Fig. 33 TURBULENCE ENERGY PROFILES NEAR AN 80° SPINNING CONE.

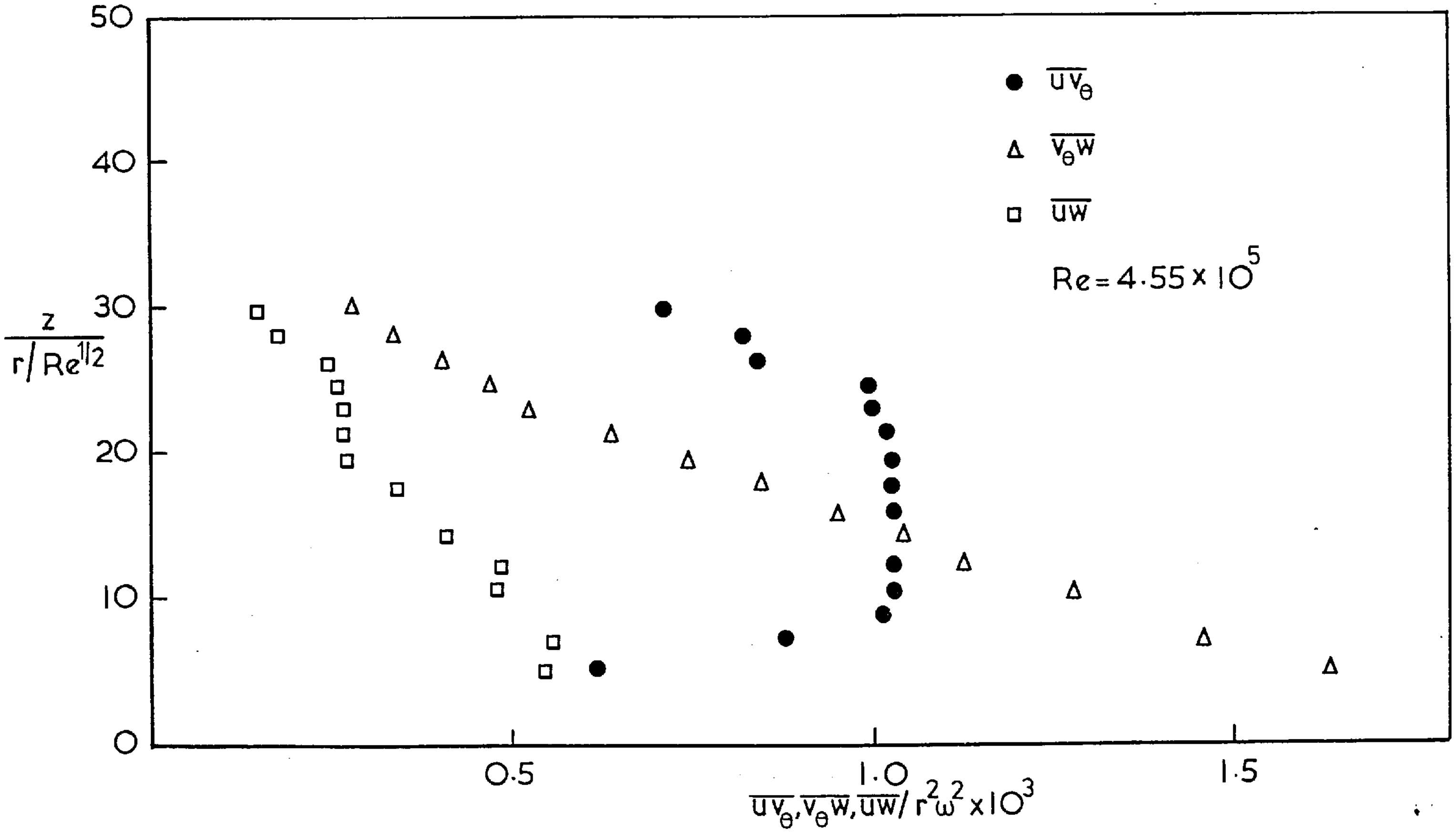

Fig. 34 SHEAR STRESS PROFILES NEAR AN 80° SPINNING CONE.

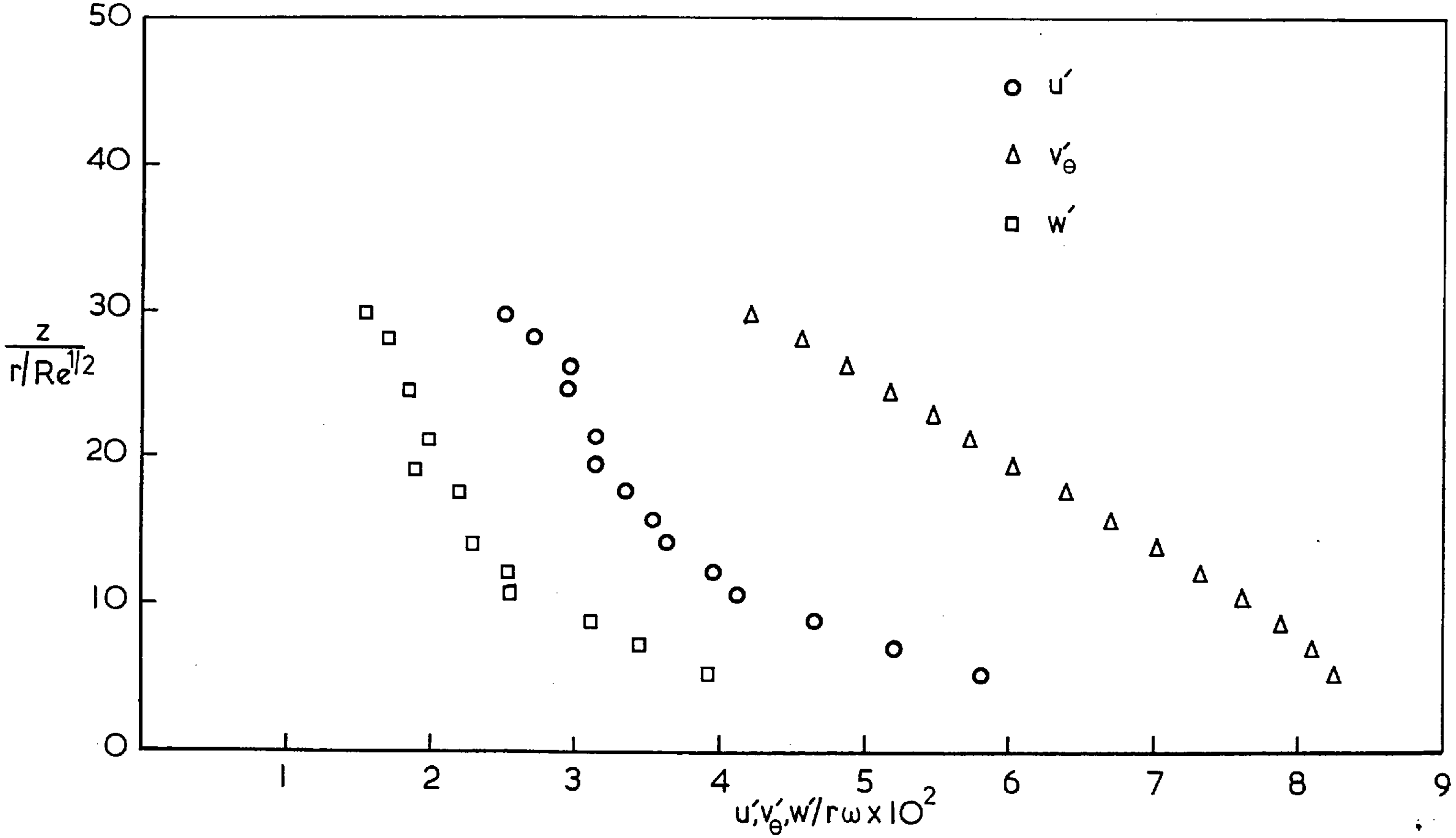

Fig. 35 RELATIVE TURBULENCE INTENSITY PROFILES NEAR AN 80° SPINNING CONE.

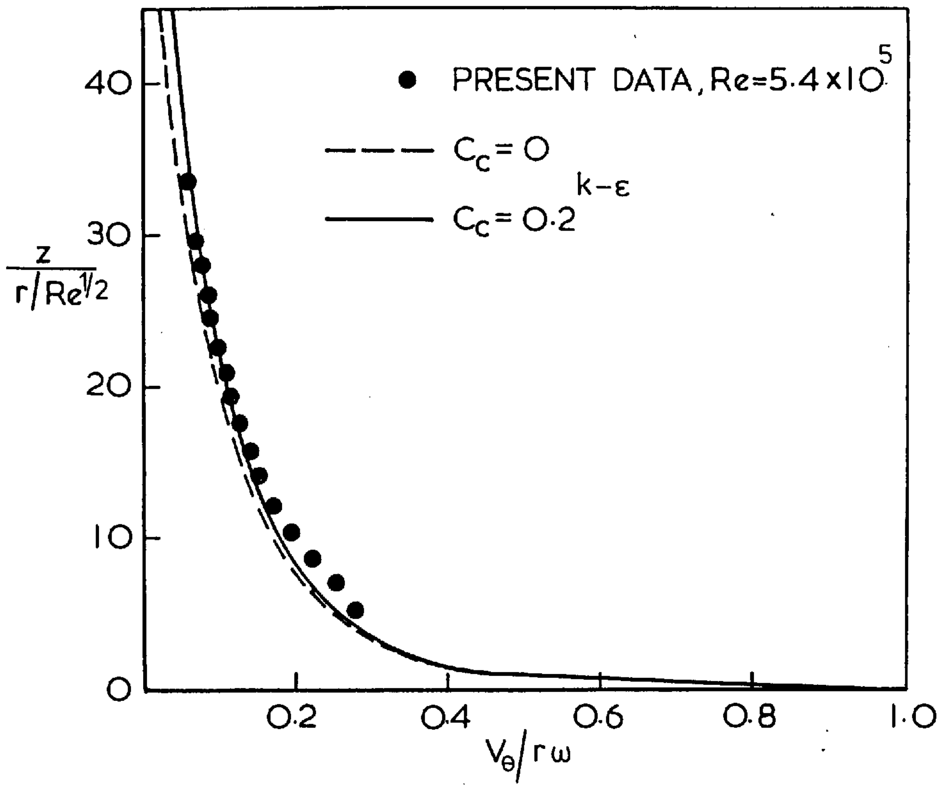

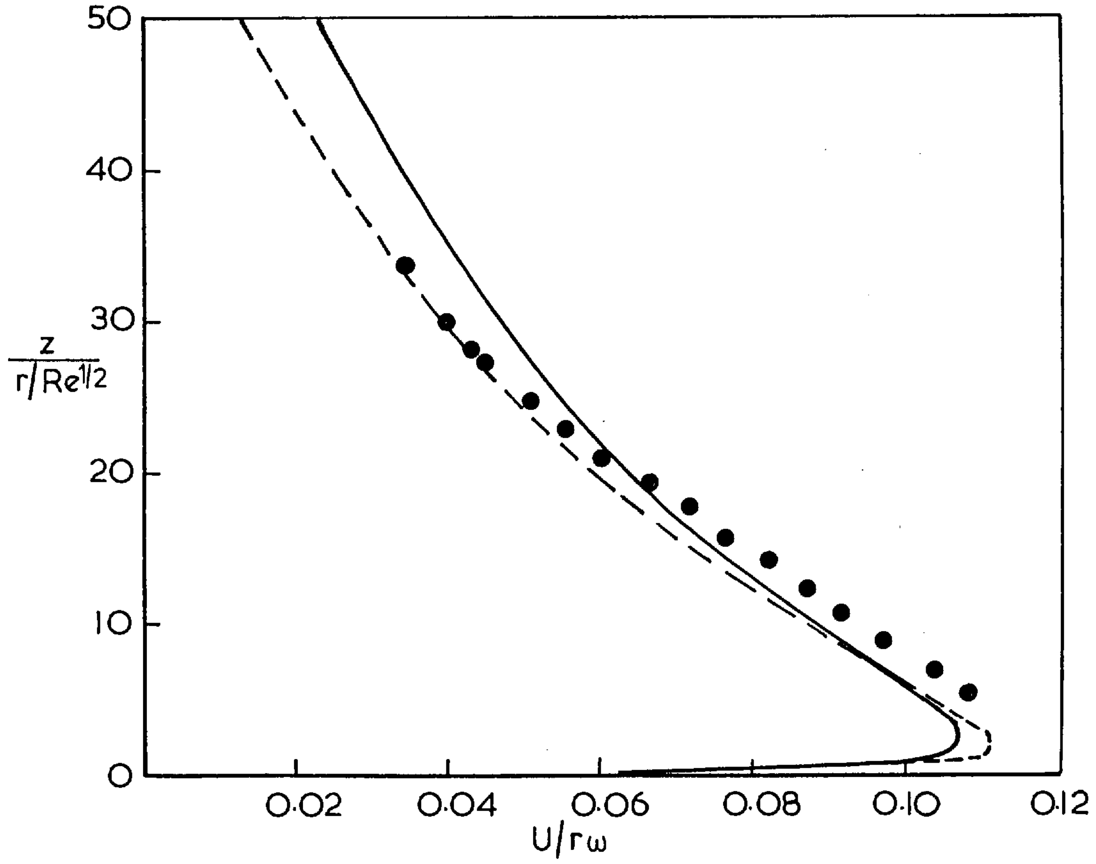

Fig. 36 VELOCITY PROFILES NEAR AN 80° SPINNING CONE, ω=1111 rpm.

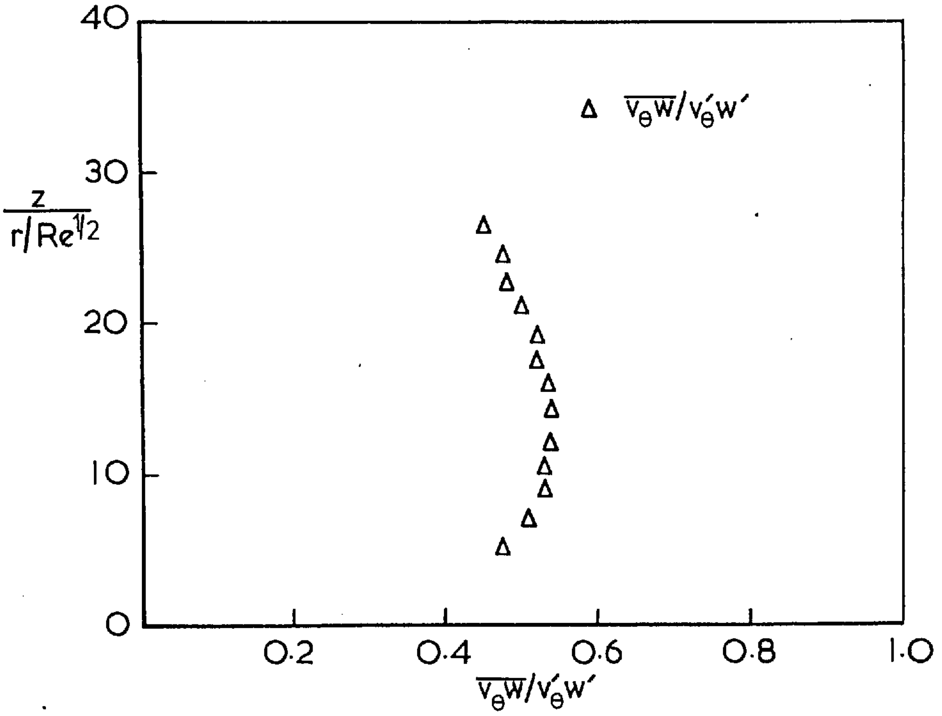

Fig. 37 COEFFICIENT OF CORRELATION ACROSS THE LAYER.

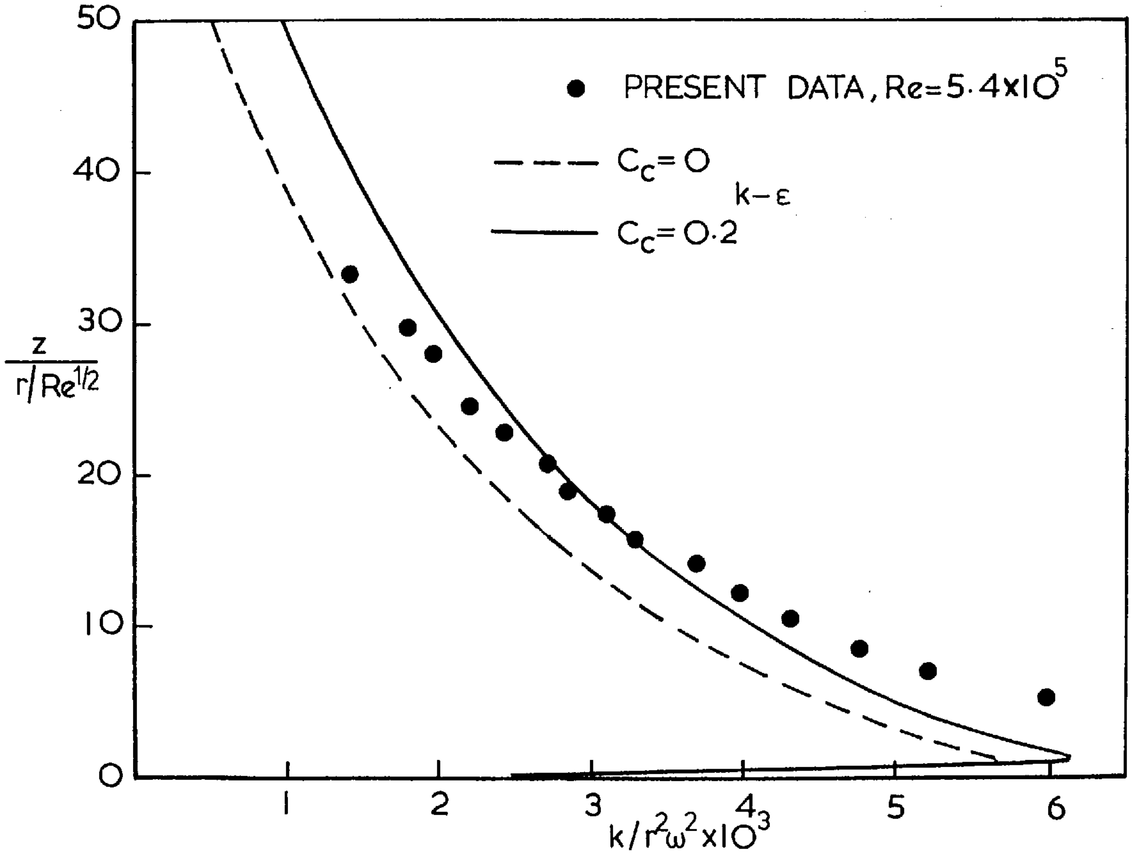

Fig. 38 TURBULENCE ENERGY PROFILES NEAR AN 80° SPINNING CONE.

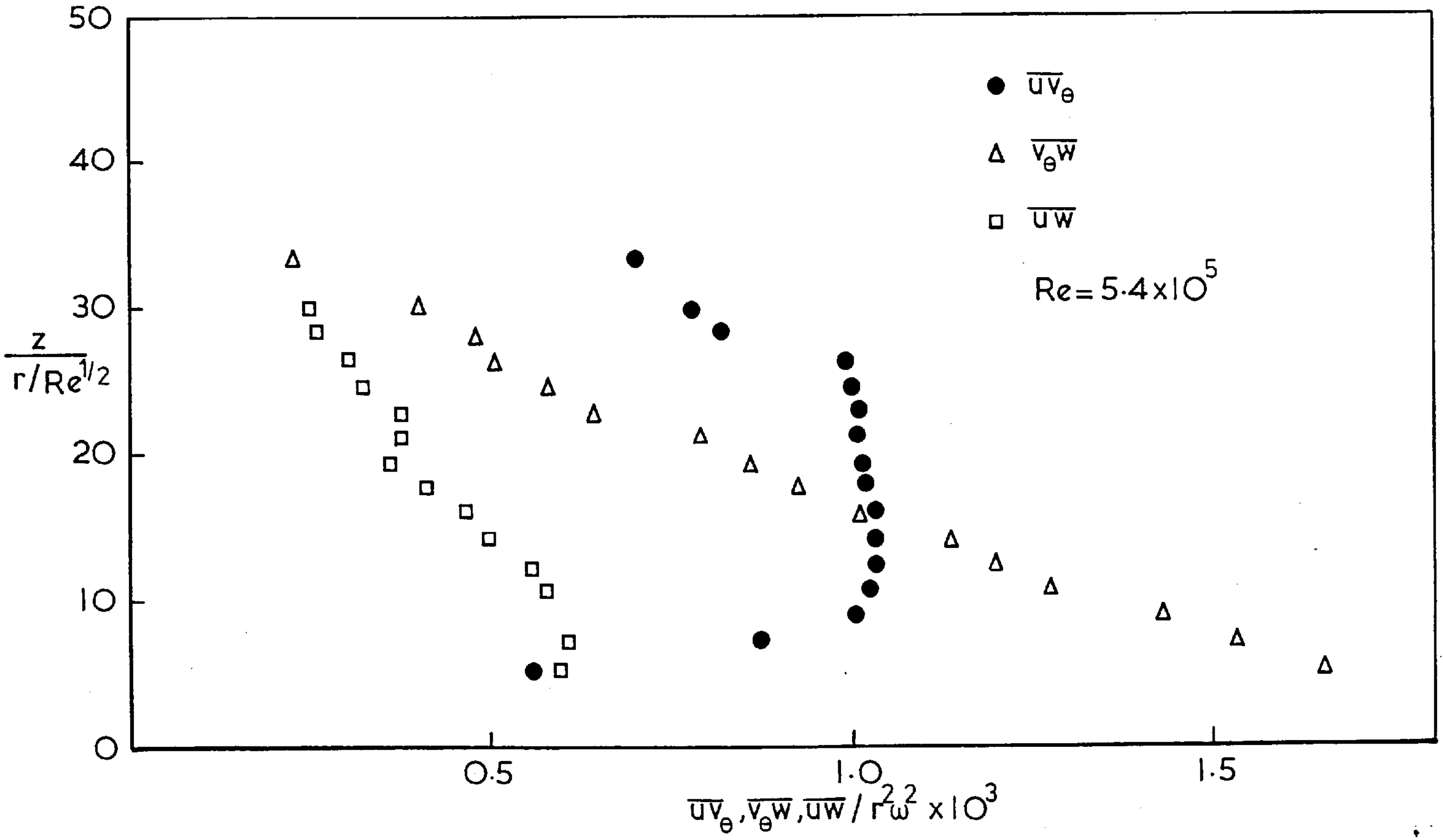

Fig. 39 SHEAR STRESS PROFILES NEAR AN 80° SPINNING CONE.

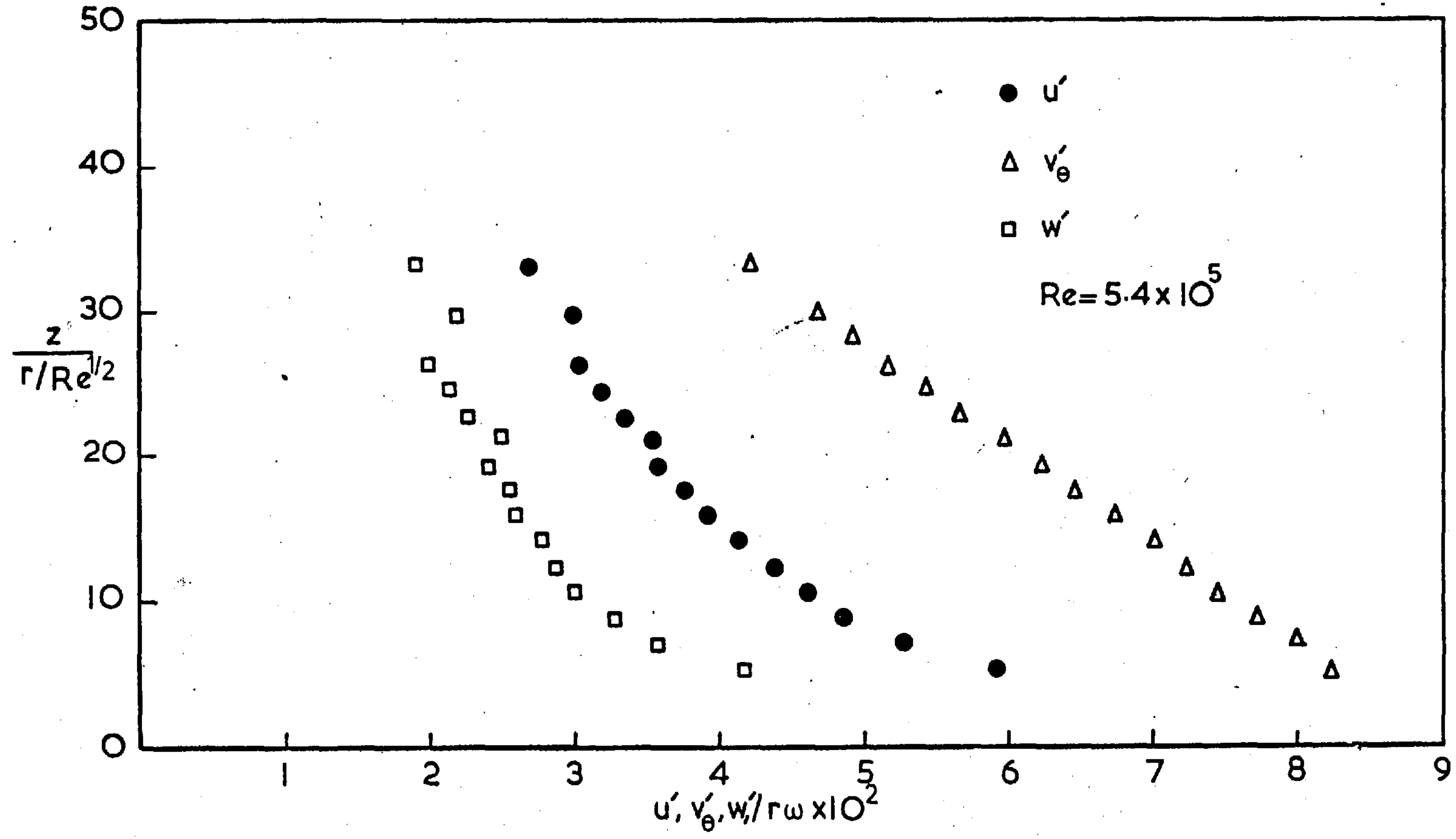

Fig. 40 RELATIVE TURBULENCE INTENSITY PROFILES NEAR AN 80° SPINNING CONE.

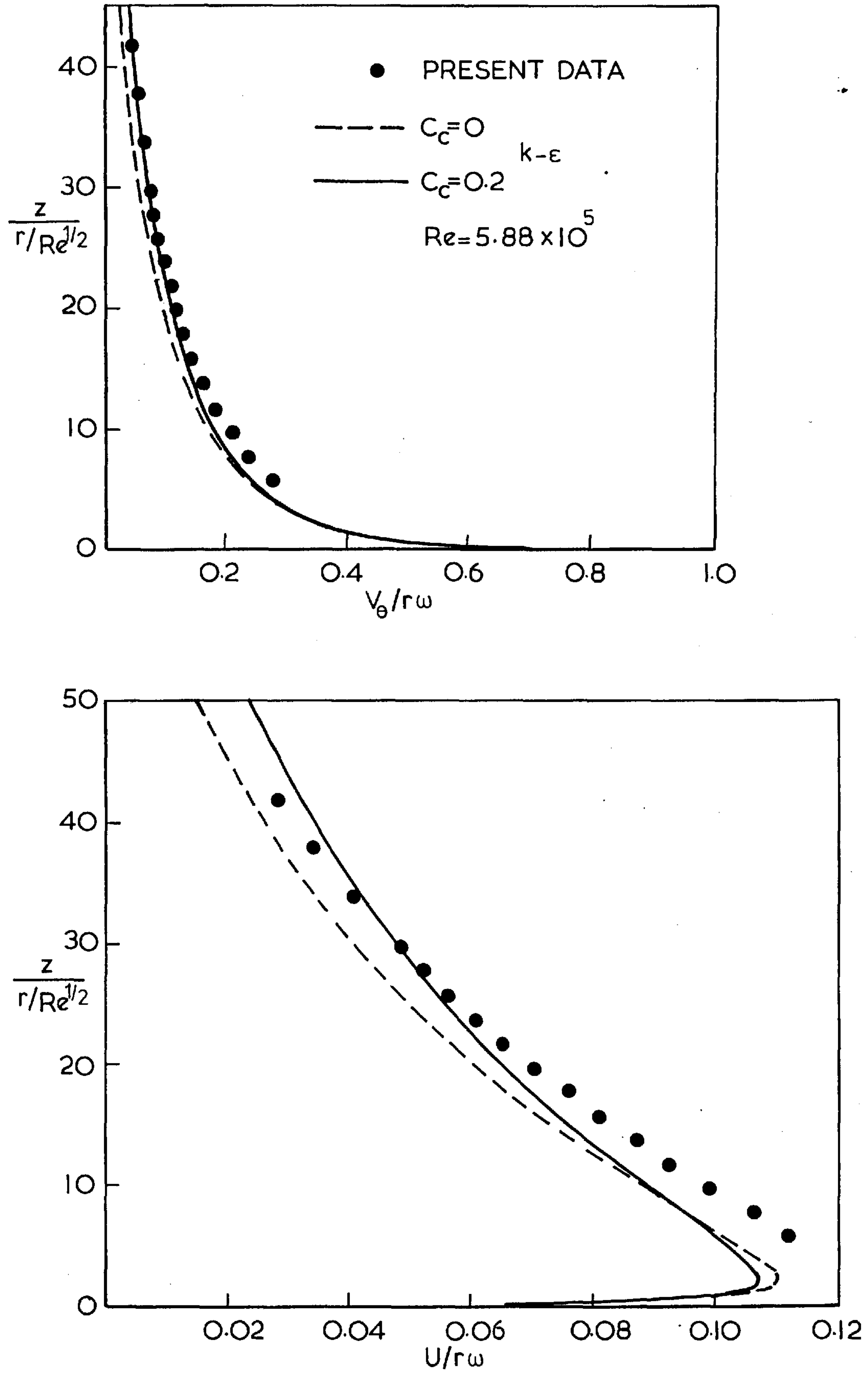

Fig. 41 VELOCITY PROFILES NEAR AN 80° SPINNING CONE. $\omega=1429$ rpm.

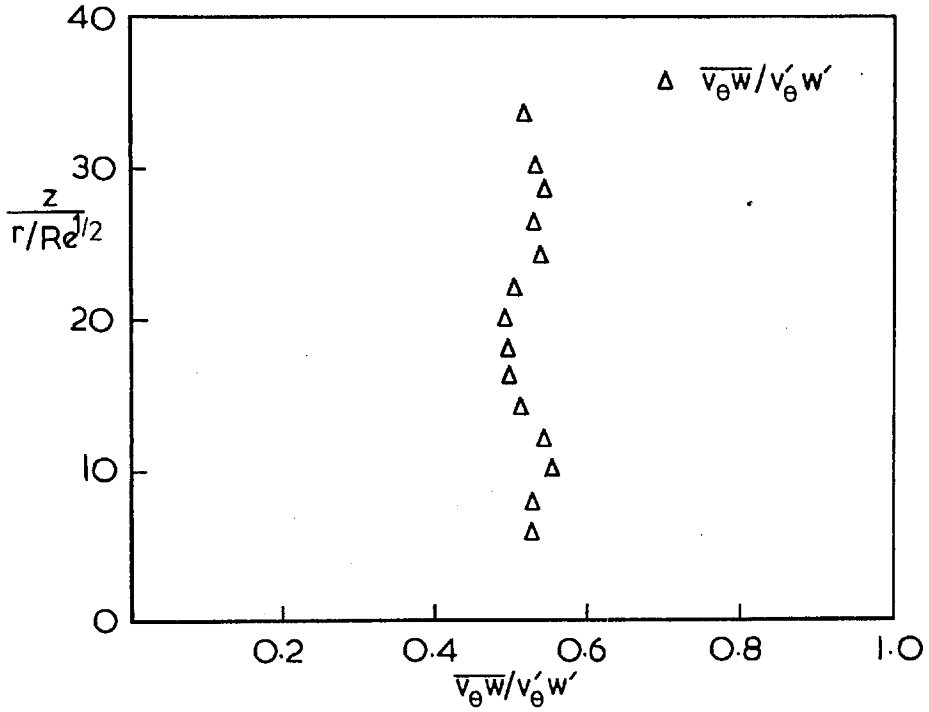

Fig. 42 COEFFICIENT OF CORRELATION ACROSS THE LAYER.

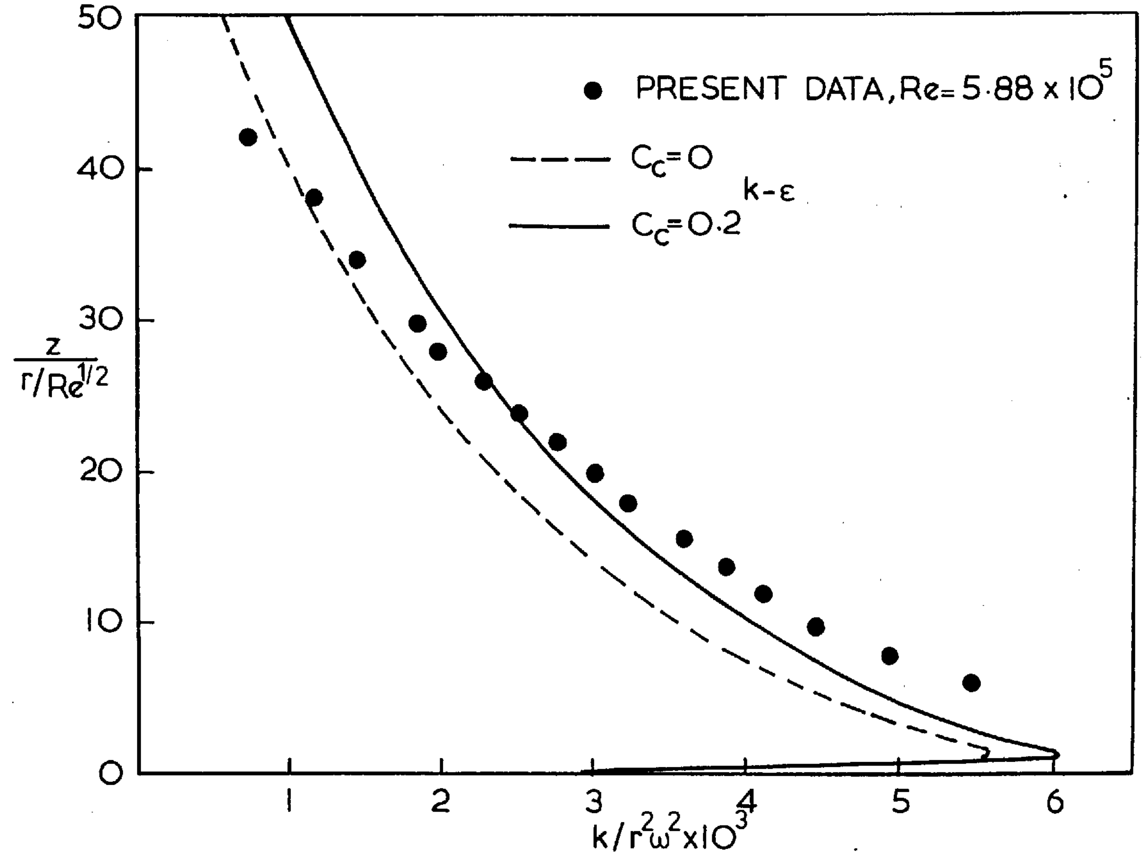

Fig. 43 TURBULANCE ENERGY PROFILES NEAR AN 80° SPINNING CONE.

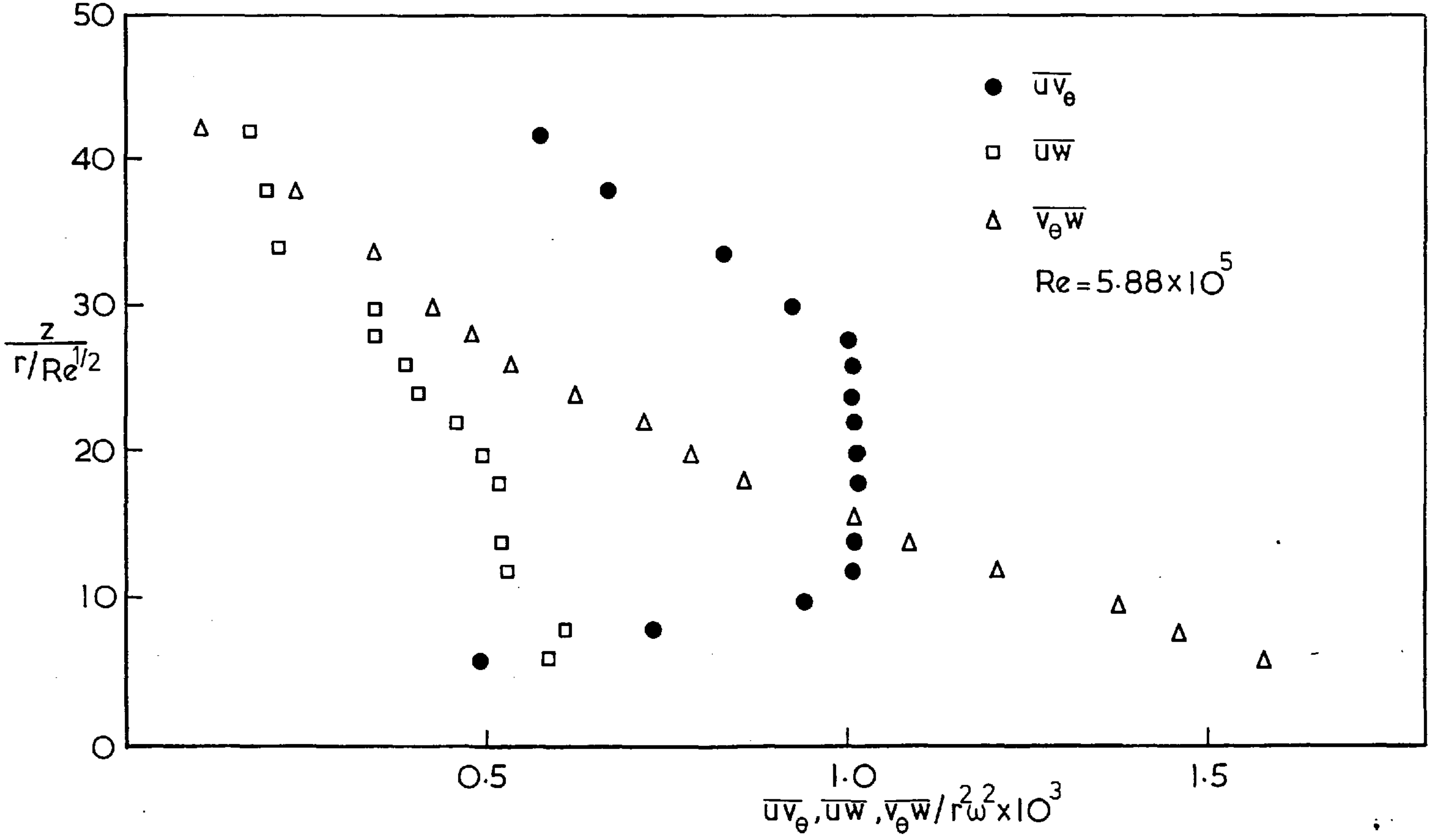

Fig.44 SHEAR STRESS PROFILES NEAR AN 80° SPINNING CONE.

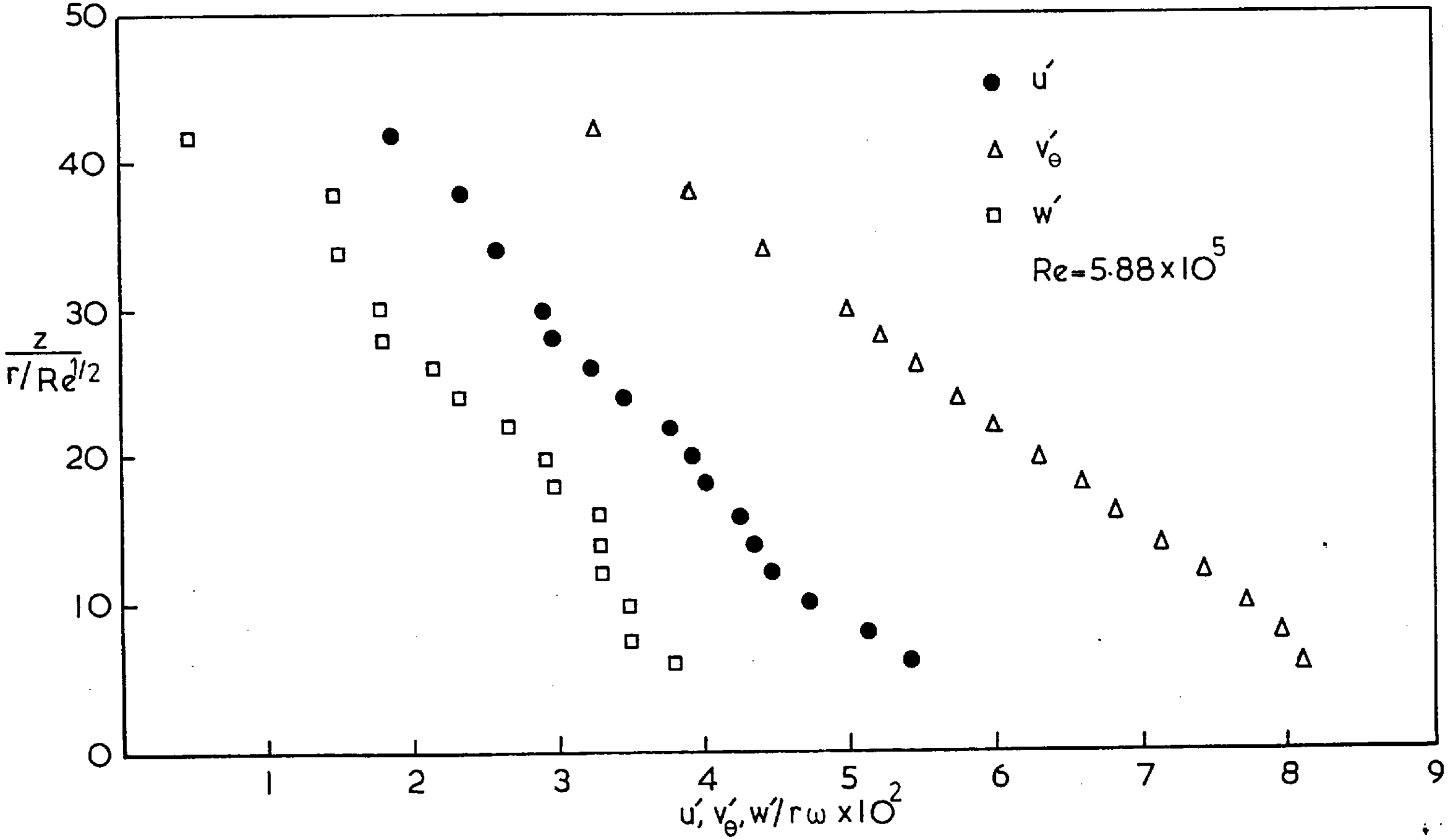

Fig. 45 RELATIVE TURBULENCE INTENSITY PROFILES NEAR AN 80° SPINNING CONE.

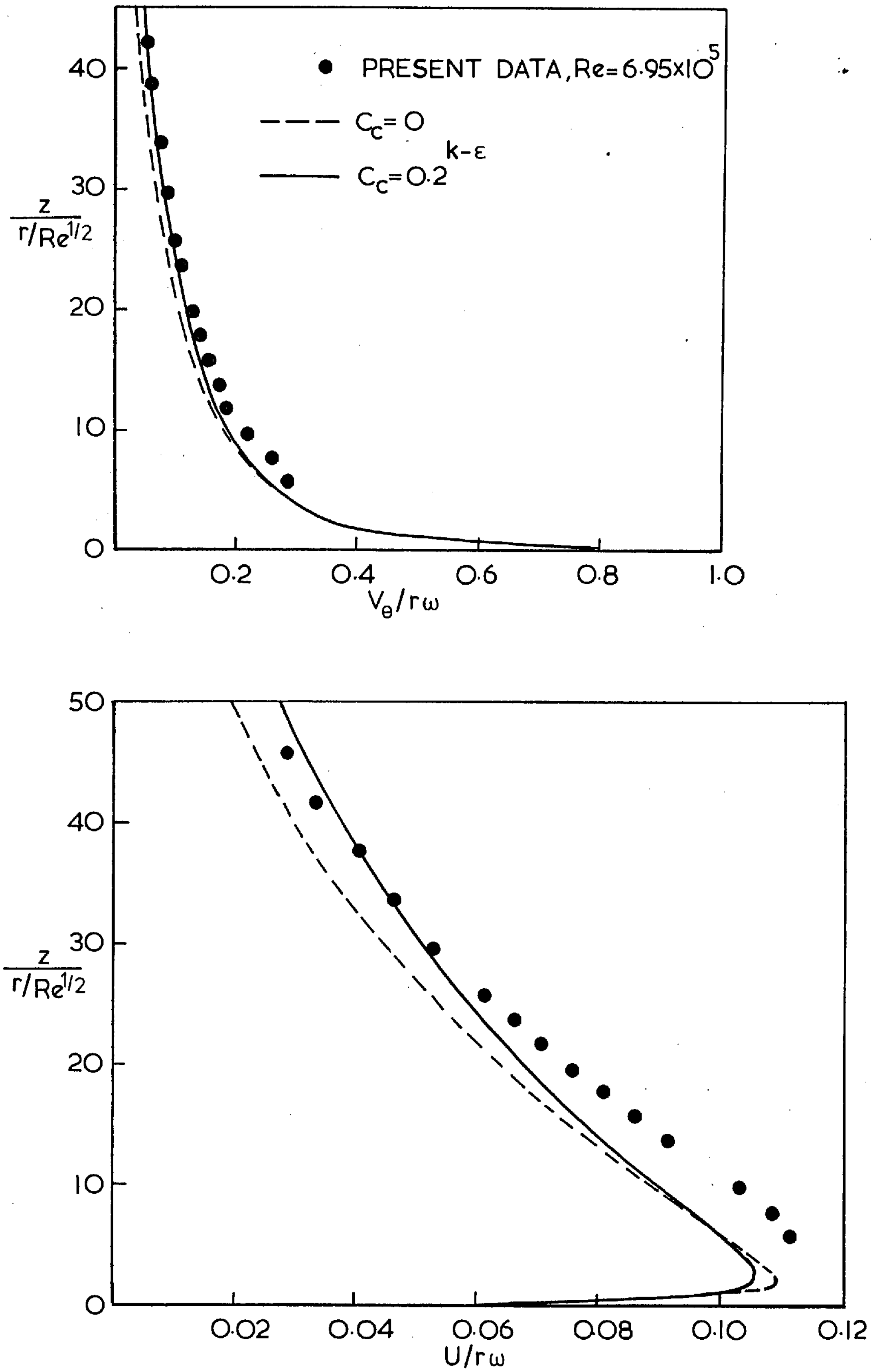

Fig.46 VELOCITY PROFILES NEAR AN 80° SPINNING CONE. ω=1428 rpm.

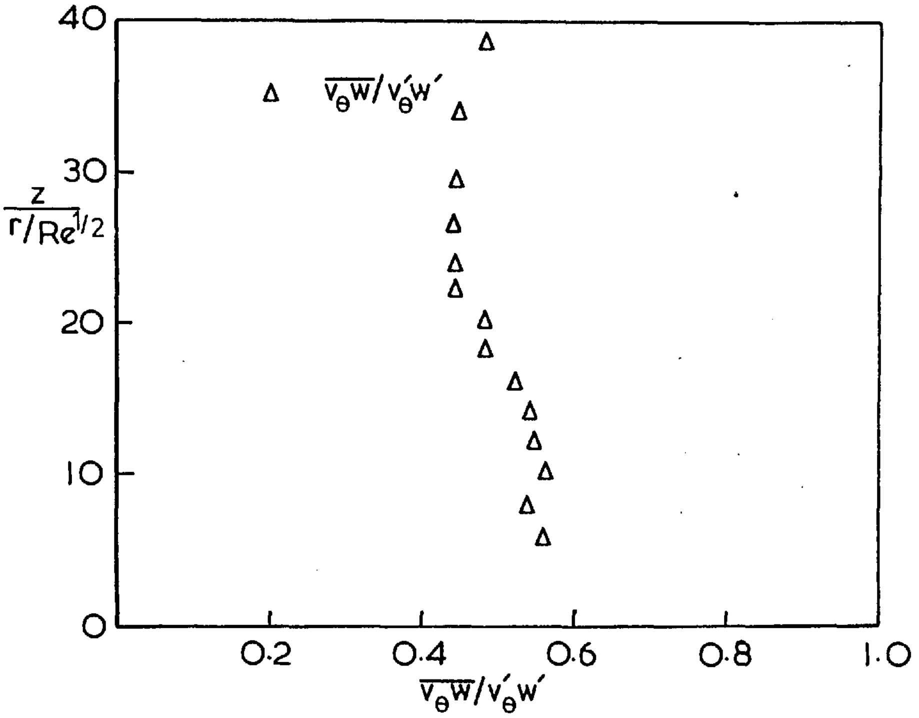

Fig. 47 COEFFICIENT OF CORRELATION ACROSS THE LAYER.

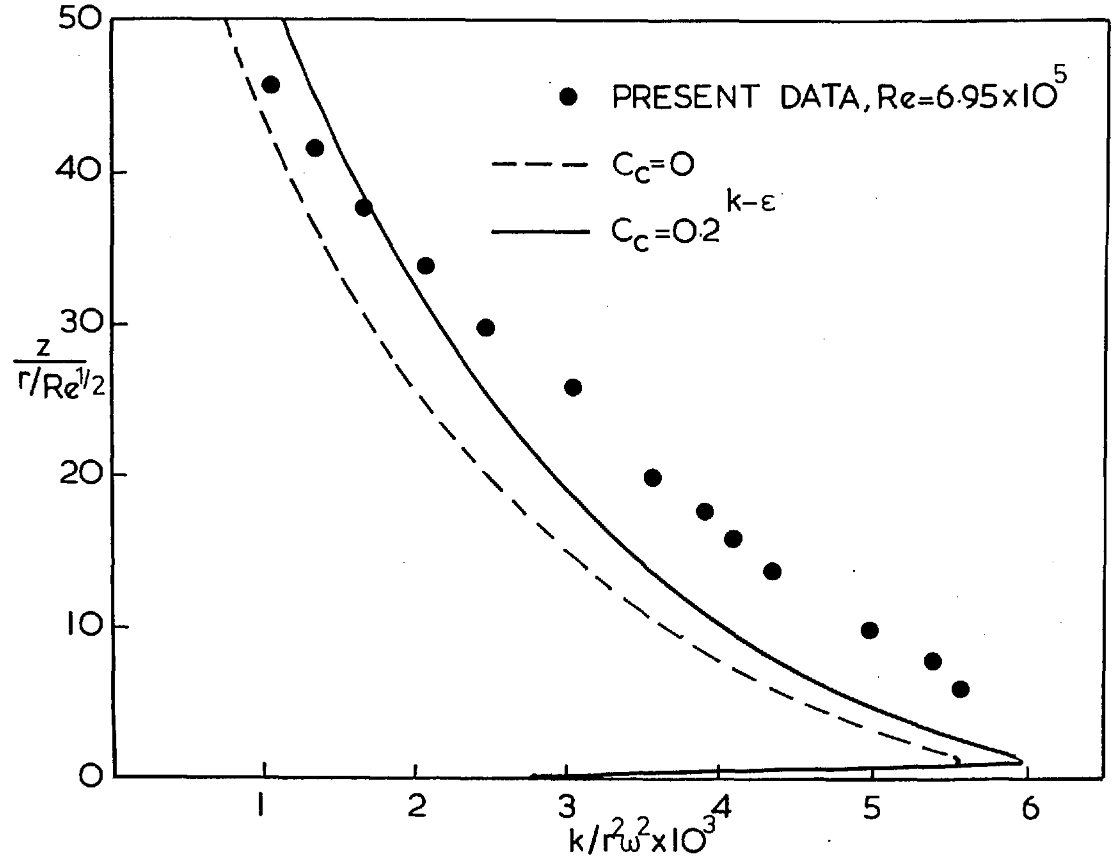

Fig. 48 TURBULENCE ENERGY PROFILES NEAR AN 80° SPINNING CONE.

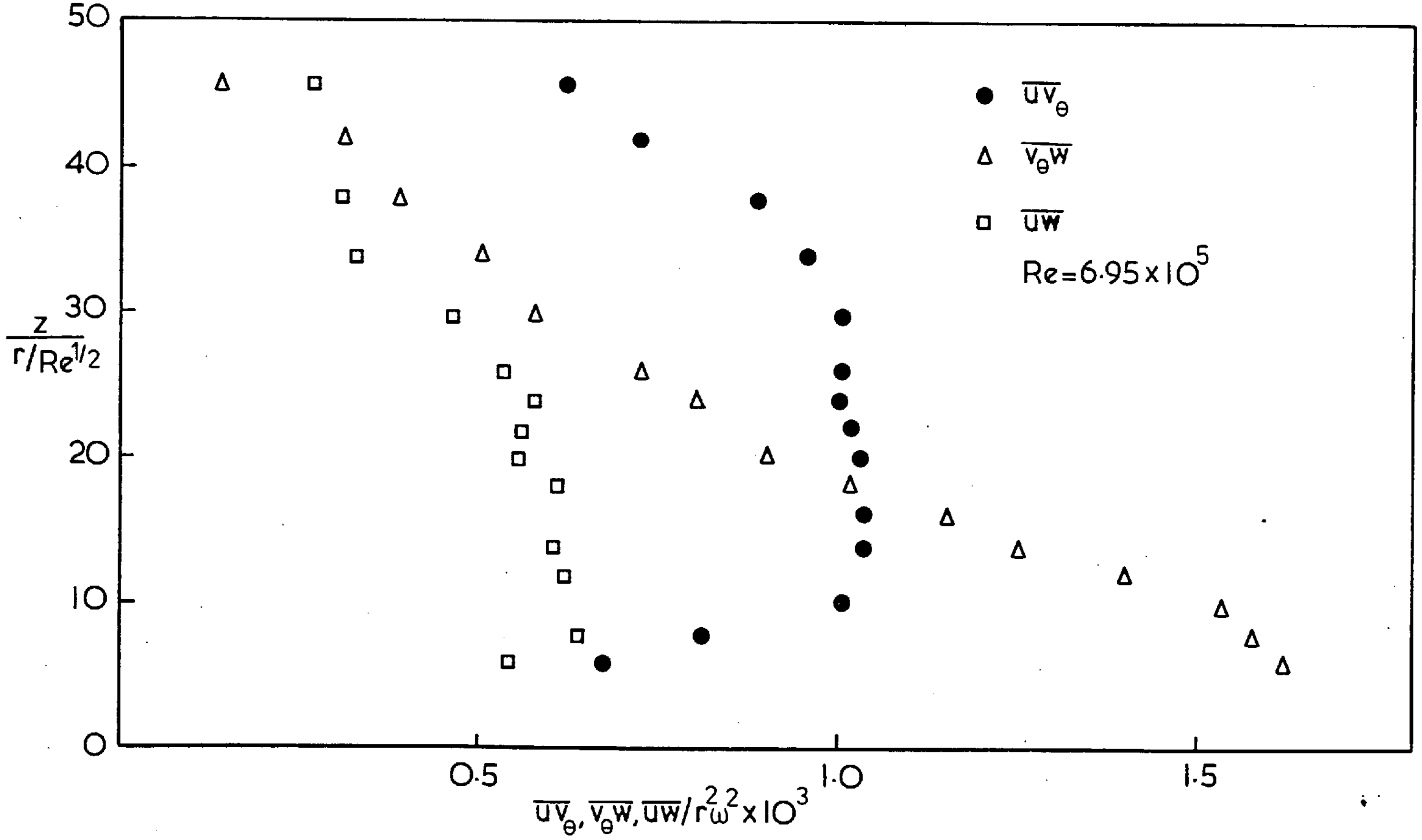

Fig. 49 SHEAR STRESS PROFILES NEAR AN 80° SPINNING CONE.

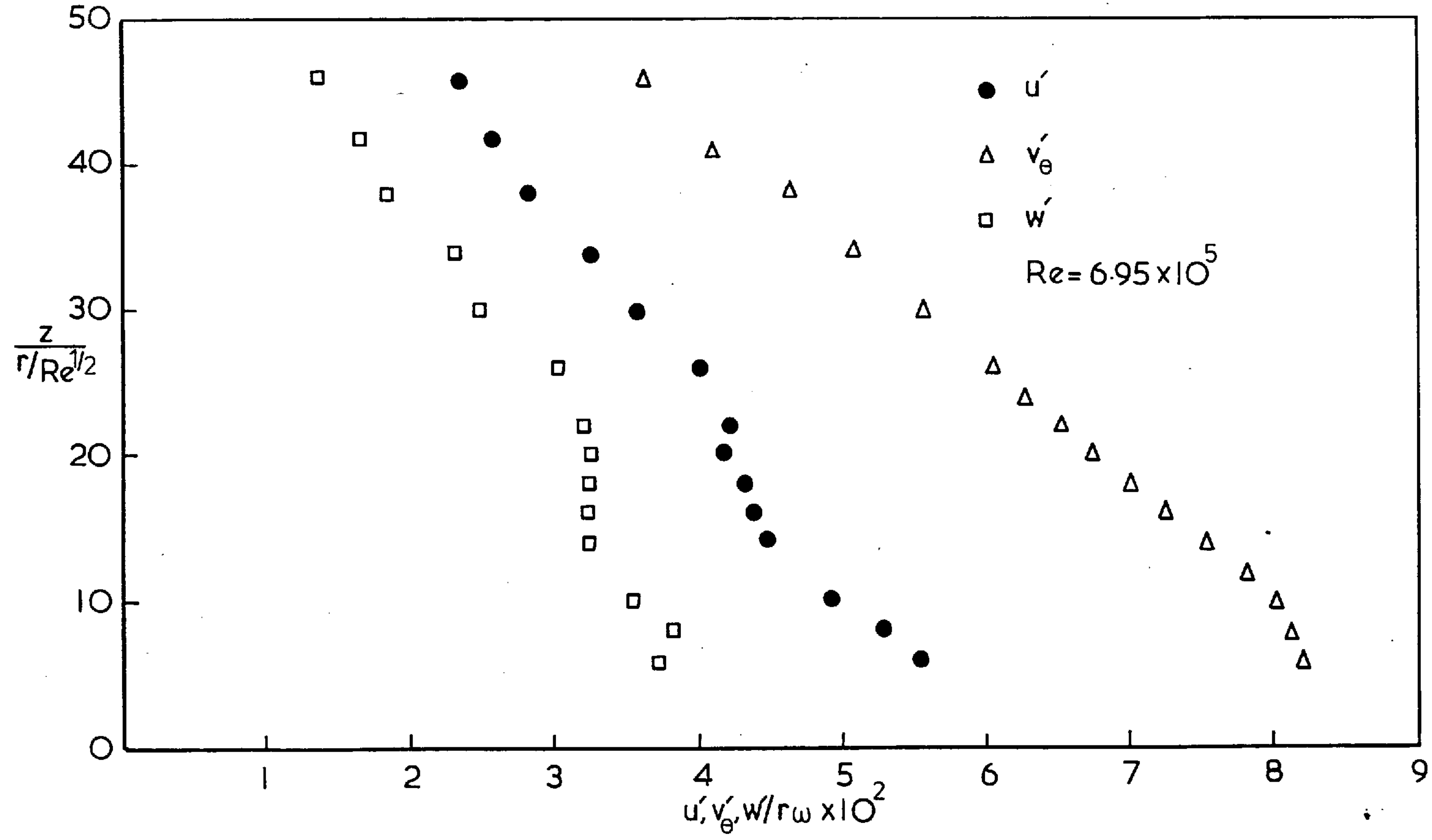

Fig. 50 RELATIVE TURBULENCE INTENSITY PROFILES NEAR AN 80° SPINNING CONE.

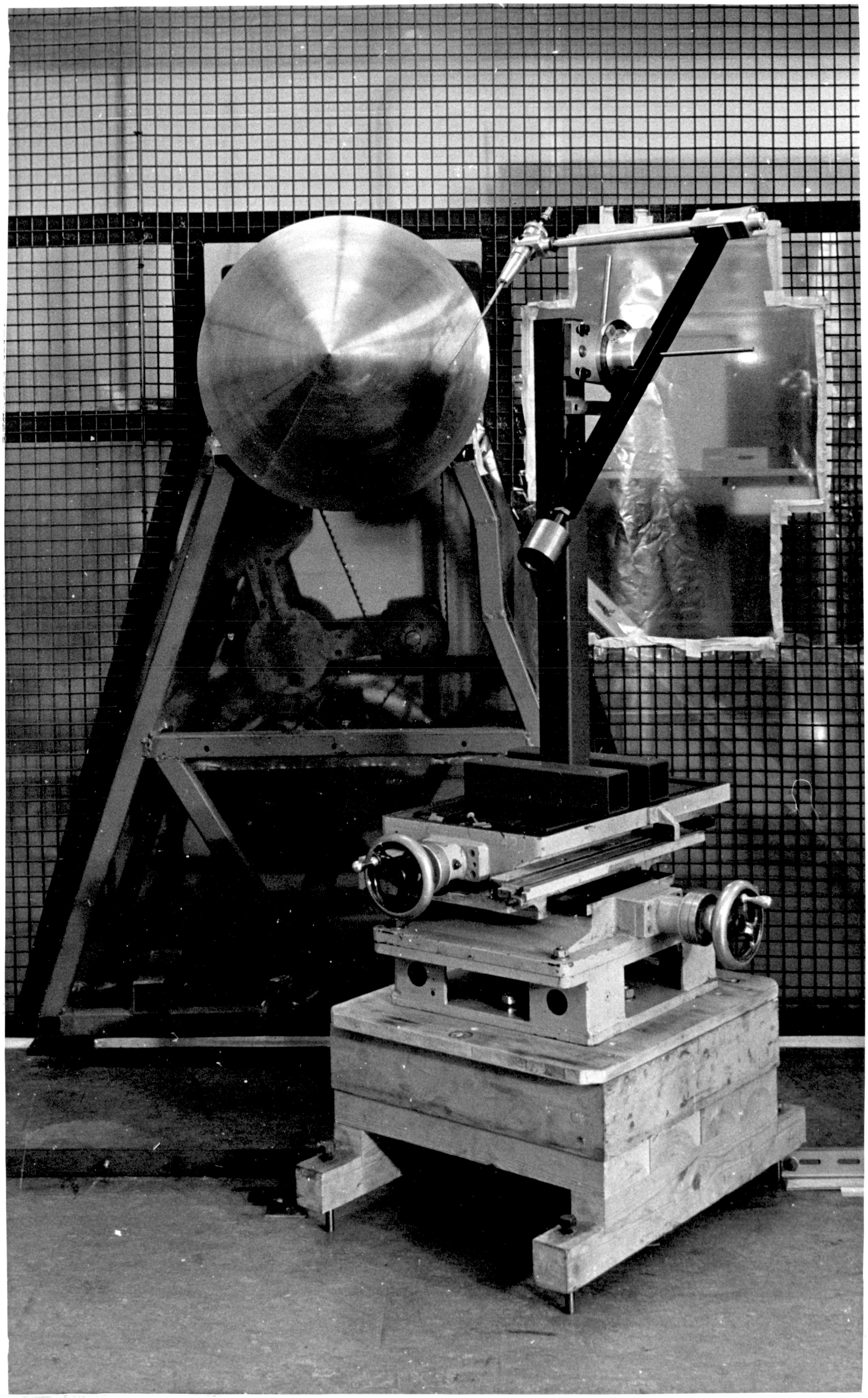

I. The spinning cone assembly.

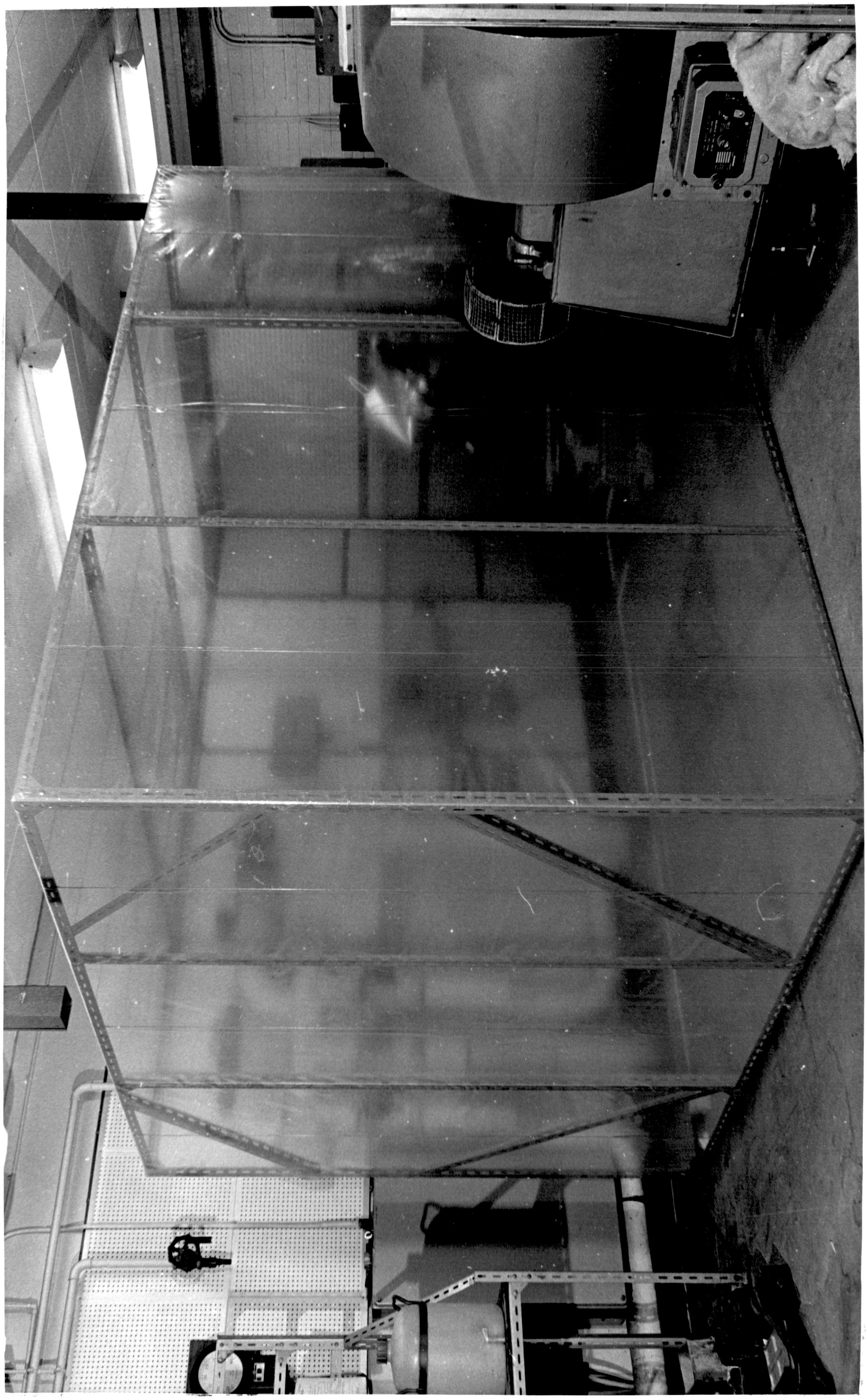

2. General layout of the rig.

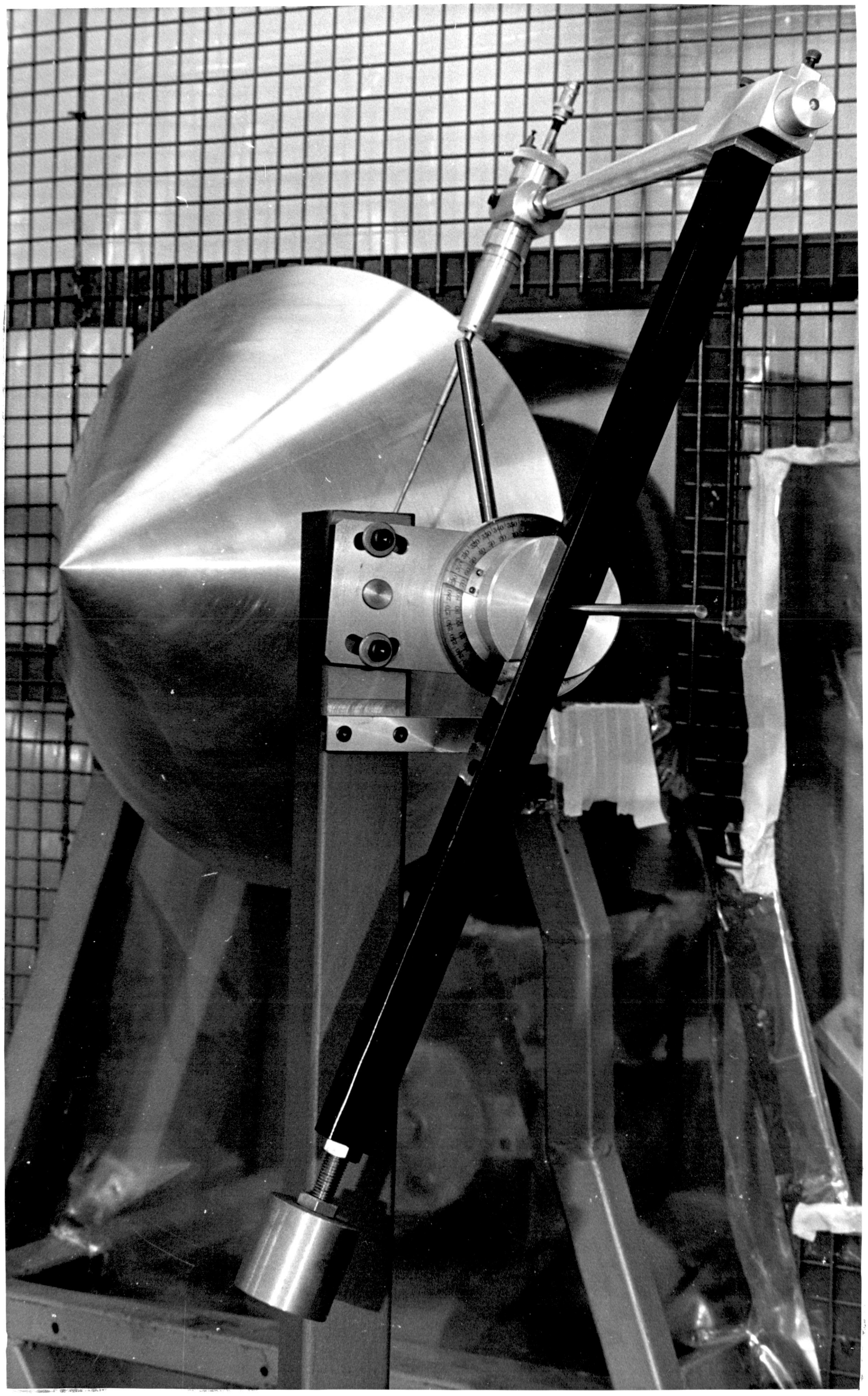

3. Traversing mechanism I.

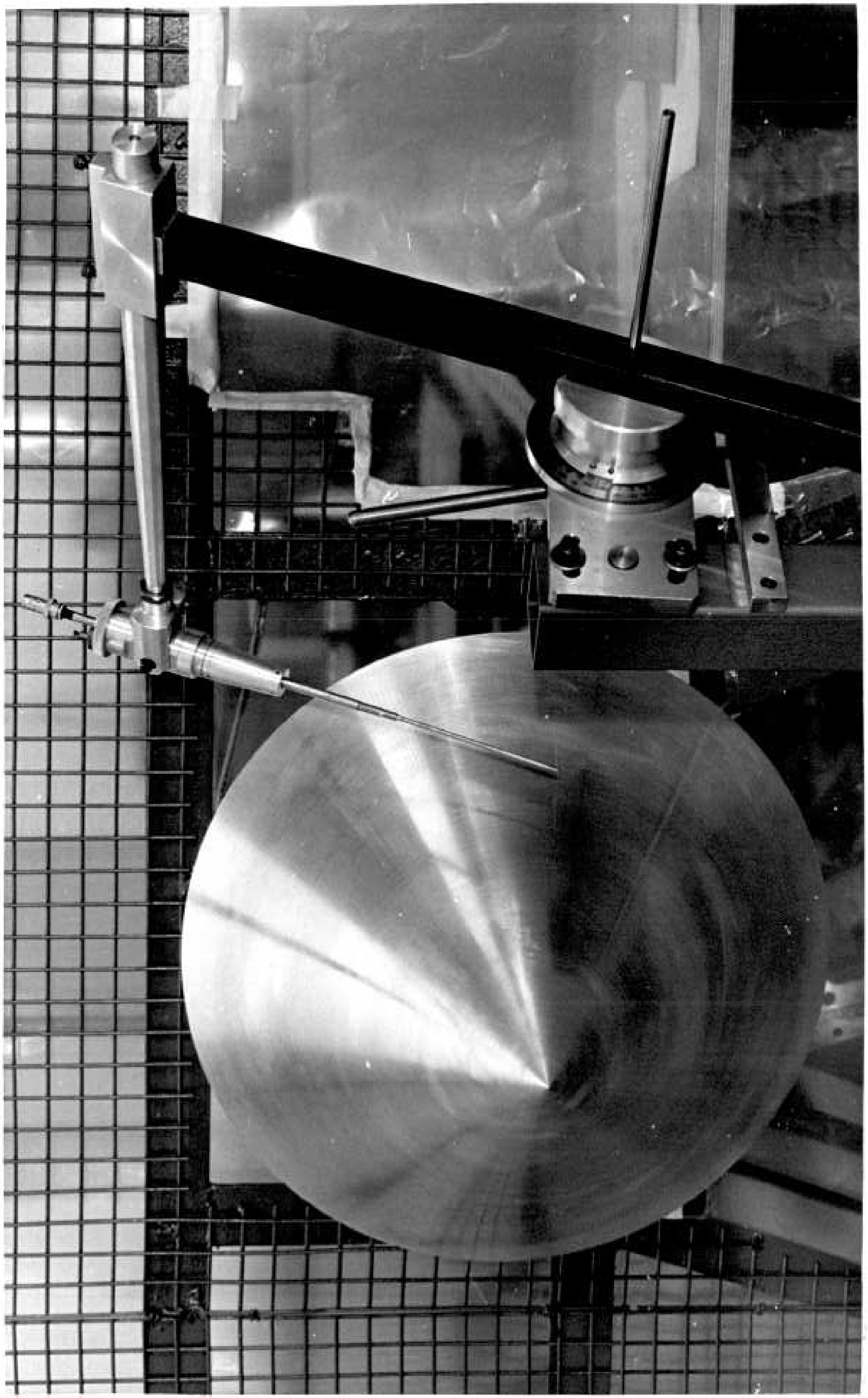

4. Traversing mechanism II.